Technische Universität München

Si on conductive self-organized TiO_2 nanotubes - A safe high capacity anode material for Li-ion batteries

Synthesis, physical and electrochemical characterization

Jassen Brumbarov

Vollständiger Abdruck der von der Fakultät für Physik der Technischen Universität München zur Erlangung des akademischen Grades eines Doktors der Naturwissenschaften genehmigten Dissertation.

Vorsitzende:
Prof. Dr. Nora Brambilla

Prüfende der Dissertation:
Prof. Dr. Julia Kunze-Liebhäuser
Prof. Dr. Peter Müller-Buschbaum

Die Dissertation wurde am 16.10.2020 bei der Technischen Universität München eingereicht und durch die Fakultät für Physik am 01.03.2021 angenommen.

Abstract

Si as an anode material for Li-ion batteries has a higher capacity for Li storage than graphite and overcomes the potential risks of Li plating and dendrite growth associated with graphite. TiO_2 offers high safety, long cycle life and high rate capability. Both materials are abundant and non-toxic, and are promising alternatives to graphite for the next generation Li-ion batteries.

Self-organized TiO_2 nanotubular arrays (TiO_2 NT) have been grown electrochemically on Ti metal. Carbon modified anatase TiO_2 nanotubular arrays (TiO_{2-x} -C NT) have been synthesized *via* a carbothermal treatment of the TiO_2 NT in a gas flow reactor using acetylene as a carbon source. Anatase TiO_2 nanotubular arrays (TiO_{2-x} NT) have been produced using the same thermal treatment but without the addition of a carbon source. Si coated TiO_{2-x} -C NT ($SiTiO_{2-x}$ -C NT) composite electrodes have been synthesized by the deposition of a thin layer of amorphous Si on the upper portion of the walls of the nanotubes of TiO_{2-x} -C NT.

In a first study, TiO_{2-x} NT and TiO_{2-x} -C NT electrodes were characterized using microscopic, (micro-)spectroscopic and diffractometric analysis tools, and their Li insertion properties were examined electrochemically in the potential window from 3 to 1.1 V vs. Li/Li^+. In a second study TiO_{2-x} -C NT and $SiTiO_{2-x}$ -C NT electrodes were characterized and compared using the same tools as in the first study, wherein the electrochemical characterization was carried out in an electrolyte with and without vinylene carbonate (VC) additive in the potential windows from 3 to 1.1 V vs. Li/Li^+ and from 0.04 to 3 V vs. Li/Li^+ . In a third study, the neutron capture reaction of ^6Li, producing a triton and an α -particle ($^6Li(n,\alpha)^3H$), was used to measure and trace the Li areal concentration on the macroscopic two-dimensional surface of lithiated TiO_{2-x} -C NT and $SiTiO_{2-x}$ -C NT electrodes, producing two-dimensional Li areal concentration maps. In a fourth study, grazing-incidence X-ray- and neutron-small-angle-scattering techniques were used to gain information on morphological parameters of the nanotubular arrays of TiO_{2-x} -C NT and $SiTiO_{2-x}$ -C NT electrodes with high statistical relevance over macroscopic electrode areas.

The four studies provided the following core insights:

1. Both TiO_{2-x} NT and TiO_{2-x} -C NT have the anatase TiO_2 structure. TiO_{2-x} -C NT electrodes have a superior lithium storage capacity and a better capacity retention over charge/discharge cycles with different cycling rates of up to 6C. This is attributed to an enhanced bulk conductivity due to oxygen vacancies, enhanced surface electronic conductivity, through a carbon layer formed on the surface, and stabilization of the reduced titania bulk through the addition of carbon all together resulting in an improved overall conductivity.

2. $SiTiO_{2-x}$ -C NT composite electrodes have a superior lithium storage capacity (~2.4 times higher) compared to TiO_{2-x} -C NT electrodes when lithiated down to 0.04 vs. Li/Li^+, where the VC additive in the electrolyte is essential for the cycling stability of the Si containing composite electrodes. The high utilization of the two active materials Si and TiO_{2-x} -C in the composite electrodes is attributed mainly to the good conductivity of TiO_{2-x} -C and to the low thicknesses of the Si layer and the walls of the nanotubes.

3. The Li mapping method based on the $^6Li(n,\alpha)^3H$ reaction is a powerful tool for studying lithiated electrodes. A weakness of the method is that it cannot be used *in situ* due to the high concentration of Li in the electrolyte of a Li-ion cell. The Li concentrations in the lithiated TiO_{2-x} -C NT and $SiTiO_{2-x}$ -C NT electrodes were comparable to the concentrations calculated from the stored charge measured electrochemically for lithiation down to 1.1 V vs. Li/Li^+, but they were significantly lower for lithiation down to 0.04 V vs. Li/Li^+. This is attributed to the accumulation of charge on the surface of the electrodes at the low lithiation potential, which is washed away in the preparation steps for the subsequent triton analysis. The surface concentration maps of Li on the TiO_{2-x} -C NT and $SiTiO_{2-x}$ -C NT electrodes showed “hot spots” on the surfaces with a higher concentration of Li, wherein some of them were found to originate from higher lengths of the nanotubes in these areas and others from a higher lithium storage capacity of the material itself.

4. The grazing-incidence small-angle-scattering techniques can only be used to characterize electrodes with a nanostructured active material when the surface-roughness of the carrier substrate is very low. Therefore, a Ti coated Si wafer was used as a substrate for growing the nanotubular arrays instead of the polished Ti discs used in the other studies, and a slightly altered nanotube growth procedure. Surprisingly, the nanotubular arrays were found to have a preferred crystallographic orientation which was not observed for the arrays grown on Ti disk substrates. The measurements provided the most prominent intertubular distance (center to center) for the nanotubular arrays of the studied electrodes, which was the same for both bare and silicon-coated nanotubes, whereas the most prominent inner radius for silicon-coated nanotubes is half the inner radius of bare nanotubes. Neutron scattering provided the porosity of the nanotubular arrays, which was the same, in the range of error, for both types of electrodes averaged over the entire film volume.

Contents

1 Introduction

1.1 Motivation

The demand for alternative energy sources and energy conversion systems is increasing, as fossil fuels are diminishing, their extraction becomes increasingly risky and expensive, and the environmental impact of their use gains importance in society. Automobiles are one of the applications for fossil fuels in combination with combustion engines where finding an alternative is most challenging. Since combustion engines have been developed and their performance improved for many decades, they have almost reached already their theoretically maximal efficiency and are very hard to reach in terms of price, energy density, power and safety simultaneously.

The two alternatives regarded as most promising by both science and industry are electric vehicles powered by fuel cells and rechargeable batteries. In both cases chemical energy is directly converted to electrical without going through thermal and mechanical energy, allowing for very high theoretical conversion efficiencies. Additionally none of the systems is using moving parts which makes them very reliable. Electric vehicles powered by fuel cell systems are using fuels from fossil or regenerative sources that can be quickly refilled and only the size of the tank is limiting the maximum distance the car can travel before refilling. On the other hand, the power output of the fuel cell stack is determined by its size making systems with a reasonable power too heavy if used mainly for short distances.

As the price of fuel cells is considered high compared to combustion engines it has to be mentioned that the price difference considering the whole systems is far smaller due to the expensive exhaust management of combustion engines formed by the amount of noble metals used as catalyst that is even about to increase with the new international regulations for exhaust gases. Fuel cell systems are using rechargeable batteries to ensure their efficient functioning, meaning that development in the battery sector is also beneficial for the future of fuel cell powered cars. In contrast to fuel cells and combustion engines, batteries are closed systems with a defined maximum amount of stored energy that depends on chemistry and size of the battery. That makes battery powered electric vehicles using state of the art chemistry of the cells too heavy and expensive when designed for long distances but superior to fuel cells when designed for shorter ranges [1].

On the other hand, battery systems do not need fuel supply and exhaust management which makes them simpler and more reliable. The maximum power output of a battery depends on the potential difference of its electrodes and the maximum allowed discharge rate of the cell. Figure 1 shows an overview of state of the art secondary battery systems in a Ragone chart (Specific Power vs. Specific Energy) [2].

Among the family of rechargeable batteries, lithium-ion batteries are attracting the most interest for the automotive application due to their high power, energy density and cycle life. However their energy density is still not sufficient for long distance travels and recharging of large systems is very slow. Furthermore, there are serious safety and environmental concerns with today's common chemistry of the cells.

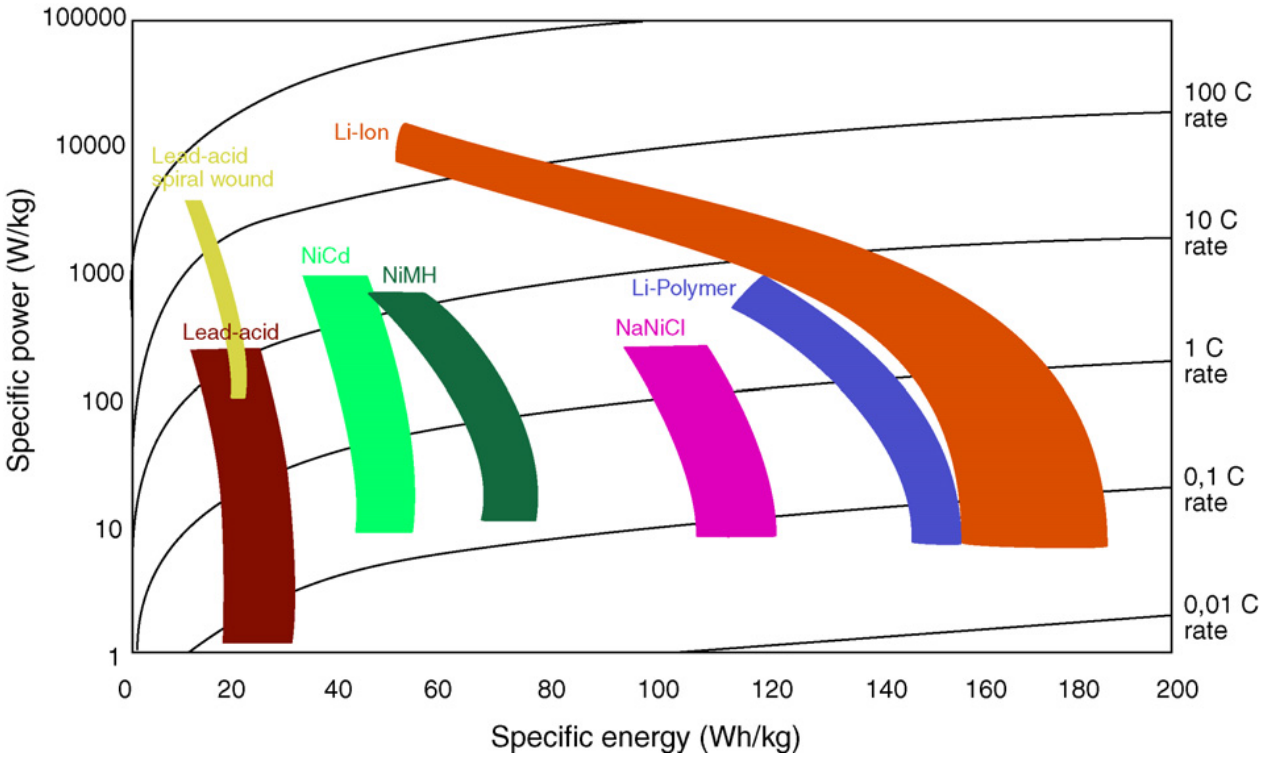

Figure 1: Ragone chart of different battery types [2].

1.2 Li-ion Batteries - cell design

A Li-ion cell consists of two electrodes and a separator soaked with electrolyte and pressed between them (Figure 2). The separator and the electrolyte are electrically insulating but ion conducting preventing short circuiting between the two electrodes and forcing the electrons to travel through the external circuit that powers a load, while allowing Li^+ ions to migrate through the electrolyte between the electrodes and thus closing the circuit. The electrode where Li^0 is oxidized giving away one e^- and becoming Li^+ ion, is called anode and the electrode where Li^+ is reduced to Li^0 by capturing one e^- is called cathode. That means that the same electrode that is an anode upon discharge is a cathode when the cell is being charged. In order to avoid confusions, the two cell electrodes are named anode and cathode with respect to the discharge process. The term anode material is referring to the active material of the electrode that is acting as an anode upon cell discharge in a full cell. The two electrodes are made of different active materials, each having a different electrochemical potential (see Figure 3) with the difference of the two potentials determining the cell voltage which is the driving force for ions and electrons when the cell is discharged. In order to charge a battery an external energy source is connected to it creating an electrical field inside the cell with the opposite direction to the field of discharge, forcing the ions back to the anode. Due to cell overpotentials, a higher voltage is needed to charge the cell than the voltage that is established at open circuit for the given state of charge.

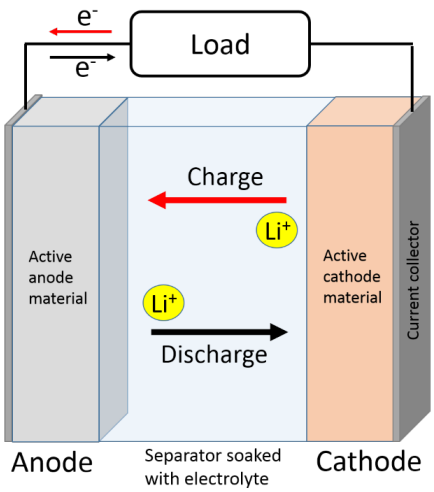

Figure 2: Schematics of a Li-ion Battery cell.

In the field of battery research, the specific lithium storage capacity of an electrode is usually expressed as the amount of electrical charge it can store per unit of mass and reported in units of mA h g^{-1} or A h kg^{-1} equivalent to 3.6 C g^{-1} (1 C = 1 A s). Both electrodes of a battery cell

should usually have the same capacity to store charge, since the same amount of lithium that is taken out of one of the electrodes, upon charging or discharging, is stored in the other electrode. The different active materials used for the two electrodes however, have different specific lithium storage capacities and therefore, their amounts are balanced to compensate for this difference. In some cell designs, for safety reasons or in order to prolong cell life, one of the electrodes might have a higher capacity. In such a case, the lower of the two electrode capacities determines the maximal cell capacity.

In order to compare the charge/discharge rate capabilities of battery cells and individual electrodes having different capacities, one uses the so called C-rate, which is defined as the ratio between the used discharge current and the electrical current necessary for fully discharging a battery cell in one hour. Full discharge is reached when the cell voltage falls under a predetermined value. Referring to one electrode, the C-rate is the ratio between the used lithiation/delithiation current and the current necessary for fully lithiating/delithiating the electrode in one hour. Full lithiation/delithiation is reached when the potential of the electrode falls below or rises above a predetermined value, respectively.

Current Li-ion batteries for electric vehicles have a specific energy of ~120 Wh_{total}/kg_{pack}. Pack components make 50% of the battery mass and the rest is distributed between the cell components (electrodes, electrolyte, separator, barrier layers etc.) [1]. Each electrode is composed of a current collector and electrode material comprising an active component, conduction enhancing additive and a binder. Among the cell components ~70% of the mass goes to the electrode materials. That means that if the specific energy of the battery is to be increased, the largest room for improvement is offered by the pack components and the electrode materials.

1.3 Materials for Li-ion batteries

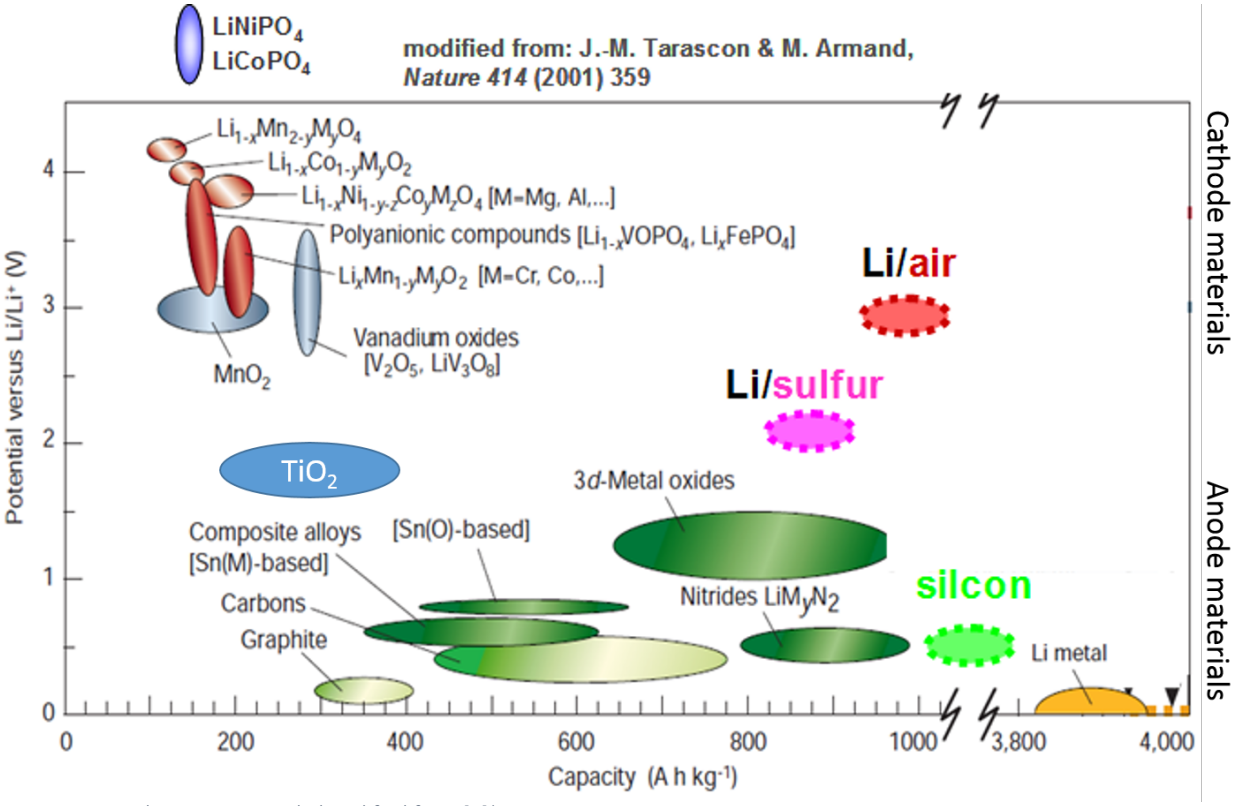

Figure 3: Li-ion battery materials (modified from [3]*).*

Figure 3 shows an overview of Li-ion battery materials including high capacity materials. The Li/air system is shown for reference even though it does not represent a battery in the classical sense as it is a semi open system. The material specific lithiation/delithiation potentials are represented against the Li/Li^+ redox potential (set at 0V) and the specific capacity of the materials to store charge in the form of lithium ions is measured in A h kg^{-1} (equivalent to 3.6 C g^{-1}). TiO_2 [4] is a material with a superior safety compared to lithium metal or graphite and other carbons due to its higher lithiation/delithiation potential. Its charge storage capacity is comparable to that of graphite. The material is also cheap, readily available, has a long cycle life and good chemical stability. Its properties for the battery application can be improved exploiting the possibility of nano-structuring the material employing relatively simple and inexpensive electrochemical methods. Silicon is capable of storing large amounts of lithium while being safer than lithium metal due to its higher lithiation/delithiation potential.

1.3.1 Cathode materials

According to the envisioned application, there is a big variety of cathode materials being used in commercial cells such as $LiFePO_4$ (160 mA h g^{-1}), $LiMn_2O_4$ (spinel, 140 mA h g^{-1}) or $LiNi_{0.33}Mn_{0.33}Co_{0.33}O_2$ (180 mA h g^{-1}). Each material is selected based on its specific properties beside capacity and potential. $LiFePO_4$ (LFP) for example has an extraordinarily high cycle life and allows charge and discharge rates unmatched so far making it the material of choice for high power applications or when a cell is needed that is capable of cycling for thousands of cycles without losing its capacity (LFP combined with TiO_2 as anode).

In LFP, there are no rare or toxic metals making it relatively cheap and environmentally friendly. For electrical vehicles however, where a higher energy density of the cell is needed, the cathode material needs to have a higher potential and/or higher specific capacity than state of the art.

High potential (above 5V) materials like $LiNiPO_4$ or $LiCoPO_4$ (see Figure 3) have the drawback of electrolyte decomposition on the cathode. A way to deal with that issue that is being investigated is replacing the common electrolytes by ionic liquids that are designed to be stable in a broad potential window. Ionic liquids, however, are difficult to synthesize and purify which makes them quite expensive.

Another option for increasing the energy density of a cell that is being studied extensively in the recent years and that is considered most promising, is the use of sulfur as a cathode material. Sulfur has a theoretical specific capacity of 1675 mA h g^{-1} when fully lithiated to Li_2S [5], which is over six times more than what conventional materials offer. Even though with 2.15V, Li_2S has a ~2/3 lower potential than state of the art materials, its capacity is still so much greater that its energy density is the highest. Additionally, sulfur is the cheapest cathode material. There are, however, big issues for the development of a practical sulfur electrode [6,7] like the formation of polysulfides which are soluble in liquid electrolytes causing an internal discharge of the cell by migrating to the anode (shuttle mechanism) and blocking the electrodes by forming an insulating layer.

1.3.2 Anode materials

1.3.2.1 Lithium metal

Among all anode materials, lithium metal has the highest capacity and the lowest potential. However, such a low potential means that the Li metal is highly reactive thus causing electrolyte decomposition. Upon charging, lithium is deposited on the surface of the anode and removed again on discharge. Thus, the surface of the electrode is constantly changing and electrolyte is continuously decomposed on the freshly exposed Li. Redeposited Li can form dendrites on the anode that can penetrate through the separator and short-circuit the cell. The high current flowing when the cell is short-circuited heats up the cell locally, which causes rapid electrolyte degradation, degasing and fire (in the case of flammable electrolyte). That is why lithium is generally being avoided and safer materials are being used on the cost of lower specific capacity and cell voltage.

1.3.2.2 Carbon

State of the art Li-ion cells employ carbonaceous anode materials like graphite with a specific capacity of 372 mA h g^{-1}. In graphite, lithium is intercalated between its graphene sheets up to a ratio of one lithium atom per six carbon atoms at potentials below 0.2V vs. Li/Li^+ [8] corresponding to the specific capacity of 372 mA h g^{-1}. The main advantages of graphite in comparison with other anode materials are its low price, high electronic conductivity, nontoxicity and low lithiation/delithiation potential allowing for high cell voltages. Due to the low potential, however, there is the risk of lithium metal plating and dendrite growth on the surface of graphite upon cell charging if the charging current is too high and/or the temperature (and thus reaction kinetics) too low. During lithium intercalation, there is the possibility of solvent molecules being dragged together with the Li^+ ion between the graphene sheets of graphite leading to a fast electrode disintegration. Therefore, the electrolytes used in conjunction with graphite are chosen such that they partially decompose on the surface of graphite upon lithiation, thus forming a solid electrolyte interface (SEI), which acts as a barrier for the solvent molecules. A stable SEI on the surface of graphite is thus crucial for its cycling stability providing a Li^+ ion conducting but electrically insulating shell that prevents solvent molecules from passing through and from decomposing further on the surface. To improve the properties of the SEI layer electrolyte additives like vinylene-carbonate (VC) or fluoroethylene-carbonate (FEC) are commonly used.

1.3.2.3 Silicon

The most promising high capacity anode material currently under study is Si, offering 3580 mA h g^{-1} when lithiated to its lithium richest form (at room temperature) $Li_{15}Si_4$ [9]. Silicon has a slightly higher conversion potential of ~0.5V compared to graphite and in contrast to graphite, it is forming an alloy with lithium upon lithiation, which reduces the risk of lithium plating and dendrite growth on the anode and thus increases the safety of the cell on the cost of a small voltage loss. However, lithium silicates with a high lithium content prove to be comparable to lithium metal in terms of reactivity which somewhat reduces the improvement in safety using silicon anodes. On the other hand, silicon has an almost 10 times higher theoretical capacity than graphite.

The biggest challenge for producing a practical silicon electrode is the high volumetric expansion of silicon of up to 280% upon lithiation [10,11] that leads to cracking and pulverization of the electrode. The large surface area change upon lithiation/delithiation due to the volumetric expansion/shrinking leads to cracking of the SEI layer and formation of fresh SEI on the newly exposed silicon. This process consumes lithium and leads to thickening of the passivation layer, which leads to an increase of the internal resistance of the cell. The properties of the SEI can be improved by certain additives in the electrolyte, like VC for a carbonate electrolyte, to mitigate these issues [12,13]. Furthermore, as Leveau *et al.* have shown [14], limiting the delithiation potential to 0.8 V and/or the specific charge to be cycled upon lithiation/delithiation to an intermediate value (900 mA h g^{-1}), significantly improves the cycle life of the electrode. Thin films of silicon have proven to generally perform better than micro particles and to have a much higher cycling stability [11,15-17].

The superior capacity and rate capability of thin silicon films can be attributed to the short diffusion path for Li^+-ions and electrons in the film-thickness direction and to their high surface to volume ratio allowing for fast ion transport to and from the volume of the material. The reduced film thickness results in reduced composition and deformation gradients leading to improved mechanical and thus cycling stability [17]. Due to the preferential increase of film volume through increase in film thickness, in the case of thin films, the increase in surface area and the consequent SEI cracking are minimized adding to the stability of the electrode.

Green *et al.* [18] proposed a mechanism for the lithiation of silicon comprising the following steps (starting from the situation where a surface layer of Li_xSi is already formed on the silicon):

- Li^+ from the electrolyte is adsorbed on the surface of the Li_xSi layer receiving an electron;
- Lithium enters a vacancy in the Li_xSi becoming Li^0 and diffuses through vacancy hopping towards the Li_xSi/Si interface;
- Lithium then reacts with silicon to form Li_xSi alloy thus pushing the Li_xSi/Si interface further towards the unreacted silicon.

The reverse process being roughly speaking the opposite:

- Li^0 from the electrolyte boundary is ionized entering the electrolyte leaving behind a vacancy in the Li_xSi;
- Neighboring Li^0 occupy the vacancy thus the vacancy moves towards the Li_xSi/Si interface;
- At the interface, Si rejoins the bulk Si and the interface is moved towards the electrolyte.

The work of Wang *et al.* [11] supported this model showing that the lithiation of amorphous silicon is a two phase process where a Li_xSi/Si interface propagates in the amorphous silicon material until its full conversion to Li_xSi (x~2.5). The movement of the Li_xSi/Si interface reduces the strain in the Li_xSi phase. Due to this mechanism, concentration gradient of lithium in the Li_xSi phase is negligible. Further lithiation to $Li_{3.75}Si$ proceeds without a visible phase boundary.

1.3.2.4 Titania

Titania (TiO_2) is an intercalation material that is extensively studied in terms of its lithium storage capacity [19]. There are eight different crystalline forms of titania from which anatase, rutile and brookite are found in nature. Titania in the anatase form can be lithiated at around 1.76V vs. Li/Li^+ and its lithiation is known to be highly reversible even at high lithiation/delithiation rates making it a good candidate for high power applications. Additionally, the material stays at a constant potential over a broad range in lithiation degree due to the coexistence of two lithiated phases of anatase in that range which is particularly favorable property for battery powered electronic devices, which require a constant voltage.

Even though the specific capacity of anatase is far lower than the capacity of silicon, it can still reach 335 mA h g^{-1} (in nanostructured form or at high temperature) which is almost the capacity of graphite (372 mA h g^{-1}). On the cost of lower cell voltage due to its relatively high lithiation potential, titania is safer than state of the art anode materials eliminating the risk of lithium plating. Also due to the high potential, SEI formation on titania electrodes is negligible, minimizing the lithium losses and inner cell resistance induced by SEI formation. However, lithiating at low potentials around 1.1V vs. Li/Li^+, leads to SEI formation which influences the electrode performance. Anatase is impermeable to solvent molecules or other electrolyte components allowing only lithium ions to enter its structure. That is why the formation of an SEI layer on titania is not needed for a good cycling performance in contrast to graphite. The low volumetric expansion of ~ 3% [19] of anatase and the low reactivity of its lithiated phases allow for the extraordinary cycling stability of anatase over thousands of cycles.

Additional advantages of titania are its low price, non-toxicity and the possibility for a well-controlled electrochemical growth of nanostructured oxide, which is characteristic for valve metals. Self-assembled titania nanotubes can be grown electrochemically on a titanium metal substrate. As an anode material they have the advantage of direct contact with the titanium that serves as a current collector, which eliminates the necessity to use conductive additives and binders in the electrode, and which makes the whole electrode material active for lithium storage [4].

1.4 Lithiation of anatase - size dependent effects from micro to nano

Li^+- ion mobility in classical electrolytes like 0.2M $LiPF_6$ in a 3:7 mixture of ethylene carbonate (EC) and ethyl methyl carbonate (EMC) is $4.1x10^{-6}$ cm^2 s^{-1} [20] which is a million times larger than the mobility in solid anode materials like graphite $6.5x10^{-15}$ cm^2 s^{-1} [21] and TiO_2 anatase $4.7x10^{-12}$ cm^2 s^{-1} [22] or cathode materials like spinel $LiMn_2O_4$ with $2.1x10^{-12}$ cm^2 s^{-1} [23] and $LiFePO_4$ with $1.8x10^{-14}$ cm^2 s^{-1} [24]. This indicates that the mobility of Li^+-ions in the solid electrode materials is an important factor that limits the obtainable charge and discharge rates.

Recent research has shown that nano-structured active materials for Li-ion batteries allow for higher lithiation and delithiation rates due to shorter diffusion paths for Li^+ ions and electrons and a larger active surface area. It enables the kinetically slow formation of lithium rich phases that would be virtually impossible in larger particles at room temperature and increases the

capacity for surface storage of lithium in the form of adsorbed species. This allows for use of new active materials that become fully accessible for lithiation only in their nanoscale form and improves the ability of the active materials to handle the accumulation of defects upon cycling, which prolongs their cycle life.

On the other hand, increasing the active surface area increases the proportion of surface reactions. Some of these reactions are reversible and contribute to the lithium storage capacity of the electrode, while others are irreversible, like the SEI formation on the electrode, which is a barrier (overpotential) for lithiation and delithiation, and additionally consumes lithium from the electrolyte.

Reducing the sizes of the particles of an active material, however, not only reduces the diffusion lengths for Li^+ but also changes the mechanism of Li^+ insertion. The size effects on the lithiation of the active material were well studied for anatase TiO_2 in particle [19,25] and in nanotubular [26] shape showing the same size dependent trends (see Figure 5, Figure 6 and Figure 8). Titania is an advantageous material for studying size effects thanks to the good stability of classical carbonate-based electrolytes in the potential window for bulk lithiation and thus the intrinsic properties of the material can be studied. Additionally, TiO_2 films with well controlled morphology can be grown electrochemically on the surface of titanium, ranging from compact to porous layers and self-organized nanotubes. Thus, different nano-sized TiO_2 materials can be designed to have the same bulk material thickness but different macroscopic morphologies, which allows the estimation of the additional effect of the particular morphology. The properties of a compact film, for example, can be compared with the properties of nanotubes having a wall thickness equal to the thickness of the compact film.

In the work of W. Borghols, the particle size effect on lithiation properties of the most commonly used TiO_2 forms anatase, rutile and $Li_{4+x}Ti_5O_{12}$ spinel was studied [19]. Wagemaker *et al.* further investigated the non-equilibrium phase transition upon lithiation of anatase TiO_2 and the impact of particle-size [25].

Figure 4 shows the change in electrode potential upon lithiation of nanostructured anatase. Figure 5 shows the particle size dependent phase diagram for lithiated anatase presented in [19] and Figure 6 is an illustration of how lithiated phases are formed depending on particle size corresponding to the phase diagram.

Four regions can be distinguished in Figure 4. In the first region (blue zone in Figure 4), the Li content is continuously increasing while the potential of the electrode is dropping rapidly to ~1.76V. In larger particles (> 120nm) this region is mainly explained by Li going in solid solution in anatase forming α-Li_xTiO_2 with x depending on particle size (x ~ 0.026 in micro-anatase TiO_2 in equilibrium [27]). The formation of α-Li_xTiO_2 induces stress in the crystal lattice. The tetragonal structure of anatase, however, is preserved with slightly larger atomic distances. As the lattice stress becomes larger upon further lithiation, the point is reached where no more lithium can go in solid solution and the crystal structure changes from tetragonal to the orthorhombic β-Li_yTiO_2 with (y ~ 0.55 in micro-anatase TiO_2 in equilibrium [27]). With decreasing particle size it becomes easier to release this induced stress and thus more lithium can go in solid solution without forcing a crystal phase transformation.

The region where the two phases coexist, each having a constant (equilibrium) composition, with the β-Li_yTiO_2 phase growing on the expense of the lithium poor α-Li_xTiO_2 phase upon lithiation, is marked by a potential plateau (orange region) in Figure 4. In large particles, the two phases coexist within each particle until the whole material is transformed (Figure 5 and Figure 6). Reducing particle size, this plateau region shrinks while the preceding non-equilibrium region grows. It was found that the orthorhombic β-Li_yTiO_2 phase starts forming already in the non-equilibrium region before the potential plateau, where its Li content is below the equilibrium one. The α and β phases share a plane with a zero misfit strain, which makes the nucleation of the β phase easier and allows its rapid growth after nucleation until reaching ~ 100nm [28]. The low diffusion coefficients for Li (10^{-18} to 10^{-16} $cm^2\ s^{-1}$), however, leads to the non-equilibrium situation where the Li supply is slower than the β phase growth even at very low lithiation rates (C/120). Independent on particle size, in the initial stage of lithiation the β phase grows mainly through nucleation of new sites rather than through growth of individual sites and phase boundary movement. In small particles, a newly nucleated β phase site quickly transforms the whole particle before an equilibrium Li content is reached, while the transformation did not start yet in other particles, thus a phase boundary is practically not observed (Figure 5 and Figure 6).

Therefore, in contrast to large particles, where the two phases coexist within each particle, in small particles, the conversion takes place particle by particle. In large particles Li is supplied to the β phase from the outside through the α phase, while in small particles the α phase does not coexist with the β phase in the same particle and it takes longer until the β phase reaches its equilibrium composition. Therefore, in small particles, the potential plateau is smaller and the non-equilibrium region marking continuously changing Li content is larger. In contrast, in larger

particles, the Li content of the β phase quickly reaches equilibrium and the β phase continues growing by expanding the phase boundary while the compositions of the two phases are in equilibrium. Additionally, an important finding for small particles is the presence of surface sites having a lower energy and thus a higher voltage which contributes to the more gradual decrease in potential in the non-equilibrium region upon lithiation.

Belak et. al. have shown that lithium ion diffusion in the β-Li_yTiO_2 phase in direction towards the phase boundary is strongly hindered and thus lithium supply for the phase growth can only be maintained through the lithium poor α-Li_xTiO_2 phase [28] (see Figure 7). In case of a particle where the whole surface is covered by the β-Li_yTiO_2 phase, this would prevent the full conversion of the material. In general, as lithium goes in solid solution in anatase or β-Li_yTiO_2, the electronic conductivity of the respective phase increases and the ionic conductivity decreases. However, as the crystal structure of the material changes so does its electronic and ionic conductivity. Even though β-Li_yTiO_2 hosts more lithium than the lithium poor α-Li_xTiO_2 its resistivity is three to four times higher (ρ_β = 6 x 10^{-5} Ω cm and ρ_α = 1.5 x 10^{-5} Ω cm) due to the different crystal structure.

Once all particles are transformed into β-Li_yTiO_2 with the amount of lithium increasing further the potential goes down again as the process repeats with lithium first going in solid solution in β-Li_yTiO_2 (above the equilibrium content) until the solubility limit is reached and the γ-$LiTiO_2$ (Li_1TiO_2) phase starts forming on their surface (green zone in Figure 4). γ-$LiTiO_2$ is the highest lithiated form for anatase with 1 Li per TiO_2 having the same tetragonal crystal structure as anatase but larger unit cell parameters and a very low ionic conductivity. The γ-$LiTiO_2$ phase is growing on the expense of β-Li_yTiO_2 (Figure 5 and Figure 6) forming another very small potential plateau (visible for small particles of < 15 nm, green zone in Figure 4), until the lithium-ion supply stops because of too low ion conductivity.

Due to the very low ionic conductivity of the γ-$LiTiO_2$ phase, only very small particles of < 7nm can be completely transformed at room temperature (Figure 5 and Figure 6). Even though anatase cannot host more than one lithium per TiO_2 molecule (γ-$LiTiO_2$ phase), still a significant amount of charge can be stored on the surface of nanostructured materials and in the electric double layer (EDL) of the electrode-electrolyte interface because of the high surface to volume ratio of nanostructured materials. This phenomenon is visible in the gray zone of Figure 4. Generally, with decreasing particle sizes below 120nm, the features in the potential vs. capacity curve start to smear. The non-equilibrium regions expand, the potential plateaus, characteristic for the (equilibrium) two-phase regions, become sloping with the orange zone (Figure 4) changing first followed by the green zone at even lower particle sizes. The relative increase of the portions where the potential is changing leads to a higher capacitive contribution to the total current and to the total charge, respectively.

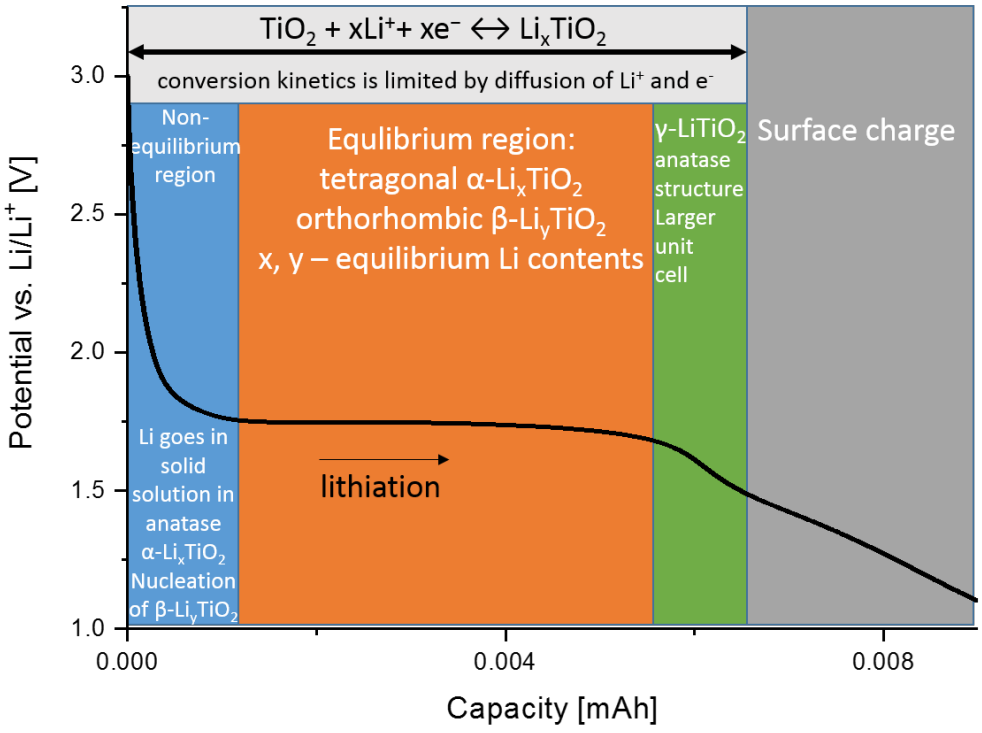

Figure 4 Lithiation of nanostructured anatase TiO_2. In the non-equilibrium region (blue), both x and y standing for the Li contents of the α-Li_xTiO_2 and β-Li_yTiO_2 phases, respectively, are below the respective equilibrium values. In the equilibrium region (orange), x and y are equal to the respective equilibrium Li contents.

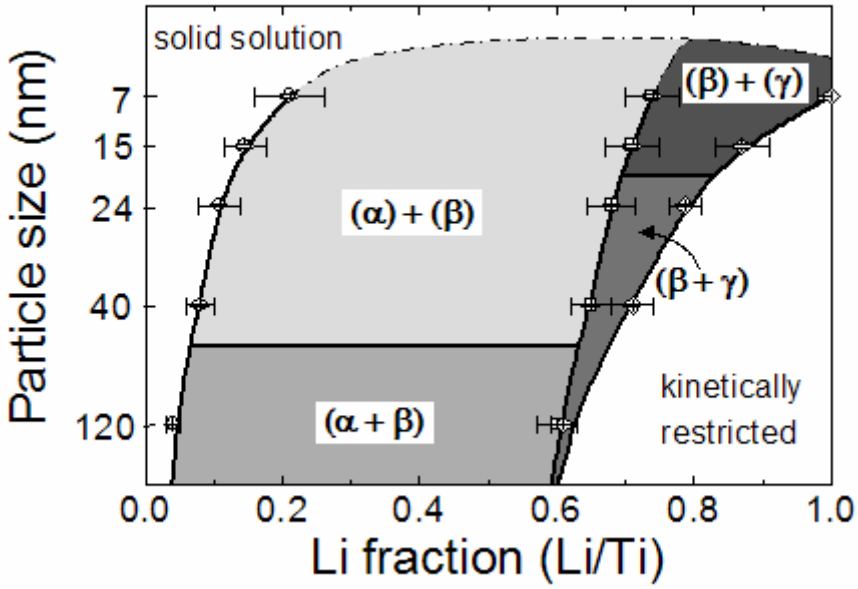

Figure 5: Li_xTiO_2 phase diagramm with tetragonal α- Li_xTiO_2, orthorhombic β- Li_yTiO_2 and tetragonal γ- Li_1TiO_2. From [19].

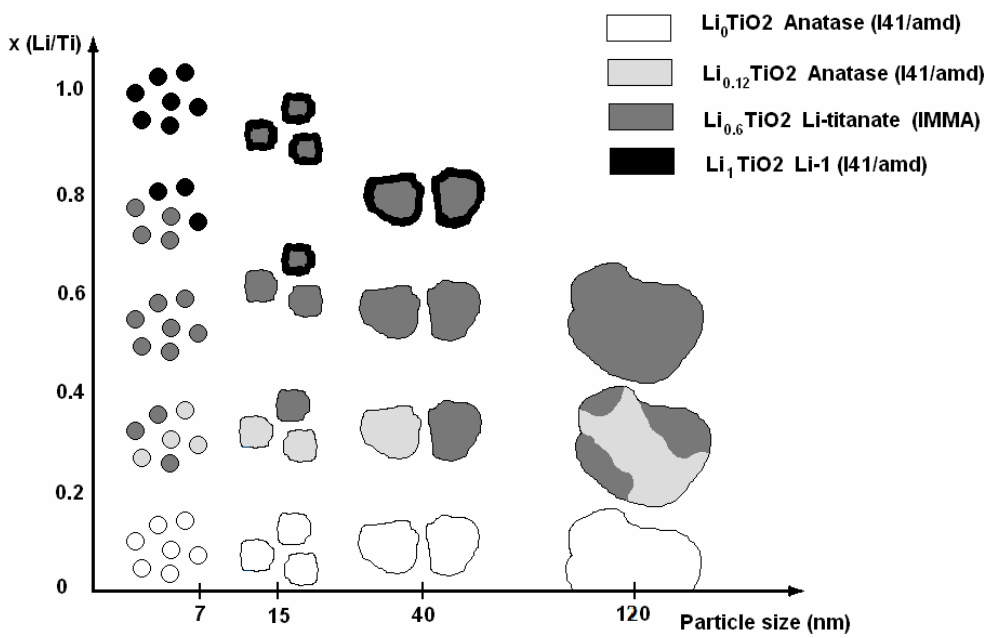

Figure 6: Grain size dependent lithiation of Anatase TiO_2. From [19]. *Light gray: tetragonal α- $Li_{0.12}TiO_2$; dark gray: orthorhombic β- $Li_{0.6}TiO_2$; black: tetragonal γ- Li_1TiO_2.*

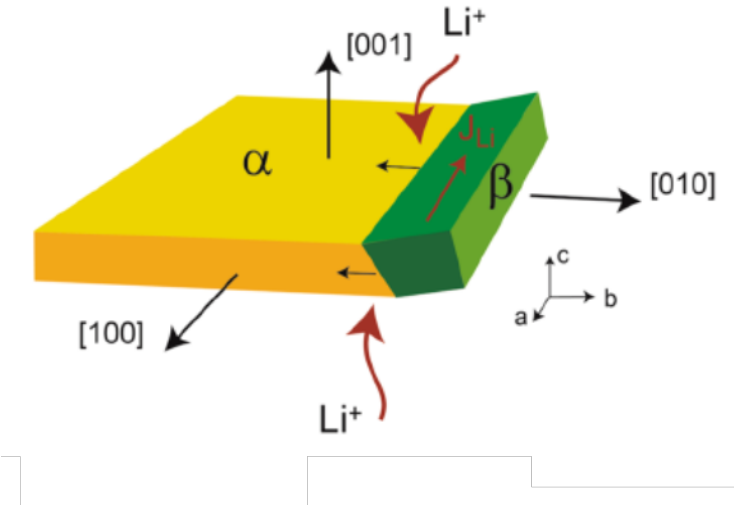

Figure 7 Phase propagation of the β- $Li_{0.6}TiO_2$ into α- Li_xTiO_2. From Belak et. al. [28].

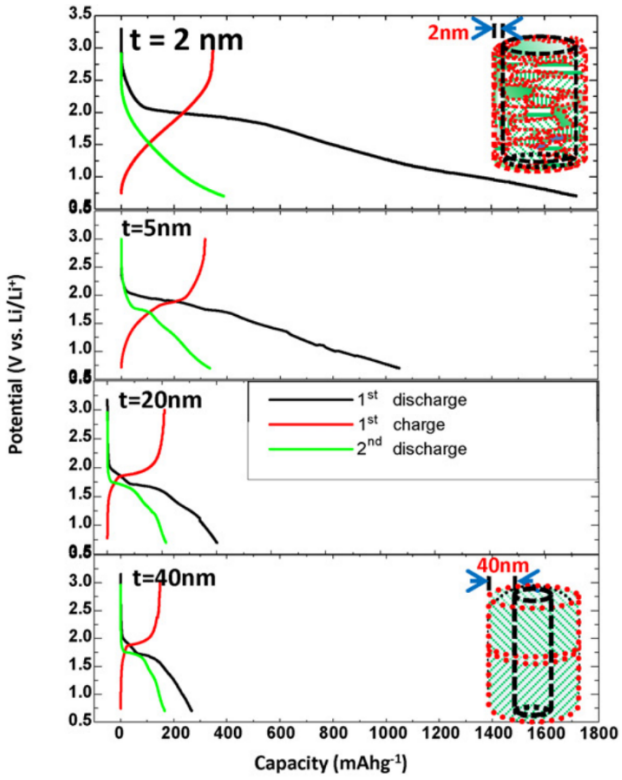

Figure 8 Wall thickness t and grain dependent lithiation of TiO_2 nanotubes. Different shadings of the grains express different degrees of lithiation. From [26].

As mentioned in chapter 1.3, titania nanotubes are a very promising lithium-ion material and a very good model material for studying size and morphology dependent effects on lithiation. S. Panda et. al. (see Figure 8) have produced anatase titania nanotubes with a very well controlled wall thickness, length and diameter and studied their size dependent electrochemical and crystallographic properties upon lithiation by applying electrochemical methods, scanning electron microscopy (SEM), transmission electron microscopy (TEM) combined with selected area electron diffraction (SAED) and X-ray diffraction (XRD) [26,29]. Their findings are very similar to the trends found by W. Borghols and Wagemaker for nano-particles [19,25]. By keeping all morphological parameters of the nanotubes the same and only varying their wall thickness as that is considered to be the limiting parameter for lithium diffusion in the bulk, they found out that decreasing the wall thickness (t) from 40 nm down to 2 nm, the reversible storage capacity of the nanotubes increases from ~170 mA h g^{-1} to ~400 mA h g^{-1}. First lithiation of 40 nm thick tubes delivers ~270 mA h g^{-1} (0.8 Li per TiO_2). In contrast, ~1700 mA h g^{-1} (5.2 Li per TiO_2) can be stored in 2 nm thin tubes. Due to the large increase in surface area, thinner tubes exhibit both a larger reversible and irreversible capacity for surface storage of lithium. Additionally, thin walls allow the full transformation of anatase to β-$Li_{0.6}TiO_2$ and the formation of the lithium rich γ-$LiTiO_2$ phase upon further lithiation. Similar to the observations on particles smaller than 7 nm, nanotubes with a wall thickness of 2 nm show the grain wise full lithiation of anatase (schematically shown on the top right of Figure 8). A remarkable improvement is also observed in the rate capability of nanotubes with decreasing thickness. The highest rate achieved with 40 nm thick tubes is 10C versus 1785C for 5 nm tubes corresponding to a full discharge in 2s.

1.5 Crystallographic orientation of anatase

It is clear from the work of Belak et. al. [28] on the effect of crystallographic orientation of the anatase grains on their lithiation properties that the surface orientation of the crystal grains forming the walls of anatase nanotubes is decisive for their ability to transform to high lithium content phases (see chapter 1.4). Grains having their (100) or (001) planes exposed to the electrolyte would have the double phase (α/β lithium titanate) interface moving in a direction parallel to the surface (upon lithiation/delithiation) leaving the remaining lithium poor α-phase in contact with the electrolyte, which enables the lithium diffusion through the lithium-poor α-phase towards the interface, thus enabling the complete transformed of the material into the β-phase.

Different studies [30-32] have shown that, under certain nanotube growth conditions, self-organized anodic titania nanotubes (TiO_2 NT) annealed to anatase can exhibit a preferred crystallographic orientation. In the work of Likodimos et. al. [31], most of the crystallites forming the walls of the nanotubes have their [101] direction parallel to the lengthwise direction of the nanotubes, whereas in the other two studies [30] and [32], the preferred crystallite orientation is such that their [001] direction is parallel to the lengthwise direction of the nanotubes. The [101] oriented nanotubes [31] were not tested in terms of their lithiation/delithiation properties. Preferential orientation of the nanotubes along the [001] direction is shown to result in a faster interfacial lithium insertion/extraction kinetics and thus to an enhanced performance as battery anode material when compared to nanotubes comprising randomly oriented anatase crystallites [30]. This effect may be ascribed to (100) surfaces exposed to the electrolyte.

1.6 Reduced titania

The key for an optimized performance of a lithium-ion storage electrode is the balance between lithium-ion and electron conductivity of the electrode [33]. Titania (TiO_2) is a semiconductor and therefore, for powder electrodes, it is usually mixed with a carbon based conductive powder to provide an electronic conduction path from the current collector to the active sites in the titania particles where lithium ions are recombining with the electrons. Reducing titania from TiO_2 through oxygen deficient oxide (titanium suboxide, TiO_{2-x}) to titanium metal (Ti), changes its electronic properties from semiconducting to semimetallic and finally to metallic. The electronic properties of titanium suboxides depend on the amount and the kind of oxygen defects introduced in the material. At the same time, reducing titania also changes lithium-ion mobility in the material as well as the reversibility of lithiation, both generally decreasing with the increase in oxygen defects. Therefore, according to the type of introduced defects there is an optimal level of reduction of titania where electronic and lithium-ion mobilities in the material are matching. In such an optimized material, lithiation performance can be significantly improved and conductive additives can be omitted which further increases the gravimetric/volumetric lithium storage capacity of the electrode.

Shin et. al. [33] reported on titania nanopowder electrodes with a 20 nm particle diameter reduced in hydrogen atmosphere at elevated temperature (500°C) to a titanium suboxide and compared their lithiation performance to untreated and argon annealed (following the same procedure as for the hydrogen annealing) electrodes. Under 0.2 C cycling rate, the untreated reference showed 64 mA h g^{-1} lithium storage capacity followed by 148 mA h g^{-1} for the argon

annealed reference and 180 mA h g^{-1} for the hydrogen annealed sample (all measured after 20 lithiation/delithiation cycles). Remarkably, at high cycling rates of 10 C the hydrogen annealed sample showed a lithium storage capacity of 70-130 mA h g^{-1} (depending on the annealing conditions) compared to a negligible capacity for the untreated and for the argon annealed electrodes used as reference. These results show that annealing itself has a beneficial effect on performance at low cycling rates and that hydrogen reduction noticeably improves electrode performance and enables high rate (de)lithiation. It is important to note that a sample annealed for 1h in hydrogen performed better during lithiation tests than a sample annealed for 7h, even though electronic conductivity was lower pointing to a better balance between electronic and ionic conductivity of the sample annealed for 1 h. Figure 9 (a) [33] displays schematically the effect of increasing oxygen deficiencies on the Li^+ and e^- mobilities wherein larger arrows indicate a higher mobility. The central sphere indicates the situation where both mobilities are balanced. Figure 9 (b) shows that the overall conductivity of the material reaches maximum in the point where its conductivity for Li^+ matches the one for e^-. In the particular case of the study reported by Shin et. al. that seems to be the case for an electrode annealed for 2h under H_2 atmosphere.

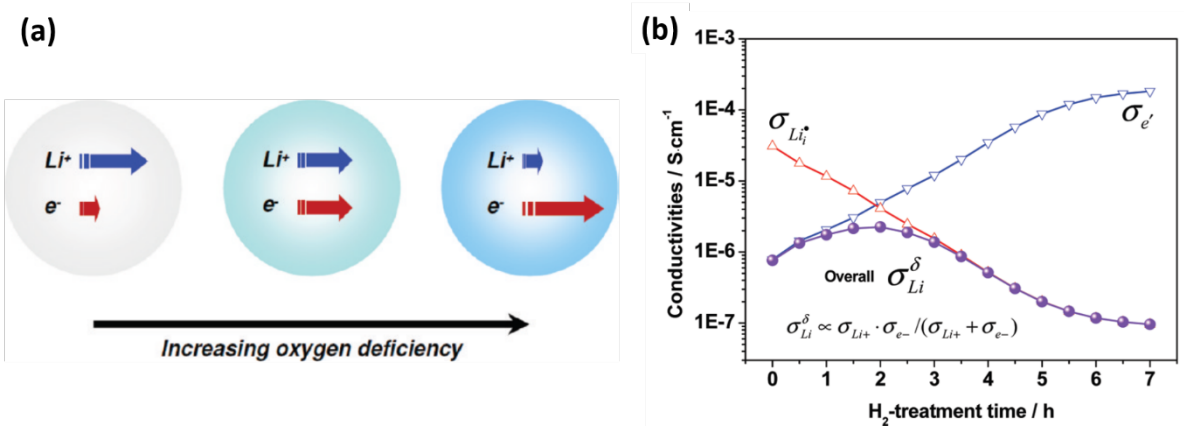

Figure 9 H_2 reduced TiO_2 nanopowder. (a) Li^+ and e^- mobility dependency on oxygen deficiencies; (b) conductivity vs. H_2 treatments time. From [33]

Lu et. al. [34] also performed hydrogen annealing on titania nanopowder (50 nm particle diameter) and anodically grown self-organized titania nanotubes with 20 nm wall thickness. For both materials, hydrogen annealing showed little effect at low rates (0.02 C), becoming significant at 1 C. Upon cycling at ~1 C rate over 100 cycles the non-treated and hydrogen annealed nanotube samples lost 22% and 13% of their capacity, respectively.Reduction of anatase nanotubes was also reported upon annealing under inert atmosphere (Ar) [35].

Unfortunately, titania suboxides are deprived from the chemical and structural stability of a saturated oxide, thus they easily reoxidize losing their beneficial properties or the nanostructures collapse during reduction. A way to stabilize the defective oxide structure is to introduce carbon as a doping agent [35] and/or as a thin protective surface layer. Carbon coating is commonly applied as a method for improving the electronic conductivity of the surface of active materials having poor intrinsic conductivity [36]. Such a coating would reduce the charge transfer resistance on the electrode electrolyte interface and passivate the sensitive oxygen deficient surface for undesired side reactions like electrolyte decomposition (SEI formation).

2 Goal of this thesis

The goal of this thesis was firstly to develop a new anode material for Li-ion batteries that would be safer than graphite, allow for higher charge and discharge rates, and have the same or possibly higher Li storage capacity. The second goal was to find appropriate analysis techniques for characterizing macroscopic (in the cm range) Li-ion electrodes with well-ordered, nano-structured active material, which would deliver morphological parameters with a high statistical relevance and would allow the direct measurement of the amount of Li stored in the electrode as well as the macroscopic distribution of Li over the electrode.

In the present work self-organized anodically grown titania nanotubes were annealed in an acetylene atmosphere for producing a stable carbon doped titanium suboxide material with a thin carbon coating. The material was expected to combine the beneficial effects of nanostructuring, partial reduction (analogues to hydrogen annealing) and conductive coating. Further, in order to increase the Li storage capacity of the titania nanotubes, these were coated with a thin (~10 nm) layer of Si.

The low thickness of the Si film was expected to prevent cracking and disintegration of the Si layer upon lithiation and delithiation. On the other hand, the high surface area of the titania nanotubes was expected to allow the deposition of a significant amount of Si.

Grazing incidence small angle X-ray and neutron scattering (GISAXS and GISANS) were used for studying the morphology of the nanotubular materials.

The amount of Li in lithiated electrodes and its two-dimensional distribution over the electrodes was studied using a dedicated setup exploiting the neutron capture reaction $^{6}Li(n,\alpha)^{3}H$.

3 Theory of methods and techniques

3.1 Self-organized titania nanotube growth

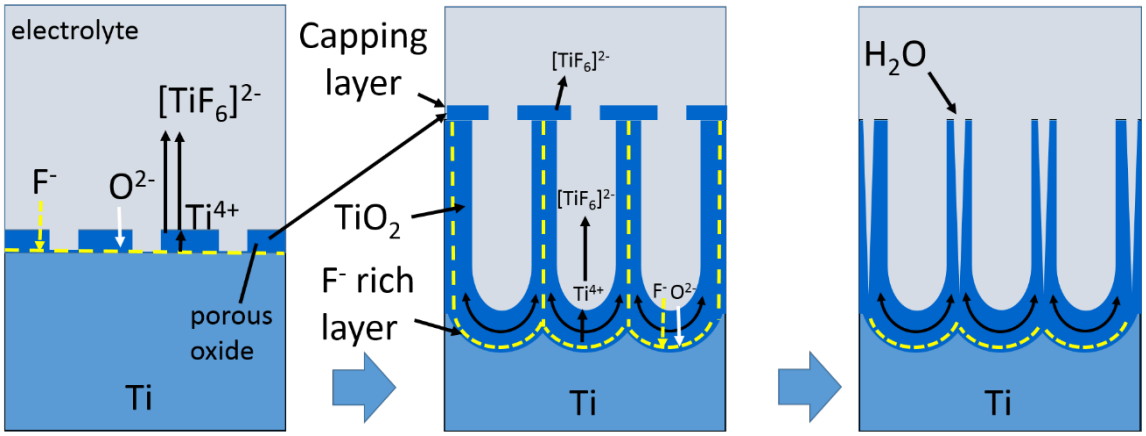

Figure 10 Titania nanotube formation. From left to right: formation of porous oxide; nanotubes growing under a capping layer; after dissolution of the capping layer, fluoride rich species are dissolved in water and the neighboring nanotubes are separated.

Self-organized Titania nanotubes supported on a titanium metal sustrate can be easily produced via one step electrochemical anodisation of titanium metal in a fluoride containing electrolyte (see Figure 10). Such nanotubes find a broad range of applications like photo catalysis [37], dye-sensitized solar cells [38], electrochromic displays [39] and lithium ion batteries.

An extensive review on the synthesis and applications of titania nanotubes by P. Roy, S. Berger and P. Schmuki [40], describes the different growth technics and growth mechanism that deliver a wide range of titania nanostructures with tunable parameters like morphology, crystallinity, electronic structure and light absorption properties for the wide field of possible applications.

Self-organized titania nanotubes are grown by applying a voltage ranging between 20V and 100V between the electrodes of a two-electrode electrochemical cell with a fluoride containing electrolyte where titanium metal is the anode. If a fluoride free electrolyte is used, a compact oxide film instead of nanotubes is growing on the metal surface by deprotonation of H_2O

according to the Equation 1 or by first forming a metal ion (Equation 2) that is further reacting with OH^- (Equation 3) and finally with O^{2-} formed by deprotonation of OH^- (Equation 4) [40].

Equation 1

$$M + \frac{n}{2}H_2O \rightarrow MO_{n/2} + nH^+ + ne^-$$

Equation 2

$$M \rightarrow M^{n+} + ne^-$$

Equation 3

$$M^{n+} + nOH^- \rightarrow M(OH)_n$$

Equation 4

$$M(OH)_n \rightarrow MO_{n/2} + \frac{n}{2}H_2O$$

Wherein M denotes the metal that is being oxidized and n is a positive integer. In the case of Titanium oxidation, M stands for Ti and n=4. The reaction of Equation 1 is balanced by the hydrogen evolution reaction on the cathode shown in Equation 5, where the reactions of Equation 2, 3 and 4 are balanced by the hydrogen evolution reaction on the cathode shown in Equation 6.

Equation 5

$$nH^+ + ne^- \rightarrow \frac{n}{2}H_2 \uparrow$$

Equation 6

$$nH_2O + ne^- \rightarrow \frac{n}{2}H_2 \uparrow + nOH^-$$

The oxide is typically growing on the metal metal-oxide interface (growth on the oxide electrolyte interface is also possible) wherein O^{2-} species are migrating through the already formed oxide driven by the electric field. Since the resistance of the oxide layer grows with its thickness (the local electrical field is decreasing), the thickness of this compact oxide film is limited by the applied voltage. Ion transport in solids requires high activation energies, which however, are lowered by the

high field strengths in the thin oxide films (10^6-10^7 V cm^{-1}) which allows ion migration in the field direction. This process known as the high field mechanism is described theoretically by N. Cabrera and N. F. Mott [41].

Equation 7

$$TiO_2 + 6F^- \xrightarrow{H^+} [TiF_6]^{2-} + 2H_2O$$

The same happens, in the beginning of the anodisation in fluoride containing electrolyte [40], [35] where a thin compact oxide layer grows on the metal surface. This compact oxide, however, gets spot wise dissolved by the fluoride species forming soluble $[TiF_6]^{2-}$ (see Equation 7). The etched spots become the seeds for the growing titania nanotubes (see Figure 10). As fresh oxide is formed in the etched spots, the old parts get pushed to the side, sliding on a fluoride rich layer formed between the titanium metal and the oxide, pressing against the neighboring fields of growing oxide and eventually bending upwards forming the spherical bottoms of the nanotubes. The fluoride rich layer extends between the walls of neighboring tubes that are initially densely packed. The constant ion exchange (F^- and O^{2-} migrate through the oxide layer towards the metal metal-oxide interface and Ti^{4+} migrates in the opposite direction) in the breading region keeps the oxide viscous and allows it to flow to the side of the zone and then upwards. In the seed region, etching and oxide growth continue while the walls of the forming nanotubes are pushed further upwards carrying the initially formed porous oxide layer on their top as a capping layer.

This porous layer protects the nanotubes from the fresh electrolyte above them while activity in the seed portions in the vicinity of the titanium metal is still strong due to the locally strong electric field. Eventually, the capping porous layer gets dissolved revealing the nanotubes underneath.

The fluoride rich layer between the neighboring tubes enters into contact with water from the electrolyte which dissolves the soluble $[TiF_6]^{2-}$ species from this interlayer, thus separating the neighboring nanotubes. From this point on, oxide growth at the Ti to oxide interface is balanced by oxide dissolution at the top of the nanotubes and therefore usually this is the point also for stopping the anodization. During anodization, the electrolyte is turning slightly acidic and small quantities of highly aggressive hydrofluoric acid (HF) are formed. Therefore, removing the

anodization potential is not enough for stopping the etching process but also the electrolyte should be removed from the nanotubes (for example by rinsing with water).

3.2 Plasma Enhanced Chemical Vapor Deposition (PECVD)

Plasma enhanced chemical vapor deposition (PECVD) is a low-pressure coating technique using a partially ionized gaseous precursor (plasma) that chemically decomposes delivering the desired solid coating on the target surface. A principle design of a PECVD system is shown in Figure 11. Inert carrier gas is mixed with the reactive gas and the mixture is fed into the reaction chamber. The plasma is produced by a radio frequency (RF) or direct current (DC) discharge of the gas in the reaction chamber. Due to the large difference in mass between the electrons and ions in the plasma, ions are moving far slower (their temperature is far lower) than the electrons which leads to high reactivity of the precursor gas at a low temperature. Therefore, PECVD can be performed at a several hundred-degree lower temperature than classical CVD which makes it less aggressive to the target substrate. The deposition is controlled through various parameters like: deposition time, gas composition, chamber pressure, target temperature and RF power [42-44].

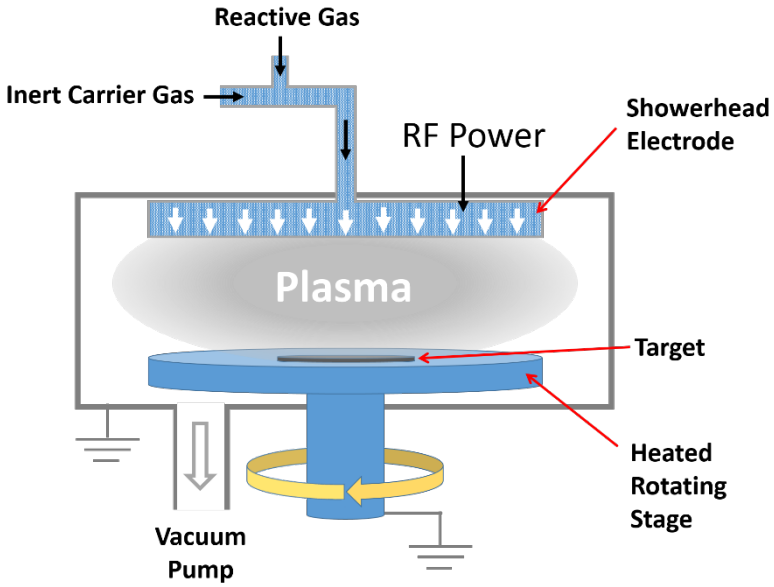

Figure 11 Principle design of a PECVD system.

3.3 Electrochemistry fundamentals

The following short introduction of the electrical double layer is based on [45].

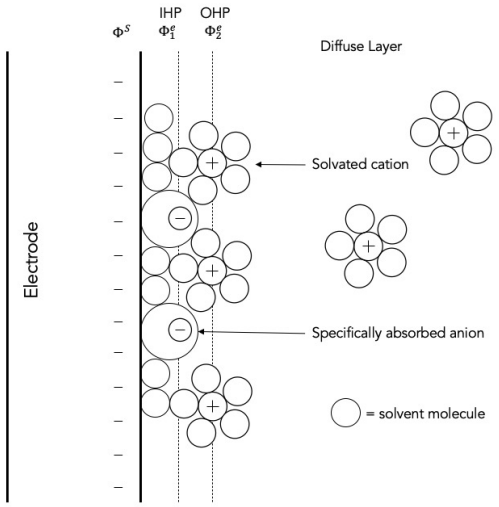

Figure 12 Model of the electrical double layer modified from [45]. *ϕ^s denoting electric potential on the surface of the solid electrode; ϕ_1^e and ϕ_1^e denote electric potentials in different layers in the electrolyte.*

When an electrode is immersed in electrolyte, an interface is formed. The charge carriers on both sides of the interface, residing in different materials (phases), have different concentrations and energies thus having different electrochemical potentials. This difference is the driving force for electrode reactions. The chemical potential of species i in phase α is given by:

$$\mu_i^\alpha = \mu_i^{0\alpha} + RT \ln a_i^\alpha$$

Wherein a_i^α is the activity of the species, $\mu_i^{0\alpha}$ is the chemical potential at standard conditions ($a_i^\alpha = 1$), T is the temperature and R the gas constant. The electrochemical potential further accounts for the work that needs to be done to bring a z-valent charged particle in the phase α with electric potential ϕ^α and can thus be expressed as:

$$\tilde{\mu}_i^\alpha = \mu_i^\alpha + z_i F \phi^\alpha = \mu_i^{0\alpha} + RT \ln a_i^\alpha + z_i F \phi^\alpha$$

The whole ensemble of charged species and oriented dipoles at the electrode - electrolyte interface is called electrical double layer (EDL). A model of the double layer is schematically depicted in Figure 12Figure 12 Model of the electrical double layer. The inner layer (layer closest

to the surface of the electrode) comprises solvent molecules, ions and other molecules, adsorbed on the surface of the electrode, wherein their chemistry plays an important role in the adsorption. These species are said to be specifically adsorbed. The centers of charge of the specifically adsorbed ions form the so-called inner Helmholtz plane (IHP). Solvated ions can only approach the electrode up to the outer boundary of the inner layer. The electrical centers of solvated ions in a layer closest to the electrode form the so-called outer Helmholtz plane (OHP). These solvated ions are distributed between the OHP and the bulk electrolyte in the so called diffuse layer and are said to be non-specifically adsorbed as their interaction with the electrode is only based on electrostatic forces and is practically independent on the chemical properties of the ions and the electrode due to the relatively large distance between the two. In concentrated electrolytes with ion concentrations greater than 10mM, the thickness of the diffuse layer is less than 10 nm. Therefore, in concentrated electrolytes (typically 1M in Li-ion cells) the diffuse layer can be safely neglected. The structure and composition of the double layer affects the potential distribution of the interface region that a reactant experiences approaching the electrode surface, which in turn affect the rates of electrode processes.

Two types of processes occur at the interface. The first type are processes in which charge carriers are transferred across the interface called charge transfer reactions or faradaic processes, being governed by Faraday's law. The second type are so called non-faradaic processes, which do not involve charge transfer, like the adsorption or desorption of electrolyte species on the surface of the electrode. Although charge carriers are not crossing the interface, external currents can still flow, analogously to the charging of a capacitor, when the surface area of the electrode, the potential or the composition of the electrolyte changes. The structure and composition of the double layer affects the double layer capacitance, which is further dependent on the electrode potential ϕ. Therefore, double layer charging is typically described using a differential capacitance

$$C_{EDL}(\varphi) = \frac{\partial q_{EDL}}{\partial \phi}$$

wherein q is the charge.

If the electrode is semiconducting, the low concentration of charge carriers results in the formation of a space charge layer (SCL) on the electrode side of the electrode - electrolyte interface, which also contributes to the total capacitance of the interface region.

For a redox reaction in equilibrium $OX + ne^- \leftrightarrow RED$, the sum of the electrochemical potentials of the oxidized species (OX) and the electrons are equal to the electrochemical potential of the reduced species (RED).

$$\tilde{\mu}_{OX}^{Electrolyte} + \tilde{\mu}_{e^-}^{Electrode} = \tilde{\mu}_{RED}^{Electrode}$$

From this equation, by substituting the potential dependent expressions for the electrochemical potentials given above, the Nernst equation for the potential difference between the electrode and the electrolyte is calculated as follows:

$$\Delta\phi = \phi^{Electrode} - \phi^{Electrolyte} = \Delta\phi^0 + \frac{RT}{nF} ln\left(\frac{a_{OX}}{a_{RED}}\right),$$

wherein a_{OX} and a_{RED} are the activities of the oxidized and reduced species, respectively, and $\Delta\phi^0$ represents the potential difference between the electrode and the electrolyte at standard conditions ($a_{OX} = a_{RED}$). T is the temperature, R the gas constant, F the Faraday constant and n is the number of exchanged electrons in the reduction reaction which is equal to the number of exchanged electrons in the oxidation reaction.

The rate of a global or an elementary charge-transfer reaction is usually modeled by a Butler-Volmer equation for the current density i as a function of overpotential η:

$$i = i_0\left(exp\left(\frac{\alpha_a nF\eta}{RT}\right) - exp\left(-\frac{\alpha_c nF\eta}{RT}\right)\right),$$

wherein the overpotential is defined as follows:

$$\eta = (\phi^s - \phi^e) - (\phi^s - \phi^e)^{eq} = (\phi^s - \phi^e) - E^{eq}$$

where ϕ^s is the electric potential of the electrode at the surface and ϕ^e is the electric potential of the electrolyte in the vicinity of the electrode. E^{eq} is the electric potential difference at equilibrium where the anodic and cathodic reaction proceed at equal rates ($i = 0$).

α_a and α_c are the anodic and cathodic symmetry factors, respectively, describing the symmetry of the potential barrier of the reaction. The first exponential term represents the anodic rate and

the second exponential term the cathodic rate. For an elementary reaction $\alpha_a + \alpha_c = 1$, whereas for a global reaction there is no such restriction. The exchange current density (current density at equilibrium) i_0 is a function of temperature and the activities of the participating species. The activities of the participating species and the rate of a charge-transfer reaction depends on the mechanism of charge-transfer. Charge-transfer reactions are usually divided in inner- and outer-sphere reactions. In outer-sphere reactions, the charge-transfer takes place without disrupting the coordination spheres (like solvent molecules surrounding an ion) of the participating species. An outer-sphere charge-transfer reaction between an electrode and an ion in the electrolyte would be a charge-transfer between the electrode and a solvated ion outside the OHP (see Figure 12), wherein the coordination sphere of the ion is preserved.

The relatively large distance between the electrode and the solvated ion results in a week dependence on the chemistry of the participants. In contrast, in an inner-sphere reaction, at least some of the reactant, product or an intermediate would be specifically adsorbed on the electrode (forming the the IHP) and the chemistry of the participants plays an important role for the reaction rate.

In Li-ion batteries with intercalation or conversion electrodes, upon discharging, lithium is oxidized on the surface of the anode, the Li^+ ion is transferred to the electrolyte and the electron that is left behind migrates through the electrode to the current collector to enter the external circuit. A Li^+ ion from the electrolyte is then reduced at the surface of the opposite electrode (cathode) via charge transfer with an electron from the external circuit and then diffuses in the bulk of the electrode material or first migrates inside the material until it gets reduced and then diffuses further in the bulk driven by concentration gradients. The reverse process takes place upon lithiation. Both electrons and lithium ions are transferred across the electrode - electrolyte interfaces and inner-sphere charge transfer reactions are of high importance. The local charge and substance densities in the different components of the cell are constantly changing. With lithium insertion/extraction, the electrode material changes its electric potential, electrical conductivity and the diffusion and migration speed of species inside the bulk also changes.

Depending on the respective speed of the relevant transport mechanism, gradients in concentration and charge appear. The EDL is constantly changing. Solid electrolyte interface (SEI) is formed on the surface of the electrodes by the decomposition of electrolyte and many other faradaic and non-faradaic reactions take place simultaneously. To reflect some of these effects Newman and coworkers proposed a model [46-48] for describing a Li-ion battery using

a set of conservation equations for charge and substance for the different components of the cell and a set of boundary conditions. The charge transfer chemistry was represented by a Butler-Volmer formulation. This formulation, however, assumes a single rate limiting step which makes it difficult to use it for modeling competitive parallel reactions. If the electrode - electrolyte interface zone is not in chemical equilibrium, then there is no explicit way of defining a single reversible potential and there are also some other limitations [49].

Seventeen years later, Andrew M. Colclasure and Robert J. Kee proposed a Li-ion battery model [50] based on the previous model by Newman, however, replacing the Butler-Volmer formulation, with a model in terms of elementary reactions, which enables the incorporation of multiple parallel pathways, heterogeneous reactions among surface adsorbed species, incorporation of parallel possibly deleterious reactions and which can provide more physical insight (like information on the SEI). The model is summarized in Figure 13, with the conservation equations and boundary conditions for the respective components of the cell indicated in the figure.

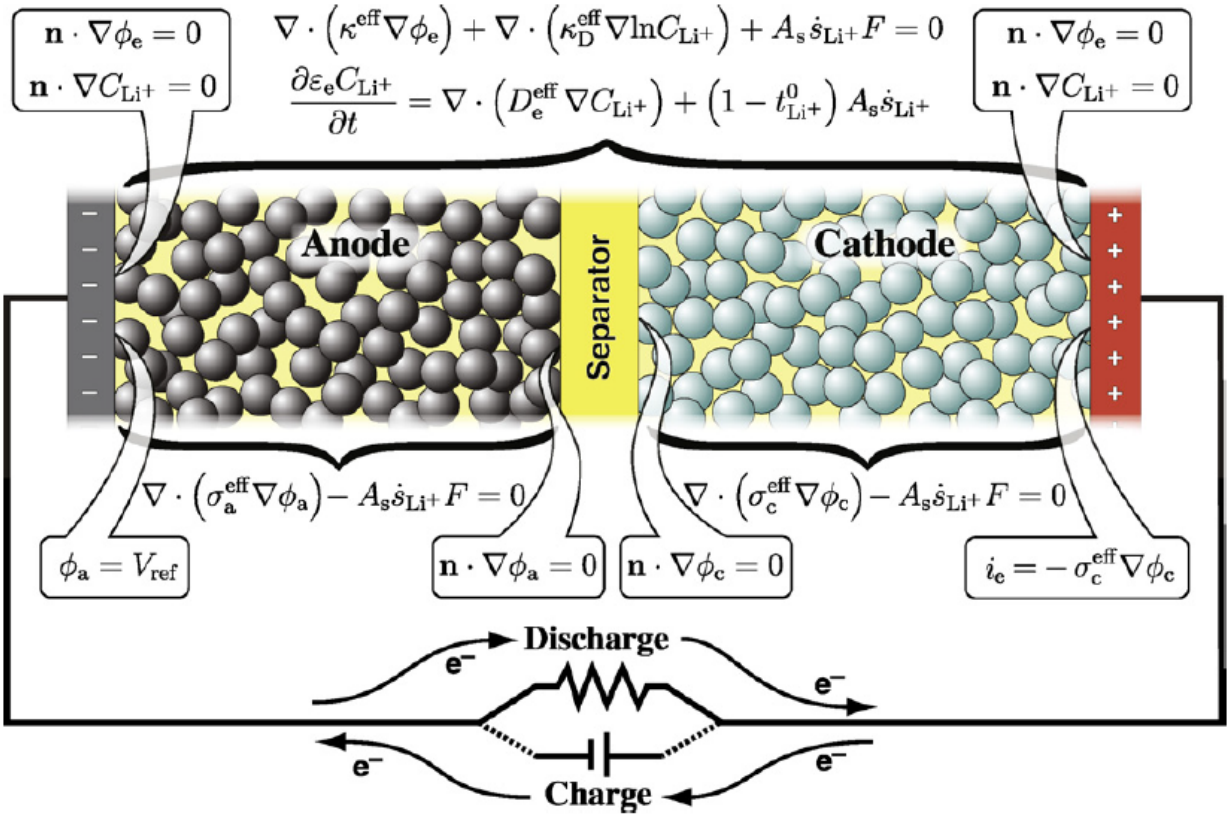

Figure 13 Section of a Li-ion cell, showing conservation equations and boundary conditions. From [50].

The model is based on a cell consisting of two porous composite electrodes with metallic current collectors and a separator. The separator and the porous electrodes are soaked with a binary liquid electrolyte. The active electrode material and the electrolyte are treated as superimposed continua. Transport within the binary electrolyte is described using concentrated solution theory [51], which is taking into account important processes like ion pairing and ion association.

The conservation of charge in the electrolyte is expressed by the following equation:

$$\nabla.\left(k^{eff}\nabla\phi_e\right)+\nabla.\left(k_D^{eff}\nabla\ln C_{Li^+}\right)+A_s\dot{s}_{Li^+}F=0$$

Wherein:

k^{eff} is the effective ionic conductivity of the electrolyte phase;

k_D^{eff} is the effective diffusional conductivity;

ϕ_e is the electric potential of the electrolyte phase;

C_{Li^+} is the Li-ion concentration in the electrolyte phase;

A_s is the specific surface area of active electrode particles per unit volume of composer material;

$\dot{s}_{Li^+}$ is the net production rate of Li-ions via charge transfer reaction;

F is the Faraday constant; and

the product $\dot{s}_{Li^+}F$ is the current density i_e.

The third term of the equation expresses that charge enters and leaves the electrolyte through surface reactions. There are no charge-transfer reactions in the separator region. Furthermore, charging of the EDL on the electrode-electrolyte interfaces, which happens very fast (in the order of

milliseconds) compared to the time scale of charging and discharging, is neglected in the model. The equation is derived assuming that the electrolyte maintains charge neutrality. That is:

$$\sum_i C_i z_i = 0$$

where C_i and z_i are concentration and charge of species i, respectively.

The conservation of species in the electrolyte is expressed by the following equation:

$$\frac{\partial \varepsilon_e C_{Li^+}}{\partial t} = \nabla.\left(D_e^{eff} \nabla C_{Li^+}\right) + \left(1 - t^0_{Li^+}\right) A_s \dot{s}_{Li^+}$$

wherein:

D_e^{eff} is the effective diffusion coefficient in the electrolyte, which is a function of local concentrations, binary diffusion coefficients and species charges;

$t^0_{Li^+}$ is the transference number for Li^+ ions, which is the fraction of current carried by the Li^+ ions relative to the total current carried by all ionic species in the electrolyte with uniform composition; and

ε_e is the volume fraction of the electrolyte phase.

The last term of the equation represents the effects of Li^+ ions entering and leaving the electrolyte through heterogeneous charge-transfer reactions at the surfaces of the electrodes. The transference term has the effect that the charge-transfer reactions lose their effect on the electrolyte concentration when the Li^+ ion transference number is unity. Since species transport through the electrolyte proceeds on similar time scales as charging and discharging of the cell, the transient term in this conservation equation is preserved.

The conservation of charge for each electrode is expressed as follows:

$$\nabla.\left(\sigma_{a/c}^{eff}\nabla\phi_{a/c}\right) - A_s\dot{s}_{Li^+}F = 0$$

wherein:

the subscript a/c denotes anode a or cathode c depending on which electrode the equation refers to;

$\sigma_{a/c}^{eff}$ is the effective solid phase conductivity of the electrode;

$\phi_{a/c}$ is the electric potential of the bulk electrode material phase.

The first term of the equation represents the charge transport *via* electronic conduction whereas the second term stands for the Li^+ ions entering or leaving the electrode phase through charge-transfer reactions.

On the current collectors, the charge (ions) and concentration fluxes of the electrolyte must vanish as the current collectors are not conductive for any of the electrolyte species. Therefore, the boundary conditions on the current collectors are:

$\mathrm{n}.\nabla\phi_e = 0$ and $\mathrm{n}.\nabla C_{Li^+} = 0.$

Similarly, the flux of electrons from the electrodes reaching the electrode - electrolyte interface (the electrolyte is not electrically conductive) must vanish, thus on the anode - electrolyte and on the cathode - electrolyte interfaces:

$\mathrm{n}.\nabla\phi_a = 0$ and $\mathrm{n}.\nabla\phi_c = 0.$

On the current collector side of the anode, the electric potential is set at a reference value $\phi_a = V_{ref}$.

For charge conservation, the ionic current inside the cell must match the electronic current of the external circuit, thus on the current collector side of the cathode:

$$i_e = -\sigma_c^{eff}\nabla\phi_c$$

The current density i_e is positive during discharging of the cell and negative during charging. The total current produced by the cell during discharge is $I_e = i_e A$, wherein A is the area of the current collector. The cell operating voltage is the difference in potential at the two electrode - current-collector interfaces:

$$V_{cell} = \phi_{c,cc} - \phi_{a,cc}$$

Neglecting the lithium transport between the particles of active material of each electrode, and assuming spherical particles of radius r, the transport of intercalated lithium Li^I can be expressed as follows:

$$\frac{\partial C_{Li^I}}{\partial t} = \frac{1}{r^2}\frac{\partial}{\partial r}\left(r^2 D_{Li^I}\frac{\partial C_{Li^I}}{\partial r}\right).$$

The diffusion coefficient of intercalated lithium D_{Li^I} typically has a strong dependence on the concentration of intercalated lithium C_{Li^I}, which renders the transport problem non-linear.

The open circuit potential E_{OCP} of the lithiated active material also depends on the state of charge of the material and can be expressed [46] against the standard potential of a reference electrode E^0_{ref} as:

$$E_{OCP} = E^0 - E^0_{ref} + \frac{RT}{nF}\left(\ln\left(\frac{C_{max} - C_{Li^I}}{C_{Li^I}}\right) + \beta C_{Li^I} + \zeta\right)$$

wherein C_{max} is the maximum concentration of intercalated lithium and β and ζ are activity correction coefficients.

The exchange current density at the electrode-electrolyte interface can be written as:

$$i_0 = k_{ct} nF (C_{Li^+})^{\alpha_a}\left(C_{max} - C_{Li^I}\right)^{\alpha_a}\left(C_{Li^I}\right)^{\alpha_c}$$

wherein k_{ct} is the rate constant for the charge-transfer reaction.

In the case where a resistive SEI film with a resistance R_{SEI} (Ωcm^2) is formed on the surface of the active material of the electrode that is weakening the driving force of the overpotential η, the current density i_e can be expressed in the Butler-Volmer form as in [52]:

$$i_e = i_0\left(exp\left(\frac{\alpha_a nF}{RT}(\eta - R_{SEI}i_e)\right) - exp\left(-\frac{\alpha_c nF}{RT}(\eta - R_{SEI}i_e)\right)\right).$$

3.4 Electrochemical analysis

Electrochemical analysis is commonly performed in a three electrode electrochemical cell consisting of a working electrode (WE) being the sample under study, a counter electrode (CE) and a reference electrode (RE), all three immersed in an electrolyte. The reference electrode is an electrode having a stable electrochemical potential in the used electrolyte. During electrochemical measurements, when current is flowing through an electrode, its potential is changing. Therefore, in order to ensure a proper determination of the potential of the WE and at the same time measure the current flowing at it, the two quantities are measured separately. The potential is measured between the WE and the RE without current flowing between them (measured over a high resistance), whereas current is measured between WE and CE.

A stable potential at the ideally non-polarizable RE is established through a redox reaction taking place at the electrode. For aqueous electrolytes, commercial electrodes are available with a very well-defined electrochemical potential. When examining materials for lithium ion batteries in non-aqueous electrolytes, Li^+, is readily available in the electrolyte, in the order of 1 mole per liter (1M).

Therefore, Li metal can be used as a pseudo RE due to an equilibrium between the oxidation of lithium metal to lithium ions ($Li^0 \rightarrow Li^+ + e^-$) and the reduction of lithium ions to lithium metal ($Li^+ + e^- \rightarrow Li^0$). This equilibrium is commonly expressed as Li/Li^+ and the electrode is called lithium reference electrode. It is important to note that in equilibrium the sum of all currents flowing over the RE is zero. If the overall current deviates from zero due to for example leak currents in the apparatus (potentiostat/galvanostat) used for the electrochemical measurements, or if the electrochemical activity of the redox species is not equal, the reference

potential shifts. The shift of the equilibrium potential caused by a difference in electrochemical activity of the redox species is expressed by the Nernst-equation:

$$\mathrm{E}_{eq} = \mathrm{E}^0 + \frac{RT}{nF} ln\left(\frac{a_{OX}}{a_{RED}}\right)$$

Where a_{OX} and a_{RED} are the electrochemical activities of the oxidized and reduced species, respectively, and E^0 is the electrode potential at standard conditions where these two activities are equal. T is the temperature, R the gas constant, F the Faraday constant and n is the number of exchanged electrons in the reduction reaction which is equal to the number of exchanged electrons in the oxidation reaction.

In the following, the electrochemical techniques used in this work are shortly introduced. For further reading on theoretical backgrounds of electrochemistry and a more detailed descriptions of electrochemical techniques see, [45-56].

3.4.1 Cyclic Voltammetry

Cyclic voltammetry is an electrochemical analysis method wherein the potential of the WE is cycled between two potential values with a constant rate measured in V s^{-1}, called scan rate, and the current at the WE is monitored. The measurement is represented in a plot called cyclic voltammogram (CV). A typical CV of anatase in a Li-ion electrolyte with one well pronounced peak in anodic and one in cathodic direction is shown on page 105 in Figure 47 a) and a CV of a composite electrode displaying characteristic peaks for anatase and Si is shown on page 114 in Figure 55 a).

For a redox reaction $OX + e^- \leftrightarrow RED$ on the surface of an electrode [45], starting off from a potential above the equilibrium potential E_{eq} (redox potential) and reducing the potential (increasing the energy of electrons in the electrode), at a very low scan rate, no significant current will be measured, apart from non-faradaic currents for capacitive charging of the EDL, until the vicinity of E_{eq} is reached where the reduction ($OX + e^- \rightarrow RED$) charge-transfer reaction starts and current increases.

Decreasing the potential further, the surface concentration of reactant (oxidized species OX) decreases, thus their flux towards the electrode increases as the current continues to rise.

Upon further decreasing the potential past the redox potential, the concentration of oxidized species on the surface drops nearly to zero as the mass transport towards the electrode reaches a maximum (for a diffusion limited reaction) and the current starts to decrease, with the depletion of reactant, forming a peak in the CV.

In the reversed scan the opposite process takes place $RED \rightarrow OX + e^-$ resulting in a reversed peak in the CV. The reduction peak appears at a potential more negative than E_{eq} and the oxidation peak at a potential more positive than E_{eq}. Typically, for a highly reversible reaction, if the reactant is adsorbed on the surface of the electrode, the two peaks are essentially at the same potential and the peak current is proportional to the scan rate.

For a reversible reaction, the peak potentials are independent of the scan rate, the two peak currents are equal, and their shape is the same (mirrored horizontally and vertically). While EDL charging current is generally proportional to the scan rate, the peak currents for a diffusion limited reversible reaction are proportional to the square root of the scan rate. Therefore, the EDL charging contribution becomes more important for high scan rates.

For an irreversible or semi-reversible reaction, with increasing scan rate, the peak potentials are shifting in scan direction, thus the two peaks are shifting apart, and the peak currents are no longer proportional to the square root of the scan rate for the diffusion limited reaction.

These and other effects in cyclic voltammetry are used to study surface reactions (reversible and irreversible) on different materials like for example electrolyte decomposition and the formation of surface species on a battery electrode. In Li-ion battery cells, reactions are not limited to the surface but are also taking place in the bulk material. Bulk reactions like phase transitions which proceed at a constant potential also give rise to current peaks in a CV analogously to surface redox reactions limited for example by diffusion. These specific potentials are related to the energy barrier that needs to be overcome for the specific reaction/transition to take place and to the rate-limiting process. Upon cycling, which represents for example the charging and discharging of a battery, the changes in the electrode material can be traced and the reversibility of the process, as a function of scan rate or electrode parameters etc., can be evaluated.

3.4.2 Galvanostatic Cycling with Potential Limitation (GCPL)

Galvanostatic cycling with potential limitation is an electrochemical analysis technique, wherein constant current is forced through the WE while monitoring its potential. A typical GCPL curve of anatase in a Li-ion electrolyte with one well pronounced potential plateau in anodic and one in cathodic direction is shown on page 105 in Figure 47 b) and a GCPL of a composite electrode comprising anatase and Si is shown on page 114 in Figure 55 b).

The potential of the electrode first falls (if a cathodic current is applied) to the characteristic potential of the reaction and then changes only slightly, following the changes in surface concentration of the participating species, until the limiting condition for the reaction is reached (like maximum mass transport rate or full phase conversion) and then falls again until the characteristic potential of another reaction is reached or the predefined limit potential for current reversal. This way a cycling is performed between two potential values. GCPL measurements are represented in a potential (E) versus charge (q = current i multiplied by time t) plot. For an irreversible process, increasing the current, the E vs. q wave shifts to lower potentials. Also, a resistance like an SEI layer between WE and RE shifts the E vs. q wave to lower potentials with, increasing current. The time elapsed (or the charge q transferred through the cell) from starting the current until the fast change in potential when a limiting condition for the reaction is reached is the GCPL analogue to the peaks in a CV.

In a GCPL measurement, where the potential is changing freely, it is more difficult to estimate the contribution of the EDL charging compared to a CV where the potential is controlled. The capacitance C_d of the EDL is generally a function of potential. The current i_c flowing for EDL charging is proportional to dE/dt and thus its largest contribution to the total charge in GCPL is in the initial and final phase and between the characteristic potentials of different reactions. It is to be noted that higher charging/discharging currents lead to higher slopes of the potential plateaus in GCPL and thus to an increased contribution of EDL charging. The features in E vs. q waves from GCPL are usually less well pronounced than those in i vs. E from CV (compare the CV and GCPL curves for a composite material with a plurality of characteristic reactions of Figure 55). Potential plateaus in the GCPL curve correspond to current peaks in the CV. Extracting potential values from GCPL is less accurate than from CV, since the position of a slightly sloping plateau is not as well defined as the position of a peak. GCPL is, however, the superior technique for determining the layer thickness of a deposited layer, which is proportional

to the charge q or, in Li-ion cells, to determine the charge storage capacity (q) of the different phases forming in an electrode upon lithiation.

As with CV, galvanostatic cycling in battery research allows for observing the changes in the electrode material and performance over a simulated life of charging and discharging. GCPL is performed at different currents to test the rate capability of the material. The so-called rate capability is the amount of charge that can be stored/extracted with a certain speed, i.e. with a certain current, and determines the speed for charging the material and the power output (depending also on the cell voltage) that can be obtained with this material. High currents in GCPL are also employed in accelerated aging tests. The aging of an electrode however, is quite different on the microscopic level depending on the speed and depth of charge/discharge used, which is why such accelerated tests can generally give only a very rough estimate on the lifetime and projected performance of an electrode and should be designed and assessed very carefully.

3.5 Physical and physical-chemical analysis

In the following, short introductions are given of the techniques used in this work.

3.5.1 Scanning electron microscopy (SEM)

When a beam of high energy electrons hits a material, they produce various events that can be used for topological, structural and chemical analysis of the material (for energy dispersive X-ray analysis (EDX) see chapter 3.5.4.5). A portion of the electrons that have impinged through the surface turns back towards the surface and leave it as back scattered electrons (BSE) after a series of elastic and inelastic scattering events. These electrons probe approximately 1 µm depth of the material. Since the scattering cross-section strongly depends on the electron density and thus on the atomic number (Z) of the material, when used for imaging BSEs give Z contrast wherein a higher Z material produces more BSEs. The primary beam also creates secondary electrons (SE) in the material through inelastic scattering. These electrons have a low kinetic energy and thus a low escape depth from the material of typically less than 50 nm. Therefore, SE electrons carry more surface information than BSE.

SEM is used to obtain a topographic image of the studied sample that is tunable in terms of surface sensitivity and Z contrast. In SEM a high energy beam (typically 5-20 keV) of electrons is focused on the sample by a series of apertures and electromagnetic lenses, and the surface is then scanned while recording the signals of BSE and/or SE. The image resolution depends on the spot size of the electron beam on the sample and the electron current in this spot. For an improved lateral resolution, in-lens detectors are used which detect the electrons leaving the surface of the sample at a very small angle with respect to the incident beam. For further information on topographic imaging with SEM see for example [57].

3.5.2 Raman spectroscopy

Raman spectroscopy is based on inelastic scattering of light mostly in the visible to near UV region (but also in IR), probing the vibrational (stretching, bending, rotation) modes of molecules or the excitation and de-excitation of optical phonons in solids, utilizing the Raman effect [58-62].

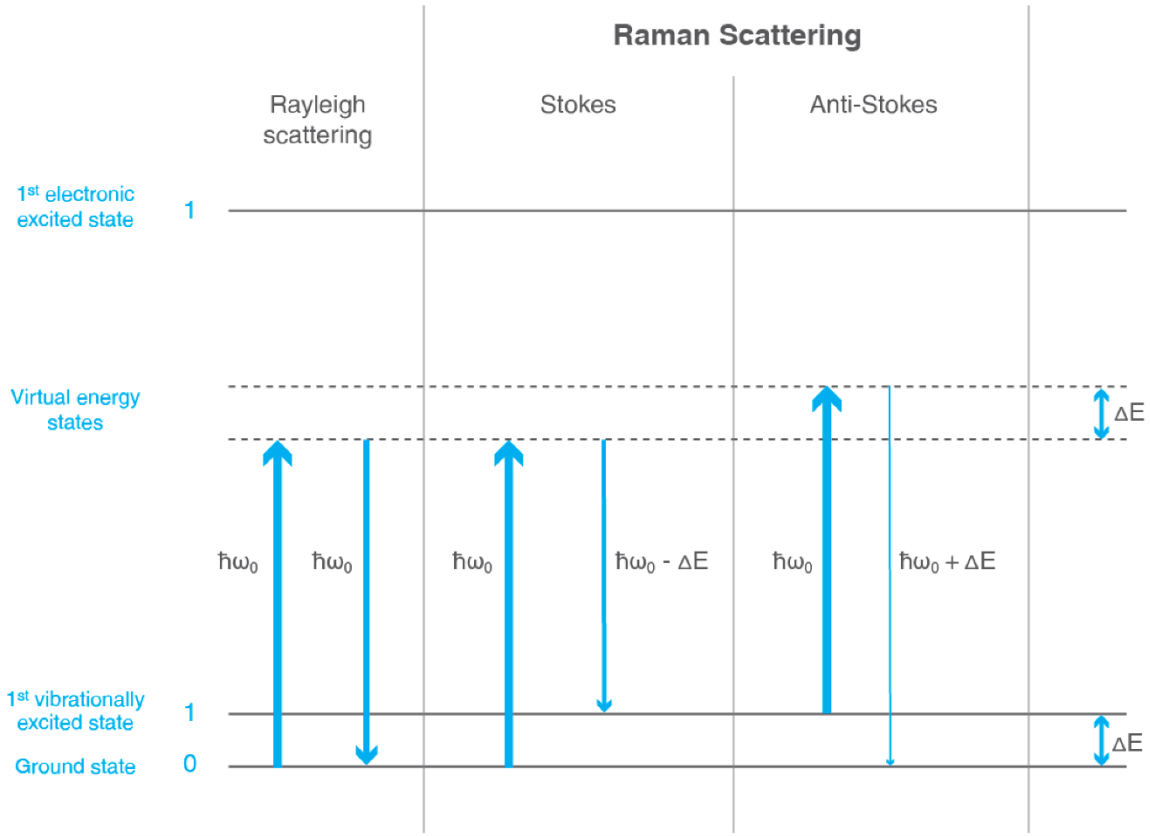

Figure 14 Energy diagram of elastic (Rayleigh) and inelastic (Raman) scattering (of visible to near UV light) by molecules. Incoming photon pointing up and scattered photon pointing down.

Vibrational modes have typical wavelengths in the IR and down to the microwave region and thus cannot absorb visible or UV light. Figure 14 shows the main processes which occur in matter under a visible to near UV light illumination (arrow pointing up) with an energy $\hbar\omega_0$ which is higher than the energy of a vibrational molecular excitation ΔE but below the energy necessary to excite an electron to the next electron shell (marked as 1st electronic exited state), which could lead to absorption of the incoming photon.

To visualize the different scattering processes, virtual energy levels are introduced, and the processes are represented in an analogy to absorption-emission events. It is however reminded that the actual processes are scattering processes, and thus instantaneous. Upward facing arrows indicate the incoming photon and downward arrows the scattered one, wherein arrow lengths are proportional to photon energy and line thicknesses of the downward arrows are proportional to the probability of the respective event. The most probable event is the elastic (photon energy is not changed) scattering of the incoming photon called Rayleigh scattering.

The so-called Raman effect is marked by the presence of the other two processes called Stokes and anti-Stokes scattering. These two processes are inelastic, thus the scattered photon has an energy which is lower (Stokes) or higher (anti-Stokes) than the energy of the incoming photon, wherein both processes subtract or respectively add the same amount of energy ΔE from/to the incoming photon. This energy difference ΔE is the energy difference between two vibrational states and thus does not depend on the energy of the incident photon. The Stokes and anti-Stokes processes which shift the energy of the scattered electron to values below or respectively above the energy of the incoming light, occur with different probabilities, wherein the Stokes process is usually the dominant one. The different probabilities of the two processes reflect different occupation of the ground and the first vibrational excitation state. In terms of energy or frequency shift, the Rayleigh scattering corresponds to zero shift, the Stokes to a negative ΔE and the anti-Stokes to a positive ΔE.

The Raman effect can be described classically based on the coupling between electromagnetic waves and induced electrical dipole moments in a molecule or solid. An incident electromagnetic wave with an electric field strength $\vec{E} = \vec{E}_0 \cos \omega_0$ induces an electrical dipole moment $\vec{p}_{el}$ that is superimposed to any permanent electrical dipole moment $\overrightarrow{p_0}$, if present, in a molecule or in the unit cell of a crystal lattice [58]:

Equation 8

$$\vec{p}_{el} = \vec{p}_{el}^{0} + \tilde{\alpha}\vec{E}$$

Wherein, $\tilde{\alpha}$ is the electrical polarizability tensor of the interatomic bonds. Electrons move much faster than nuclei, thus their contribution to the time-dependent total dipole moment is

negligible, which than depends on the time-dependent displacement (vibration) Q_n of the nuclei only. There are 3N-6 normal displacements in a crystalline solid with N nuclei which in the limit N >> 1 equals 3N. For small displacements, the dipole moment can be developed in Taylor series around the equilibrium positions $Q_n = 0$ of the nuclei and the normal displacements can be expressed as harmonic oscillations of amplitude Q_{n0} and frequency ω_n. With these, the time dependent dipole moment becomes [58]:

Equation 9

$$\vec{p}_{el}(t) = \vec{p}_{el}^{0} + \sum_n \left(\frac{\partial \vec{p}_{el}}{\partial Q_n}\right)_{Q_n=0} Q_{n0} \cos \omega_n t + \tilde{\alpha}^0 \vec{E}_0 \cos \omega_0 t + \left(\sum_n \left(\frac{\partial \alpha_{ij}}{\partial Q_n}\right)_{Q_n=0} Q_{n0} \cos(\omega_0 \pm \omega_n)t\right) \cdot \frac{\vec{E}_0}{2}$$

Wherein, α_{ij} $(i, j = x, y, z)$ are the components of the electrical polarizability tensor. The first term is the permanent dipole moment. The second term describes an oscillation of the dipole moment coupled to a transition between normal displacements. When such a dependency of the dipole moment is non zero $\left(\frac{\partial \vec{p}_{el}}{\partial Q_n}\right)_{Q_n=0} \neq 0$, the transitions are allowed and proceed with the absorption or emission of a photon with the corresponding energy of the vibration (usually in the IR). Molecules and solids where such transitions in the IR are observed are referred to as IR-active. Their IR absorption line frequency corresponding to a vibration mode is the same as the Raman shift frequency corresponding to ΔE. The third term corresponds to the induced dipole moment related to elastic (Rayleigh) scattering and the fourth term expresses the induced dipole moments related to the Stokes $(\omega_0 - \omega_n)$ and anti-Stokes $(\omega_0 + \omega_n)$ processes of inelastic (Raman) scattering. The inelastic scattering term shows that the Raman effect is only observed if $\left(\frac{\partial \alpha_{ij}}{\partial Q_n}\right)_{Q_n=0} \neq 0$, which means, only if a vibrational transition produces a change in the local electrical polarizability of the interatomic bonds. This condition is fulfilled in the so-called Raman active materials.

For a more intuitive understanding of Raman scattering, the process can be virtually split in a sequence of three sub-processes [59]:

1) Photon-electron interaction producing an excited electron;
2) Electron-phonon scattering event where a phonon is created or absorbed (vibrational transition); and
3) Electron-photon interaction resulting in the emission of the scattered photon.

Recorded Raman spectra are represented in terms of wave number (frequency divided by the speed of light) shift $\Delta\bar{\nu}$ in cm^{-1} versus intensity. The wave number shift being defined as $\Delta\bar{\nu} = \frac{1}{\lambda_0} - \frac{1}{\lambda_s}$ wherein λ_0 is the wavelength of the incident beam and λ_s, the wavelength of the scattered beam. The intensity of the Raman lines is usually below 0.001% of the intensity of the incident beam. Therefore, in order to produce a detectable Raman signal, illumination of the sample is usually done with laser light.

Raman spectra is analyzed with the help of tabulated vibrational signatures, providing information on chemical compounds and structure of the studied sample. Further reading on the theory of Raman spectroscopy and data analysis can be found in [58-62].

3.5.3 Attenuated total reflection Fourier-transform infra-red spectroscopy (ATR-FTIR)

IR spectroscopy measures the frequency dependent IR absorption for dipole moment changes corresponding to different transitions between vibrational states (second term of Equation 9). Symmetrical diatomic molecules like N_2 do not have an IR absorption line but they are Raman active. Therefore, the two techniques are often used in conjunction to detect the different species on a sample. IR absorption occurs when the photon energy of the incoming beam is equal to the energy of a vibrational normal mode or to the energy of a collective excitation of a plurality of normal modes called Fermi resonance (also observed in Raman spectroscopy). Collective excitations appear when two or more modes of the same symmetry have a similar energy and leads to a shift in the energies, and a redistribution of the intensities of the respective normal modes.

The position of an absorption peak depends on the type (and energy) of the probed chemical bond as well as on the masses of the participating nuclei, which is why IR spectroscopy is also sensitive to isotopes. The effect of exchanging two nuclei in a two-atom bond for their isotopes can easily be assessed by representing the two atomic bond as a spring connecting two masses m_A and m_B. The strength of the chemical bond does not depend on the isotopes of the participating atoms thus the spring constant k will not change. The period of oscillation of a mass m hanging on a spring with a spring constant k is:

$$T = 2\pi\sqrt{\frac{m}{k}}$$

Thus, the wave number, which is the frequency divided by the speed of light c, for the system of two bond atoms is:

$$\bar{\nu} = \frac{1}{2\pi c}\sqrt{\frac{k}{\mu}}$$

Wherein the mass of the single hanging object is replaced by the reduced mass of the system of two bond atoms $\mu = \frac{m_A m_B}{m_A + m_B}$. Building the ratio of the wave numbers of an atomic pair and the pair of their isotopes we get:

$$\frac{\bar{\nu}_1}{\bar{\nu}_2} = \sqrt{\frac{\mu_2}{\mu_1}}$$

IR spectroscopy can either be performed by scanning through a range of IR wavelengths with a monochromatic beam and measuring the wavelength dependent absorption or using a polychromatic beam and then using Fourier transformation to extract the absorption as a function of wavelength. The Fourier-transform method (FTIR) is faster since absorption is measured at all wavelengths simultaneously and also the signal to noise ratio of the spectra is better which allows the measurement of lower light intensities with the FTIR method. Therefore, modern IR spectrometers apply the Fourier-transform method. In order to reduce background from the instrument and focus the measurement on the desired substance, usually a suitable reference sample is also measured, and its spectra subtracted as background. For example, for improving the spectra of a solute, a reference measurement in the same setup is usually performed with only the solvent.

Classical IR spectroscopy is performed in transmission and is therefore not suitable for samples with a very low transmittance or samples consisting of a thin film on a thick substrate. For such cases, the method of choice is the so called attenuated total reflection (ATR) mode. In this method, a waveguide, in which the probing IR beam is propagating under total internal reflection conditions, is positioned in contact with the surface of the sample. In order to maintain the total internal reflection, the refractive index of the waveguide must be higher than the refractive index of the sample for the probed wavelengths. Under total internal reflection conditions, an evanescent wave propagates parallel to the reflection interface. The intensity I of the evanescent wave degreases exponentially with distance into the probed material as

$$I = I_0 e^{-\frac{z}{d}}$$

Wherein z is the distance from the interface and d is the penetration depth, defined as the distance from the interface at which the intensity is 1/e times smaller than the intensity I_0 at the surface. The penetration depth d depends on the IR wavelength λ, the incident angle α_i and the refractive indices of the waveguide n_w and the sample n_s as follows:

$$d = \frac{\lambda}{2\pi n_w \sqrt{\sin^2 \alpha_i - \left(\frac{n_s}{n_w}\right)^2}}$$

d is proportional to the wavelength (anti-proportional to the wave number $\bar{\nu}$) and is typically in the order of few µm. The evanescent wave penetrating the sample experiences wavelength dependent absorption (as in the transmission mode IR spectroscopy) which is transferred to the exiting beam detected in the instrument. Each time the beam propagating in the waveguide is reflected from the waveguide/sample interface the evanescent wave is formed in the illuminated spot and thus the contributions of all reflections are summed up in the exit beam. Therefore, ATR-IR spectroscopy has a very high surface sensitivity and in combination with the Furrier-transform mode (ATR-FTIR) delivers a quick and easy to use surface analysis method. For more theory on IR absorption and related methods see [60] and [63].

3.5.4 X-ray analysis

Some important properties of X-ray scattering can be described to a large extent by a semi-classical model in which the atom is comprised of a massive positively charged nucleus surrounded by electrons held at discrete binding energies [64,65].

When an electromagnetic wave passes through the medium, the nuclei are too massive to respond to the high frequency incident field, whereas the electrons are caused to oscillate at the frequency ω of the electric field E_i of the incoming driving wave. The electrons being bond by different restoring forces, respond differently to the impressed field, the response depending on the difference ω-ω_s between the frequency ω of the driving field and the resonant frequencies ω_s of the different electrons. The oscillating electrons emit dipole radiation, which interferes with the incident wave to produce a modified propagating wave, compared to that in vacuum. The influence of matter on an electromagnetic wave is described by the material-

dependent index of refraction n, which is a complex quantity, describing the modified phase velocity compared to that in vacuum (the speed of light c) and the decay in amplitude of the propagating wave. The refractive index has a strong frequency dependence, especially close to the resonant frequencies ω_s.

It can thus be expressed in terms of the sum of the contributions from the different electrons of the atoms with their resonant frequencies ω_s and corresponding resonator strengths g_s (Equation 10). The resonator strengths in the semi-classical model are integers which denote the number of electrons in an atom associated with a given resonant frequency ω_s. These strengths sum up to the total number of electrons per atom Z.

$$\sum_s g_s = \mathrm{Z}$$

Equation 10

$$n(\omega) \equiv \left[1 - \frac{e^2 \rho_e}{\varepsilon_0 m} \sum_s \frac{g_s}{(\omega^2 - \omega_s^2) + i\gamma\omega}\right]^{1/2}$$

In Equation 10, ρ_e is the number of electrons per unit volume, ε_0 the permeability of vacuum, m and e the electron mass and charge, respectively, and γ is a dissipative factor.

This equation can be simplified for

$$\omega^2 >> \frac{\mathrm{e}^2 \rho_e}{\varepsilon_0 \mathrm{m}}$$

which is the case for X-rays, thus arriving at Equation 11

Equation 11

$$n(\omega) = 1 - \frac{1}{2} \frac{e^2 \rho_e}{\varepsilon_0 m} \sum_s \frac{g_s}{(\omega^2 - \omega_s^2) + i\gamma\omega}$$

With the refractive index of vacuum being unity, the equation compares the frequency dependent refractive index in medium with that in vacuum. This equation can be rewritten in a simpler form in terms of the classical electron radius

$$r_e = \frac{e^2}{4\pi\varepsilon_0 mc^2}$$

and the complex atomic scattering factor (superscript 0 denotes forward scattering)

$$f^0(\omega) = \sum_s \frac{g_s \omega^2}{(\omega^2 - \omega_s^2) + i\gamma\omega} = f_1^0(\omega) - i f_2^0(\omega)$$

as

Equation 12

$$n(\omega) = 1 - \frac{\rho_e r_e \lambda^2}{2\pi}[f_1^0(\omega) - i f_2^0(\omega)]$$

Grouping the real and imaginary parts in

$$\delta = \frac{\rho_e r_e \lambda^2}{2\pi} f_1^0(\omega)$$

$$\zeta = \frac{\rho_e r_e \lambda^2}{2\pi} f_2^0(\omega)$$

We get

$$n(\omega) = 1 - \delta + i\zeta$$

Wherein, the real part describes the modified phase velocity compared to that in vacuum and the imaginary part, the decay in amplitude of the propagating wave. The values of δ and ζ for X-rays are typically in the order of ~10^{-6} and ~10^{-8}, respectively. Thus, the wavelength dependent absorption expressed by the imaginary term can often be neglected. Due to this frequency dependence, waves of different frequencies travel at different phase velocities and separate (disperse). It is visible from this expression for n(ω) that both positive and negative dispersion are possible. The index of refraction for electromagnetic waves displays resonant behavior at frequencies corresponding to electronic transitions in atoms and molecules. On the low frequency side of a resonance ω_s, n increases with ω, and this is known as normal dispersion.

Immediately above the resonance frequency ω_s it decreases, and as more and more resonances are passed, the magnitude of the index of refraction decreases. X-ray frequencies are usually higher than all transition frequencies, perhaps with the exception of those involving the inner K- or maybe L-shell electrons. As a result, in the X-ray region, n turns out to be less than unity [64,65].

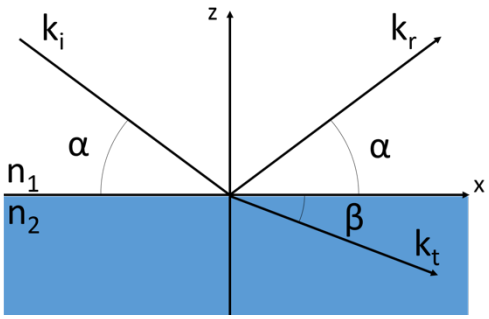

Figure 15 Reflection and refraction of an incident beam k_i upon an interface between two uniform dielectric media wherein $n_1 > n_2$, k_i – incident beam, k_r – reflected beam, k_t – transmitted (refracted) beam.

Figure 15 shows the reflection and refraction of a beam incident from an optically denser medium on an interface. In accordance with Snell's low (Equation 13), when X-rays impinge from vacuum ($n_1 = 1$) on an interface with a medium having a lower refractive index (n_2), under a grazing incidence angle α below a material specific critical angle α_c, they are totally reflected (no transmitted beam k_t). This phenomenon is called total external reflection, in analogy to the total internal reflection observed for visible light (where $n_2 > n_1$) in the opposite direction (from material to vacuum).

Equation 13

$$n_1 \cos\alpha = n_2 \cos\beta$$

For total reflection at the critical angle $\alpha = \alpha_c$, with $n_1 = 1$ and $\beta = 0°$, Equation 13 becomes:

$$\cos\alpha_c = n_2$$

The real part of the refractive index of the medium which is slightly below the refractive index of vacuum is

$$n_2 = 1 - \delta$$

where δ can be expressed in terms of the real part of the scattering length density (SLD) of the material as

Equation 14

$$\delta = \frac{\lambda^2}{2\pi}\mathrm{Re(SLD)}, \quad \mathrm{Re(SLD)} = \rho_e r_e f_1^0(\omega).$$

Further using the approximation for a small angle

$$\cos\alpha_c \approx 1 - \frac{\alpha_c^2}{2} \rightarrow n_2 \approx 1 - \frac{\alpha_c^2}{2}$$

we get:

Equation 15

$$\alpha_c \approx \sqrt{2\delta} = \lambda\sqrt{\frac{SLD}{\pi}}$$

With these equations, the angle of the scattered beam can be expressed in terms of the incident and critical angles

$$1 - \frac{\alpha^2}{2} = \left(1 - \frac{\beta^2}{2}\right)\left(1 - \frac{\alpha_c^2}{2}\right)$$

$$\rightarrow \beta = \sqrt{\alpha^2 - \alpha_c^2}$$

For an incident angle $\alpha<\alpha_c$, the angle of the refracted beam becomes imaginary $\beta = i\alpha_c$ and the refracted beam becomes an evanescent wave with an intensity I which is exponentially decreasing with distance r from the surface (Equation 16).

Equation 16

$$I = I_0 e^{-\left(\frac{4\pi\zeta}{\lambda}\right)r}$$

The distance at which the intensity has dropped to 1/e times its initial value, called exponential decay length $r_{1/e}$ is then

Equation 17

$$r_{1/e} = \frac{\lambda}{4\pi\zeta}$$

These conditions allow a highly surface sensitive study of the scattering medium.

From the above it is clear that the way how the medium influences the electromagnetic wave impinging on it, depends on the incident angle and the energy of the wave. Thus, various depths and properties of the scattering material are accessible by varying these two parameters.

In the following, different techniques used in this work, will be explained, which are based on different X-ray scattering or absorption phenomena, allowing the non-destructive characterization of samples in terms of their material specific properties like critical angle of total external reflection, elemental and chemical (oxidation states) composition, crystal structure, and surface morphology.

3.5.4.1 X-ray reflectivity (XRR)

X-ray reflectivity (XRR), also called X-ray reflectometry is a non-contact, non-destructive analytical technique to determine thickness, density profile in direction normal to the surface, roughness and interstitial roughness of thin films. In XRR (see Figure 16), the reflected beam intensity is measured as a function of incident angle or the corresponding momentum transfer vector Q_z normal to the surface (z direction), at low angles close to the critical angle for total external reflection. The momentum transfer $Q_z = k_r - k_i$, wherein k_i and k_r denote the wave vectors of the incident and reflected beam, respectively, which have, for elastic scattering, equal magnitudes of $2\pi/\lambda$.

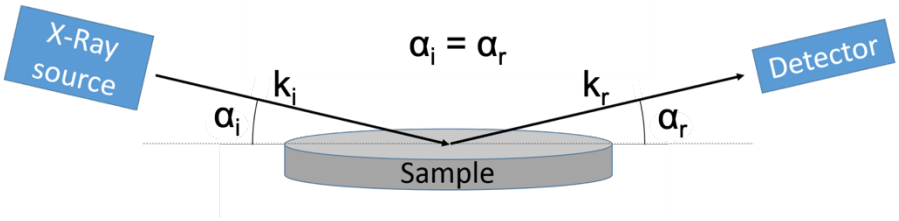

Figure 16 Schematic representation of XRR geometry with incident angle α_i equal to the reflection angle α_r.

The vertical momentum transfer depends on the incident angle α_i (equal to the reflection angle α_r) and the wavelength λ as follows:

$$Q_z = \frac{2\pi}{\lambda}(\sin\alpha_i + \sin\alpha_r) = \frac{4\pi}{\lambda}\sin\alpha_i$$

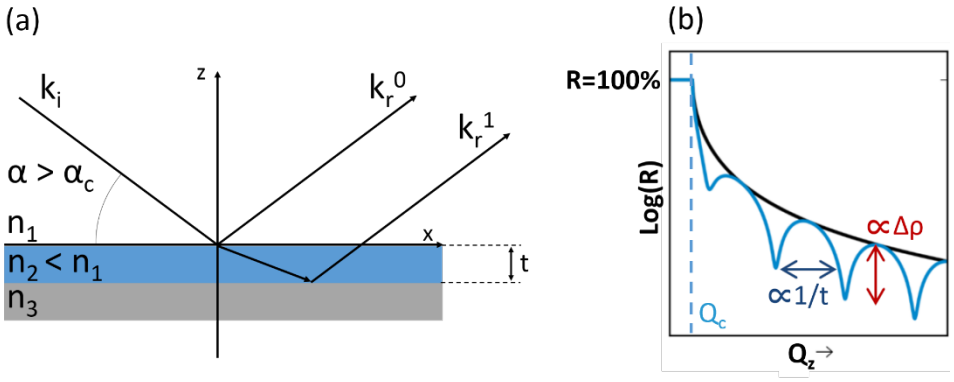

Figure 17 (a) Reflection from a thin film of thickness t and (b) Kiessig fringes in a reflected intensity versus momentum transfer plot with a marked critical momentum transfer value Q_z=Q_c at the critical angle.

Figure 17 shows the reflection of an X-ray beam from a thin film. Below the critical angle ($Q_z < Q_c$), the beam is totally reflected, thus the reflected intensity R=100% whereas for $Q_z >> Q_c$ the reflected beam intensity $R \propto Q_z^{-4}$. When the incident angle is gradually increased beyond the critical angle, the intensity drops abruptly, X-rays impinge through the outer interface, reflect from the different interfaces of the sample and give rise to interference fringes, called Kiessig fringes [65]. The peaks of the fringes correspond to constructive interference whereas the dips correspond to destructive interference. The period of the fringes (ΔQ_z) is inversely proportional to the thickness t of the film (Equation 18), the decrease in intensity is proportional to the roughness of the film, and the amplitude of the fringes is proportional to the density contrast of the top and bottom layers $\Delta\rho$ [66].

Equation 18

$$t = \frac{2\pi}{\Delta Q_z}$$

In order to find all sample parameters, experimentally obtained data need to be fitted with a model including the layer thickness, surface roughness etc. as parameter. This fitting is usually performed following the recursive Parratt formalism [65,66] or the Abeles matrix formalism [67,68].

3.5.4.2 Grazing incidence small angle X-ray scattering (GISAXS)

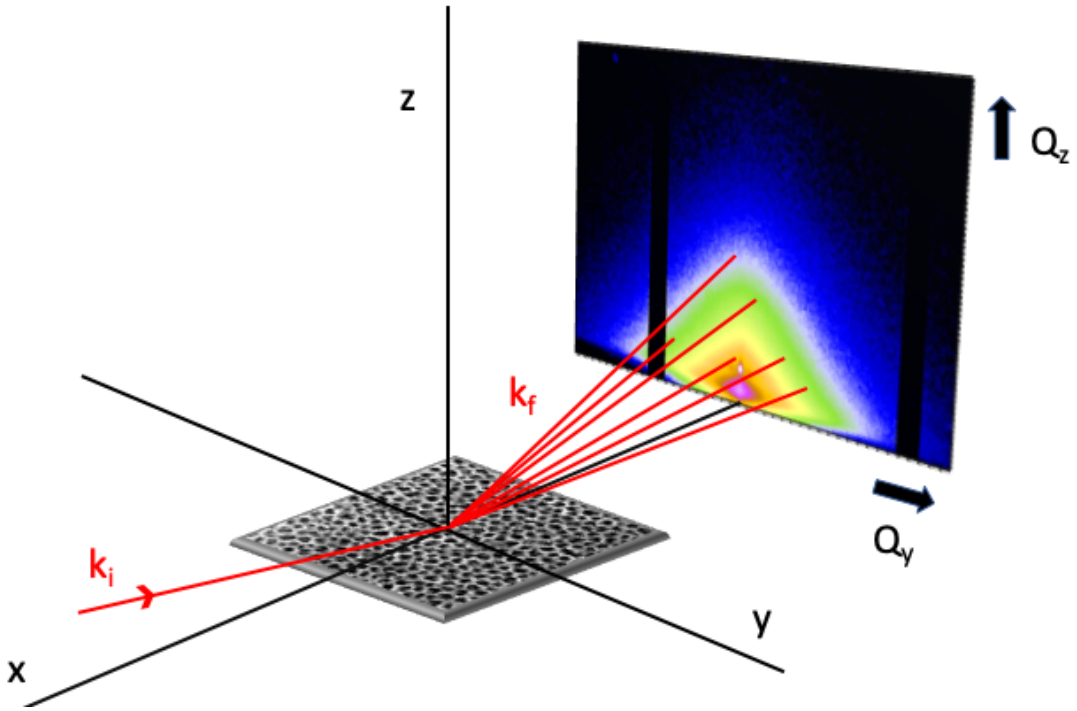

Figure 18 GISAXS geometry wherein k_i is the incoming beam wave vector and k_f is the wave vector of a "final" beam reaching the detector.

Grazing incidence small angle X-ray scattering (GISAXS) is a technique for analyzing the morphology of nanoscaled surface structures and buried structures in thin films.

Classically, the morphology of nanostructures is studied by direct imaging techniques like scanning electron microscopy (SEM) and transmission electron microscopy (TEM) or for low roughness surfaces by atomic force microscopy (AFM) or scanning tunneling microscopy (STM).

Information about the morphology of the studied layers in their depth is gathered in SEM and TEM by preparing cross-sections, which destroys the sample.

Apart from the exposed surface of the cross-sections, however, buried and inner structures are not accessible. Furthermore, conductivity of the studied surface is crucial for SEM, TEM and STM, sample preparation for TEM can be challenging and measurement times for AFM and STM are rather long. These methods deliver a direct but only a very local information on the morphological parameters, observing electrode areas in the order of 10x10 μm^2 (for structures in the order of 10 nm). Repeating such measurements over a plurality of spots on the surface improves the statistical value of the measured parameters. However, covering the whole area is practically impossible and the chance for overseeing spots, with a significantly different morphology, is high.

GISAXS is a fast technique that is applied as a complementary method to direct imaging techniques. It can be performed at ambient conditions and each scattering pattern takes only a few seconds to record (depending on scattering contrast and beam intensity) while covering large surface areas in the order of 10x20 mm^2 and probing the surface morphology of the sample, and structures buried below the surface.

These properties make GISAXS so interesting for the investigation of dynamic structure changes in physical and chemical processes at surfaces and in films, and also for determining structural parameters of surfaces and thin layers over large areas with a high statistical relevance.

GISAXS investigations are performed at synchrotron radiation sources or in smaller laboratory setups. The smaller setups have a lower resolution and recording speed, which however suffice in many cases. GISAXS is performed with a monochromatic X-ray beam. As with all X-ray scattering techniques, GISAXS is sensitive to electron density fluctuations. The chosen photon energy is most frequently in the range of 5 keV to 20 keV, due to the good scattering to absorption ratio. The optimal energy for soft matter samples is around 8 keV while a higher energy is recommended for heavier elements.

The grazing incidence of X-rays in GISAXS makes it a highly surface sensitive technique, in contrast to transmission scattering techniques, allowing the study of coatings, films and

particles on surfaces of nanoscale thickness and dimensions. The high path-length of the X-ray beam through the film plane delivers the necessary signal strength.

The scattered intensity is recorded by a 2D detector at angles of a few degrees thus enabling the observation of lateral sizes ranging from a few nm up to hundreds of nm. The sample detector distance for GISAXS is normally in a range of 1 to 5 meters. At distances of up to 13 meters, the detectable lateral size increases to several micrometers and the technique is then referred to as grazing incidence ultra-small angle scattering (GIUSAXS). The 2D detectors commonly in use are of the gas-filled wire frame type, CCD-type as well as imaging plates. In order to prevent damage or saturation of the detector, small beam-stops are often used to block the direct (transmitted through the sample) and the reflected specular beam.

The geometry of GISAXS gives the possibility to perform so-called out-of-plane scans, which alleviates the problem that information at and around the reflected beam spot (at $Q_y = 0$) is hidden by a beam-stop. GISAXS can be applied to determine internal as well as surface morphologies of thin films.

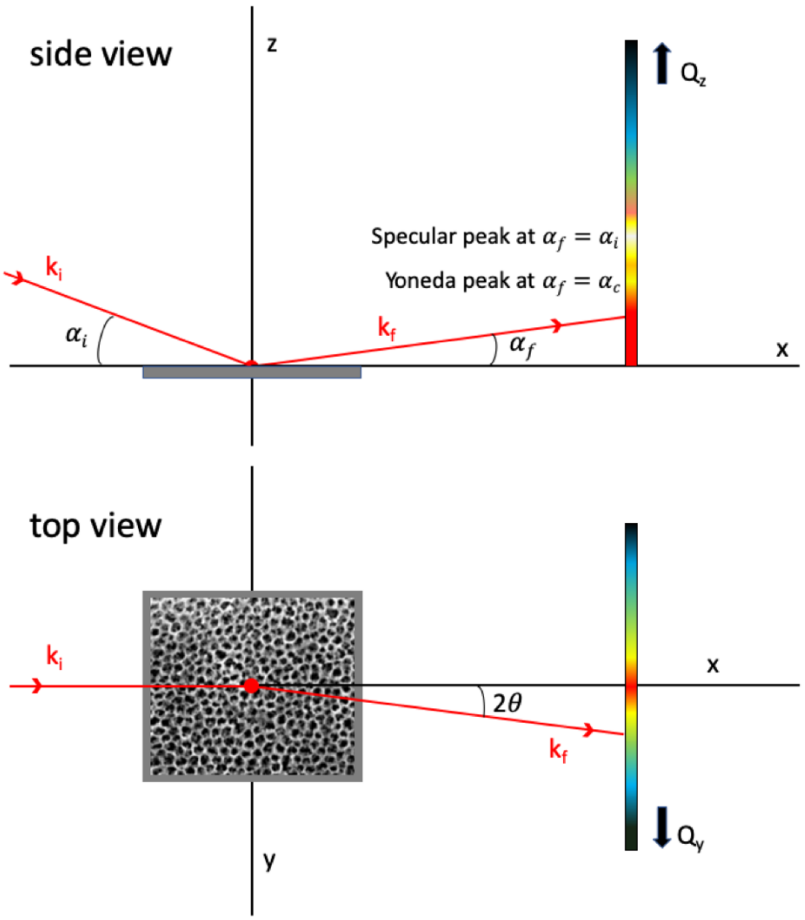

Figure 19 GISAXS geometry side and top view. The subscript i denotes the incident wave and the subscript f denotes the "final" wave recorded by the detector.

Figure 19 shows the geometry of a GISAXS experiment with Cartesian x,y,z coordinates, wherein the sample plane is the xy plane and the projection of the incident beam with a wave vector k_i is on the x axis. The incident beam hits the sample at the incident angle α_i. The scattered beam with a wave vector k_f leaves the sample at an angle α_f above the sample horizon in the incident plane xz normal to the sample plane and an angle $2\theta_f$ in the sample plane xy. At an exit angle α_f of the scattered beam k_f close to the sample-specific critical angle of total external reflection α_c, a signal enhancement is observed due to the Vineyard effect [69]. At $\alpha_f = \alpha_c$, the Fresnel transmission coefficients, which contribute to the differential cross-section for diffuse scattering, have a maximum resulting in a bright intensity band called Yoneda peak (in the lower Q_z part of the scattering image in Figure 19 side view, slightly below the specular peak).

The existence of the Yoneda peak can be rationalized considering the conditions for total external reflection, where the angles of the incident and reflected beam are equal to the critical

angle α_c, under this condition, the two beams are in phase and have a similar amplitude, which leads to the signal enhancement [65,69,70]. In order to reduce the penetration depth of the beam and thus reduce the background scattering in the measurements, a very small incident angle α_i is used that is slightly above the critical angle α_c, thus a specular peak produced by the reflected beam at $\alpha_f = \alpha_i$ is visible together with the Yoneda peak at $\alpha_f = \alpha_c$. The X-rays are scattered by any type of electron density fluctuations at the illuminated portion of the surface. The appearing scattering wave vector Q, also referred to as the momentum transfer vector, for the three spatial directions is defined by:

$$Q_{x,y,z} = \frac{2\pi}{\lambda}\begin{pmatrix} \cos(\alpha_f)\cos(2\theta_f) - \cos(\alpha_i) \\ \cos(\alpha_f)\sin(2\theta_f) \\ \sin(\alpha_f) + \sin(\alpha_i) \end{pmatrix}$$

The scattering intensity I(Q) resulting from a lateral electron density variation can be represented by

$$I(\vec{Q}) = \langle |F|^2 \rangle S(Q_{\parallel})$$

where F is the form factor and S(Q) is the total interference function. The total interference function is the Fourier transform of the island position autocorrelation function and describes the lateral correlations of the scattering objects. F, in the simple Born approximation (BA), is the Fourier transform of the shape function of the scattering objects, and is defined as

$$F(\vec{Q}) = \int \rho(r) e^{i\vec{Q}\vec{r}} d^3r$$

wherein $\rho(r)$ is the spatial electronic distribution of the scattering object with center at r=0. In order to account for reflection-refraction effects at the surface, F has to be calculated within the distorted wave Born approximation (DWBA) where it has a more complex expression. For the full calculation of the scattering cross section in the DWBA, four terms, corresponding to four different scattering events, are used. Figure 20 illustrates the physical picture of these four terms.

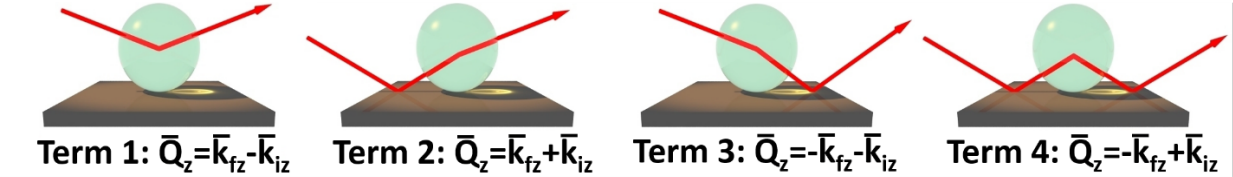

Figure 20 The four scattering events in DWBA reproduced with modified Q symbol. From [71].

These four events involve reflection and refraction of the incident and the final beam collected on the detector. Each term is weighted by the corresponding Fresnel coefficient. The waves interfere coherently, giving rise to the effective form factor (FDWBA), in which the classical form factor comes into play but with respect to the specific wavevector transfers. Uncorrelated roughness of the surface reduces its reflectivity and can be calculated in a classical way with a mean standard deviation. The scattered cross section is proportional to the scattered intensity and thus to the modulus square of the Fourier transform of the electron density. For X-rays, the polarization effect at small scattering angles can be safely neglected. The combination of the form factor F, calculated within the DWBA, with the total interference function S(Q) gives the expression for the total incoherent differential cross section:

$$\frac{d\sigma}{d\Omega} = \langle |F_{DWBA}|^2 \rangle S(Q_{\parallel})$$

wherein Ω stands for the solid angle.

Form Factor F

Simulated form factors $|F(Q_y,Q_z)|^2$ for differently shaped scattering objects are presented (log scale intensity) in Figure 21. The comparison of the different scattering distributions show, that the different form factors are indeed distinguishable. The positions of the observed spots can be translated into shape parameters of the scattering objects. For example, by measuring the angle between the horizon and the scattering maxima in the case of the pyramidal shaped scatterer (see Figure 21d), one can obtain the angle of its side walls.

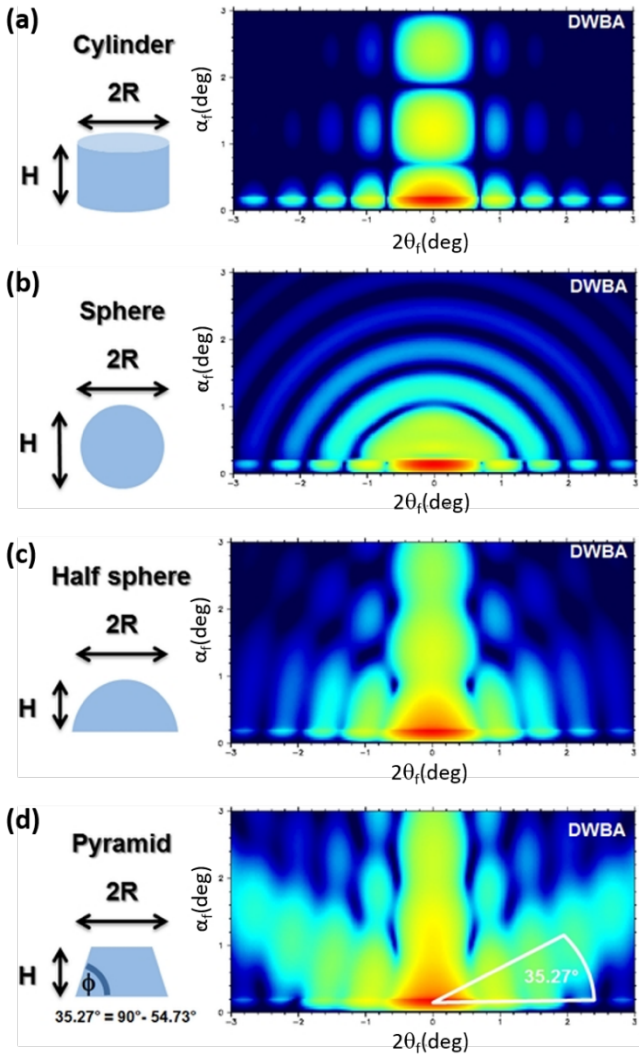

Figure 21 Simulated form factors F for (a) a cylindrical scattering object (R = 5 nm; H/R = 1) (b) a spherical scattering object (R =5 nm; H/R = 2) (c) a half-spherical scattering object (R = 5 nm; H/R = 1) (d) a pyramidal scattering object (R = 5 nm; H/R = 1; $\phi = 54.73°$), reproduced from [71].

Interference Function S (structure factor)

When the scattering objects are organized in a lateral pattern, an interference pattern appears parallel to the probed surface, along the Q_y direction, described by the interference function S. Figure 22a shows the interference function S for a scattering layer with a 2D hexagonal arrangement of the scattering objects. Figure 22b displays a simulated scattering pattern combining the contributions of the form factor F of upright standing cylinders (Figure 21a) with the structure factor S describing an organization of the cylinders in a 2D hexagonal lattice (Figure 22a). A scattering is only observable at positions where both F and S (Figure 21a and Figure 22a) have a maximum.

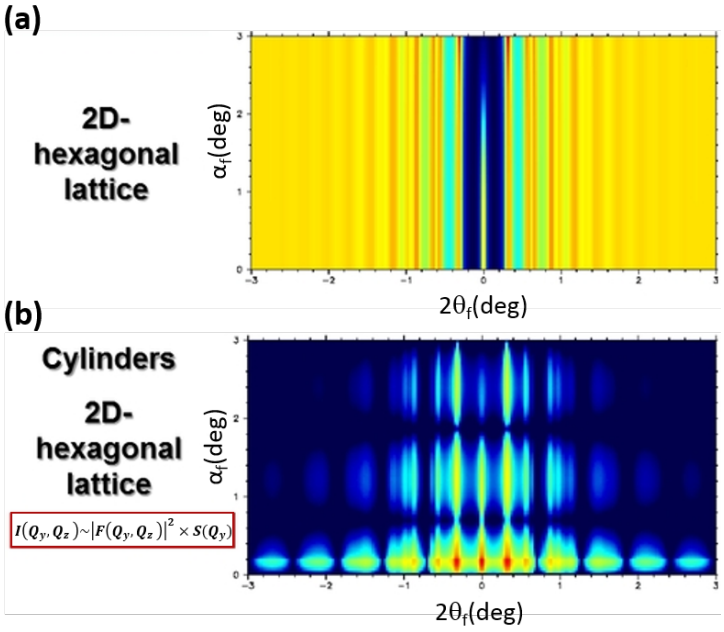

Figure 22 Simulated (a) 2D hexagonal lattice structure factor (lattice parameter a = 20 nm) (b) intensity pattern $I(Q_y,Q_z)$ for scattering from a 2D hexagonal arrangement of cylinders (R =5 nm; H/R = 1; a = 20 nm) reproduced from [71].

Figure 23 shows the simulated patterns for the same lateral organization (structure factor S) of differently shaped (different form factors F) scattering objects.

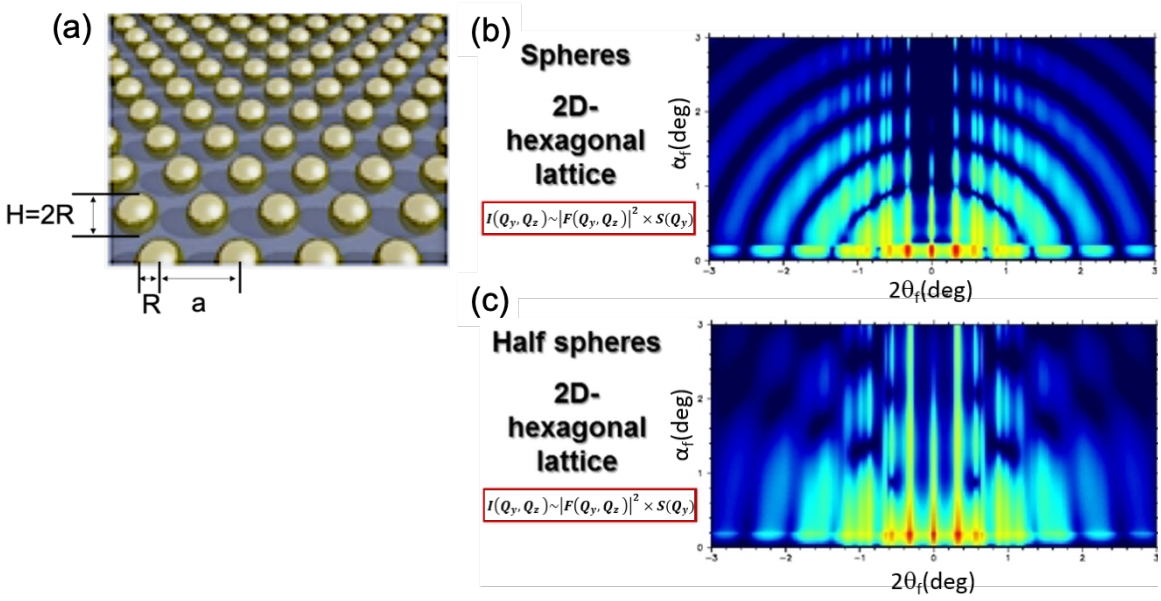

Figure 23 (a) scattering surface with a 2D hexagonal arrangement of spheres (b) simulated intensity patterns $I(Q_y,Q_z)$ for scattering from a 2D hexagonal arrangement of spheres (R =5 nm; H/R = 2; a = 20 nm) (c) simulated intensity patterns $I(Q_y,Q_z)$ for scattering from a 2D hexagonal arrangement of half-spheres (R =5 nm; H/R = 1; a = 20 nm) reproduced from [71].

Analysis of 2D intensity pattern data from GISAXS

Out-of-plane cuts

In order to extract the desired structure parameters, the recorded patterns are fitted using different models for the scattering layer. Instead of fitting the whole 2D pattern, however, usually only cuts are taken in horizontal direction along Q_y at the Q_z position of the Yoneda peak, where the scattering signal is the strongest, and the interference function S(Q) is analyzed directly. After the scattering curve $I(Q_y)$ for the cut is extracted, it is fed in a SAXS-analysis software.

In order to get the precise radius R(y) of the scattering objects in the surface plane, the form factor F needs to be obtained taking the full DWBA into account. A good starting point for doing so is to use the cylindrical form factor for the calculation, as its intensity oscillation along Q_y is

independent from Q_z and α_i. If a full analysis is required, the radius obtained from the out-of-plane cut is already a good starting point.

For a deeper understanding of X-ray scattering [65], [72] and [73] provide an extensive theoretical background as well as an overview of currently used calculation methods and experimental setups.

3.5.4.3 X-ray diffraction (XRD) and grazing incidence diffraction (GID)

X-ray diffraction (XRD) is an analytical method for determining the atomic or molecular structure of materials, or more generally for determining their three dimensional electronic density distribution. Grazing incidence diffraction (GID) is in principle XRD wherein the incident beam of X-rays hits the sample under a low angle (grazing incidence) which increases the surface sensitivity of XRD. X-rays are used since they have a wavelength (~1 Å) in the order of an atomic radius or the length of a covalent bond. In contrast, radiation with a longer wavelength like UV light would not be sensitive enough to resolve the atomic positions in the material. Gamma-rays on the other hand have a shorter wavelength and thus enable a better resolution, however they are hard to focus, difficult to produce in the form of a high flux beam, and have a very high ionizing power. X-ray diffraction is an elastic scattering technique. When a plane wave of X-rays hits the surface of a material, each atom reemits a spherical wave. When the atoms in the material are organized regularly like in a crystal lattice, the reemitted spherical waves will interfere destructively in most directions except for some specific directions determined by Braggs law (Equation 19).

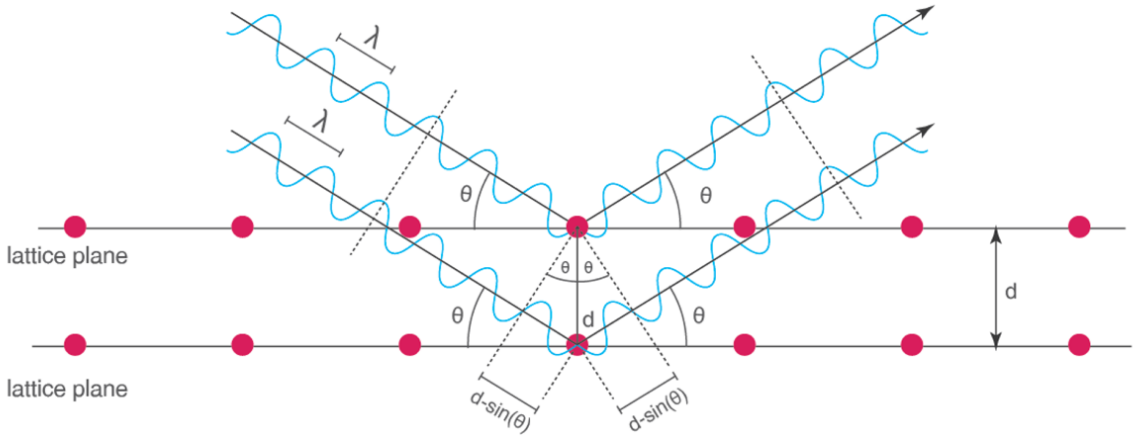

Figure 24 Bragg reflection from a crystal.

Figure 24 illustrates the condition for constructive interference of X-rays elastically scattered from two neighboring crystal planes following Braggs law. Two waves with the same or nearly the same wavelength, which overlap in the point of observation, will interfere constructively if they are in phase, i.e. if their phase difference is equal to an even multiple of π, and destructively if they are phase shifted by an odd multiple of π.

More generally speaking, the amplitude of the resulting wave in the point of observation is the vector sum of the amplitudes of the two interfering waves. When the difference in traveled distance between the two beams is equal to an integer of the wavelength, the two waves will have their electrical field vectors pointing in the same direction and their vector sum will be larger than the individual vectors thus interfering constructively. In contrast, if the difference in traveled distance between the two beams is equal to an integer of half a wavelength, the two waves will have their electrical field vectors pointing in opposing directions and their vector sum will be smaller than the individual vectors, thus interfering destructively.

Comparing the paths of the two beams in Figure 24 it becomes evident that this condition for constructive interference translates to

Equation 19

$$2d \sin\theta = n\lambda$$

which is Braggs law for a lattice plane distance of d, incident angle θ and wavelength λ, wherein n is an integer. This rule allows the determination of the distance between lattice planes of a crystal simply by measuring the diffraction angle. A structured material has more than one lattice plane, thus different lattice planes having different spacings will produce diffraction spots at different angles. Such a diffraction pattern is characteristic for the studied material. If the crystallites in the material are arbitrarily oriented as in powder diffraction, all lattice planes get the chance to produce a reflection. In preferentially oriented materials (investigated without rotation) however, one of the planes will produce a significantly higher reflection while others won't be observed at all. From the angular position of this reflection then, the preferential orientation of the material can be determined. It is important to note that even in a powder diffraction pattern, diffraction peaks corresponding to different crystal lattice planes like the (100) and the (004) plane will generally have different intensities. This among other reasons is due to the different degree of correlation of the planes (measured in terms of correlation length). Planes which are nearest neighbors have a stronger correlation whereas planes which are far apart in the lattice are practically uncorrelated meaning that the uncertainty in their relative position is in the order of the lattice spacing. Thus, care needs to be taken when assessing preferential orientation.

Real materials are not infinite crystals. Therefore, the angular position of a reflection is not infinitely sharp but has a certain spread (broadening). There are various factors that contribute to such a peak broadening in an XRD pattern [74], such as instrumental broadening, imperfections in the crystal lattice and inhomogeneous strain, but most importantly it is the finite dimensions of the crystallites in the material. The finite dimensions mean a limited number of parallel planes of the same kind (hkl) which contribute for a certain reflection, with a lower number (smaller grains) resulting in broader (less defined) diffraction paks. Paul Scherrer found the dependence of peak broadening and crystallite size. In fact he found a lower limit for the size of the crystallites L described by the Scherrer equation (Equation 20), which is exact if all other contributions to the peak broadening are zero, and it is an underestimate for the crystallite size if other contributions are non-zero.

The equation relates the mean size of the crystallites L to the peak width at half maximum height B(2θ) in radian called Full Width Half Maximum (FWHM), the Bragg angle θ in degree, the X-ray wavelength λ and a dimensionless shape factor K with a value close to 1 which depends on the shape of the crystallites.

Equation 20

$$L = \frac{K\lambda}{B(2\theta)\cos\theta}$$

3.5.4.4 X-ray photo-electron spectroscopy (XPS)

Through irradiation of a material with a monochromatic X-ray beam photo-electrons are produced having a kinetic energy that is equal to the difference of the photon energy and the binding energy of the electron. Thus, knowing the energy of the incident beam and the energy of the detected electron, the binding energy of the electron is calculated. In praxis the binding energy is further corrected for the energy lost in the detector by additionally subtracting its work function, which is known for the used apparatus. The measured spectrum of binding energies of the electrons of the illuminated material carries information on the elemental composition and chemical state of the ingredients of the surface layer. The relative intensities of XPS peaks corresponding to different electron binding energies are used to determine the relative amounts of different materials in the probed surface layer with a precision in the order of parts per thousand. The number of photo-electrons produced by the X-rays at a certain depth under the surface of the sample, that manage to escape the material, is decreasing exponentially with depth. Therefore, XPS is a highly surface sensitive method probing typically only the top 0-10 nm of the surface layer. The low escape depth of electrons sometimes helps to assess the layer thickness of the surface film studied by XPS. If, for example, a signal is detected from the substrate carrying the layer under study, that is a clear indicator that the layer thickness is below the escape depth of electrons for the material. In order to avoid diffraction patterns and increase the number of electrons produced within the escape depth, thus improving the sensitivity of an XPS measurement, the incident beam is usually directed under a low angle between the critical angle of total external reflection and the first Bragg-diffraction angle. The sample detector distance in XPS is typically ~1 m. Under ambient pressure most of the photo-electrons would be lost in collisions with air and create and additionally create noise. Therefore, XPS is commonly performed under high vacuum conditions at pressures below 10^{-8} mbar, which however requires that the samples do not contain any volatile components. XPS has a very good sensitivity for elements heavier than Li but practically none for the lighter ones H and He (at least for laboratory scale devices). Detecting Li with XPS is in most cases challenging. Peak assignment in XPS is performed using tabulated signatures of the different

elements and their different oxidation states, which are usually integrated in the analysis software, and measured spectra of standard samples with well-known composition of materials comprised in the sample under study. The most common bias in XPS measurements, which is shifting the whole measured spectra is the presence of surface charge. Correction is commonly performed by adjusting the spectra to the peak position of carbon (C 1s), which is always to be found on the surface. In case the C 1s signal is too complex or itself subject of the analysis, another unambiguous reference must be chosen for the correction like an easily distinguishable oxidation state of the material. For more details on XPS the reader may refer to [75-77].

3.5.4.5 Energy dispersive X-ray analysis (EDX)

Energy Dispersive X-ray analysis (EDX) is a technique used to study the elemental composition of a sample. In EDX, the sample is bombarded with fast particles like electrons or X-rays which produces electron holes in the atomic shells. When an electron from an outer shell recombines with the hole, it emits a characteristic X-ray line with an energy equal to the difference in energies between the shells of the electron transition. Using an energy-dispersive detector, these characteristic X-rays are recorded in a spectrum, which is a characteristic footprint of the chemical composition of the surface layer. Since however, many elements have overlapping X-ray emission peaks and there are also additional effects lowering the accuracy of the measurement, quantitative analysis of the spectra is challenging. EDX is usually used inside a scanning electron microscope (SEM) by using the accelerated electrons as an excitation source and providing the energy-dispersive X-ray spectrometer (usually a silicon drift detector) inside the vacuum chamber. Such a combined setup allows the coupling of morphological and chemical analysis of structures down to the nanometer scale. For further reading see [57].

3.5.5 Neutron analysis

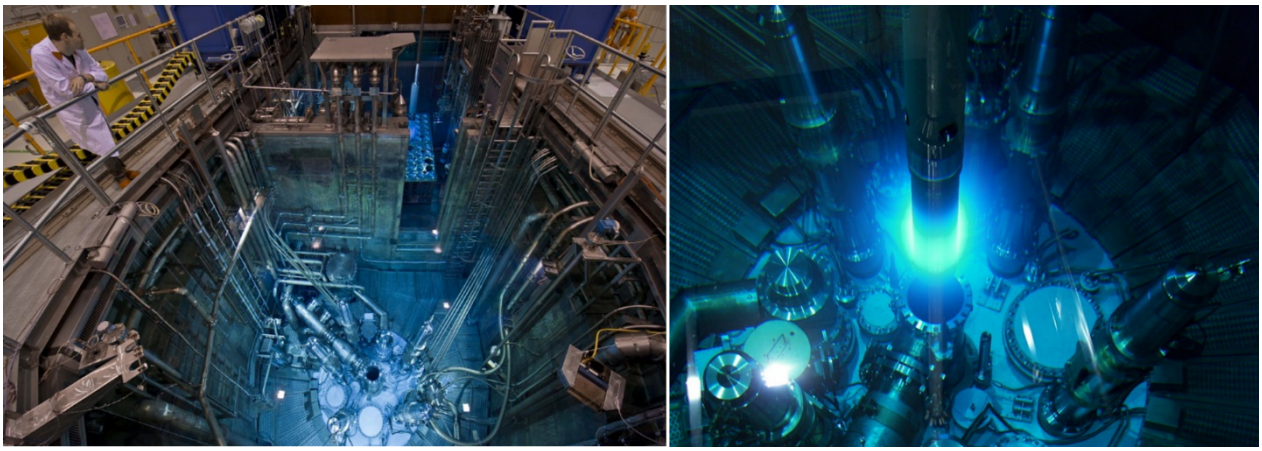

Figure 25 Left: Reactor pool (Picture: Heddergott, TUM); Right: Cherenkov radiation in the reactor pool of the FRM II (Picture: Jürgen Neuhaus, FRM II) from [78].

The nuclear fission reactor in FRM II is used as a high flux (more than $10^{}$ free neutrons per square centimeter and second) neutron source for scientific and medical purposes. The facility is equipped with multiple secondary sources providing neutron beams with different energies and positrons [78].

3.5.5.1 Time-of-flight grazing incidence small angle neutron scattering (TOF-GISANS)

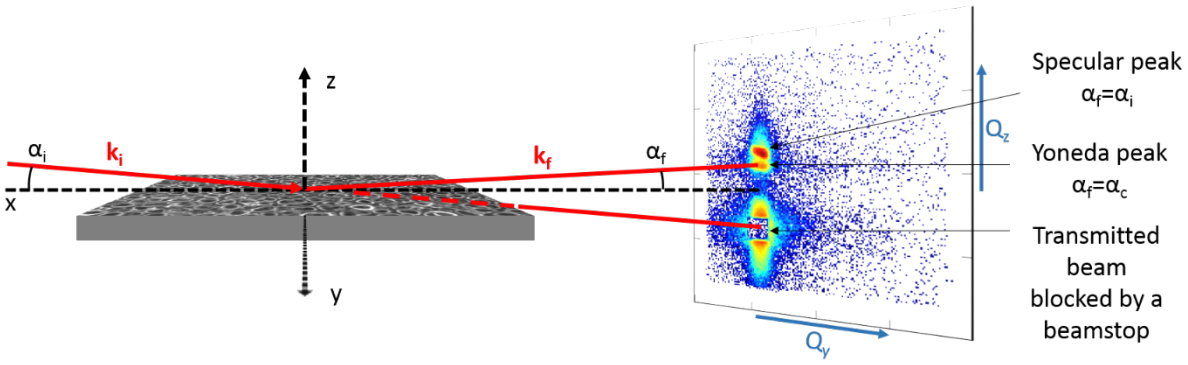

Figure 26 GISANS geometry.

Grazing incidence small angle neutron scattering (GISANS) is a technique very similar to GISAXS used for studying surface and in-depth morphology of thin films, and therefore in this chapter only the important differences between using GISAXS and GISANS will be emphasized. GISANS, as the name says, uses a neutron beam in contrast to GISAXS, which uses X-rays.

Figure 26 displays a typical GISANS geometry which is in principle the same as the one used in GISAXS (chapter 3.5.4.2). The only difference is that a large portion of the neutron beam is transmitted through the sample. In order to protect the detector and reduce background, the transmitted beam is usually blocked by a beamstop. In contrast to synchrotron GISAXS, the reflected beam in GISANS does not need to be blocked since the reflected intensity is lower. This difference allows the analysis of very low Q_y values close to the specular peak and corresponding to large lateral structures on the sample.

Neutrons do not have an electrical charge and therefore interact with matter via nuclear forces. Nuclear forces are very short range, in the order of few fermis (1 fermi = 10^{-15} m) and the sizes of nuclei are typically 100,000 times smaller than the distances between them. Neutrons can therefore travel long distances in a material that are in the order of 0.1-0.01 m, without being scattered or absorbed. The attenuation of low energy neutrons by Al for example is ~1% per mm compared to >99% per mm for X-rays. The strength of the neutron-nucleus interaction is measured by the scattering length of the nucleus b, which determines the scattering cross section $\sigma = 4\pi b^2$ that is the apparent cross section of the nucleus as seen by the neutron. Nuclei are point like scattering objects. Therefore, in contrast to X-rays, neutron scattering lengths do not show an angular dependence.

The product of the scattering length b and the atomic number density N of the material gives the scattering length density (SLD) for neutrons, whereas for X-rays it is the product of the electron radius r_e and the electronic density ρ_e of the material. In contrast to X-ray scattering lengths, which increase with the number of electrons of the investigated atoms, neutron scattering lengths vary randomly from element to element and from isotope to isotope. This enables tuning of the SLD and refractive index [79] for contrast enhancement and contrast matching [80], through isotopic substitution (the neutron scattering lengths of hydrogen and deuterium, for example, differ both in sign and magnitude).

The time-of-flight (TOF) mode is a general method for determining the kinetic energy of a traveling neutron, by measuring the time it takes to travel over a well-known distance. To filter a particular velocity, the technique uses a system of rotating disc choppers. TOF is particularly useful in the case of the neutron spectroscopy, where the energy of the scattered neutrons has to be determined. According to de Broglie's relationship: $\lambda = h/mv$, where h is the Planck constant, m is the neutron mass and v its velocity, the wavelength of the beam corresponding to a particular neutron speed can be calculated. Considering a beam of neutrons produced at

the same time and traveling in the same direction, the higher their kinetic energy the shorter their wavelength (and conversely for lower kinetic energy). At large neutron wavelengths, gravitational effects become visible that may need to be considered. Such an effect that can be used for correction, is a shift of the specular reflection peak towards lower angles.

By using a polychromatic incident neutron beam (λ = 0.1-1.0 nm) and time-of-flight (TOF) wavelength resolution, TOF-GISANS gives simple access to a large Q range [81], [82], [83]. Instead of probing different incident angles, the TOF mode provides direct information about the full Q range from a single incident angle. To achieve the Q_y resolution necessary for GISANS experiments, a point-shaped neutron beam source must be used instead of the slab-shaped beam source used in conventional diffuse scattering or reflectivity experiments. Therefore, usually multiple point beams are impinging on the sample and point focused on the 2D position sensitive detector placed at a distance of around 10 m. Such a setup allows to resolve lateral structures with dimensions of up to several micrometer.

The position of the material specific Yoneda peak, corresponding to maximum scattering is observed at an angle in the incident plane between the sample plane and the scattered beam α_f equal to the critical angle of total external reflection α_c. Therefore, its position depends on the radiation wavelength as

Equation 21

$$\alpha_c = \lambda \sqrt{\frac{SLD}{\pi}}$$

In TOF-GISANS, various neutron wavelengths are used, and thus the position of the Yoneda peak is also changing. Equation 21 shows that with increasing wavelength, the critical angle α_c increases, which means that the Yoneda peak will be moving towards the specular peak. This effect corresponds to reducing the incident angle at constant wavelength where the specular peak moves toward the Yoneda peak and the surface sensitivity is increased (scattering depth is decreased). By plotting the Yoneda peak positions α_c versus wavelength λ, for different wavelengths, and performing a linear fit, the SLD of the film averaged over different depths can be graphically determined from the inclination of the line fit.

The scattering patterns obtained with GISANS for the different wavelengths are analyzed the same way as in GISAXS (see chapter 3.5.4.2) by performing a vertical cut along Q_z at $Q_y = 0$ to examine the film thickness, and horizontal cuts at the Q_z height of the Yoneda peak, where scattering is the strongest, along Q_y to examine the lateral morphology of the film.

3.5.5.2 Triton analysis

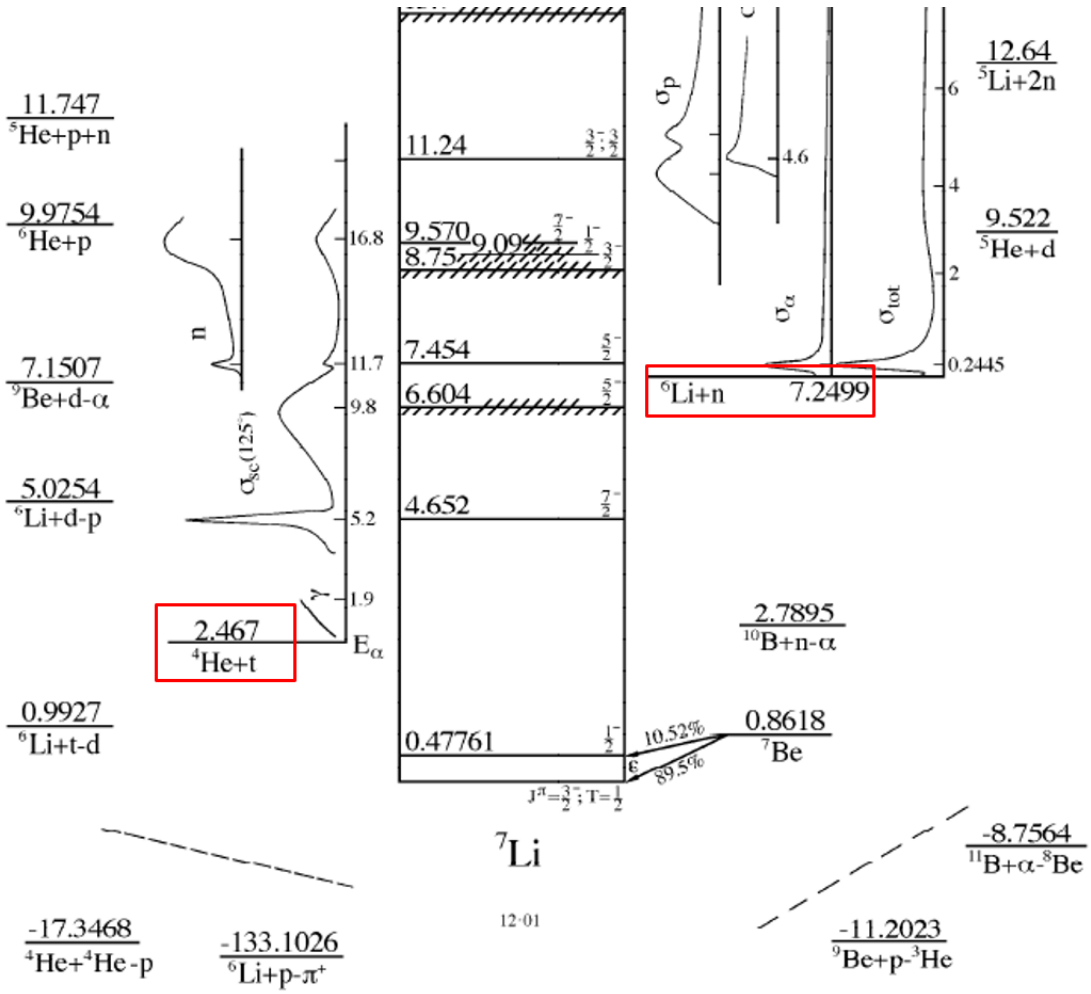

Figure 27 Energy levels of ^{7}Li in MeV. From [84].

Triton analysis exploits the neutron capture reaction of ^{6}Li producing a triton and an α -particle (written in short form as $^{6}Li(n,\alpha)^{3}H$) to determine the two dimensional Li distribution in a sample. Triton (t) is the name of the ^{3}H (tritium) nucleus as a free particle. ^{6}Li has a large neutron capture cross section σ_{th} = 940±4 barn [85] for thermal neutrons and an isotopic abundance in natural

Li of 7.42% [86]. In the neutron capture reaction, the compound nucleus $^{7}Li^{*}$ immediately decays into an alpha particle (α, the nucleus of ^{4}He) and a triton (t), which in the laboratory system are emitted in opposite directions due to momentum conservation (see Figure 28). The Q value of the reaction of 4782 keV, being the amount of energy released by that reaction, can be calculated by subtracting the energy levels of ^{7}Li marked in red in Figure 27 (^{6}Li+n with 7249.9 keV and ^{4}He+t with 2467 keV). Corresponding to the reaction Q value, the α and the triton particles obtain a fixed and relatively high kinetic energy of $E_{\alpha} = 2055$ keV and $E_{triton} = 2727$ keV, respectively [84].

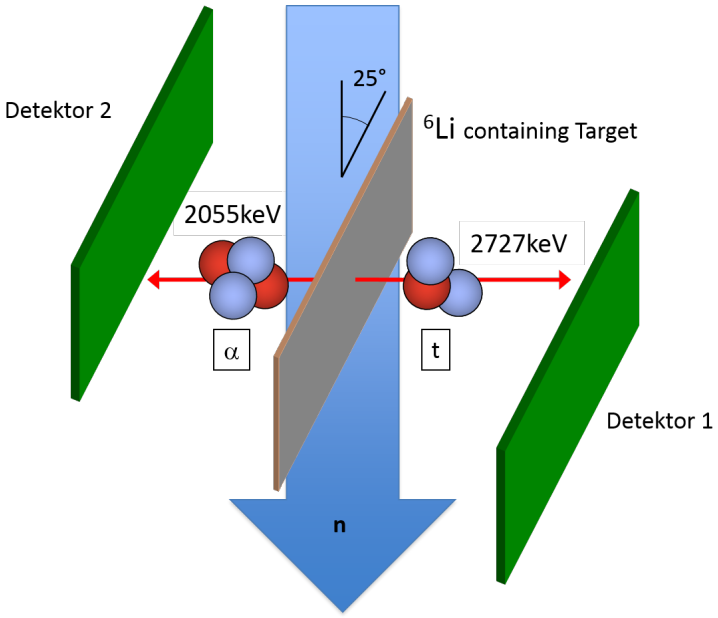

Figure 28 Principle geometry of the triton analysis setup.

The basic concept of the detection method is schematically shown in Figure 28. Two parallel position sensitive detectors are arranged on both sides of the target which is irradiated by thermal (~0.025 eV corresponding to λ ~2 Å) or preferably cold neutrons (0-0.025 eV) due to the larger (3.6 times) cross section $\sigma_c = 3474$ barn of cold neutrons compared to thermal neutrons for the neutron capture reaction. For a thin enough sample of typically less than 1 mg cm^{-2}, the alpha particles and tritons emitted in the same event under 180°, can be detected in coincidence on each side of the sample, one of the particles passing through the sample. Their impact positions on the detectors define nearly a straight line (particle tracks) with a typical broadening of 10 mrad as a result of multiple scattering in the target material. With the target centered and parallel to both detectors, the intersection point of that line with the target plane corresponds to the position of the decay event. Detectors and target are tilted by 25° with respect to the axis of the neutron beam.

This allows a reduction in the sample-detector distance, thus maximizing the solid angle coverage, without irradiating the detectors and the target frame with the collimated neutron beam.

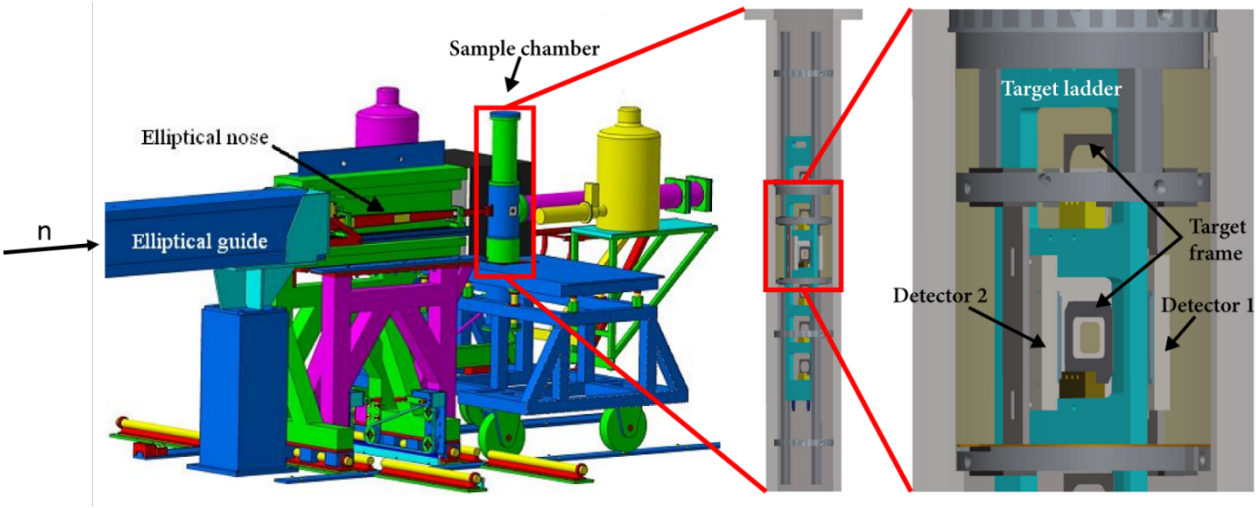

Figure 29 Experimental setup for triton analysis. From [87]

The measurements performed in this work were carried out using the setup, shown in Figure 29, that was developed for the PGAA (prompt gamma-ray activation analysis) facility [87] at the research neutron source Heinz Maier-Leibnitz (FRM II) technical university of Munich. The setup is modified [88] to enable the triton and alpha particle detection by installing two 20x20 mm^2 windowless silicon position sensing UV photon detectors (PSD) on a ceramic substrate (see Figure 30) [89]. Their very thin dead layer of only 100 nm makes these detectors particularly well suited for this application [89]. Two resistive layers on top and bottom of the detector split each signal to two opposite contact stripes (bond pads) which provide a rather linear x and y position information. When a particle hits the detector, it generates photoelectric current, which flows through the device and can be seen as two input currents, X_1 and X_2, and two output currents, Y_1 and Y_2 (http://www.sitek.se).

The impinging particle position on the x and y axis is then determined using the equations

$$x = \frac{L_x}{2} \cdot \frac{X_1 - X_2}{X_1 + X_2}; \qquad y = \frac{L_y}{2} \cdot \frac{Y_1 - Y_2}{Y_1 + Y_2}$$

wherein L_x and L_y are the lengths of the PSD in x and y direction, respectively. This method of determining the impact position is not affected by the intensity of the irradiation, thus providing an improved linearity compared to other kinds of two-dimensional PSD.

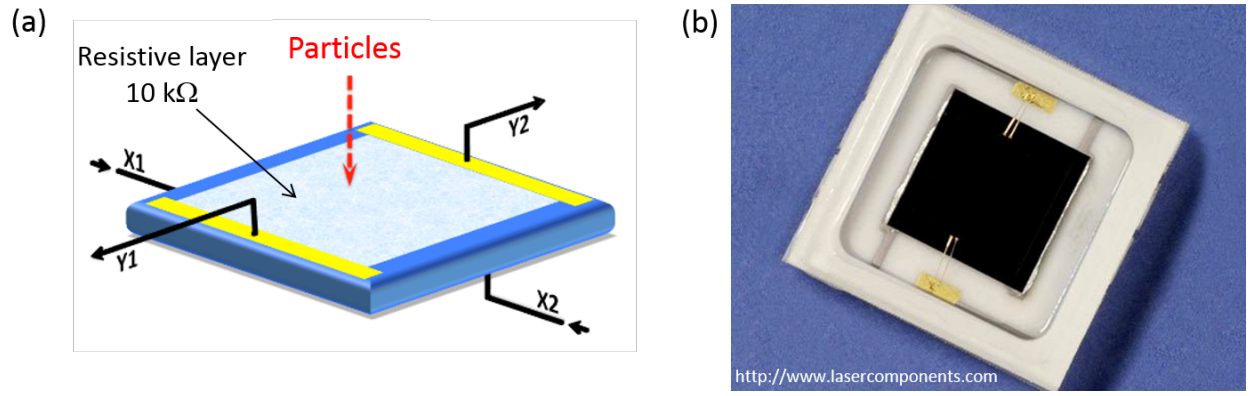

Figure 30 Schematical representation of the PSD detector (a) and a real image (b) reprinted from www.lasercomponents.com

The PSDs were installed inside the sample chamber of the PGAA setup on an aluminum stage. The stage is equipped with rails for a polytetrafluoroethylene (PTFE) target ladder with six measurement positions (see Figure 29), which can be selected remotely. A sample holder can be mounted on each position with a target detector distance of d = 20 mm corresponding to an average solid angle efficiency of 5%. To remove neutron halo around the beam core, an additional 8.5x16 mm^2 aperture, fabricated from a ^{6}LiF-loaded polymer matrix material (produced at Petersburg Nuclear Physics Institute (PNPI), Gatchina, Russia) covered with PTFE, is installed 30 mm in front of the target, between the target and the beam line collimation system.

Under ambient conditions or in a poorly evacuated sample chamber, a strong proton background is caused by the ^{14}N(n,p)^{14}C reaction during neutron irradiation. This reaction is prevented by flushing the sample chamber with helium (P = 50 mbar).

For properly adjusting the position of the sample and the detectors, the spot where the neutron flux is maximal is first determined using X-ray sensitive film material (Gafchromic RTQA-1010, X-ray sensitive film, Gafchromic), which is also sensitive to neutrons (see Figure 31).

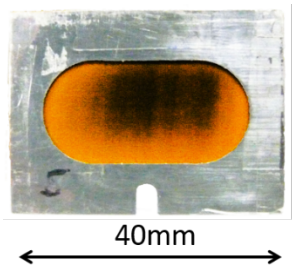

Figure 31 Beam profile visible as a dark spot on the orange neutron sensitive film mounted on an aluminum target holder obtained with a neutron beam incident angle of 25°, before adjustment.

The setup is operated with a cold neutron flux of up to Φ_{max} = 1.64x10^{10} cm^{-2} s^{-1} [87] with a mean kinetic energy of E_n = 1.83 meV and a beam profile of WxH = 17x19 mm^2. With various attenuators, the neutron flux can be reduced down to 1.3% of the initial neutron flux.

4 Materials and methods

4.1 TiO_2 nanotube (TiO_2 NT) preparation

Materials

Titanium (Ti) discs (99.6 %, Advent);

Grinding paper (4000P SiC, Buehler) for mechanical polishing;

1 µm-thick sputter deposited titanium film on phosphorus-doped silicon wafer;

Ethylene glycol (99.5 %, Merck);

Deionized water (18.2 MΩ cm, Milli-Q, Millipore);

NH_4F (99.99 %, Merck).

Anodization:

TiO_2 nanotubes (TiO_2 NT) were electrochemically grown on titanium metal by exposing the titanium surface to an electrolyte in a two electrode anodization cell (described in chapter 4.5.1 above) and by applying an anodic potential for a certain amount of time, after ramping up the potential to the desired value with a certain ramp rate. After anodizing, the sample was thoroughly rinsed with deionized water to prevent further etching of the surface. The following five types of titania nanotube samples were produced for the different experiments.

4.1.1 Type 1 TiO_2 NT samples

Substrate: mechanically polished titanium disk (see Figure 32)

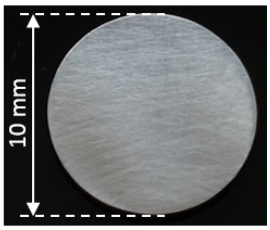

Figure 32 Photograph of mechanically polished Ti disk substrate with a thickness of ~1 mm, used in different diameters for the growth of Type 1-4 TiO_2 NT samples.

Exposed surface: 50.3(±6.7) mm^2;

Electrolyte: 50 vol% ethylene glycol in deionized water + 2 wt% NH_4F;

Ramp rate: 1 V/s;

Anodization potential: 20 V;

Anodization time: 1h.

4.1.2 Type 2 TiO_2 NT samples

Substrate: mechanically polished titanium disk (see Figure 32);

Exposed surface: 37.1(±0.6) mm^2;

Electrolyte: 50 vol% ethylene glycol in deionized water + 1 wt% NH_4F;

Ramp rate: 1 V/s;

Anodization potential: 20 V;

Anodization time: 1h.

4.1.3 Type 3 TiO_2 NT samples

Substrate: mechanically polished titanium disk;

Exposed surface: 254 mm^2;

Electrolyte: 50 vol% ethylene glycol in deionized water + 1 wt% NH_4F;

Ramp rate: 1 V/s;

Anodization potential: 20 V;

Anodization time: 1h.

4.1.4 Type 4 TiO_2 NT samples

Substrate: mechanically polished titanium disk;

Exposed surface: 254 mm^2;

Electrolyte: 50 vol% ethylene glycol in deionized water + 1.5 wt% NH_4F;

Ramp rate: 1 V/s;

Anodization potential: 20 V;

Anodization time: 1h.

4.1.5 Type 5 TiO_2 NT samples

Substrate: 1 µm thick sputter deposited titanium film on phosphorus-doped silicon wafer (see Figure 33);

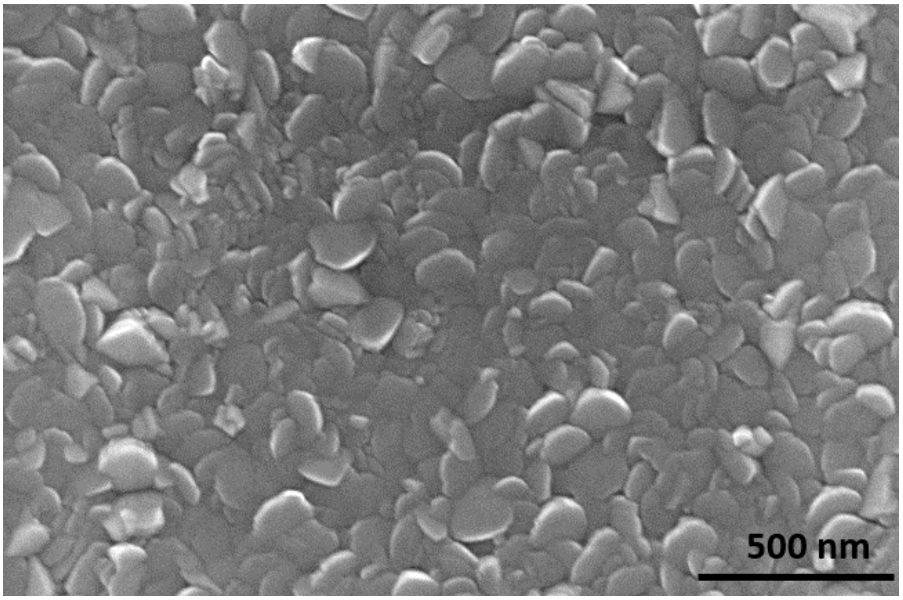

Figure 33 Top view SEM micrograph of 1µm thick Ti layer sputter deposited on a silicon wafer.

Exposed surface: 254 mm^2;

Electrolyte: 50 vol% ethylene glycol in deionized water + 1.5 wt% NH_4F;

Ramp rate: 1 V/s;

Anodization potential: 20 V;

Anodization time: 15min.

4.2 Annealing

Annealing was performed in a horizontal tube furnace under argon or argon-acetylene atmosphere. Annealing under argon atmosphere changes the crystalline structure of the as grown amorphous titania nanotubes. The addition of acetylene modifies the material chemically and can also result in a deposition of a surface layer of carbon. The used gasses were Ar 4.8 (Linde) and acetylene (C_2H_2) solvent-free (Linde). The horizontal tube furnace, schematically depicted in Figure 34, was equipped with mass-flow controllers for the inlet gasses, a low-vapor-pressure oil bubbler for preventing backflow of gas and a vacuum pump for a quicker exchange of the atmosphere in the furnace. The desired temperature profiles of the furnace were controlled by a computer, and the flowrates of gasses were set manually in the controlling unit of the mass-flow controllers.

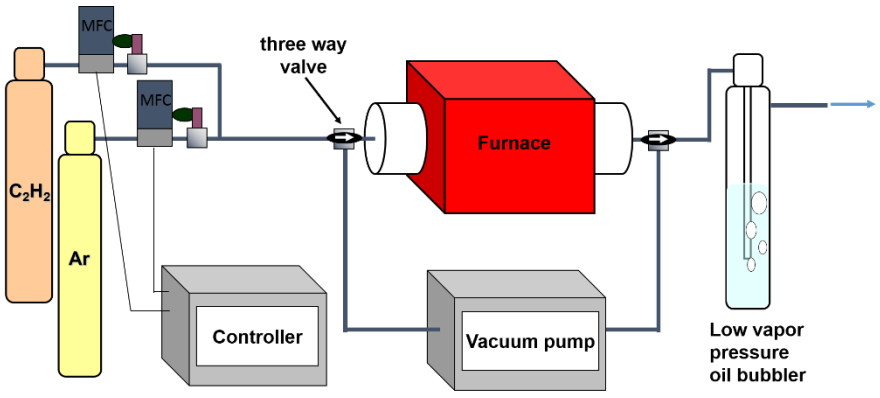

Figure 34 Schematically illustrated annealing setup.

4.2.1 Annealing under argon-acetylene atmosphere

In order to remove air from the 1307 cm^3 quartz reactor tube, its volume was first exchanged three times by evacuating it down to 10^{-2} mbar and refilling with Ar, and then the reactor tube was purged with 750 sccm argon for 2 h at room temperature (RT) (72 times volume exchange).

The argon flow was then reduced to 200 sccm and kept constant until the end of the annealing procedure. Prior to increasing the temperature, 5 sccm acetylene were added to the argon flow for 3 min. To avoid thermal stress during the temperature increase to 400 °C, the ramping speed was gradually reduced from 10 °C min^{-1} until 200 °C, to 5 °C min^{-1} until 300 °C, and finally 3 °C min^{-1} until 400 °C. After 20 min dwell time at 400 °C, 0.1 sccm acetylene were added to the argon flow for 1 h. The system was then kept for another 280 min at 400 °C to allow for the complete transformation of the samples and then cooled down to RT with 3 °C min^{-1}. The annealing procedure is schematically depicted in Figure 35.

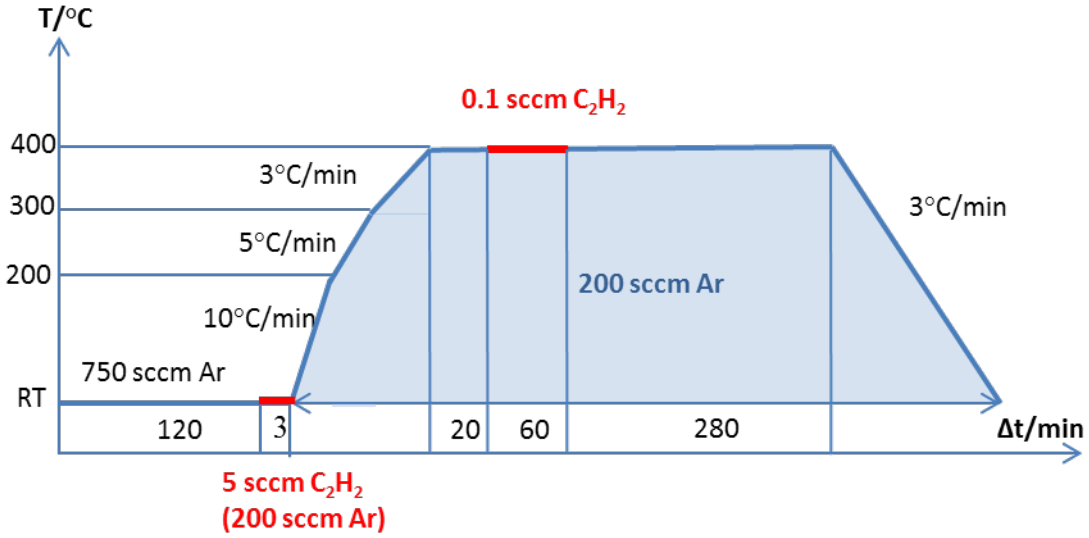

Figure 35 Annealing profile with indicated gas flow rates in sccm and rates of change in temperature in °C/min. Shown in red are the time intervals where acetylene (C_2H_2) is added to the Ar flow.

4.2.2 Annealing under argon atmosphere

In order to change the crystal structure of the as grown amorphous TiO_2 NT and use them as a reference for the carbo-thermally annealed nanotubes (see chapter 4.2.1), the same annealing procedure was used without the addition of acetylene.

4.3 Si deposition on nanotubular electrodes

Composite lithium storage electrodes were prepared based on Ti disc electrodes with titania nanotube array active material by depositing amorphous Si on the nanotubular array. The deposition of amorphous Si was carried out in an argon (Ar) diluted monosilane (SiH_4) atmosphere at 1 Torr total pressure, with 465 sccm Ar and 35 sccm SiH_4 at 250 °C for one minute with 10W RF excitation using plasma enhanced chemical vapor deposition (PECVD) performed on an Oxford Plasmalab 80+ device. Figure 36 shows images of nanotubular electrodes on Ti disc substrates with and without a Si coating.

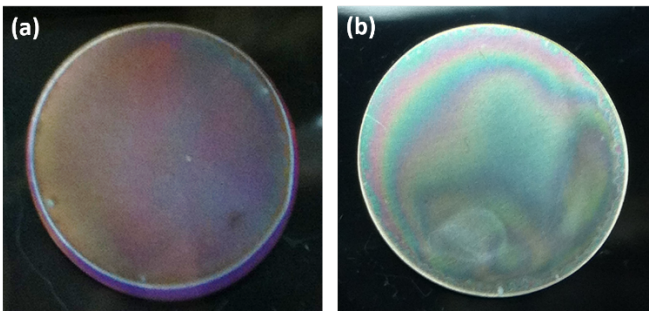

Figure 36 Photograph of samples functionalized with a layer of titania nanotubes (a) without Si coating and (b) with a Si coating. The nanotubes are grown, on Ti disc substrates with a 2 cm diameter, according to the procedure of chapter 4.1.3 and carbo-thermally annealed according to the procedure of chapter 4.2.1.

4.4 Mass determination of nanotubular electrode material

Determining the mass of active material of lithium storage electrodes is essential for calculating their gravimetric storage capacity and for estimating which lithiated phases are present in the material at different states of charge. These can show the utilization efficiency of the active material in the electrode and allows the comparison with studies reported in literature.

The majority of material studies for lithium storage electrodes are focused on electrodes having a high loading of active material (in the order of milligrams per square centimeter) in powder form applied on a current collector foil, thus determining the mass of active material with a good precision is generally not an issue. However, determining the mass of the nanotubular array active material, grown electrochemically on a Ti disc, of the present work proved to be challenging. The nanotubular array is not added to the current collector as in classical electrodes, which would allow weighing the active material beforehand, but instead is grown on the surface of the Ti base consuming some of the Ti in the process (while another part is dissolved in the electrolyte during anodization). Attempts were made to directly measure the

mass of nanotubes by first weighing the whole electrode, comprising titanium disc substrate and nanotubes grown on its surface, then mechanically or chemically stripping the nanotubes off the substrate, weighing the substrate again and subtracting the obtained mass from the mass of the pristine electrode. Such direct measurement with a good precision proved to be very difficult due to the large difference in mass (~ four orders of magnitude) between the titanium disc substrate and the nanotubular array grown on its surface. Additionally, the high specific surface area of the nanotubes translates in large amounts of adsorbed water, compared to the mass of the nanotubes, that is difficult to remove without heating up the sample, which would lead to reoxidation of the reduced titania nanotubes and growth of thermal oxide on the interface between titanium metal and titania nanotubes. The error of these direct measurements was comparable with the mass of the nanotubes.

Therefore, instead of directly measuring the mass of the nanotubes, SEM imaging was used to estimate their volume similarly as in [90], [91], the bulk nanotube density was assumed to be the density of anatase (3.9 g cm^{-3}) and their mass was calculated. Top view SEM micrographs of intact nanotube layers were used to count the number of nanotubes per unit electrode area and to measure the inner, outer diameters and wall thicknesses of the top sections of the nanotubes. Cross-sectional micrographs of nanotube layers scratched off the surface of the substrate were used to measure the length of the nanotubes and their diameters at different heights along their length. Some of the nanotubes observed in the cross-sectional view were broken horizontally or vertically (having the shape of a half-pipe) which allowed for the measurement of their wall thickness at different heights. The shape of the nanotubes is schematically represented in Figure 37 (left part) and is slightly conical with an open top and closed spherical bottom wherein wall thickness, inner and outer diameter in the top section of a nanotube were smaller than those in the bottom section.

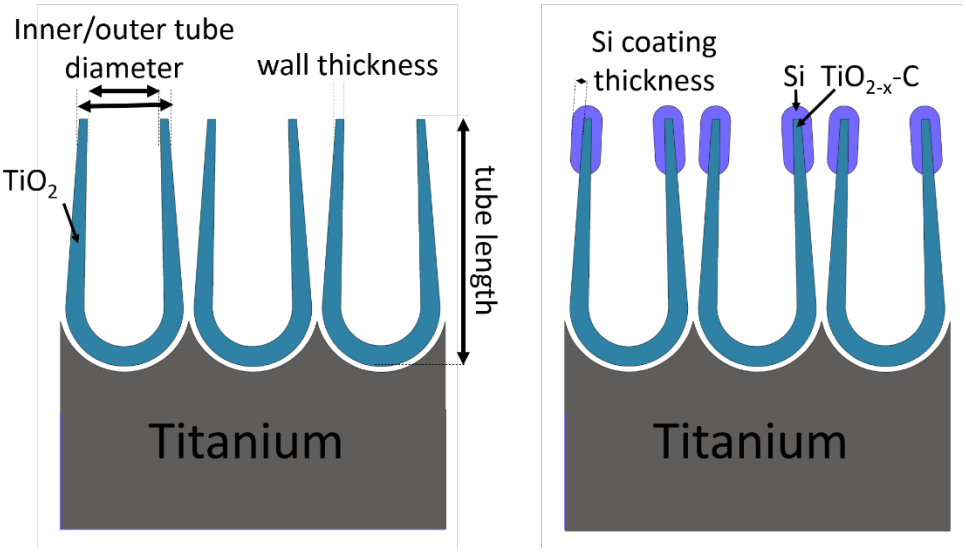

Figure 37 Cross-sectional view of titania nanotubes (left) and silicon coated acetylene annealed titania nanotubes (right) on titanium substrate.

This data was then used to calculate mean values with standard deviations and construct a model of the nanotube layer. Measurement errors were all negligible, in the order of ±2 nm for a one dimensional profile measurement in SEM, compared to the standard deviations of the measured morphology parameters (number of nanotubes per unit area, nanotube length, wall thickness, inner and outer diameters). The modeled nanotube layer comprised nanotubes (perfect hollow cylinders) with open top and a flat closed bottom. Their continuous wall thickness, inner and outer diameters corresponded to the calculated mean values, their length was equal to the calculated mean length and the number of nanotubes per unit electrode area was the mean value calculated from top view micrographs (these mean values are referred to as parameter values x, y, z,…). Additionally, an electrode diameter (diameter of the area of the Ti disc covered with the nanotubular array) uncertainty of 0.5 mm was also taken into account. The uncertainty (σ_f) of the calculated mass values (the mass being a function f of parameter x, y, z…) was estimated by applying the variance formula for error propagation with independent parameters (Equation 21) on the mean parameter values (x, y, z…) with their corresponding standard deviations (σ_x, σ_y, σ_z…).

Equation 22

$$\sigma_f = \sqrt{\left(\frac{\partial f}{\partial x}\right)^2 \sigma_x^2 + \left(\frac{\partial f}{\partial y}\right)^2 \sigma_y^2 + \left(\frac{\partial f}{\partial z}\right)^2 \sigma_z^2 + \cdots}$$

The mass of the additional active material (Si) of the composite lithium storage electrodes prepared in this work was calculated in a similar way. The composite electrodes schematically depicted in Figure 37 (right part) comprise a thin amorphous Si coating on the top potion of the inner and outer walls of the nanotubes. The mass of the Si coating was estimated by assuming for its density a density of 2.33 g cm^{-3} and multiplying it with its volume calculated by comparing SEM micrographs of the electrode before and after silicon deposition. The deposition depth of silicon was measured in cross-sectional view micrographs and the deposited layer thickness was calculated from the increase in the mean wall thickness of the nanotubes in their top portion where the silicon coating was observed. The silicon coating on each nanotube was modeled by two concentric hollow cylinders on both sides of the nanotube, both having the same length corresponding to the measured mean deposition depth, and the same layer thickness corresponding to half the measured increase in the nanotube wall thickness after the silicon deposition.

4.5 Electrochemical cell design

4.5.1 Anodisation cell for producing titania nanotube electrodes

The anodization cell (see Figure 38) was a vertical cylinder made of Polytetrafluorethylene (PTFE) with a vertical cylindrical opening forming the electrolyte filled inner volume of the cell. A copper plate disposed on the bottom of the cell was supporting and electrically contacting the working electrode (WE: Ti disk to be anodized) and a platinum mesh disposed in parallel to the surface of the sample was used as a counter electrode (CE). A fluorinated rubber O-ring (Viton) was used for sealing between the sample and the cell body. A computer-controlled power supply was used for applying the desired potential profile for anodization. A drawback of the cell design was occasional trapping of bubbles in the corners between O-ring and working electrode that were manually removed with a pipette. To prevent the concentration of water in the electrolyte from changing over prolonged anodization periods, the opening on the top of the cell was sealed with parafilm.

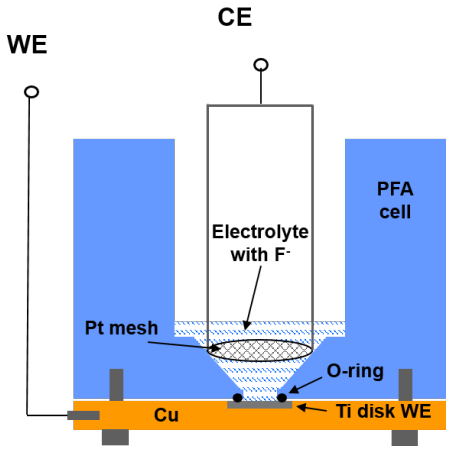

Figure 38 Anodisation cell.

4.5.2 Li-ion cells for EC characterization and ex-situ emersion analytics

Lithium foil (99.9%, Alfa Aesar) was used as counter (CE) and pseudo reference (RE) electrode. The electrolyte (SelectiLite battery electrolyte LP 30, Merk) used in all measurements was 1M $LiPF_6$ in a 1:1 (w/w) mixture of ethylene carbonate (EC) and dimethyl carbonate (DMC) with or without a 2 wt.% vinylene carbonate (VC) additive [12,13]. All cells were assembled in an Ar filled glove box (MBraun) with a water and oxygen content below 0.1ppm. The assembled cells were connected to a potentiostat (BioLogic VSP) outside (1^{st} and 2^{nd} generation) or inside (separator free cell) the glove box and the measurements were performed at room temperature.

4.5.2.1 1^{st} generation thee electrode Li-ion cells for EC characterization

The first generation three electrode T-cell had a body (Union Tee Tube Fitting PFA-820-3, Swagelok) and sealing rings of perfluoralkoxy-polymer (PFA) and stainless steel rods (316 stainless steel) for contacting the working (WE), counter (CE) and reference (RE) electrodes (see Figure 39).

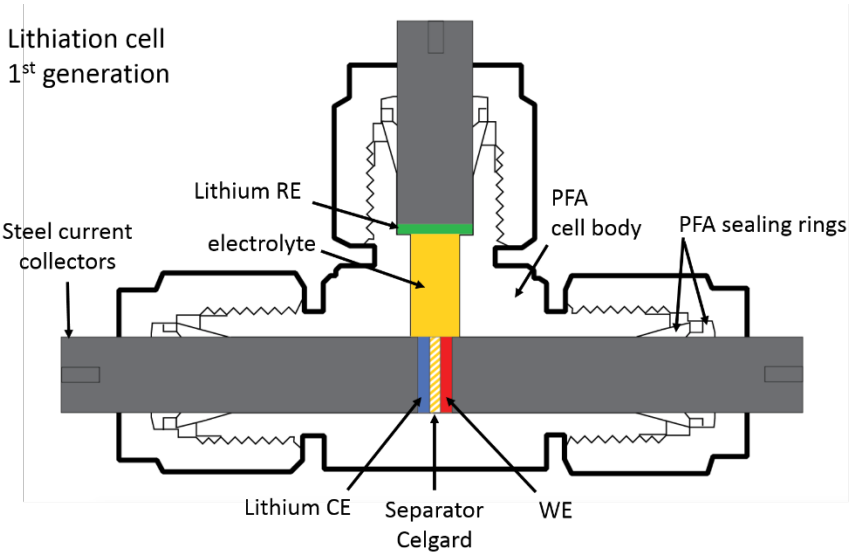

Figure 39 Principle cell design of 1st generation thee electrode Li-ion cells for EC characterization.

Working and counter electrodes were pressed against each other and separated by a separator (Celgard) soaked with electrolyte. The reference electrode was dipped in the cell filled with electrolyte in a 1 mm distance from the WE. The assembled cells were connected to a potentiostat (VSP, BioLogic) outside the glove box and all experiments were performed at room temperature.

The cell was easy to assemble without a risk of short circuiting the cell since its body was not conductive.

A drawback of this design proved to be side reactions on the steel current collectors exposed to the electrolyte visible as a yellowish colored layer. Therefore, additional measurements with dummy WE without an active material were performed and used for correcting the data of the real samples. The measurements with dummy WE did not show any noticeable features in CV but a low capacity contribution in GCPL.

4.5.2.2 2nd generation three electrode Li-ion cells for EC characterization

The second generation three electrode T-cell schematically depicted in Figure 40, had the same principle design as the one shown on Figure 39 with a stainless steel body (Union Tee Tube Fitting, Swagelok). PFA sealing rings (Swagelok) and stainless-steel rods (1.4404 stainless steel, StahlRING GmbH) were used for contacting the working (WE), counter (CE) and reference (RE) electrodes. The steel rod for contacting the working electrode was composed of two parts connected by a spring for applying a constant (over time and between experiments) predefined pressure of 189 kPa (corresponding to the fully contracted spring). Two glass fiber (GF) separators (VWR Glass microfibers filter, 691) soaked with electrolyte were used to separate WE and CE. The steel rod current collectors for WE and CE were separated from the cell body by a cylinder made of high-density polypropylene (HDPP) provided with an opening at a position between the two separators. The reference electrode was a thin stripe of lithium foil interposed between the two separators in their peripheral portion and plugged through the opening in the HDPP cylinder to be contacted by the reference electrode steel rod. The assembled cells were connected to a potentiostat (VSP, BioLogic) outside the glove box and all experiments were performed at room temperature.

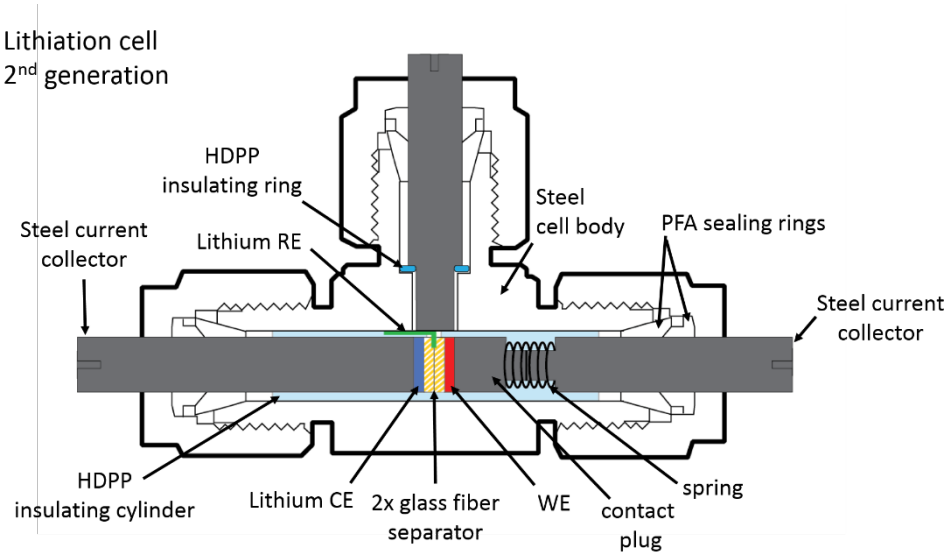

Figure 40 Principle cell design of 2nd generation thee electrode Li-ion cells for EC characterization.

The smaller distance between the reference electrode and the working electrode in the second-generation cell compared to the first, improves the potential control of the working electrode. Through the addition of a spring in the current collector of the WE, the applied pressure could be controlled and kept constant throughout the experiments. Furthermore, since only the two separators were wetted with electrolyte with the RE interposed between them and surrounded by the WE, CE and the HDPP cylinder, side reactions on the stainless-steel current collectors were minimized.

However, cell assembly with the second-generation cell was considerably more complicated and time consuming.

4.5.2.3 Separator-free three electrode cell for ex-situ emersion analytics

With both the first- and second-generation cell designs it proved to be impossible to clean the surface of a sample from residues of the separator after electrochemical measurements for further analysis.

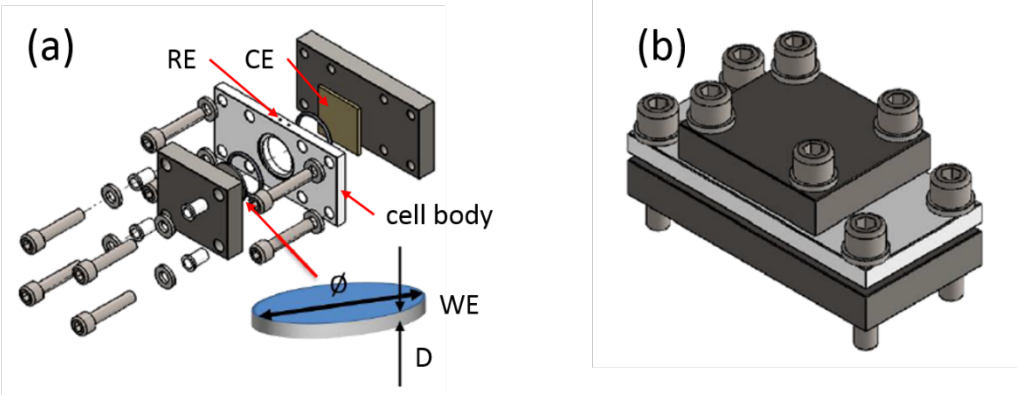

Figure 41 Separator-free cell (a) exploded view and (b) assembled. [92]

Therefore, a separator free-cell was designed (Figure 41) wherein the distance between the parallel WE and CE was kept constant by the cell body made of PTFE. A thin stripe of lithium foil RE was plugged through one of two holes on the top edge of the cell body in the electrolyte filled space (large circular opening of the cell body) between the WE and the CE. The hole for the RE was drilled inclined towards the WE to ensure a minimal distance between WE and RE for a better potential control. A second hole on the top edge of the cell body was provided for filling the cell with electrolyte which was sealed with a plug made of the same material as the cell body (PTFE). The sealing between the WE, CE and the cell body was achieved through

fluorinated rubber O-rings. However, the side opening of the cell accommodating the RE was only partially sealed through pressing a piece of lithium foil on it by a spring-loaded contact pin. Therefore, the cell was operated inside the glove box. The cell was designed for Ti disk (carrying the active electrode material) WE with a diameter of Ø = 20±0.01 mm and a thickness D of 0.95±0.02 mm. The WE and CE had the same surface area exposed to the electrolyte. Two stainless steel plates, which were not in contact with the electrolyte, were used for pressing the WE and CE to both sides of the cell body. The design shown on Figure 41 allowed for opening of the WE side of the cell independently and for easy recollection of the sensitive lithiated electrode with a minimal amount of mechanical stress. Drawbacks of this cell design were a large cell resistance, due to the much higher distance between WE and CE (4 mm), poor sealing (compared to 1st and 2nd generation cells), and occasional trapping of bubbles in the corners between O-ring and WE. Therefore, the cell was only used for fully lithiating samples for further analysis.

Figure 42 shows images of a pristine and a lithiated titania nanotube electrode, wherein the separator free cell was used for lithiation. The lithiated electrode has a clean surface, well suited for further analysis. Titania exhibits a strong electrochromic effect, changing color to dark blue/black upon lithiation.

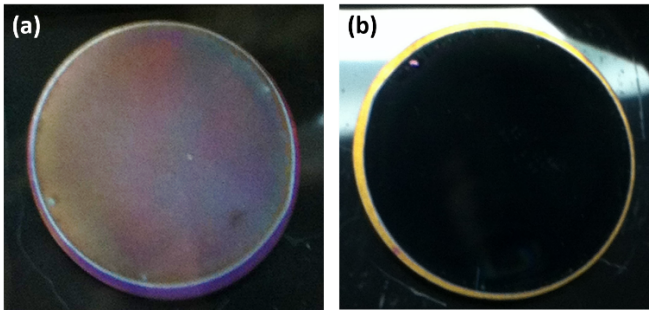

Figure 42 Titania nanotubes on Ti disc substrate with a 2 cm diameter grown according to the procedure explained in chapter 4.1.3 and carbo-thermally annealed according to the procedure explained in chapter 4.2.1 (a) pristine sample and (b) electrode lithiated at 1.1 V in the separator free cell, rinsed with dimethyl carbonate (DMC) and dried.

4.6 Target box for triton analysis

An airtight target box (Figure 43) was developed for transferring lithiated electrodes from the glove box to the triton analysis setup (see chapter 5.3, [92]). The box made of Al had a ring shaped back-plate (Figure 43c,d,f) and a machined front-plate (Figure 43a,b,e) fixed together by screws. To avoid background emissions from steel or hydrogen containing polymers, the screws were made of PTFE. The front-plate had a 2 mm central opening covered with Al coated mylar foil functioning as a pinhole aperture. An O-ring, pressing on the circumferential edge of the Ti disk target sample, was used for airtight sealing of the space between the target sample and the front plate. Wherein the target sample was positioned such that the active material was facing the front plate. The rear surface of the target sample was pressed against the O-ring by the back-plate.

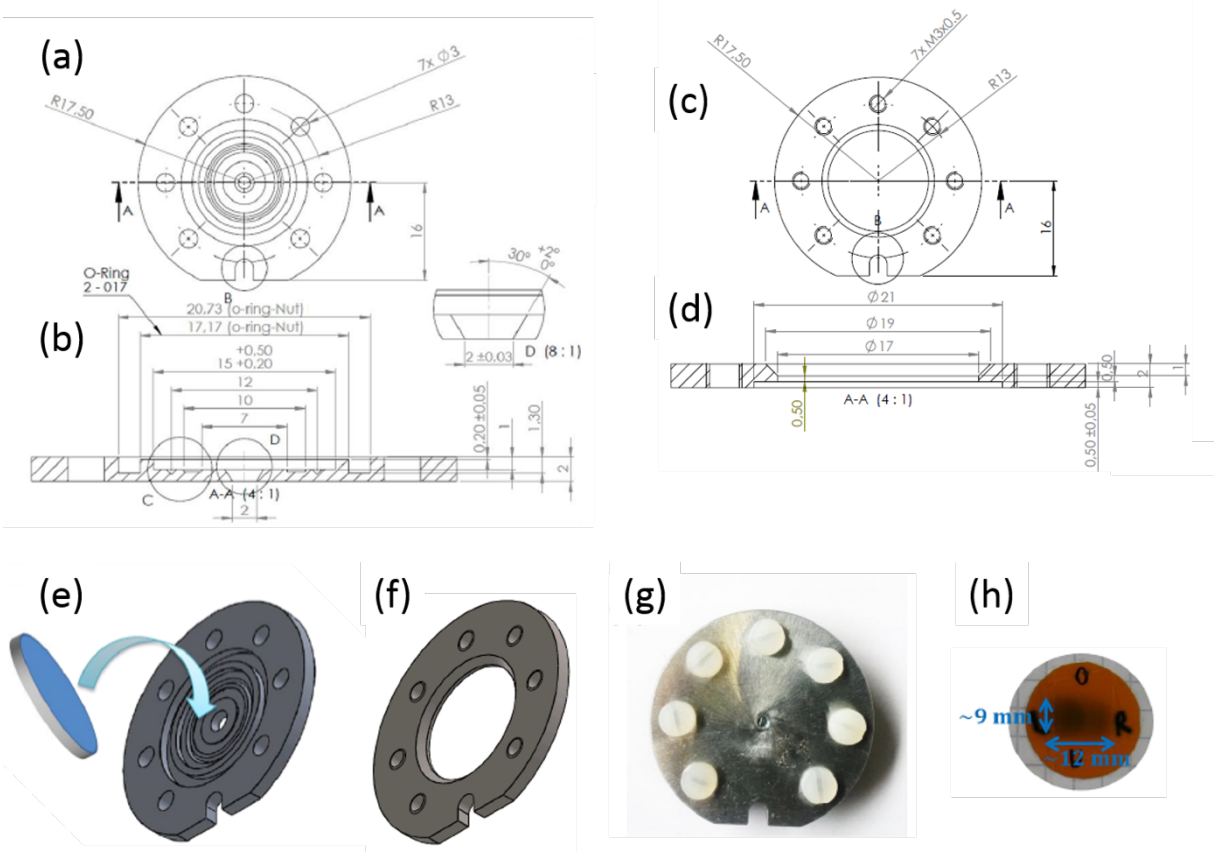

Figure 43 Airtight target box for triton analysis [92]. *(a) Technical drawing top view of the Al front plate with a pinhole aperture of 2 mm in the center covered with an Al coated mylar foil; (b) A-A cut of (a); (c) Technical drawing top view of the Al back plate; (d) A-A cut of (c); (e) Isometric view of the inner side of the front plate and illustration of the positioning of the target sample therein; (f) Isometric view of the outer side of the back plate; (g) Real image of the fully assembled target box with PTFE screws; (h) Cold neutron beam spot at the target position for an average neutron energy of 1.8 meV (6.7 Å), a neutron flux of 2.7x10^{8}-1.7x10^{10} neutrons cm^{-2} s^{-1} and a beam size of 9 mm x 12 mm.*

4.7 Analytical instrumentation

For the sake of clarity, the parameters for electrochemical and physical characterization of the samples are given separately for each chapter in section *5 Performed studies*.

The following instruments were used in the experiments:

- SEM imaging was performed on CrossBeam NVision 40 from Zeiss;
- Energy Dispersive X-ray spectroscopy (EDX) was performed on a JSM-7500F from JEOL for creating a 2D chemical composition map of the studied electrodes;
- X-ray Photoelectron Spectroscopy (XPS) was carried out for determining the chemical composition of the surface layer of the studied electrodes and the oxidation states of their components using Specs Phoibos 100 hemispherical electron energy analyzer and a MCD-5 detector. The X-ray source was Al Kα (1486.6 eV) used without a monochromator. The takeoff angle of photoelectrons was 0° relative to the surface normal. The acquired XPS data were evaluated using CasaXPS software version 2.3.14dev38;
- Grazing Incidence X-ray Diffraction (GDI) analysis was performed on a Bruker D8 Advance Diffractometer, comprising a Soller Slit on the detector, for obtaining structural and compositional information about the studied electrodes;
- X-ray diffraction (XRD) was performed on a Siemens D5000 difractometer. Diffractograms were acquired between 15 and 75 degree (2 theta) with a step size of 0.02 degrees (2 theta) and an acquisition time of 1s per step.
- GISAXS was performed on a Ganesha 300XL small/wide-angle X-ray scattering system (SAXSLAB ApS, Copenhagen, Denemark).
- TOF-GISANS analysis was performed at the REFSANS instrument of the Heinz Maier-Leibnitz Zentrum in Garching, Germany.
- Triton analysis was performed on a modified setup of the PGAA (Prompt Gamma Activation Analysis) station of the Heinz Maier-Leibnitz Zentrum in Garching, Germany.
- ATR-FTIR was performed on a Nicolet iS5.

5 Performed studies

5.1 Anatase TiO_{2-x} NT vs. anatase TiO_{2-x}-C NT

This work has been published under the title “Oxygen deficient, carbon coated self-organized TiO_2 nanotubes as anode material for Li-ion intercalation” [93] and reports on the lithiation and delithiation characteristics of anodically grown, self-organized TiO_2 nanotubes annealed in Ar (TiO_{2-x} NT) and Ar/C_2H_2 (TiO_{2-x}–C NT). Anatase TiO_{2-x}–C NT demonstrate a superior Li storage capacity as high as 320(±68) mA h g^{-1} ($Li_{0.96}TiO_2$) compared to 180(±38) mA h g^{-1} ($Li_{0.54}TiO_2$) for anatase TiO_{2-x} NT.

Experimental

This chapter compares the (de)lithiation properties of Type 1 (see chapter 4.1.1) titania nanotube electrodes annealed in Ar (TiO_{2-x} NT) and Ar/C_2H_2 (TiO_{2-x}–C NT) atmosphere, following the annealing procedures described in the corresponding chapters 4.2.2 and 4.2.1 above. All electrochemical measurements were performed in a 1st generation T-cell (described in chapter 4.5.2.1 above) filled with a commercial electrolyte (SelectiLite LP 30, Merk) composed of a 1M $LiPF_6$ solution in a 1:1 (w/w) mixture of EC and DMC. All herein provided potentials are defined with respect to the Li/Li^+ reference electrode potential unless otherwise stated. Cyclic voltammetry (CV) measurements were performed in the potential window from 1.1 to 3 V with a scan rate of 0.1 mV s^{-1}. Current densities of 50, 100, 200, 500 and 1000 mA g^{-1} were used in galvanostatic cycling with potential limitation (GCPL) measurements corresponding to 0.3, 0.6, 1.2, 3, and 6 C rates wherein the rate of 1 C is defined for the theoretical lithium storage capacity of anatase of 168 mA h g^{-1} ($Li_{0.5}TiO_2$) [94,95]. Electrochemical impedance was measured prior to CV and GCPL at open circuit potential (OCP) in a frequency range from 100 kHz to 0.5 Hz with an amplitude of ±0.5 mV and the real value of the high frequency impedance corresponding to the electrolyte resistance (typically in the range of 1-4 Ω) was checked as an indicator for the proper assembly of the cell (no short circuit or gas bubbles). High resolution X-ray photoelectron spectra for Ti 2p, C 1s and O 1s regions were recorded with a 0.025 eV step size and a dwell time of 0.5 s. Grazing incidence X-ray diffraction (GID) was carried out between 20 and 60 degree 2θ with a 0.02 degree step size and acquisition time per step of 60 s.

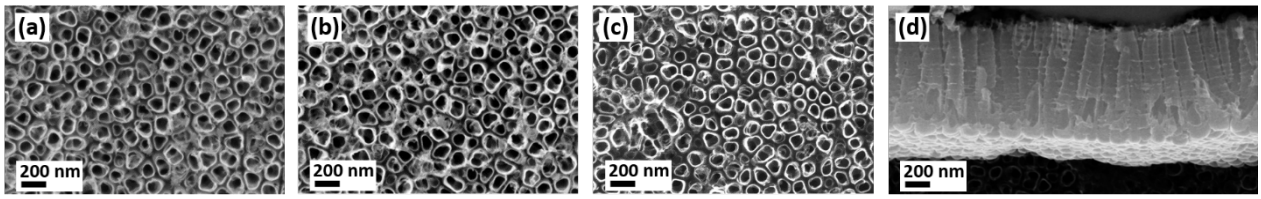

Figure 44 SEM micrographs of: (a) as grown amorphous TiO_2 NT; (b) anatase TiO_{2-x} NT; (c) anatase TiO_{2-x}–C NT; and (d) cross-sectional view of anatase TiO_{2-x}-C NT.

Top view and cross-sectional view SEM micrographs of as grown amorphous (TiO_2 NT), argon annealed (TiO_{2-x} NT) and acetylene annealed (TiO_{2-x}-C NT) nanotubes are recorded (see Figure 44) and used to extract the morphological parameters of the nanotubes showing that annealing had no effect, visible with SEM with this resolution, on the nanotube morphology. The nanotubes have a 120 nm average inner diameter, 18 nm average wall thickness and 1 µm average length. Their cross-sectional shape is schematically displayed in Figure 37 (left part). With these values, the surface area of the nanotube layer is 30 $m^2\ g^{-1}$ and the mass of the nanotube layer is 138(±37) µg, calculated according to the method described in chapter 4.4, corresponding to an active material porosity of 40%. Figure 45 depicts the GID spectra of the TiO_{2-x} and TiO_{2-x}–C nanotubes. Both spectra show strong Ti peaks from the Ti metal substrates and TiO_2 anatase peaks confirming the crystallization of the as grown amorphous nanotubes in both annealing atmospheres. Analysis of the broadening of the full width at half maximum (FWHM) of the diffraction peak at $2\theta = 25.2°$, corresponding to the (101) plane of anatase, using the Scherrer equation, delivers a crystallite size of ~30 nm for both TiO_{2-x} NT and TiO_{2-x}-C NT (which is similar to crystallite sizes reported in the literature [35]). No TiC or Ti sub-oxide peaks are observed for the acetylene annealed nanotubes (TiO_{2-x}-C NT). Therefore, it is assumed that only a thin layer of carbon is deposited on the surface of the nanotubes upon acetylene annealing at the relatively low temperature of 400°C instead of forming a TiO/TiC solid solution or double phase typical for a high temperature (> 550°C) annealing in the presence of carbon [96].

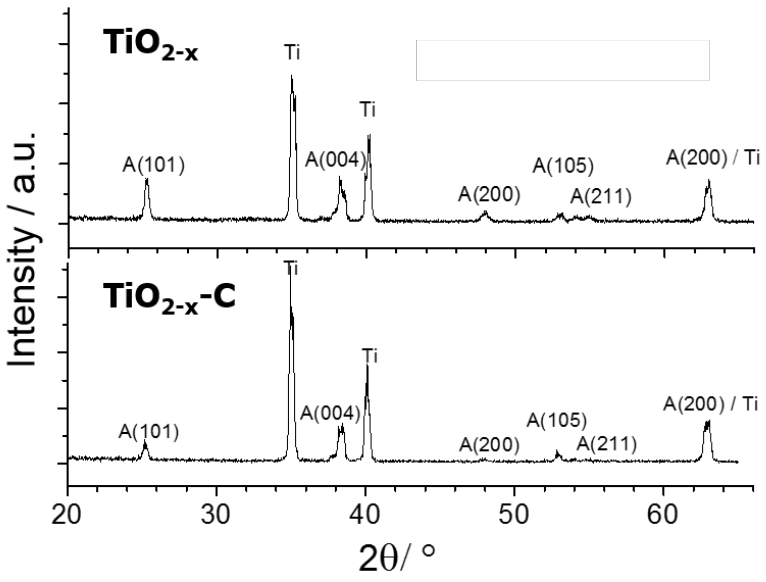

Figure 45 GID spectra of TiO_{2-x} (top) and TiO_{2-x}-C (bottom) nanotubes. Reproduced from [93].

X-ray Photo-electron Spectroscopy (XPS) is an analytical tool probing only a few nanometers (usually less than 10 nm) of the surface of compact solids (due to the low escape depth of the photo-electrons). The probing depth is higher for porous materials like titania nanotubes, however, the measurement remains surface sensitive. As confirmed by SEM, the morphology and porosity of TiO_{2-x}-C NT and TiO_{2-x} NT are the same, thus the probing depth of XPS is also expected to be the same for the two materials. Therefore XPS is considered most appropriate for testing the assumption made above that acetylene annealing results in a thin carbon coating on the surface of the nanotubes. Figure 46 depicts the X-ray photoelectron Ti 2p and C 1s spectra of TiO_{2-x} NT and TiO_{2-x}-C NT. Building the TiO_2 to C ratios for both materials (93:7 at% in TiO_{2-x} NT and in 82:12 at% in TiO_{2-x}-C NT) and comparing them, the XPS data reveals a higher amount of carbon on the surface of TiO_{2-x}-C NT compared to TiO_{2-x} NT, thus confirming the presence of a carbon layer.

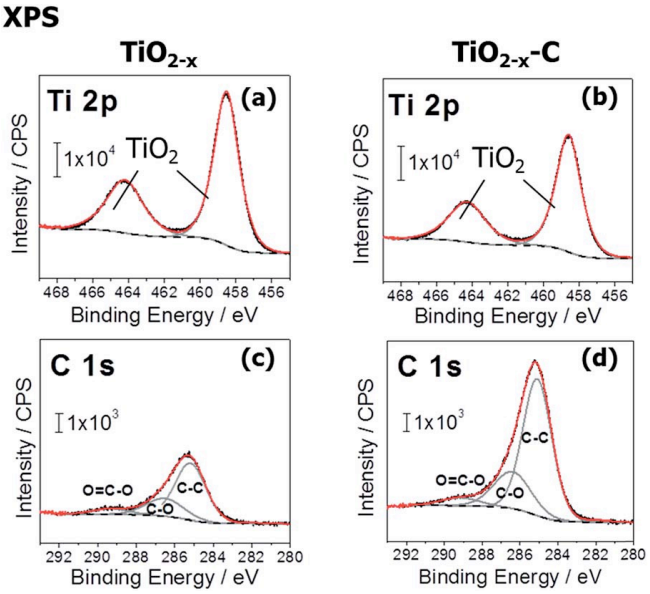

Figure 46 Ti 2p and C 1s spectra of TiO_{2-x} (a) and (c), and TiO_{2-x}-C (b) and (d). From [93]

The following electrochemical analysis was carried out after the initial physical characterization. Figure 47 displays the first cycle CV (a) and the 3rd (b) and 110th (c) cycle GCPL curves of TiO_{2-x} and TiO_{2-x}-C NT. Both CV curves comprise peak pairs at 1.70/2.07 V (TiO_{2-x}) and 1.72/2.00 V (TiO_{2-x}-C) corresponding to the two phase region (α/β lithium titanate) lithiation and delithiation reactions in anatase discussed in chapter 1.4. The earlier lithiation onset and smaller peak separation for TiO_{2-x}-C indicates lower reaction overpotentials and higher reversibility. Additionally, a second peak pair is observed for both materials (see inset in Figure 47a) at 1.48 and ~1.78 V (shoulder) indicating the second two-phase region (β/γ lithium titanate) of lithiation and delithiation. The current peaks for TiO_{2-x}-C NT are higher indicating a higher lithium storage capacity for the material. Furthermore, the second lithiation peak at 1.48 V is better pronounced for TiO_{2-x}-C which points to a better defined second double phase region.

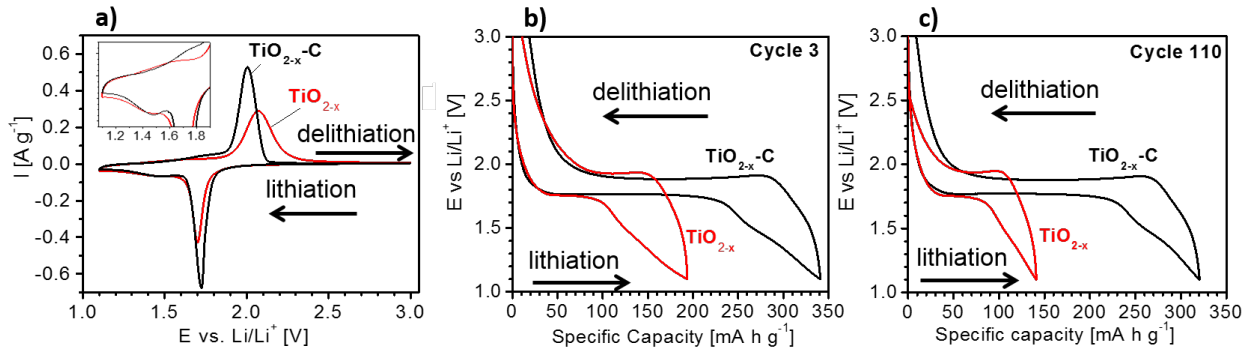

Figure 47 CV (a) and GCPL (cycle 3 (b); cycle 110 (c)) of TiO_{2-x} (red) and TiO_{2-x}-C (black) NT. Reproduced from [93]

The same behavior is observed in the constant current experiment (GCPL) in graphs b) and c) of Figure 47 where constant potential plateaus are observed at the lithiation delithiation potentials corresponding to the peak pairs observed in the CVs. The curves follow the shape typical for anatase TiO_2 as described in chapter 1.4. TiO_{2-x}-C NT show a remarkable reversible capacity of 320(±68) mA h g^{-1} in the third cycle compared to 180(±38) mA h g^{-1} for TiO_{2-x} NT corresponding to 0.96 and 0.54 mole Li^+ per mole TiO_2, respectively. The irreversible capacity loss in the initial cycles is attributed to the irreversible reaction of Li^+ with water adsorbed on the surface of the electrodes [97-99] and trapping of Li^+ in defect sites of the nanotubes [100]. In the third cycle, TiO_{2-x}-C NT loses 21(±4.5) mA h g^{-1} and TiO_{2-x} NT loses 13(±2.8) mA h g^{-1}. Graph c) of Figure 47 depicts the 110th GCPL cycle. Apart from the decrease in capacity, the curves are unchanged showing the excellent stability of the materials. The reversible capacities in the 110th cycle are 313(±66) mA h g^{-1} for TiO_{2-x}-C NT and 141(±30) mA h g^{-1} for TiO_{2-x} NT corresponding to a capacity retention from the 3rd to the 110th cycle of 98% and 78%, respectively. Here the acetylene treatment brings a great improvement in lithium storage capacity and cycling stability.

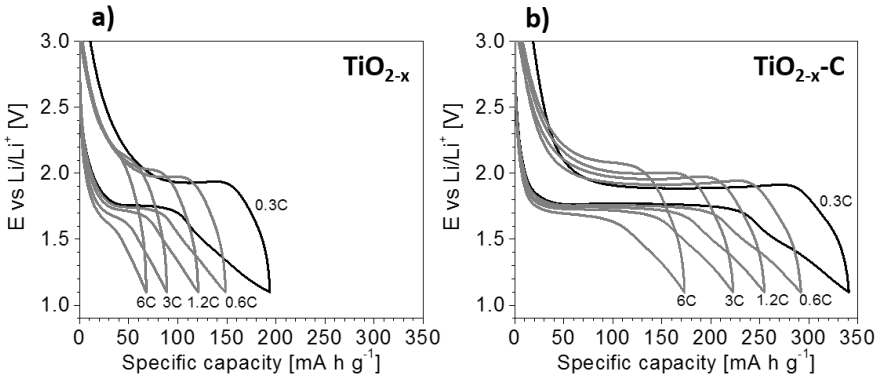

Figure 48 GCPL of TiO_{2-x} (a) and TiO_{2-x}-C (b) at cycling rates of 0.3C, 0.6C, 1.2C, 3C and 6C. Reproduced from [93]

Table 1 Capacities extracted from Figure 48.

Capacity [mA h g^{-1}]	0.3C	0.6C	1.2C	3C	6C
TiO_{2-x} NT	180(±38)	146(±31)	118(±25)	84(±18)	64(±14)
TiO_{2-x}–C NT	320(±68)	285(±61)	249(±53)	214(±46)	162(±35)

Figure 48 displays a comparison of the rate capability test performed on TiO_{2-x} NT and TiO_{2-x}–C NT. The corresponding capacities are presented in Table 1 Capacities extracted from Figure 48. The acetylene annealed nanotubes show a remarkable performance with a 162(±35) mA h g^{-1} capacity at a rate of 6C compared to 64(±14) mA h g^{-1} for the argon annealed nanotubes corresponding to 50% and 36% of their capacity at 0.3C, respectively. With increasing cycling rate (current), the potential plateaus in the respective GCPL curves become shorter and the lithiation and delithiation plateaus shift apart. The relative increase of the portions where the potential is changing leads to a higher capacitive contribution to the total current and to the total charge, respectively.

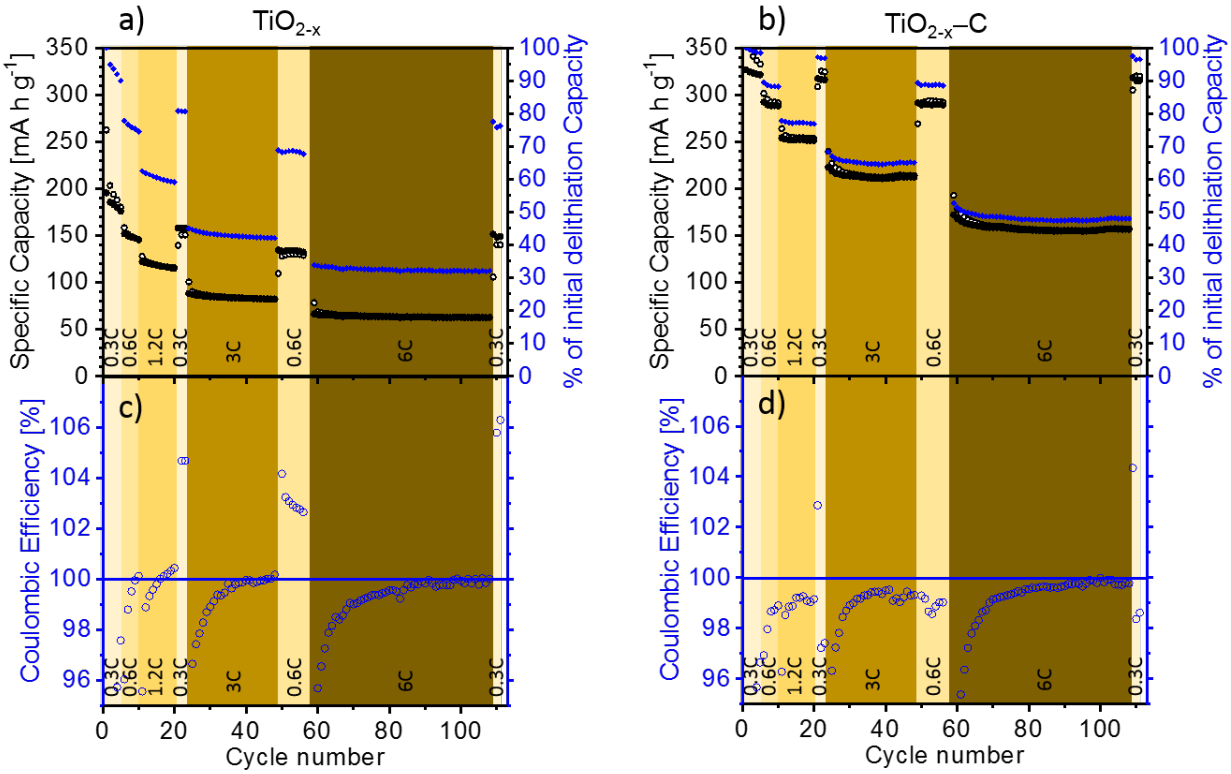

Figure 49 Gravimetric capacities (black circles) and corresponding percentage of initial delithiation capacity (blue diamonds) of TiO_{2-x} (a1) and TiO_{2-x}-C (b1) nanotubes at different cycling rates (0.3C, 0.6C, 1.2C, 3C, 6C). Open circles: lithiation, closed circles: delithiation. Coulombic Efficiency for TiO_{2-x} (a2) and TiO_{2-x}-C (b2) at the different cycling rates.

Figure 49 displays the results of a GCPL sequence performed at different C rates over a total of 111 cycles, where argon annealed (a, c) and acetylene annealed (b, d) nanotube electrodes are compared. 0.3C rate cycling is performed in the beginning and at the end of the GCPL sequence wherein the TiO_{2-x} NT and TiO_{2-x}–C NT electrodes show 76% and 97% capacity retention (between the 2nd and 110th cycle), respectively. Both electrodes show a stable cycling performance at 6C with 63(±13) mA h g^{-1} and 156(±33) mA h g^{-1} for TiO_{2-x} NT and TiO_{2-x}–C NT, respectively. The coulombic efficiency of the lithiation/delithiation cycles is calculated for the TiO_{2-x} NT (c) and TiO_{2-x}–C NT (d) electrodes as the ratio of delithiation capacity to lithiation capacity. Each time the cycling rate is increased, the efficiency drops (by 4 to 5%) and then approaches 100% upon constant rate cycling. When the cycling rate is decreased, efficiency goes beyond 100% (by approximately 4%) and then approaches 100% upon constant rate cycling. Coulombic efficiency below 100% is usually explained with irreversible reactions upon lithiation (charge trapping), however, there is no obvious explanation for coulombic efficiencies above 100%. The measured capacities are the sum of capacities delivered by charging of the EDL, the pseudo capacitive contribution of surface species, bulk lithiation and electrolyte

decomposition. One possible explanation for the coulombic efficiency being higher than 100% in the initial cycles after switching from high to low cycling rate is that charge that was trapped during high current cycling becomes accessible again once the current is lowered and the individual reactions are given more time. For example, if a thick surface layer, accumulated during the high current cycling and trapping a high amount of charge, is gradually removed and replaced by a thinner layer, possibly with a different composition, during low current cycling, this could explain the observed coulombic efficiencies.

Figure *50* shows an SEM micrograph of a TiO_{2-x}–C NT electrode, taken in a delithiated state after the electrochemical measurements (and after gently rinsing the sample with DMC to remove electrolyte residues). No changes in morphology or solid state deposits are observed which is in a good agreement with the high cycling stability of the electrode observed in GCPL measurements.

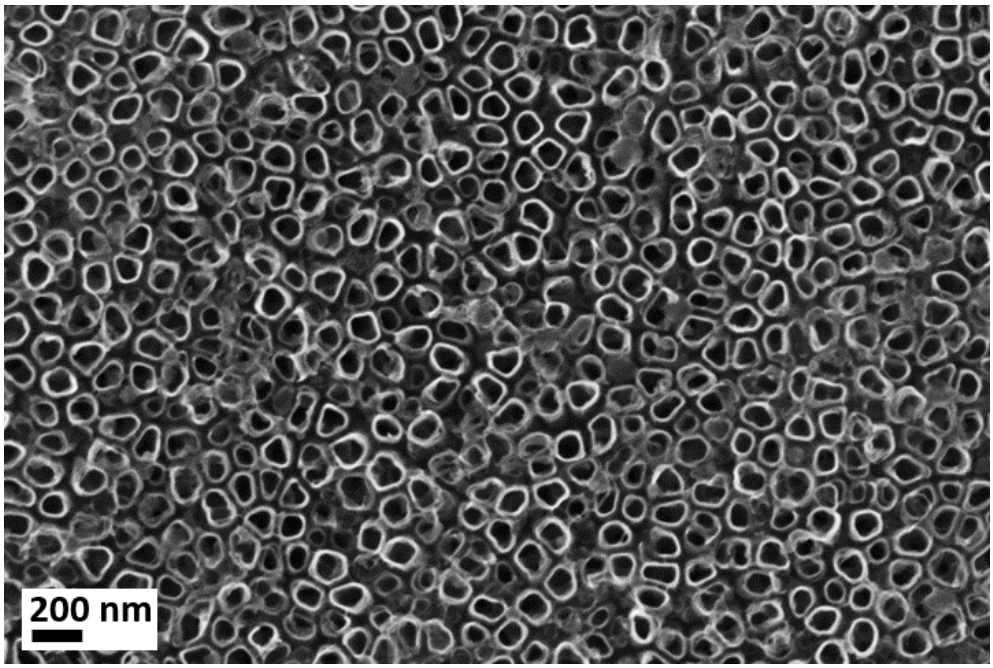

Figure 50 *SEM micrograph of TiO_{2-x}–C NT in delithiated state after 100 GCPL cycles.*

Conclusions

Both nanostructured materials have a good accessibility of the active material through its well-organized porous morphology and the low thickness (18nm) of the nanotube walls. The reduced diffusion path length for Li^+ ions enables the formation of lithium titanates with high lithium content and allows for high lithiation/delithiation rates. The surface area of the nanotube electrode calculated from SEM micrographs is 30 $m^2 g^{-1}$ which is comparable to the surface area of a powder electrode with the same layer thickness (1 µm) and a mean particle diameter of 50 nm. The nanotube electrode however, contains only active material, in contrast to a powder electrode that needs at least a binder and a conductive additive. Therefore, the whole surface area of the nanotubes can be utilized offering a large amount of reaction sites thus enabling high rate lithiation and delithiation, and more room for surface storage of lithium. The acetylene annealed nanotubes (TiO_{2-x}–C NT) show superior lithium storage capacity and capacity retention over prolonged cycling and high cycling rates. This is attributed to an enhanced bulk conductivity due to oxygen vacancies, enhanced surface electronic conductivity through a carbon layer formed on the surface and stabilization of the reduced titania bulk through the addition of carbon all together resulting in an improved overall (for Li^+ and e^-) conductivity.

5.2 Silicon coated titania nanotubes composite electrodes

Silicon, as introduced in chapter 1.3, is currently the most attractive high lithium storage capacity anode material offering over 3500 mA h g^{-1} (3580 mA h g^{-1} for $Li_{15}Si_4$) [9]. This large capacity however is accompanied with a large volume expansion leading to a quick disintegration of bulky electrodes (see chapter 1.3.2.3). In contrast, thin layers of Si show a stable cycling performance [15,16].

In this study, a composite anode material was developed with an active material consisting of TiO_{2-x}–C nanotubes (TiO_{2-x}–C NT) coated with a thin layer (~10 nm) of silicon. The high surface to volume ratio of the nanotubes allows for the incorporation of a larger mass of silicon while keeping its layer thickness low and assures a large contact area of the silicon layer with both the electrolyte and the current collector (represented by the TiO_{2-x}-C NT). The composite electrode was expected to show the stable cycling performance of the TiO_{2-x}-C nanotubes described in chapter 5.1 above, when cycled between 3 V and 1.1 V vs. Li/Li^+, and additionally allow for higher storage capacities when cycled between 3 V and 0.04 V vs. Li/Li^+. In a full cell, the lower anode potential of 0.04 V vs. Li/Li^+ would have the additional effect of increasing the cell voltage and thus the amount of energy stored in the cell.

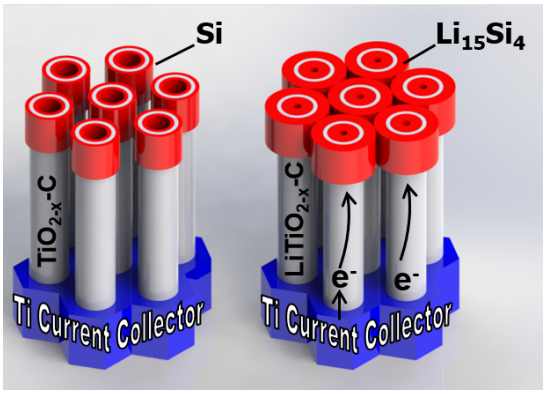

Figure 51 Schematical illustration of the composite electrode with an active material consisting of TiO_{2-x}–C NT coated with a thin layer of silicon in delithiated state (left) and in lithiated state (right). The nanotubes are supported on a Ti current collector and function as a lithium storage material and as current collector for the Si coating. From [101].

This work was published under the title “Silicon on conductive self-organized TiO_2 nanotubes – A high capacity anode material for Li-ion batteries” [101].

Experimental

To prepare the composite electrode, Type 2 (see chapter 4.1.2) titania nanotube electrodes were first annealed in Ar/C_2H_2 (TiO_{2-x}–C NT) atmosphere following the annealing procedure described in chapter 4.2.1. These were then coated with a thin layer of silicon using PECVD as described in chapter 4.3. The morphological parameters of the acetylene annealed Type 2 titania nanotubes were the same (in the range of standard deviation) as the Type 1 nanotubes described in chapter 5.1 (120 nm average inner diameter, 18 nm average wall thickness and 1 µm average length). The mass of the nanotube layer on a 37.1 ± 0.6 mm^2 electrode, calculated according to the procedure described in chapter 4.4, was 75 ± 11 µg and the mass of the silicon coating 9 ± 3 µg, which results in a total composite mass of 84 ± 14 µg. The large error in mass accumulated along its calculation, limits the possibility to compare the results of the lithium storage capacity measurements of the studied composite electrode with other materials in terms of their gravimetric capacity. Therefore, in the following, areal capacities (in mA h cm^{-2}) calculated with an error of < 2% are reported instead of gravimetric capacities (in mA h g^{-1}). Knowing the active material layer thickness of the electrodes (average nanotube length) of 1 µm, that allows for a good comparison with other materials. Electrochemical measurements were performed in the 2nd generation T-cell described in chapter 4.5.2.2 with the electrolytes described in chapter 4.5.2. All herein provided potentials are defined with respect to the Li/Li^+ reference electrode potential unless otherwise stated. CV measurements were performed in the potential window from 0.04 to 3.00 V with a scan rate of 0.05 mV s^{-1}. GCPL was performed between 0.04 and 3.00 V vs. Li/Li^+ at constant currents of 4.3, 8.6, 21.5, 43, 86, 430 µA corresponding to current densities of 11.6, 23.2, 58.0, 115.9, 231.8 and 1159.0 µA cm^{-2}. Defining a constant j_0 for current density and setting its value to 115.9 µA cm^{-2}, the used current densities read as follows $j_0/10$, $j_0/5$, $j_0/2$, $1j_0$, $2j_0$ and $10j_0$, respectively. The theoretical gravimetric charge storage capacities of the Si and TiO_2 components of the composite electrode are 3580 mA h g_{Si}^{-1} and 168 mA h g_{TiO2}^{-1}, respectively. The composite comprises 10.7 wt% Si which translates to a theoretical gravimetric charge storage capacity of the composite electrode of 534 mA h $g_{composite}^{-1}$. With a total mass of the composite material in an electrode area of 0.371 cm^2 of 84 µg, the theoretical rate of 1C for the composite is 120 µA cm^{-2}.

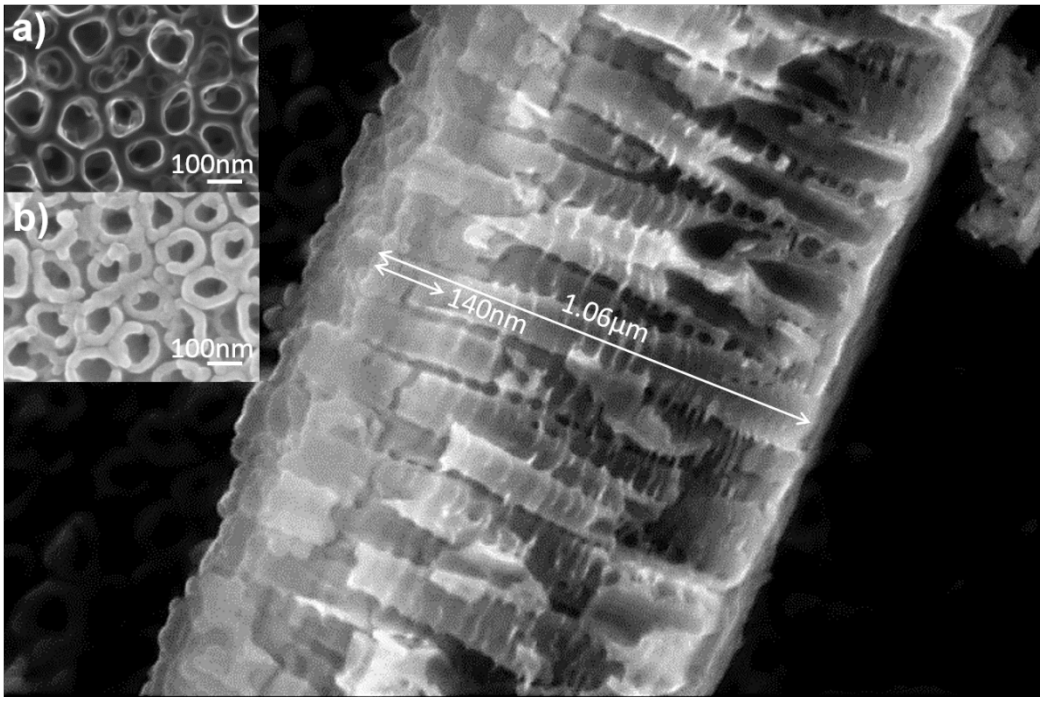

Figure 52 SEM cross-section of TiO_{2-x}–C NT coated with Si; inset a): top view of non-coated TiO_{2-x}–C NT; inset b): top view of Si-coated TiO_{2-x}–C NT. From [101].

Figure 52 shows a cross-sectional view micrograph of Si-coated TiO_{2-x}–C NT as well as top views of bare and Si-coated TiO_{2-x}–C NT. The top view micrographs of the nanotubes before and after Si deposition reveal a Si coating thickness, on both sides of the sidewalls of the nanotubes, of ~10 nm. The cross-sectional view reveals that the top 140 nm of the nanotubes have different scattering properties (shaded) and that their edges are rounded. Furthermore, upon scratching off the nanotube layer for the cross-section SEM, cracks are formed approximately at the boundary of this shaded top layer. Therefore, it is concluded that Si is deposited mostly on the upper 140 nm of the nanotubes, which is also expected for the chosen PECVD deposition parameters (see chapter 4.3). EDX performed in top view of the Si coated TiO_{2-x}–C NT under magnification (see Figure 53a) delivered a two dimensional Si map that confirms that the layer deposited on the nanotubes causing the thickening of the nanotube walls is Si. In a macroscopic view of the electrode, EDX confirms that the Si coating is homogenously distributed over the entire surface of the electrode.

Compositional analysis based on the EDX spectra of Figure 53 delivers a Si content in the Si coated TiO_{2-x}–C NT electrode of 7.6 wt% of the active material consisting of Si, O and Ti. However, the probing depth of EDX can be assumed to be larger than the nanotube layer thickness, especially due to the porous morphology of the probed layer, which leads to a contribution from the Ti current collector to the Ti signal leading to an underestimation of the Si content in the electrode. Furthermore, overlapping peaks in the spectra introduce further error in estimating the proportions of oxygen and titanium. Correcting the atomic percentage of titanium to half of the atomic percentage of oxygen and recalculating the weight fraction of silicon delivers 8.4 wt% which is in good agreement, within the error margin, with the value of 10.7 wt% calculated using the silicon volume fraction from the modeled nanotube layer as described in chapter 4.4.

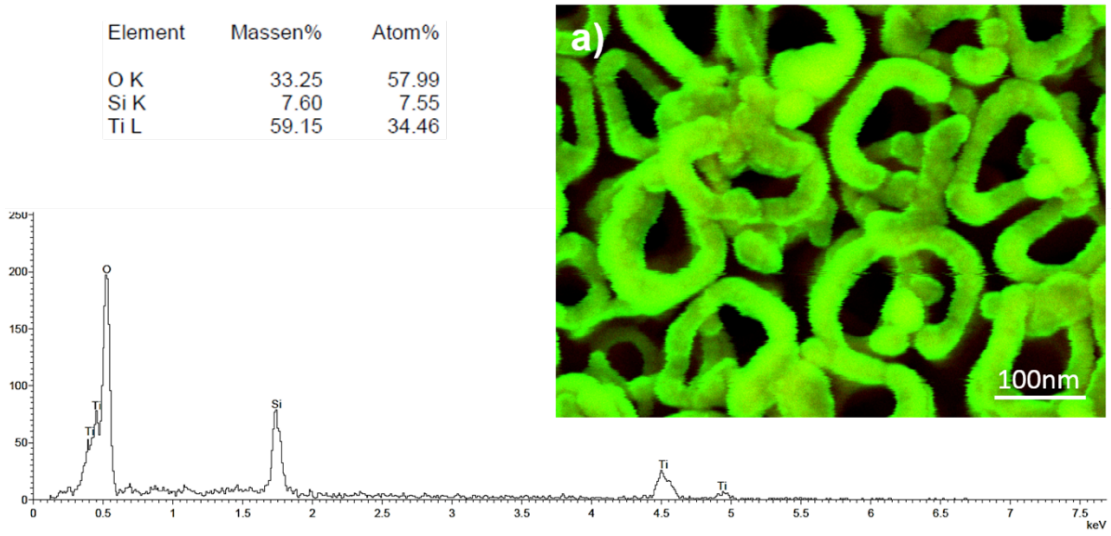

Figure 53 EDX spectra of Si coated TiO_{2-x}–C NT with peak assignment and uncorrected elemental composition. Inset a): two dimensional Si (green) map.

XPS applied on the Si coated TiO_{2-x}–C NT electrode (see Figure 54) delivers an atomic ratio of SiO_2 to Si of approximately 20:60, wherein Si and SiO_2 are identified by their characteristic Si 2p peaks at 98.8 eV and 102.8 eV, respectively [12]. The Si 2p peaks are fitted using suboxide peaks according to [102] and the energy separation between the Si^{n+} species is set according to the expected energy separation of approximately 1 eV per oxidation state [103]. The high-resolution spectra for Ti 2p and C 1s show that the TiO_{2-x}–C NTs mainly consist of TiO_2 and a thin carbon coating. The peaks in the Ti 2p region are fitted using additional peaks for suboxides according to [104], however, the signal to noise ratio is poor and the information is only qualitative.

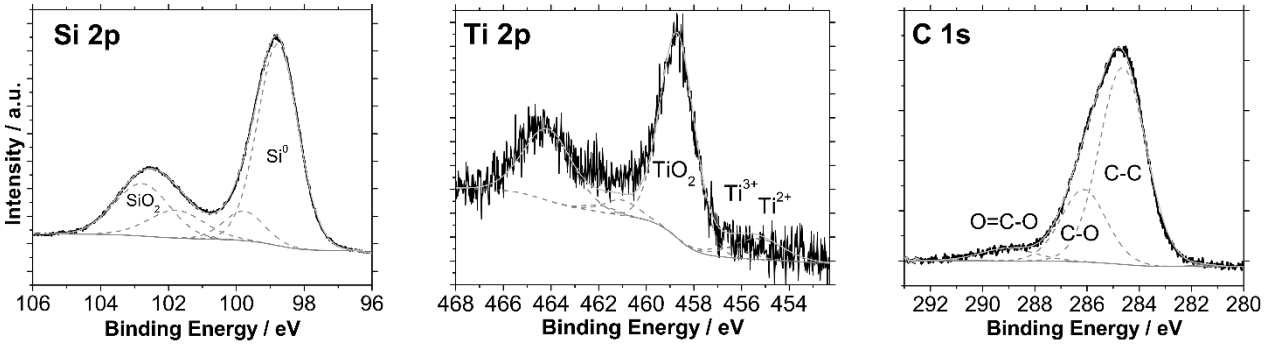

Figure 54 High resolution XPS spectra of the Si 2p, Ti 2p and C 1s regions of the surface of a Si coated TiO_{2-x}–C NT electrode. From [101].

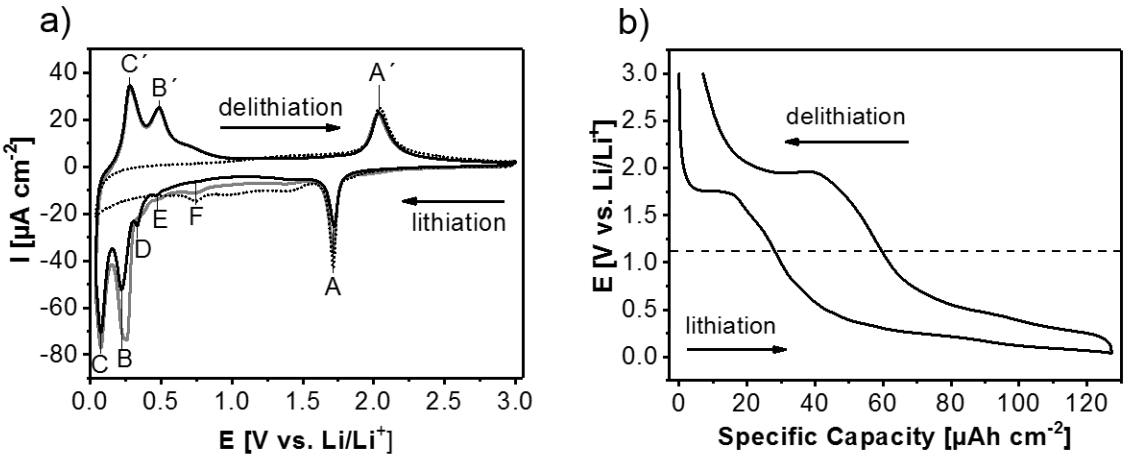

Figure 55 a) CV of Si coated TiO_{2-x}-C NT (solid gray line: 1st cycle, solid black line: 2nd cycle) and TiO_{2-x}-C NT (broken line), scan rate: 0.05 mV s^{-1}, b) GCPL first cycle after CV of Si coated TiO_{2-x}-C NT; electrolyte: 1 M $LiPF_6$ in 1:1 EC:DMC with 2 wt% VC. From [101].

The cyclic voltammetry measurement (Figure 55a) on Si coated TiO_{2-x}-C NT reveals, in the high potential region 1.1 V to 3 V, the characteristic anatase lithiation/delithiation peaks A and A´ at 1.72 V and 2.03 V, respectively, corresponding to the α/β-lithium-titanate double phase formation/destruction potentials (see chapter 1.4 and Figure 4). A broad peak around 1.48 V can be attributed to the β/γ-lithium-titanate double phase region of anatase. The hysteresis of the anatase peaks (A, A') for Si coated TiO_{2-x}-C NT (solid line) is the same as for TiO_{2-x}-C NT (broken line), thus there is no additional over-potential caused by the Si layer. The reason might be that the large portion of the nanotubes that is not coated with Si enables direct access of Li in the TiO_{2-x}-C material.

However, the peak currents at A and A´ for TiO_{2-x}-C NT are slightly higher than those for Si coated TiO_{2-x}-C NT, which may be the result of the partial shielding of the TiO_{2-x}-C material by the Si coating. At lower potentials between 0.04 V and 1.1 V, two prominent lithiation/delithiation peak pairs are visible at 0.25 V (B)/0.48 V (B´) and 0.08 V (C)/0.28 V (C´). These peaks are associated with double phase regions for the transitions from Si to $Li_{2.5}Si$ and further to $Li_{3.75}Si$ [11,16]. Peak B in the first cycle appears as a double peak with sub peaks at 0.24 V and 0.26 V. The two peaks B and C are typically observed for lithiation of amorphous Si [16,18,105,106] or after amorphisation of polycrystalline Si upon lithiation/delithiation [107]. Three additional broad peaks are observed during the first CV cycle upon lithiation at 0.36 V (D), 0.49 V (E) and 0.75 V (F), and a broad shoulder from 0.6 V (end of peak B´) to 1 V upon delithiation. In the second cycle of the CV, peak B is transformed to a single peak at 0.22 V, and the broad peak F disappears. Peaks D and E become sharp and shift to 0.33 V and 0.46 V, respectively whereas the broad shoulder on delithiation remains unchanged. Peaks D and E can be explained by a formation of intermediate double phase regions of coexisting Li_xSi phases preceding the formation of $Li_{2.5}Si$ (peak B). Peak F, that is present in the first cycle CVs of both TiO_{2-x}-C NT and Si coated TiO_{2-x}-C NT and disappears in the second cycle, is attributed to the irreversible reduction of VC containing electrolyte on the surface of the electrode [108].

The constant current (11.6 µA cm^{-2}) lithiation/delithiation curve of Figure 55b shows generally two distinctive regions corresponding to the two active materials of the composite electrode. During lithiation, in the high potential region, a potential plateau followed by a small kink correspond to the peak A (1.72 V) and to the shoulder at ~ 1.48 V in the CV. In the low potential region, a long potential plateau with multiple slope changes corresponds to the Si lithiation peaks of the CV. Upon delithiation, less charge is regained in the low-potential region whereas more charge is regained in the high potential region compared to the charges accumulated during lithiation. This shows that the two active materials influence each other's lithiation properties, an effect that might be even more pronounced if a larger portion of the nanotubes is coated with silicon. It is noticed that the silicon region delivers around 56% of the total capacity of the composite electrode that contains ~10.7% silicon. With the calculated masses, and their deviations, of the composite and its components, their gravimetric capacities are as follows: composite capacity of 556 mA h g^{-1} with a deviation interval of [478; 664] mA h g^{-1}; TiO_{2-x}-C NT capacity of 273 mA h g^{-1} [240; 318] mA h g^{-1}; Si capacity of 2960 mA h g^{-1} [2184; 4583] mA h g^{-1}. Even the lower limit for the gravimetric capacity of TiO_{2-x}-C NT lies beyond the commonly used theoretical capacity of 168 mA h g^{-1} corresponding to $Li_{0.55}TiO_2$. The uncertainty in the measured Si capacity however is so high that no meaningful comparison

can be made between the measured value and theoretical values for different Li_xSi alloys to determine the alloy composition. Here it is also noted that TiO_{2-x}-C NT and Si are not lithiated simultaneously but rather sequentially (in the high and low potential regions) which results, due to their different masses and gravimetric capacities, to different effective lithiation/delithiation speeds under constant current conditions. For a constant current of 4.3 µA (11.6 µA cm^{-2} = j_0/10) and theoretical capacities for composite, anatase and silicon of 534 mA h g^{-1}, 168 mA h g^{-1} and 3580 mA h g^{-1}, respectively, the corresponding effective currents are 51 mA $g_{composite}^{-1}$ (~0.1$C_{composite}$), 57 mA g_{TiO2}^{-1} (0.34C_{TiO2}) and 478 mA g_{Si}^{-1} (0.13C_{Si}).

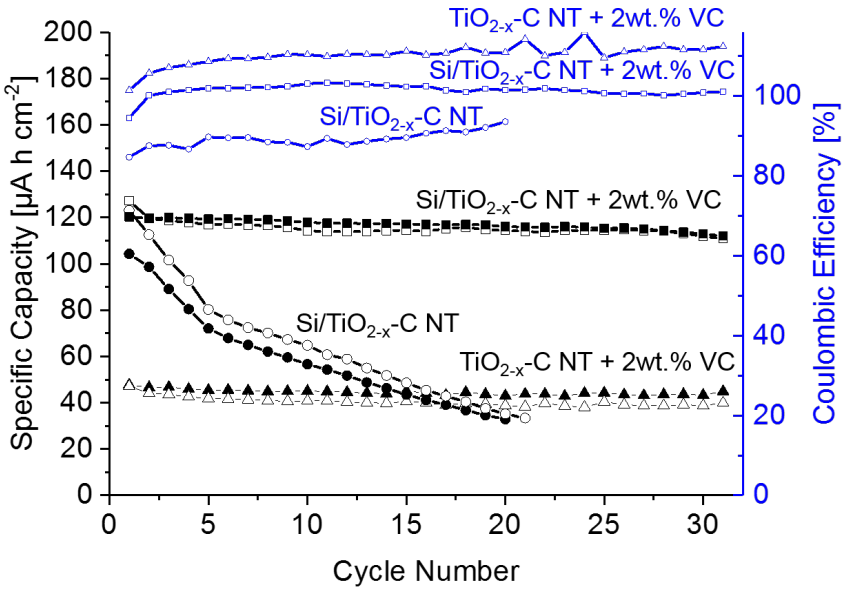

Figure 56 Specific areal capacity (black) and coulombic efficiency (blue) versus cycle number GCPL at 11.6 µA cm^{-2} (~C/10) in 1 M $LiPF_6$ in 1:1 EC:DMC for Si coated TiO_{2-x}-C NT (with and without 2 wt% VC) and TiO_{2-x}-C NT. Lithiation: open symbols, delithiation: closed symbols. From [101].

It was shown by Chen *et al.* [12] and Profatilova *et al.* [13] for Si electrodes that the addition of vinylene carbonate (VC) in the electrolyte improves the properties of the SEI layer and thus the cycling stability of the electrode. They found that the SEI formed in the presence of VC is impermeable to electrolyte (1M $LiPF_6$ solution in a 1:1 (w/w) mixture of EC and DMC), has a practically constant impedance upon cycling and that it contains less LiF than an SEI formed in the same electrolyte in the absence of VC. Therefore, in the present work, the effect of the VC additive on the cycling stability of the studied electrodes was examined. Figure 56 shows the cycling properties of Si coated TiO_{2-x}-C NT in electrolyte with and without a 2 wt% VC additive compared with TiO_{2-x}-C NT in electrolyte with 2 wt% VC additive. TiO_{2-x}-C NT were already shown in chapter 5.1 [93] to cycle stably also without the additive. The figure clearly shows the

crucial effect of the additive on the cycling stability of the composite electrode confirming the previous findings [12,13]. The poor capacity retention (32% after 20 cycles) of the composite electrode in electrolyte without VC is attributed to a massive formation of unstable SEI. The delithiation capacity of the Si coated TiO_{2-x}-C NT electrode in the first GCPL cycle (after one CV cycle for conditioning) in the VC containing electrolyte is 120±2 µA h cm^{-2} that decreases to 110 µA h cm^{-2} or 93% after 30 cycles. The capacity of the TiO_{2-x}-C NT electrode is approximately 2.4 times lower than the capacity of the composite electrode in the same electrolyte. The coulombic efficiency of the TiO_{2-x}-C NT electrode is noticeably above 100% (delithiation charge > lithiation charge).

The same effect in a lesser extent is also present in the composite electrode cycled in the same VC containing electrolyte. A CV (Figure 57) of TiO_{2-x}-C NT electrode in the VC containing electrolyte performed over 11 cycles shows a shift of the delithiation peak (A′) of anatase from 2.04 V (first cycle) to 2.12 V (11^{th} cycle) and the formation of a shoulder at ~2.17 V. The charge under the delithiation part of the CV increases and the charge of the lithiation part decreases (coulombic efficiency > 100%). This effect may be ascribed to oxidative processes on the nanotube surface covered with decomposition products of the electrolyte, such as ethylene, carbon monoxide and dioxide, and methane, as described in Ref. [108], where also higher anodic currents are applied on composite graphite electrodes in 1 M $LiPF_6$ in 1:1 EC:DMC with 2 wt% VC.

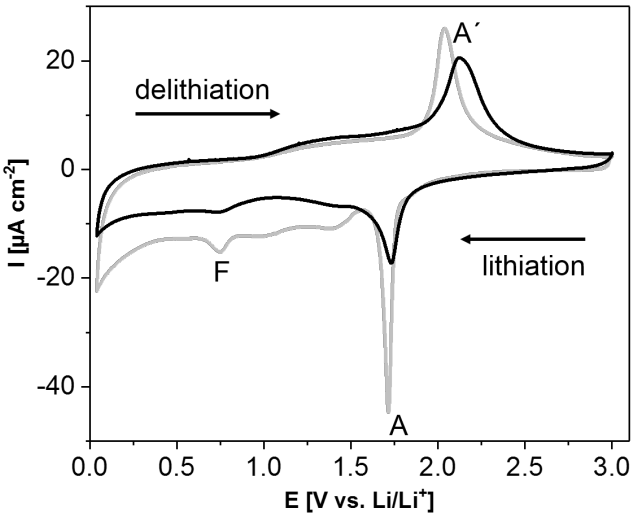

Figure 57 1st (gray) and 11th (black) cycle CV of TiO_{2-x}-C NT in 1 M $LiPF_6$ in 1:1 EC:DMC with 2 wt% VC.

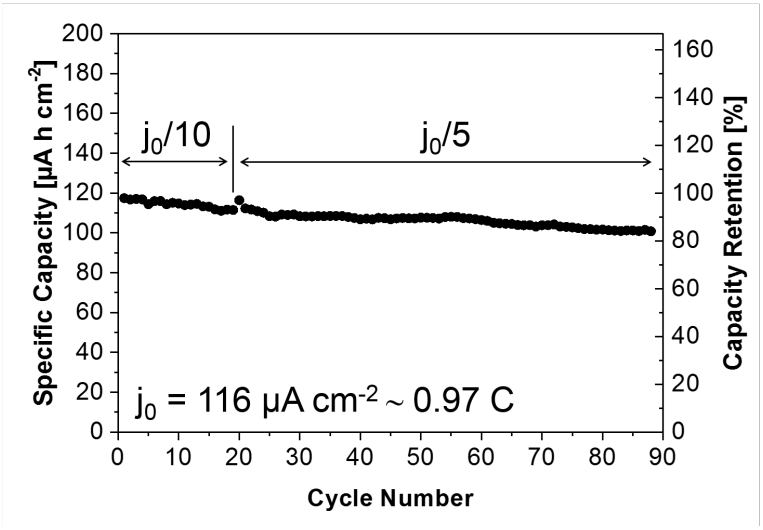

Figure 58 Specific areal capacity and capacity retention versus cycle number of Si coated TiO_{2-x}-C NT in 1 M $LiPF_6$ in 1:1 EC:DMC with 2 wt% VC. From [101]

Figure 58 shows the cycling stability of the Si coated TiO_{2-x}-C NT composite electrode when cycled under GCPL conditions at a constant current of $j_0/10$ for the first 19 cycles and a $j_0/5$ current for cycles 20-88 in a VC containing electrolyte. No significant change in capacity is observed upon the two-fold increase in cycling current. Over the 88 cycles, 86% of the initial 117 µA h cm^{-2} delithiation capacity are retained.

The rate capability of the Si coated TiO_{2-x}-C NT composite electrode was tested at different GCPL cycling rates (Figure 59). At the probed current densities of $j_0/10$, $j_0/5$, $j_0/2$, $1j_0$, $2j_0$ and $10j_0$, the corresponding specific delithiation capacities are 120 µA h cm^{-2} (100%), 112 µA h cm^{-2} (93%), 104 µA h cm^{-2} (87%), 95 µA h cm^{-2} (79%), 82 µA h cm^{-2} (68%) and 60 µA h cm^{-2} (50%), respectively. Reducing the cycling rate from $j_0/2$ to $j_0/10$ returns 116 µA h cm^{-2} (97%), a step from $2j_0$ to $j_0/5$ returns 109 µA h cm^{-2} (97% of the first $j_0/5$ scan), which is almost identical to the capacity retention of prolonged cycling at $j_0/5$ displayed in Figure 58. This finding suggests that (at least short) cycling at rates of up to 10C have no accelerated aging effect on the composite electrode.

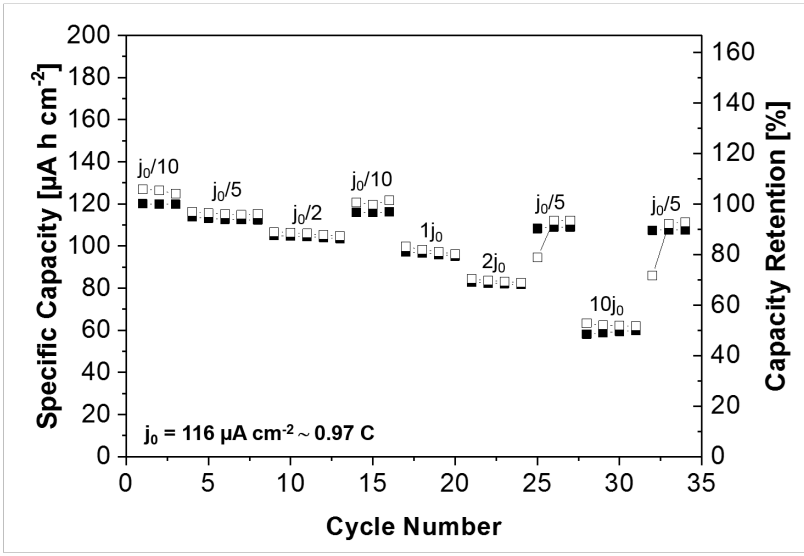

Figure 59 Specific areal capacity and capacity retention versus cycle number at different GCPL cycling rates for a Si coated TiO_{2-x}-C NT in 1 M $LiPF_6$ in 1:1 EC:DMC with 2 wt% VC. From [101]

Conclusions

This study demonstrates that prolonged cycling of silicon electrodes is feasible given a low thickness (~10 nm) of the silicon layer combined with an electrolyte additive that improves the properties of the SEI layer. A two active components composite electrode, of silicon and anodically grown self organised titania nanotubes fixed on the titanium metal used as titanium source for their growth and serving as current collector, obviates the need for binders, conductive additives, and coating procedures, and improves the gravimetric lithium storage capacity of the electrode. The surface area of the nanotubular support is ~72 times larger than the electrode area which allows for a large area thin Si coating. The composite electrode features two potential windows for lithiation/delithiation making new applications feasible where the advantages of both active materials can be accessed in a single cell. Even though the flow of electrolyte through the pores of the TiO_{2-x}-C NT is hindered by the silicon layer on the nanotube walls and the SEI layer formed on the silicon, reducing their pore size, TiO_{2-x}-C NT still show reversible lithium storage capacities of over 240 mA h g^{-1} making approximately one half of the lithium storage capacity of the composite electrode (~550 mA h $g_{composite}^{-1}$).

5.3 Macroscopic areal lithium distribution in lithiated nanotubular electrodes

This work was published under the title “Tracking areal lithium densities from neutron activation – quantitative Li determination in self-organized TiO_2 nanotube anode materials for Li-ion batteries” [92].

The nanotubular electrodes presented in chapter 5.1 and 5.2 exclusively contain active material without binders and conductive additives. This makes them very well suited for fundamental research. However, the low amount of active material compared to classical powder electrodes makes it nearly impossible to accurately quantify the Li-content and distribution in lithiated electrodes. For the further development and up-scaling of nanostructured electrodes like the TiO_2 NT arrays and the composite electrodes based on them, it is essential to map and quantify the Li content and distribution over macroscopic electrode areas with high spatial resolution. The known methods in literature, like X-ray diffraction (XRD) [109], nuclear magnetic resonance spectroscopy (NMR) [110] and X-ray photoelectron spectroscopy (XPS) [111] that can potentially deliver quantitative Li-detection, cannot be easily employed for obtaining spatial information on the Li content [112]. Energy loss spectroscopy in transmission electron microscopy can be used for Li mapping [113,114] but not for macroscopic length scales in the order of mm. In this work, triton analysis exploiting the neutron capture reaction of ^6Li producing a triton and an α -particle, written in a compact form as $^6Li(n,\alpha)^3H$, was used to determine the 2D Li content distribution for as grown amorphous TiO_2 NT, acetylene annealed anatase TiO_{2-x}-C NT and Si coated TiO_{2-x}-C NT composite electrodes ($SiTiO_{2-x}$-C NT). This method allows for non-destructive 2D areal Li mapping over macroscopic electrode areas and to detect the very small quantities of Li (10-20 µg cm^{-2}) in these electrodes.

Experimental

Type 3 TiO_2 NT were prepared according to the procedure described in chapter 4.1.3. The as grown amorphous nanotubes were used directly as one of the studied electrode materials. Anatase TiO_{2-x}-C NT were prepared by carbo-thermal annealing of the Type 3 TiO_2 NT as described in chapter 4.2.1. $SiTiO_{2-x}$-C NT composite electrodes were prepared by PECVD Si deposition on the anatase TiO_{2-x}-C NT as described in chapter 4.3. Electrochemical lithiation of the studied electrodes was performed in a separator free cell described in chapter 4.5.2.3, filled with 1M $LiPF_6$ in a 1:1 (w/w) mixture of EC and DMC with a 2 wt.% VC additive. All herein

provided potentials are defined with respect to the Li/Li^+ reference electrode potential unless otherwise stated. Lithiated electrodes were sealed under Ar atmosphere in a target box, described in chapter 4.6, and transferred to the triton detection setup. The amount of Li stored in an electrode was calculated from the charge (q) under the corresponding lithiation curve as follows:

Equation 23 $$m_{Li}[g] = n[mol\ Li] \times M_{Li}[g\ mol^{-1}]$$

Equation 24 $$n[mol\ Li] = \frac{n_{electrones}}{N_A} = \frac{q[C]}{e} \times \frac{1}{N_A}$$

Equation 25 $$q[C] = q[A\ h] \times 3600$$

Equation 26 $$\xrightarrow{yields} m_{Li}[g] = \frac{q[A\ h] \times 3600 \times M_{Li}[g\ mol^{-1}]}{e \times N_A}$$

wherein: m_{Li} is the mass of Li in g; M_{Li} is the molar mass of Li = 6.94 g mol^{-1}; n[mol Li] is the number of moles of Li; $n_{electrons}$ is the number of electrons; q[C] and q[A h] represent the charge measured in Coulombs and A h, respectively; e is the electron charge = 1.6×10^{-19} C and N_A is the Avogadro number $N_A = 6.02 \times 10^{23}$.

SEM was used to determine the mass of the active materials of each electrode according to the method described in chapter 4.4. XRD was performed in Ar atmosphere on a Siemens D5000 difractometer. Diffractograms were acquired between 15 and 75 degree (2 theta) with a step size of 0.02 degrees (2 theta) and an acquisition time of 1s per step. Additional chemical composition, surface and structural characterization was performed using attenuated total reflection Fourier-transform infrared spectroscopy (ATR-FTIR) and micro-Raman. ATR-FTIR (Nicolet iS5) absorption spectra were recorded in the $-\Delta T/T$ mode with a spatial resolution of 4 cm^{-1}, using a polished Ti disk as a reference. Micro-Raman spectra were recorded with an Olympus BX40 instrument comprising a He/Ne laser (632.8 nm) used in non-focal operation mode and without a polarizer. The diameter of the laser spot on the examined electrodes was determined to be ~1 mm using the 50x magnification of an optical microscope.

Back-scattered Raman signals were recorded with a resolution of less than 2 cm^{-1} (determined by measuring the Rayleigh line) in a spectral range from 90 to 2000 cm^{-1}.

Triton analysis was performed based on the neutron capture reaction $^{6}Li(n,\alpha)^{3}H$. ^{6}Li has a large neutron capture cross section $\sigma_{th} = 940\pm4$ barn [85] for thermal neutrons and an isotopic abundance in natural Li of 7.42% [86]. In the neutron capture reaction, the compound nucleus immediately decays into an alpha particle (α) and a tritium (^{3}H) nucleus called, in its free particle form, triton (t), which in the laboratory system are emitted in opposite directions due to momentum conservation. Because of the reaction Q value, the α and the triton particles obtain a fixed and relatively high kinetic energy of $E_{\alpha} = 2055$ keV and $E_{triton} = 2727$ keV, respectively [84].

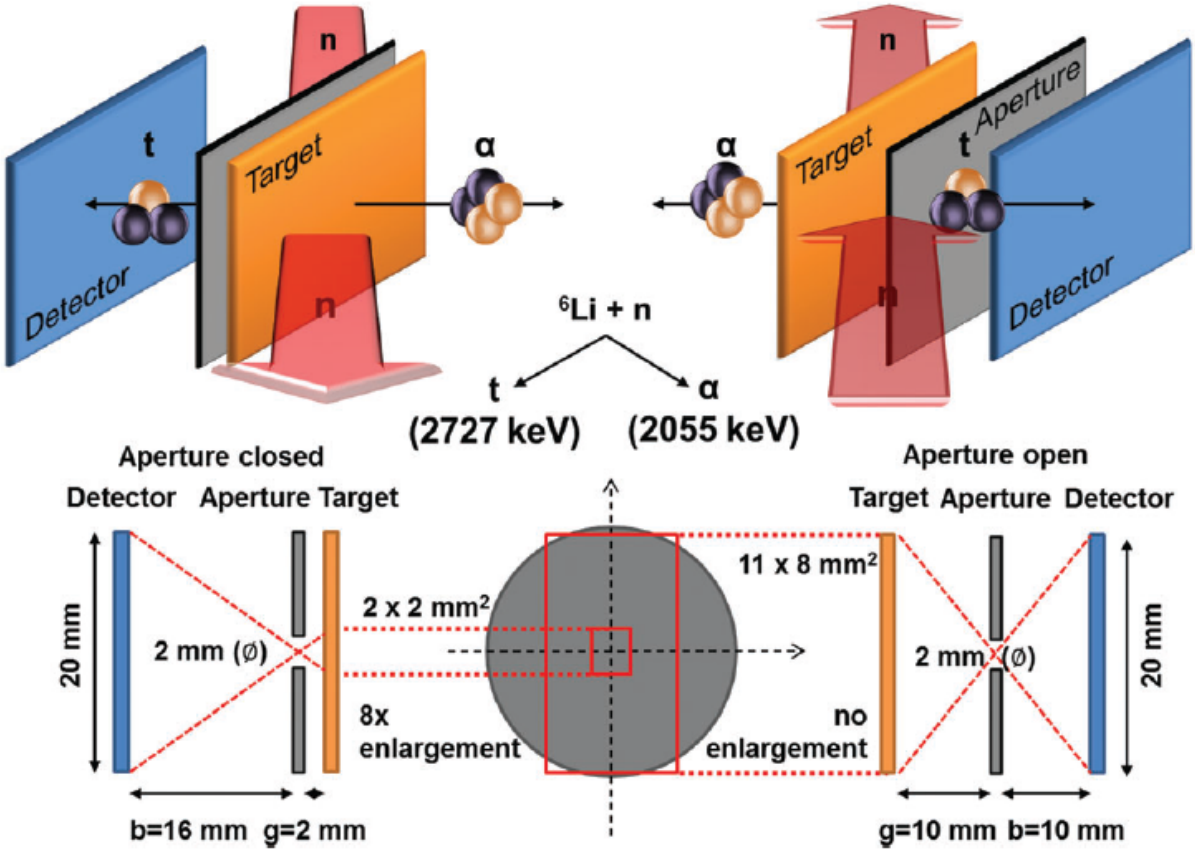

Figure 60 Experimental setup for triton- or α-particle detection with closed aperture (left) or open aperture (right) geometry. Closed aperture geometry allows the analysis of a 2 x 2 mm² area with an 8x magnification. In open aperture geometry an area of 11 x 8 mm² is examined without a magnification (drawing is not true to scale). From [92]

Figure 60 schematically depicts the basic concept of the detection method. In this setup, cold neutrons (1.8 meV; 6.7 Å), are used which increase the cross section for the neutron capture reaction 3.6 times ($\sigma_C = 3474$ barn) compared to thermal neutrons. The targets are the

nanotubular electrodes grown on a Ti disk with a 1 mm thickness and a diameter of 20 mm disposed such that the nanotubular layer is on the side of the Ti disk directly exposed to the neutron beam and facing a position sensitive silicon detector.

Due to the high thickness of the Ti disk, coincidence detection of an alpha particle and a triton from the same decay event, that would allow a significantly higher space resolution, is not possible since one of the particles would have to travel through the Ti disk. Therefore, both particles are detected alternatively. A 2 mm pinhole positioned between the target and the detector is used to prevent overload of the detector and allow for a full area analysis, with the open aperture geometry of Figure 60 (right side), or a reduced area analysis that provides 8x magnification with the closed aperture geometry (Figure 60 left side). The detector and the target parallel to it are tilted by 25 degree with respect to the axis of the neutron beam [88]. This allows for a close configuration of the detectors to maximize the solid angle coverage while the detectors and the target frame are not irradiated by the collimated neutron beam. Tritons and alpha particles are detected by a position-sensitive silicon detector with a spatial resolution of 300 µm.

Results and Discussion

As already shown in chapter 5.2, Si coated TiO_{2-x}-C NT composite electrodes have two distinctive lithiation regions corresponding to the potential windows for lithiation of the two active materials titania (3 V – 1.1 V) and silicon (1.1 V – 0.04 V). Furthermore, it was shown that electrolyte decomposition on the surface of the electrodes becomes significant below 1.1 V. Therefore, to compare the lithiation degree dependent changes in the electrodes, a first batch of the three electrode materials TiO_2 NT, TiO_{2-x}-C NT and $SiTiO_{2-x}$-C NT is lithiated down to 1.1 V and a second batch down to 0.04 V. To achieve full lithiation of the electrodes, these are first lithiated galvanostatically from OCP down to the desired potential and then potentiostatically until the rate of change of the lithiation current falls under a threshold (see Figure 61).

The first batch is lithiated down to 1.1 V at a constant current of 6.7 µA cm^{-2} (~0.1C) and kept at 1.1 V until the current is no longer changing by more than $3x10^{-5}$ µA s^{-1}. The second batch is lithiated down to 0.04 V at a constant current of 6.7 µA cm^{-2} and kept at 0.04 V until the current is no longer changing by more than $1x10^{-4}$ µA s^{-1}. The threshold, for the potentiostatic lithiation of the batch lithiated at 0.04 V, is set higher since more side reactions are expected to take place at this potential.

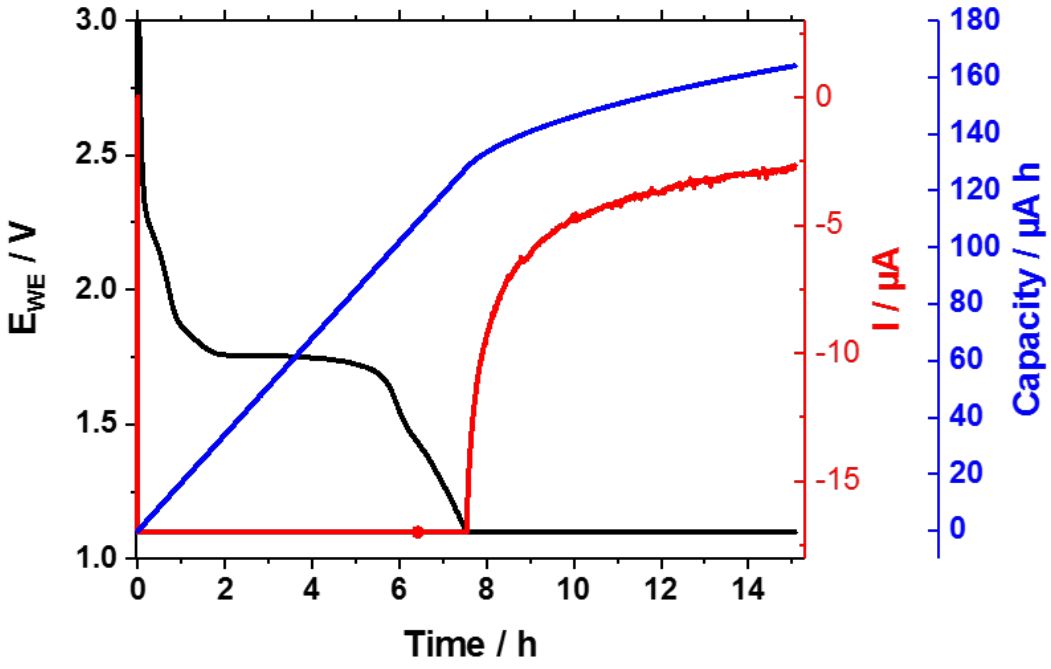

Figure 61 Lithiation procedure: galvanostatic lithiation from OCP to 1.1V followed by potentiostatic lithiation until current change rate falls under a threshold. Potential (black), current (red) and charge (blue) vs. time. [92]

Analysis of SEM top view and cross sections of the nanotube arrays of the three electrode materials reveal a 1.1 µm average nanotube length, 115 nm average pore diameter and an average wall thickness of 15 nm. The Si coating on the $SiTiO_{2-x}$-C NT has a layer thickness of 10 nm covering the top 160 nm of the inner and outer walls of the nanotubes. Applying the procedure described in chapter 4.4, the mass of Si was calculated to be ~5 wt% of the $SiTiO_{2-x}$-C NT composite electrode.

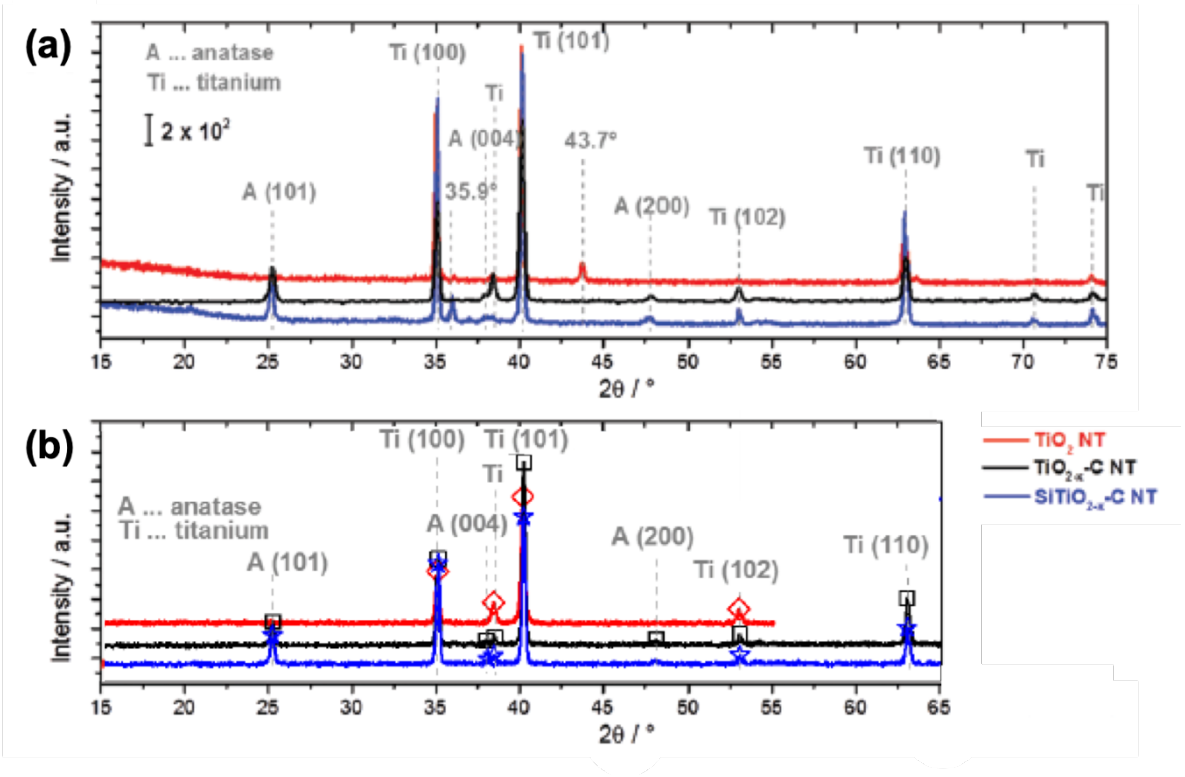

Figure 62 XRD spectra of TiO_2 NT (red), TiO_{2-x}-C NT (black) and $SiTiO_{2-x}$-C NT (blue) (a) after lithiation to 1.1 V and (b) before lithiation. From [92].

The structure of the three electrode materials before (Figure 62b) and after lithiation to 1.1 V (Figure 62a) is probed by *ex situ* XRD under Ar atmosphere to prevent reactions of the lithiated material with ambient moisture or oxygen. The structure of the titania compound in TiO_{2-x}-C NT and $SiTiO_{2-x}$-C NT, that have been converted carbo-thermally to anatase, remains that of anatase after lithiation to 1.1 V with the prominent anatase peaks (101), (004), and (200) at $2\theta = 25°$, 38°, 48°, respectively. This finding is consistent with the XRD analysis of the similar TiO_{2-x}-C NT presented in chapter 5.1 and also the findings of Wang *et al.* [115]. A new peak at 35.9° is however observed for the lithiated $SiTiO_{2-x}$-C NT electrode (blue line, Figure 62a) that is not present in the pristine sample (Figure 62b) and could not be clearly identified. As expected [116], XRD of the as grown amorphous TiO_2 NT shows only Ti peaks corresponding to the (100) and (101) planes of the Ti metal substrate at ~35° and 40°. After lithiation, TiO_2 NT (red line, Figure 62a) show a peak at 43.7°, which is possibly related to an electrochemically driven transformation of amorphous titania to a face-centered cubic crystalline phase [117], as previously reported by Johnson and Rajh *et al.* [118].

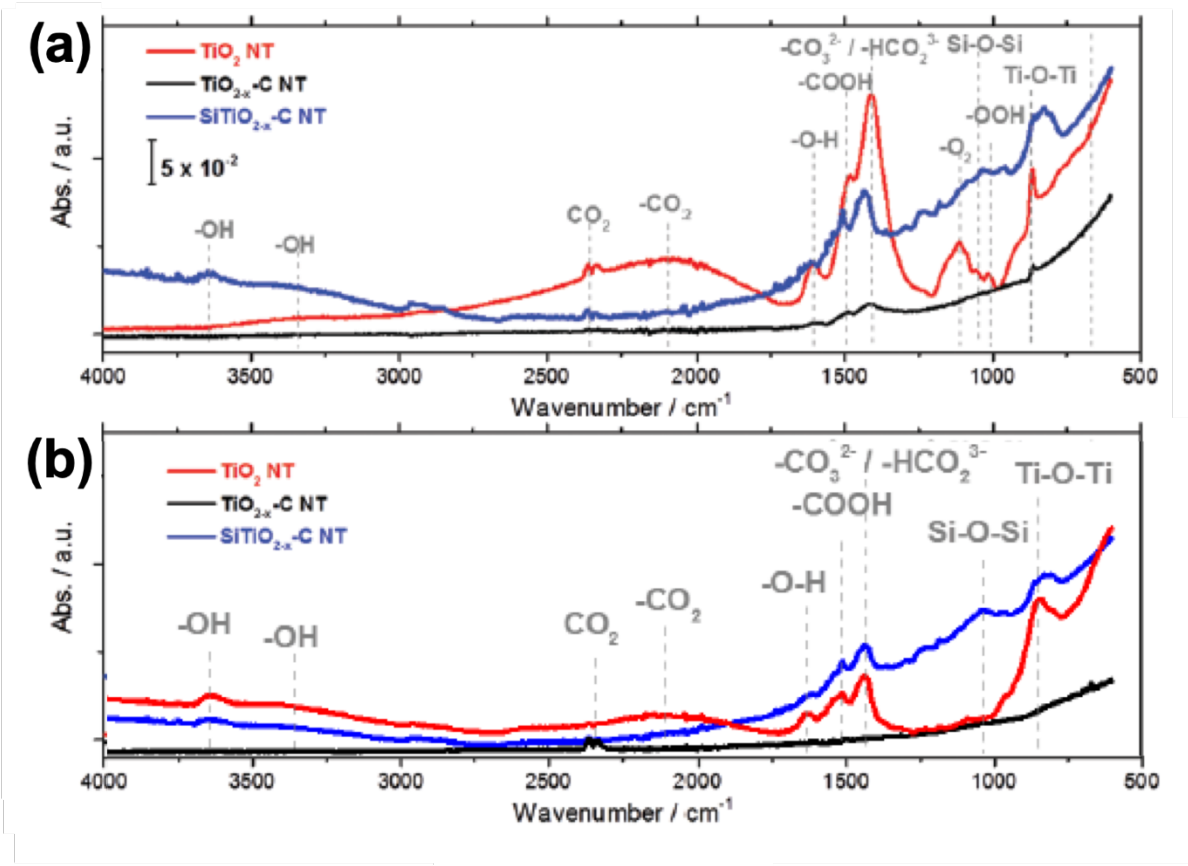

Figure 63 ATR-FTIR spectra of TiO_2 NT (red), TiO_{2-x}-C NT (black) and $SiTiO_{2-x}$-C NT (blue) (a) after lithiation to 1.1 V and (b) before lithiation. From [92].

Ex situ ATR-FTIR spectra of the electrodes before (Figure 63b) and after lithiation to 1.1 V (Figure 63a) show a number of peaks recorded for the amorphous TiO_2 NT that are not observed for the TiO_{2-x}-C NT and $SiTiO_{2-x}$-C NT electrodes. The corresponding species on the surface of the amorphous nanotubes can be assigned to adsorbed OH groups [119,120], or adsorbed carbonate, carbon dioxide or COOH species, which are almost entirely removed upon annealing, as in the case of TiO_{2-x}-C NT and $SiTiO_{2-x}$-C NT, which is consistent with literature [121]. Vibrations around 3375 cm^{-1} are characteristic of hydroxyl groups of Ti-OH formed on the TiO_2 surface [122,123]. The double peak at 2350 cm^{-1} is assigned to atmospheric CO_2 that could not be removed completely during the measurement and the partially overlapping broad peak around 2100 cm^{-1} originates from weakly adsorbed CO_2 [123]. The peak at 1630 cm^{-1} corresponds to the deformation vibration of –O-H from physisorbed water [122]. The absorption band at 1480 cm^{-1} belongs to the symmetric and antisymmetric stretching vibrations of carboxylate (-COOH) groups [124].

A band assigned to antisymmetric stretching modes of CO_3^{2-} and HCO_2^{3-} positioned at 1415 cm^{-1} is found to increase significantly for TiO_2 NT (red) upon lithiation [122,125,126]. The Ti-O stretching mode is observed at 837 cm^{-1} [120]. The spectrum of pristine TiO_{2-x}-C NT does not show any features apart from the atmospheric CO_2 double peak. After lithiation the features at 1415 cm^{-1} (CO_3^{2-} and HCO_2^{3-}) and 837 cm^{-1} (Ti-O stretching) appear additionally. The spectrum of $SiTiO_{2-x}$-C NT additionally shows a small peak at 1045 cm^{-1}, before and after lithiation that is indicative of Si-O-Si [127,128], as well as a plurality of further very small features at ~1500 cm^{-1} (-COOH), 2100 cm^{-1} (-CO_2), ~3300 cm^{-1} (Ti-OH stretching) and 3630 cm^{-1} (unsymmetrical stretching of water molecules [121]).

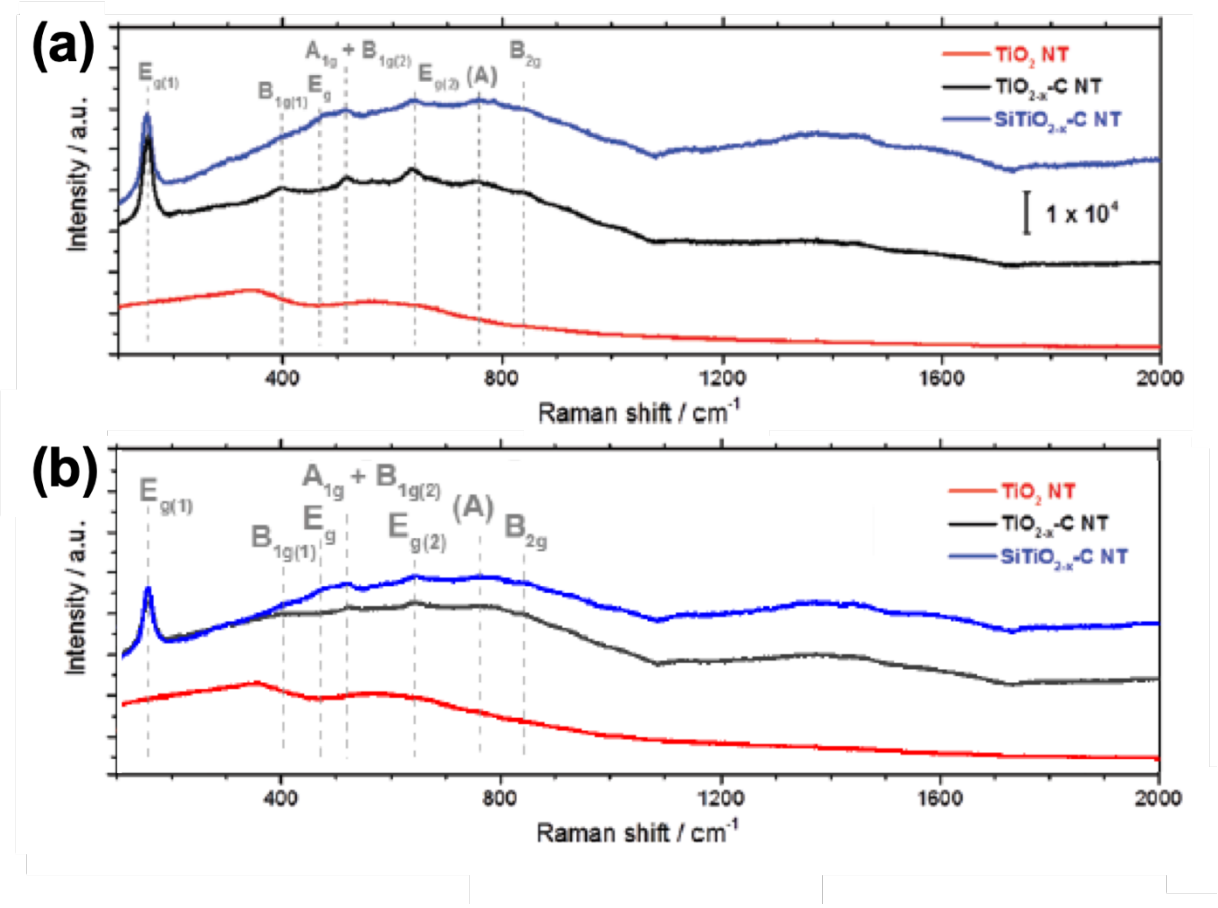

Figure 64 Raman spectra of of TiO_2 NT (red), TiO_{2-x}-C NT (black) and $SiTiO_{2-x}$-C NT (blue) (a) after lithiation to 1.1 V and (b) before lithiation. From [92].

The crystallinity of the pristine (Figure 64b) and at 1.1 V lithiated electrode (Figure 64a) materials is further investigated using micro-Raman spectroscopy. Amorphous TiO_2 NT (red) show no distinct Raman signals before or after lithiation. In the spectra of the TiO_{2-x}-C NT (black) and

$SiTiO_{2-x}$-C NT (blue) electrodes, four main Raman peaks are observed at 145, 399, 516, and 634 cm^{-1}, that can be attributed to the E_g, $B_{1g}(1)$, $A_{1g}/B_{1g}(2)$, and $E_g(2)$ vibration modes of the anatase phase of pure TiO_2, respectively [129,130]. The weak features between 700 and 800 cm^{-1} may be assigned to the combination bands of anatase (indicated by (A)) [131], while the peaks detected at ~460 cm^{-1} (only in the spectrum of $SiTiO_{2-x}$-C NT) and at 826 cm^{-1} can be assigned to E_g and B_{2g} bands of rutile TiO_2 [132]. In the presence of anatase, the small B_{1g} vibration of rutile at 143 cm^{-1} is usually obscured due to its proximity to the E_g band of anatase. However, there is also no distinct peak visible at 612 cm^{-1} that is caused by the Raman-active A_{1g} mode of rutile, suggesting a very low fraction of the rutile phase in the TiO_2 compared to the anatase phase [131,133]. The small amount of rutile in the $SiTiO_{2-x}$-C NT may have formed, on the interface between nanotubes and Ti substrate, due to residual oxygen in the deposition chamber in the initial phase, of heating to 250 °C and purging with Ar, of the PECVD procedure for Si deposition. In line with the XRD analysis, no new lithium-related phase can be identified from the Raman spectra of the lithiated electrodes. However, the band maximum position of the E_g mode of anatase slightly shifts from 639 to 634 cm^{-1}, which is consistent with previous findings reported for similar systems [134]. Furthermore, the Raman spectra of the carbo-thermally annealed electrodes TiO_{2-x}-C NT and $SiTiO_{2-x}$-C NT show two weakly distinguishable bands at 1352 and 1457 cm^{-1} that may originate from amorphous carbon [135] and adsorbed polyenes present on the nanotube surface after the acetylene annealing at 400°C [129,130]. It has been shown earlier that this carbon originates from the carburization treatment during nanotube preparation [116]. The weakly resolved band at 1125 cm^{-1} is assigned to the asymmetric stretching vibration of Ti-O-Si [136,137].

Figure 65 displays a proof of principle triton analysis of areal Li density on a lithiated TiO_{2-x}-C NT electrode. The dark portion of the electrode surface in Figure 65b is covered with the lithiated active material whereas the brighter portion is blank Ti substrate exposed by peeling off the nanotubular active layer after lithiation upon rinsing the electrode with DMC. The color scale in Figure 65c reflects the Li areal concentration increasing from dark blue towards red. The superposition of the Li map from triton analysis Figure 65c and the optical micrograph of the electrode surface, displayed in Figure 65d, reveals a perfect match between the Li containing regions derived from triton analysis and the active material covered regions where Li is expected.

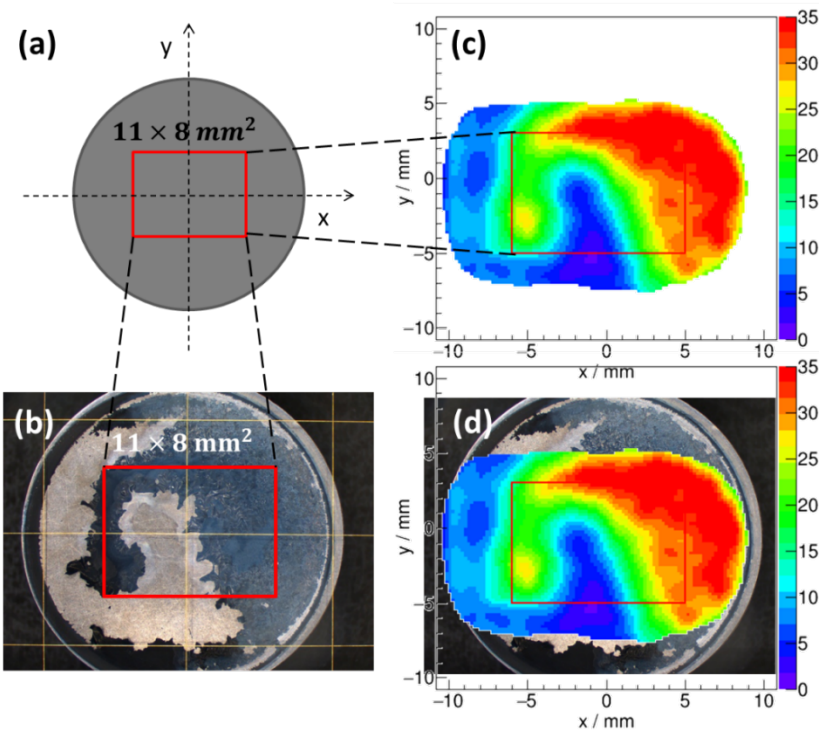

Figure 65 Triton analysis on lithiated TiO_{2-x}-C NT electrode: (a) top view scheme of the electrode with a red marking of the analyzed area of 11x8 mm²; (b) top view optical micrograph of the electrode with TiO_{2-x}-C NT covered region (dark) and blank Ti region (bright) where nanotubes are peeled off, and a red marking of the analyzed area; (c) reconstructed areal Li density in µg Li cm^{-2}; (d) superposition of (b) and (c). From [92]

Figure 66 a_1-c_1 shows the galvanostatic lithiation to 1.1 V (C/10), followed by potentiostatic lithiation at 1.1 V of TiO_2 NT, TiO_{2-x}-C NT and $SiTiO_{2-x}$-C NT, respectively. (a_2)-(c_2) represent the corresponding reconstructed 2D-maps of Li areal density on a 2x2 mm^2 area in the center of the sample in µg cm^{-2}, and (a_3)-(c_3) depict the Li areal density distributions in µg cm^{-2} for the analyzed area. The as grown amorphous nanotubes show a rather continuous potential decrease (with some slope changes) upon lithiation indicating a continuous macroscopic change in lithium concentration in the active material. The anatase-based electrodes TiO_{2-x}-C NT and $SiTiO_{2-x}$-C NT, on the other hand, exhibit the typical potential plateau at 1.72 V indicative of the double phase region where the lithium poor α-Li_xTiO_2 ($0 < x < 0.21$) coexists with the β-$Li_{0.5}TiO_2$. In TiO_{2-x}-C NT, the end of the plateau which marks the end of the α to β lithium-titanate phase transition, is observed at a charge density of 31 µA h cm^{-2}.

This amount of charge corresponds macroscopically to 0.33 mole of Li per mole of TiO_2, indicating that not all of the active mass of TiO_2 is transformed to the β-$Li_{0.5}TiO_2$ phase (corresponding to 0.5 mole of Li per mole of TiO_2). The same plateau in the lithiation curve of $SiTiO_{2-x}$-C NT ends at 38 µA h cm^{-2} corresponding macroscopically to 0.41 mole of Li per mole

of TiO_2, which is also below the amount of Li in the β-$Li_{0.5}TiO_2$, indicating partial transition. TiO_{2-x}-C NT and $SiTiO_{2-x}$-C NT behave identically down to the cutoff voltage of 1.1 V since this potential is far from the activity region of Si in the $SiTiO_{2-x}$-C NT electrode, which typically starts below 0.6 V (see Figure 55 of chapter 5.2). At the end of the galvanostatic lithiation, when 1.1 V are reached, the TiO_2 NT electrode has accumulated an areal charge of 61 µA h cm^{-2}, the TiO_{2-x}-C NT electrode 44 µA h cm^{-2}, and the $SiTiO_{2-x}$-C NT electrode 50 µA h cm^{-2}, corresponding to 15.80 ± 1.97, 11.40 ± 1.42 and 13.17 ± 1.65 µg cm^{-2} of Li. These results are in agreement with literature, where amorphous titania nanoparticles are showing higher capacities, especially in the first lithiation, compared to anatase nanoparticles [119]. At the end of the potentiostatic lithiation, the total charge density for TiO_2 NT, TiO_{2-x}-C NT and $SiTiO_{2-x}$-C NT is 95, 61 and 65 µA h cm^{-2}, respectively, corresponding to 24.6 µg cm^{-2}, 15.82 µg cm^{-2} and 16.85 µg cm^{-2} of Li. In all three electrodes, triton analysis reveals a homogeneous lithiation degree over the analyzed surface area of 2x2 mm^2. The average Li areal densities measured by triton analysis in this area in the center of each electrode (determined from the lithium areal density distributions in Figure 66a_3-c_3) for TiO_2 NT, TiO_{2-x}-C NT and $SiTiO_{2-x}$-C NT are 14.18 ± 1.75, 12.15 ± 1.51 and 11.43 ± 1.42 µg cm^{-2}, respectively. These values correspond, in the range of error, to the values measured electrochemically at the end of galvanostatic lithiation.

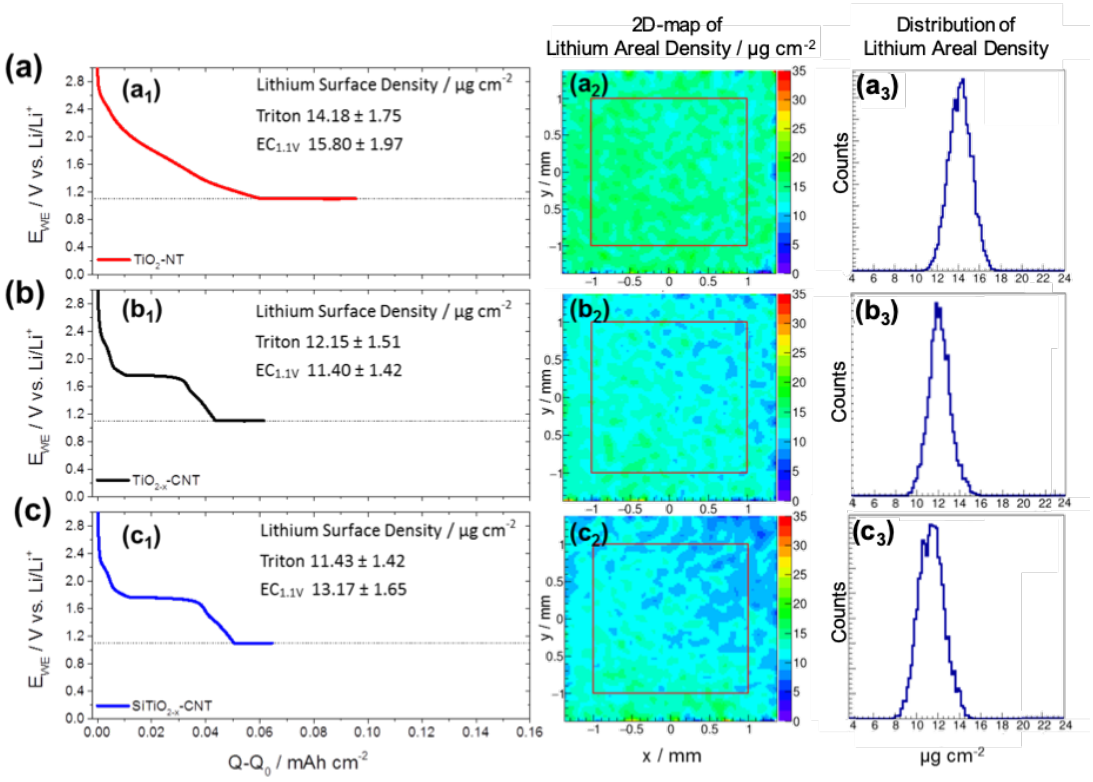

Figure 66 (a) TiO_2 NT, (b) TiO_{2-x}-C NT and (c) $SiTiO_{2-x}$-C NT electrodes. Index subscripts: 1 - galvanostatic lithiation to 1.1 mV (C/10), followed by potentiostatic lithiation at 1.1 mV; 2 – reconstructed 2D-map of Li areal density with a color scale in µg cm^{-2} for a 2x2 mm^2 analyzed electrode area; 3 - distribution of Li areal density in µg cm^{-2} for the analyzed area. From [92]

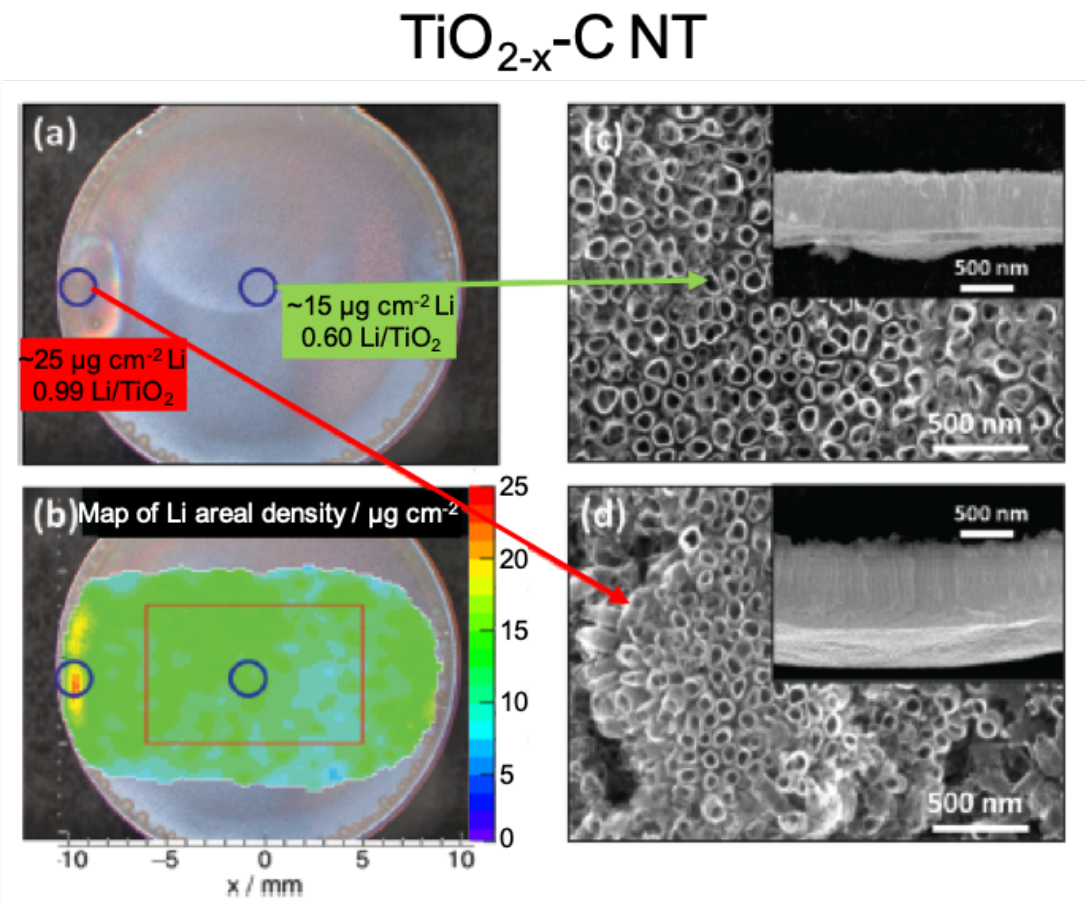

Figure 67 ***TiO_{2-x}-C NT*** *electrode lithiated at 1.1 V: (a) optical image with indicated areas for SEM analysis (blue circles) and the corresponding Li areal densities from triton analysis in µg cm^{-2} highlighted in the red and green textbox; (b) reconstructed 2D-map of Li areal density from triton analysis overlaid with the micrograph, with a color scale in µg cm^{-2}; (c) and (d) SEM micrographs of the areas marked in (a) connected with the corresponding green and red line, with insets showing cross sections of the nanotubes in this areas. From* [92].

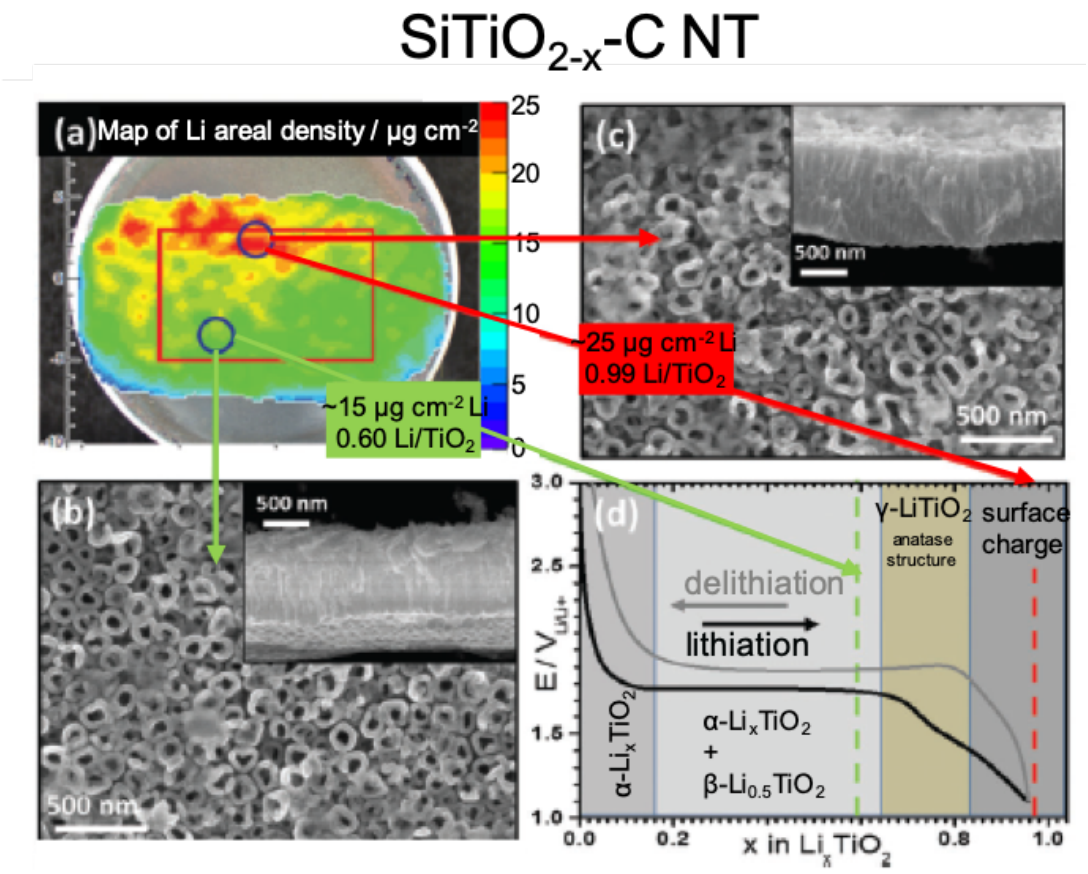

*Figure 68 **SiTiO$_{2-x}$-C NT** electrode lithiated at 1.1 V: (a) reconstructed 2D-map of Li areal density from triton analysis, with a color scale in µg cm^{-2} overlaid with an optical image with indicated areas for SEM analysis (blue circles) and the corresponding Li areal densities from triton analysis in µg cm^{-2} highlighted in the red and green textbox; (b) and (c) SEM micrographs of the areas marked in (a) connected with the corresponding green and red line with insets showing cross sections of the nanotubes in the corresponding areas; (d) exemplary lithiation/delithiation curve of anatase showing potential vs. molar fraction x of Li in TiO$_2$ and lithiation stages emphasized by different background colors wherein the corresponding molar fractions of the regions marked in (a) are indicated by dashed lines. From* [92].

Figure 67 and Figure 68 display a TiO$_{2-x}$-C NT and a SiTiO$_{2-x}$-C NT electrode, respectively, lithiated at 1.1 V and analyzed by triton detection and SEM. The large area Li content map (recorded with the open aperture geometry) of the electrodes shows the presence of hot spots with increased Li concentration (red regions) of ~25 µg cm^{-2} Li compared to the average concentration in the central portion of the electrode of ~15 µg cm^{-2} Li (green region). Top view and cross-sectional SEM micrographs of the TiO$_{2-x}$-C NT electrode in the hot spot and in the homogeneous region show an increased length of the nanotubular array in the hot spot of 1.7±0.1 µm compared to 1.1±0.1 µm in the homogeneous region. This increase in length increases the active mass of the material in the hot spot. Normalizing the Li concentration by the corrected mass for the hot spot, its degree of lithiation becomes ~0.64±0.20 mole of Li per mole of TiO$_2$, which is, in the range of error, the same as the Li density in the green region of ~0.54±0.10 mole of Li per mole TiO$_2$. The region of the electrode, with nanotubes of increased

length, corresponding to the hot spot, originates from an edge effect, which can occur in the vicinity of the O-ring during the anodic growth of the nanotubes. The same analysis performed on the $SiTiO_{2-x}$-C NT electrode, reveals an even larger hot spot of about 11 mm length and a 5 mm width. However, the nanotubes in the hot spot have the same length (950±100 nm) and outer diameter (135±20 nm) as the nanotubes in the homogeneous region of the electrode, which means that the source of inhomogeneous lithiation is different.

According to these observations, the higher charges (discussed with regard to Figure 66) measured electrochemically at the end of the potentiostatic step of lithiation compared to the Li densities measured by triton analysis, can be explained by the following:

- side reactions like electrolyte decomposition that contribute to the overall current without increasing the amount of Li stored in the electrode material;
- lithium containing layers on the electrode surface (SEI) are partially washed away by rinsing the electrode with DMC prior to triton analysis;
- there are hot spots in the large area Li content map outside of the surface area of 2x2 mm^2 analyzed by triton detection, which contribute to the charge measured electrochemically.

The molar fractions of Li calculated from the Li areal density from triton analysis, are compared in Figure 68d with the lithiation curve of anatase discussed in chapter 1.4 (Figure 4), wherein the horizontal axis is displayed in terms of molar fraction of Li in TiO_2. The colored background regions mark the presence of certain lithium containing phases in the electrode, whereas the horizontal axis represents the average proportion of Li to TiO_2 in the electrode, thus the region corresponding to the formation of the γ-$LiTiO_2$ with 1 mole of Li per TiO_2 does not coincide with the 1:1 molar ratio on the horizontal axis since only portions of the electrode are transformed to this phase. The homogeneous region in $SiTiO_{2-x}$-C NT has ~15 µg cm^{-2} Li corresponding to $Li_{0.6}TiO_2$ whereas the hot spot with ~25 µg cm^{-2} Li corresponding to $Li_{0.99}TiO_2$ indicates either the full transformation of the titania active material to the γ-$LiTiO_2$ phase or a lower phase combined with Li stored on the surface of the electrode.

In order to analyze the nature of adsorbates on the surface of $SiTiO_{2-x}$-C NT at the positions of hot spots and medium Li concentration, local micro-Raman and ATR-FTIR have been performed (Figure 69 a and b). Both methods do not show any significant difference between areas with high and intermediate Li concentration. Therefore, the origin of the hot spot does not seem to be related to surface storage of Li but rather a bulk phenomenon. This could be due to differences in the crystalline orientation of the nanotubes (see chapter 1.5) or another effect caused by inhomogeneities in the local fluoride and water concentrations during nanotube growth. The high amount of adsorbed species detected on amorphous TiO_2 NT (black line in Figure 69b), which do not contain Li, explains the high charge measured electrochemically and the mismatch with the amount of Li determined by triton analysis.

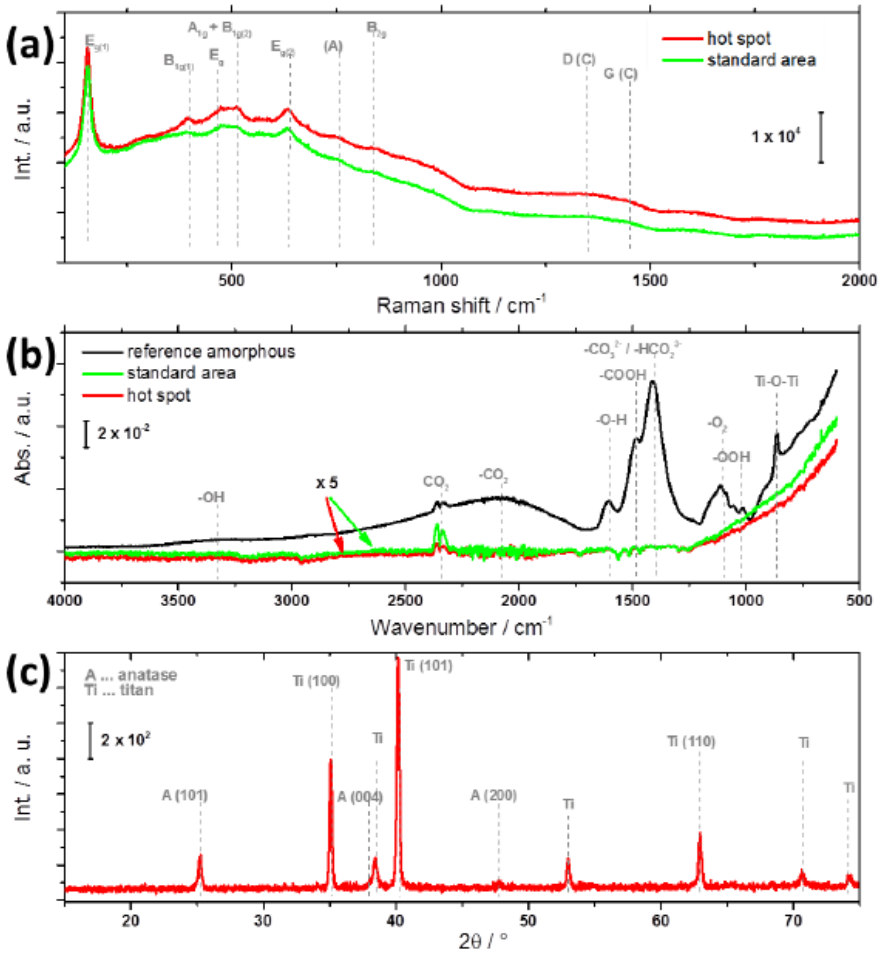

Figure 69 Spectroscopic analysis after lithiation to 1.1 V: (a) Micro-Raman spectra of areas with high Li concentration ('hot spot', red), and areas with intermediate Li concentration (green). (b) ATR-FTIR spectra of areas with high Li concentration (red), and intermediate Li concentration (green). A reference measurement of an amorphous, as grown TiO_2 NT electrode is shown (black). (c) XRD spectra of $SiTiO_{2-x}$–C NT, showing anatase TiO_2 structure. [92]

In a next phase, the second batch of TiO_2 NT, TiO_{2-x}-C NT and $SiTiO_{2-x}$-C NT electrodes is lithiated down to 0.04 V following the same two-step lithiation procedure. The resulting electrochemical lithiation curves (a_1-c_1), small area (2x2 mm^2) 2D-maps of Li areal density from triton analysis (a_2-c_2)

and Li areal density distribution (a_3-c_3) are shown in Figure 70. Both methods show the presence of significantly higher Li contents in all three electrodes as compared to the first batch lithiated at 1.1 V. The contribution of Si is visualized in Figure 71 through the comparison of the lithiation curves of the TiO_{2-x}-C NT and $SiTiO_{2-x}$-C NT electrodes where the high potential (>1.1 V) portion of the lithiation curves where only titania is active for Li storage, are shifted to the negative side of the charge axis (horizontal axis). After galvanostatic lithiation to 0.04 V, the gravimetric capacity of the $SiTiO_{2-x}$-C NT composite electrode is 462±114 mA h g^{-1} and that of the TiO_{2-x}-C NT electrode is 332±82 mA h g^{-1} (as calculated from the lithiation charge), yielding a gravimetric capacity for the Si compound of 2671±662 mA h g^{-1}. These results are comparable to the findings reported in chapter 5.2.

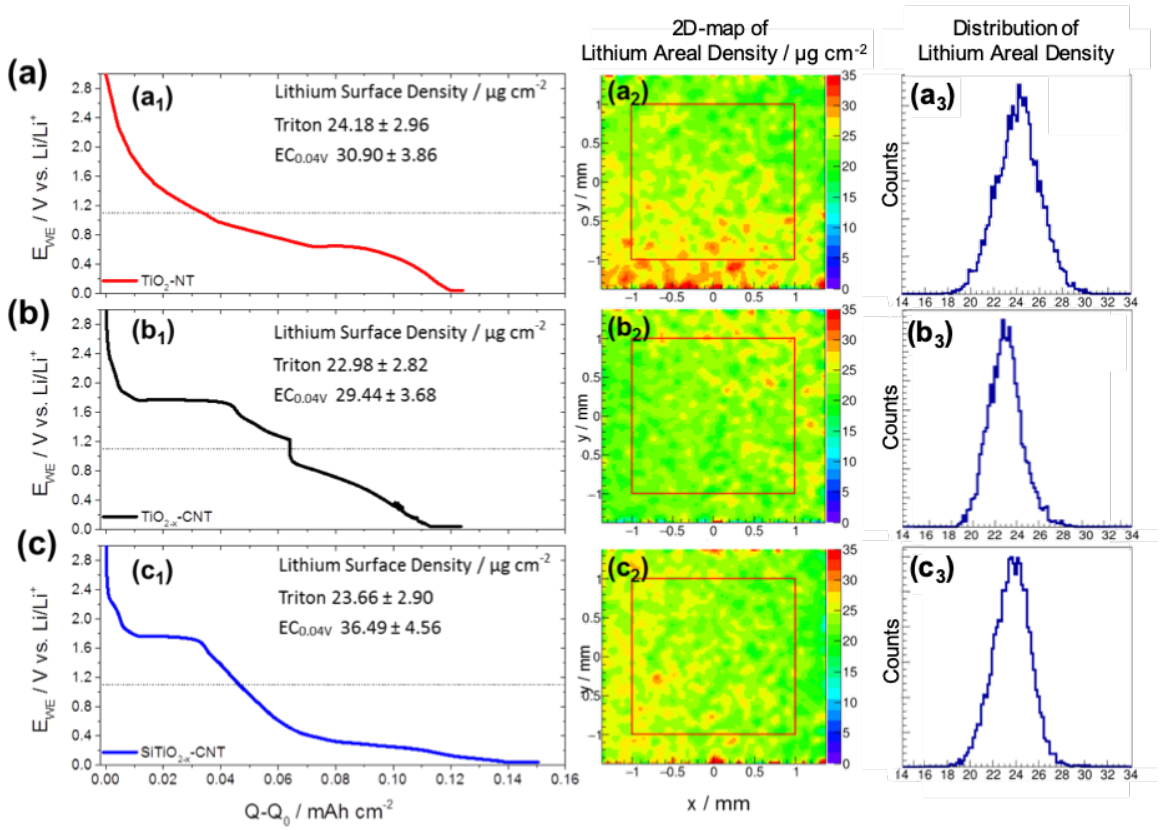

Figure 70 (a) TiO_2 NT, (b) TiO_{2-x}-C NT and (c) $SiTiO_{2-x}$-C NT electrodes. Index subscripts: 1 - galvanostatic lithiation to 40 mV (C/10), followed by potentiostatic lithiation at 40 mV; 2 – reconstructed 2D-map of Li areal density with a color scale in µg cm^{-2} for a 2x2 mm^2 analyzed electrode area; 3 - distribution of Li areal density in µg cm^{-2} for the analyzed area. From [92]

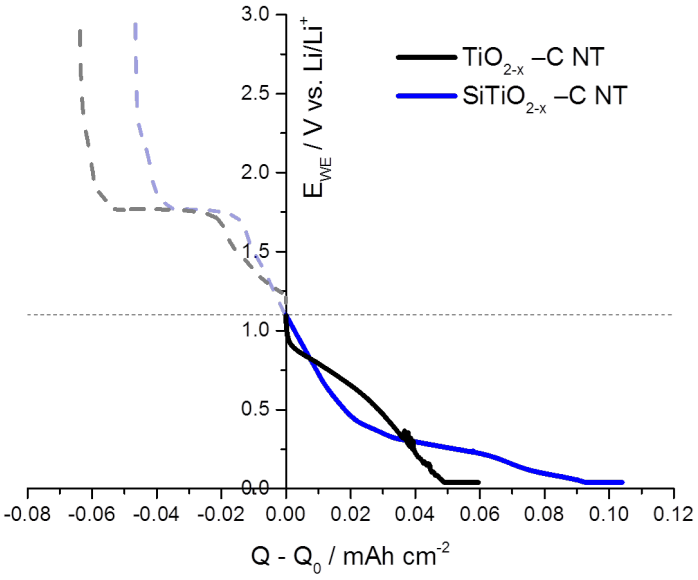

Figure 71 Comparison of TiO_{2-x}–C NT and $SiTiO_{2-x}$–C NT lithiated to 40 mV galvanostatically (C/10) and potentiostatically at 40 mV. In this representation the 0 point for Q-Q_0 has intentionally been set to the point where the voltage drops below 1.1V to highlight the post TiO_2 lithiation characteristics. From [92]

A summary of the Li areal densities (with corresponding error estimation) of all electrodes measured electrochemically and by using small area (2x2 mm^2) triton analysis is displayed in Table 2, wherein the difference in Li areal density from both methods is also calculated and displayed for each sample. As we already saw, the assumption that the whole charge measured electrochemically corresponds to Li stored inside the electrode, is incorrect and even more so in the case of the second batch of electrodes lithiated at 0.04 V where the contribution of surface charge storage, especially in the first lithiation cycle, is significant.

Table 2 Average Li areal density in µg cm^{-2} from triton analysis (2x2 mm^2) and virtual Li areal density from electrochemistry (EC) and their corresponding error estimations. [92]

Structure/ sample	Lithiation potential [$V_{vs.\ Li/Li^+}$]	Areal Li density – triton [$\mu g_{Li}\ cm^{-2}$]	Error [$\mu g_{Li}\ cm^{-2}$]	Areal Li density – EC [$\mu g_{Li}\ cm^{-2}$]	Error [$\mu g_{Li}\ cm^{-2}$]	Areal Li density difference [$\mu g_{Li}\ cm^{-2}$]	x in Li_xTiO_2[a]
TiO_2 NT	1.10	14.18	±1.75	15.80	±1.97	1.62	0.58
TiO_2 NT	0.04	24.18	±2.96	30.90	±3.86	6.72	0.99
TiO_{2-x}–C NT	1.10	12.15	±1.51	11.40	±1.42	0.75	0.50
TiO_{2-x}–C NT	0.04	22.98	±2.82	29.44	±3.68	6.46	0.94
$SiTiO_{2-x}$–C NT	1.10	11.43	±1.42	13.17	±1.65	1.74	0.47
$SiTiO_{2-x}$–C NT	0.04	23.66	±2.90	36.49	±4.56	12.83	0.97

[a] Mole Li per mole TiO_2, calculated from the areal Li density measured by triton analysis and using the average 24.4 $\mu g_{Li}\ cm^{-2}$ as $x = 1$.

Conclusions

The virtual Li concentration from EC and the concentration measured by triton analysis for each electrode is, within the range of error, the same for the electrodes lithiated at 1.1 V. For the electrodes lithiated at 0.04 V however, the difference between the concentrations delivered by the two methods is significant. This can be explained by the increased amount of side reactions on the electrodes at this potential, producing surface layers, which contribute to the electrochemically measured charge but washing away these layers before the triton analysis caries away the charge associated with them. The difference between the EC Li concentration and the concentration measured by the triton analysis for the Si containing electrode at 0.04 V is twice higher compared to the other two electrodes. This behavior can be explained by the very high reactivity of the lithium silicates formed at this low potential, which is leading to an increase in electrolyte decomposition and possibly to loss of lithiated silicon or SiO_2 upon rinsing the electrode with DMC prior to triton analysis.

This work shows that triton analysis is a very powerful tool for mapping very low lithium concentrations (< 10 µg of Li cm^{-2}) on macroscopic electrode areas while directly determining the true content of lithium. The main disadvantage of the method is that it cannot be applied in-situ because the high amount of lithium in the electrolyte would make an examination of the electrode impossible. Furthermore, additional characterization is necessary for distinguishing between lithium inside the active material and lithium on the surface. The analysis performed on nanotubular electrodes revealed regions with significantly higher lithium content (“hot spots”) which were found to correspond in some cases to higher nanotube lengths and in other cases to different properties of the bulk active material of the nanotubes. Comparison of the triton analysis with data gathered electrochemically helps assess the contribution of side reactions, depending on lithiation potential and electrode material, to the charge measured electrochemically. The incites gathered through this study will therefore provide guidance for the design, optimization and upscaling of nanostructured lithium battery electrodes.

5.4 Morphology and structure of nanotubular electrodes from X-ray and neutron scattering

This work was published under the title “GISAXS and TOF-GISANS studies on surface and depth morphology of self-organized TiO_2 nanotube arrays: model anode material for Li-ion batteries” [138].

It has been shown in chapter 5.3 that the morphology of self-organized TiO_2 nanotube arrays used as active material of Li-ion battery electrodes, can vary significantly over the macroscopic area of an electrode. Such variation reduces the accuracy of the estimation of active mass of the electrodes (see chapter 4.4) and leads to differences in lithium density across the area of the electrode. Furthermore, the interpretation of other measurements performed on such an electrode also depends on the assumed morphological model. Classically, the morphology of nanostructured electrodes is studied by scanning electron microscopy (SEM) or transmission electron microscopy (TEM). In order to gather information about the morphology of the studied layers in their depth, cross-sections are prepared, thus destroying the electrode. Furthermore, both methods deliver only a very local information on the morphological parameters, observing electrode areas in the order of 10x10 μm^2 (depending on the dimensions of the structures to be observed). Repeating such measurements over a large number of different areas of the electrode improves the statistical value of the measured parameters. However, covering the whole electrode area is practically impossible and the chance is high that regions of the electrode with a significantly different morphology are not sampled.

Only a few studies have been performed in literature on nanostructured layers, determining morphological parameters with a high statistical relevance, like the grazing-incidence small-angle X-ray scattering (GISAXS) study of carbon nanotubes [139]. Time-of-flight grazing-incidence small-angle neutron scattering (TOF-GISANS) can be employed to investigate the in-depth morphology of porous titania nano-structures [140,141]. In the time-of-flight mode, neutrons with a broad range of wavelengths illuminate the sample, and the scattered neutrons are recorded on a two-dimensional detector as a function of their respective times of flight corresponding to their individual wavelengths. The penetration depth of neutrons decreases with increasing wavelength. Thus, with a single TOF-GISANS measurement, a complete set of GISANS patterns is acquired corresponding to different wavelengths, which allows the simultaneous investigation of lateral nanostructures with a depth sensitivity [82]. Although GISAXS and GISANS deliver the same information about the studied structure, the neutron

scattering method does not bear the risk of any potential radiation damage to the sample, compared to the high-energy synchrotron X-rays used for GISAXS for a comparable resolution. A drawback of both analysis methods however, is that the surface underneath the layer under study needs to be extremely flat. The goal of this study was to obtain morphological parameters of self-organized TiO_2 nanotube arrays (with and without a Si coating) for macroscopic electrode areas with high statistical relevance.

Experimental

TiO_2 nanotube arrays are commonly prepared by anodization of mechanically polished Ti disks or Ti foil. Both substrates, however, do not fulfill the low roughness requirement of the scattering techniques (GISAXS and GISANS) used in this study. Therefore, a 1 µm thick Ti layer, sputter deposited on a silicon wafer, was used as a substrate to grow Type 5 titania nanotubes as described in chapter 4.1.5. These electrodes, however, could not be used in the electrochemical cells for electrochemical characterization. Therefore, for the electrochemical characterization, Type 4 titania nanotubes were grown according to the procedure described in chapter 4.1.4, which was developed such that the resulting nanotubular array was very similar to the one grown on sputter deposited Ti. Both types of electrodes were then subjected to carbo-thermal annealing according to the procedure of chapter 4.2.1. A batch of each type was then coated with Si as described in chapter 4.3.

The electrochemical characterization was performed in the 2nd generation cell described in chapter 4.5.2.2 and the electrolyte had a 2 wt% of a VC additive.

SEM characterization was performed on CrossBeam NVision 40 from Zeiss using an accelerating voltage of 5 and 20 kV and a working distance of 4-6 mm. JMicroVision (Roduit, 2014) software was used to analyze the SEM micrographs with a precision of ±2 nm for a one-dimensional profile measurement. The opening of the nanotubes was elyptical, thus having a large and a small inner diameter. The nanotube inner diameter was therefore defined as the mean value of the measured large and small inner diameter. The crossing point of the large and small nanotube diameters was defined as the center of the nanotube and the intertubular distance was defined as the distance between the centers of two neighboring nanotubes.

XRD and XRR were performed on a Bruker D5000 diffractometer operating at 40 kV/40 mA and the wavelength of Cu Kα.

GISAXS was performed on a Ganesha 300XL small/wide-angle X-ray scattering system (SAXSLAB ApS, Copenhagen, Denemark). The X-ray source was operated at 50 kV/0.6 mA and had the wavelength of Cu Kα (1.5406 Å). The horizontal and vertical beam dimensions were 0.1 and 0.1 mm, with a divergence of 1.0 and 0.1 mrad respectively. The beam-spot on the sample was 15 mm in the beam direction and 0.1 mm across. The intensity of the scattered X-rays was recorded at room temperature and 1.058 m distance from the sample by a two-dimensional position sensitive photon-counting detector Pilatus 300k having a pixel width of 172 µm. The X-rays were directed onto the sample at incident angles of 0.26° and 0.35° depending on the point of interest. The geometry and basics of the GISAXS experiment are described in chapter 3.5.4.2. In order to reduce the penetration depth of the incident beam and reduce the background scattering in the GISAXS and GISANS measurements, an incident angle α_i is used that is close to the critical angle for external reflection α_c, thus a specular peak produced by the reflected beam at $\alpha_f = \alpha_i$ is visible together with the Yoneda peak at $\alpha_f = \alpha_c$.

TOF-GISANS analysis was performed at the REFSANS instrument of the Heinz Maier-Leibnitz Zentrum in Garching, Germany [81]. With the scattering geometry described in chapter 3.5.5.1, the momentum transfer vector Q can be written as:

27 $$Q_x = \frac{2\pi}{\lambda}\left(\cos 2\theta_f \cos\alpha_f - \cos\alpha_i\right),\ Q_y = \frac{2\pi}{\lambda}\left(\sin 2\theta_f \cos\alpha_f\right),\ Q_z = \frac{2\pi}{\lambda}\left(\sin\alpha_f + \sin\alpha_i\right).$$

For each wavelength, each recorded two-dimensional intensity data set corresponds to a (Q_y, Q_z) range. Thus, using a single incident angle and a polychromatic neutron beam with a TOF wavelength resolution, access was gained to several scattering depths/scattering vector (Q_y, Q_z) ranges.

The incident angle α_i was fixed at 0.3°. The sample to detector distance was 10.52 m and the wavelength range for the measurement 0.27-1.00 nm. The neutron beam spot on the sample was 20 mm in the beam direction and 20 mm across. For each data set I(y,z), the corresponding pixel positions were converted to the α_f and $2\theta_f$ angles of the scattered beam or to the corresponding momentum transfer vectors, resulting in an I(α_f, $2\theta_f$) or an I(Q_y, Q_z) data set. Gravity related deviations were corrected for in the analysis. Both type of electrodes (Type 5 nanotubes with and without Si coating) were measured for 24 h to obtain sufficient statistics. The probed depth resulting in the observed scattering, called scattering depth, is calculated as a function of incident angle for a fixed wavelength taking into account the exit angles and the scattering length density of the probed layer [142]. Here it is noted that such depth calculation,

is biased by the 10% wavelength spread of the neutrons. Neglecting the wavelength spread, one can roughly estimate that for wavelengths larger than 0.7 nm, the scattering depth is within the top 100 nm of the probed surface and varies slowly with wavelength allowing a good depth resolution in this region. For shorter wavelengths however, the scattering depth increases dramatically covering the whole film thickness and the depth resolution is practically lost. The maximal size of accessible lateral structures depends both on the maximum Q_y and on the resolution $\delta Q_y/Q_y$ [143]. This, in turn, depends on the wavelength and angular resolution. Thus GISANS measurements at different wavelengths have different resolutions which was accounted for in the analysis.

Results and Discussion

The spectra acquired via GISAXS and GISANS are modeled by an effective interface approximation, wherein the nanotubular array of the examined electrodes is approximated by an array of cylinders being the scattering objects. Such cylinders resemble the hollow cylindrical interior of the nanotubes. The modeled data then gives information on cylinder sizes and the distances between the centers of cylinders of the same kind, as well as the size and distance distributions [144-147]. The model calculates the intensity for a one-dimensional horizontal cut along Q_y at a particular Q_z and the contributions from the cylinders along the Q_z direction (the height of the cylinders) is neglected. For very low Q_y values, the experimental resolution limit of the instrument is considered and is modeled by a Lorentzian-shaped function. The shape of the curve is resolved by the cylindrical form factors, corresponding to the cylindrical scattering objects, the radii of which follow a Gaussian distribution. The peak positions are resolved by the structure factor, which denotes the distances between the centers of cylinders of the same kind and which also follows a Gaussian distribution. A large width of the peaks is a signature of a broad distribution of cylinder sizes and distances in the system. The presence of more than one prominent peak corresponds to the occurrence of different dominant length scales, scattering arrays with different radii and spacings. The size distributions comprise the instrumental resolution as well. In the modeling, a constant background was assumed and adapted to the data in the fitting. It is noted that the cylindrical scattering bodies used for modeling have only their outer interface (cylinder to air) participating in the scattering whereas the nanotubes of the examined electrodes have an inner and an outer interface (titania to air) which are both cylindrical, thus a cylinder from the model can correspond to the inner or the outer cylindrical interface of a nanotube. Furthermore, the pores separating the nanotubes, which are also ordered, can also be represented by cylindrical species from the model.

SEM

Figure 72 shows top view and cross-sectional SEM micrographs of the Type 5 titania nanotubes grown on a Ti coated Si wafer substrate, which were: as grown amorphous TiO_2 NT, bare anatase TiO_{2-x}–C NT and Si coated anatase TiO_{2-x}–C NT ($SiTiO_{2-x}$–C NT). The top view micrographs show a slight increase in surface roughness of the nanotubes after annealing. The cross-sectional micrographs of the TiO NT and $SiTiO_{2-x}$–C NT show the nanotubular arrays detached from the surface of the substrate, whereas in the cross-section of TiO_{2-x}–C NT, the nanotubular array is still attached to the substrate. The three nanotubular arrays have the same nanotube length of 600 nm. The inner diameter of 20 measured bare (no Si coating) nanotubes is ranging from 52 to 80 nm (radius: 26-40 nm) and their wall thickness is 8-13 nm. The nanotubes are found to often merge near the surface of the array, forming larger tubes with a diameter of 110-160 nm (55-80 nm). The intertubular distance (center to center) is 95-130 nm. Similarly, to the Si coated electrodes of chapter 5.2, only the top portion ~150 nm of the $SiTiO_{2-x}$–C NT is coated with Si. After Si coating the nanotubes are still open on the top with a reduced inner tube radius. Their wall thickness is increased to 21-32 nm. Assuming an equal Si film thickness on the inner and outer tube walls, this increase in thickness translates to a Si film thickness of 6-12 nm. The morphology of the nanotubes under the Si coating layer is not changed, thus parameters like the intertubular distance are the same for all three electrode types.

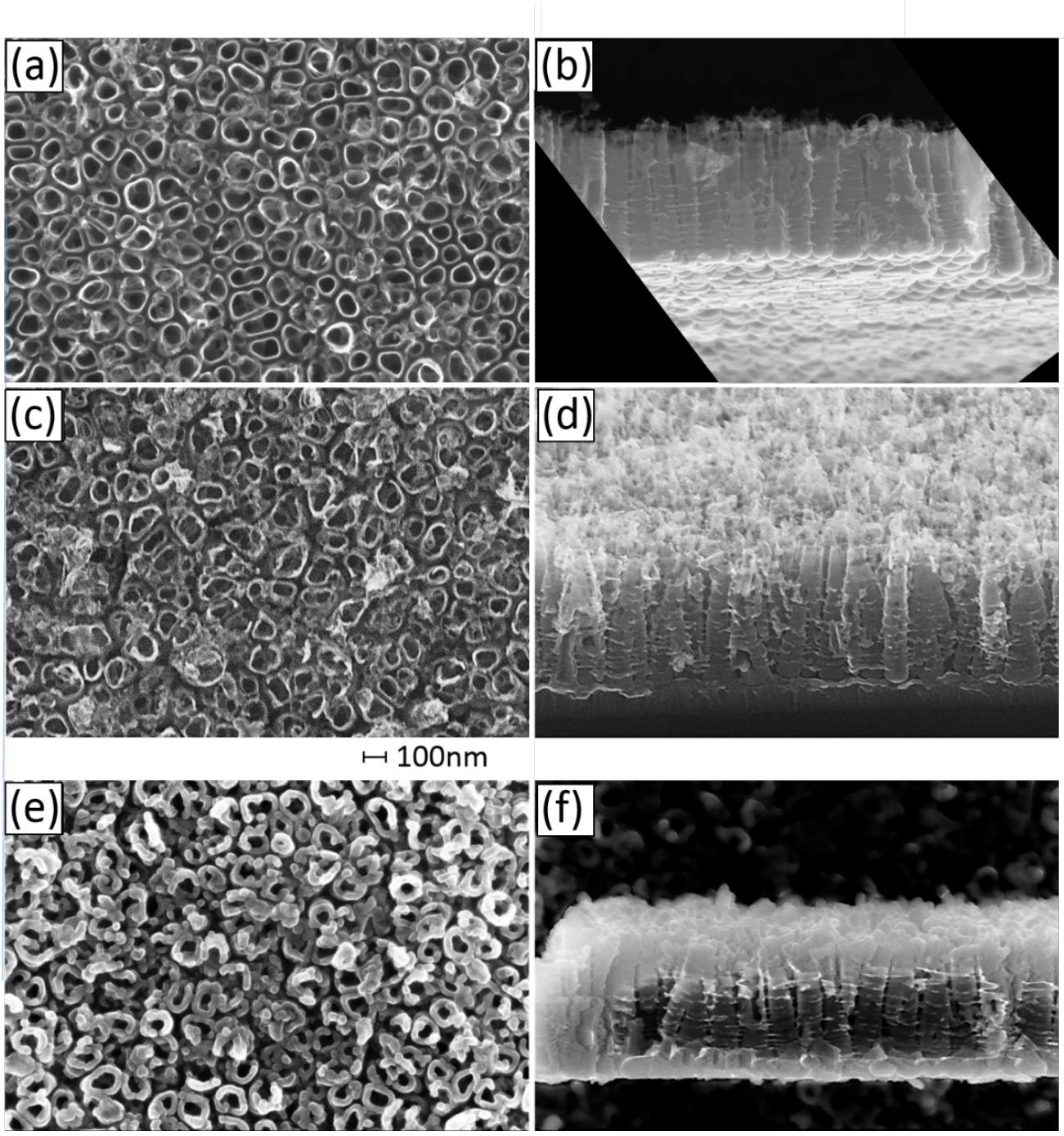

Figure 72 Top view SEM micrographs of (a) TiO_2 NT (c) TiO_{2-x}-C NT and (e) $SiTiO_{2-x}$-C NT; and cross-sections of (b) TiO_2 NT (d) TiO_{2-x}–C NT (f) $SiTiO_{2-x}$–C NT. The nanotubes are grown on a Ti coated Si wafer. The black corners in (b) come from rotating the image such that the nanotube array is horizontal with the openings of the nanotubes facing up. (c)-(f) [138]

XRD

XRD was employed to analyze the crystallographic structure of the nanotubular electrodes. Figure 73 shows the XRD pattern of $SiTiO_{2-x}$–C NT, which is identical to the pattern recorded for TiO_{2-x}–C NT (not shown), both having anatase structure after the carbo-thermal annealing step of electrode preparation. The sputter deposited Ti film on the Si wafer substrate is amorphous. The peaks at 25.3° and 38.0° correspond to the (101) and (004) reflections of anatase (JCPDS card No. 78-2486) whereas the Si peaks marked in the graph are reflections from the Si wafer supporting the nanotubular array.

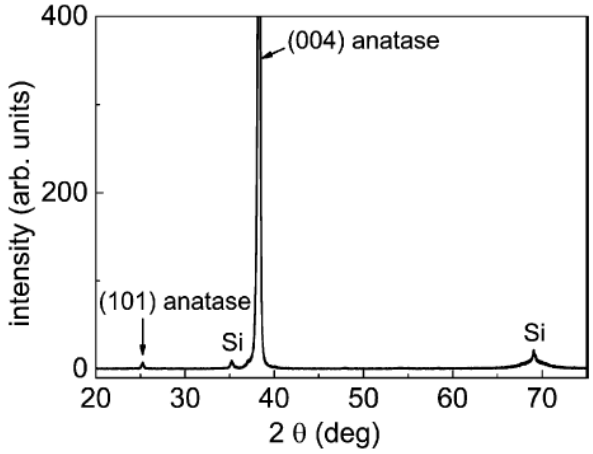

Figure 73 XRD of $SiTiO_{2-x}$–C NT, showing a preferential orientation of the anatase phase. The Si peaks originate from the Si wafer substrate and not from the amorphous Si coating. From [138]

The Si coating in $SiTiO_{2-x}$–C NT is amorphous and thus, has no reflections in the XRD pattern. Comparing the anatase peak intensities in the diffractogram of the nanotubular electrode with those in the diffractogram of a randomly oriented anatase powder, it is evident that in the nanotubular electrode there is an unusually high proportion of (004) anatase planes in the growth direction of the nanotubes. This suggests a preferential growth of the nanotubes along the anatase [001] direction. Such a preferential orientation has recently been shown to impair an enhancement in performance of titania nanotubes as anode material for Li-ion batteries, due to faster interfacial Li insertion/extraction kinetics [30]. With the full width at half maximum B(2θ) of the (004) reflection at 38.0°, the average crystallite size of the anatase phase in the nanotubes is L = 20 nm.

This estimation is made using the Scherrer equation 28, assuming a constant value of the Scherrer constant K of 0.89 and with λ being the used X-ray wavelength of Cu Kα.

Equation 28 $$L = \frac{K\lambda}{B(2\theta)cos\theta}$$

XRR

XRR performed on the TiO_{2-x}–C NT and $SiTiO_{2-x}$–C NT electrodes reveals information on the density variation in direction perpendicular to the electrode surface and the different critical angles for total external reflection for the two materials. The theoretical scattering length densities (SLDs) of compact Ti, compact anatase TiO_2 and compact Si for X-rays are $3.55x10^{-5}$ $Å^{-2}$, $3.07x10^{-5}$ $Å^{-2}$ (for an anatase TiO_2 density of 3.77 g cm^{-3})[148] and $2.0x10^{-5}$ $Å^{-2}$, respectively. According to equation 29 these values correspond to critical angles (α_c) of 0.296, 0.275 and 0.222.

Equation 29 $$\alpha_c = \lambda\left(\frac{SLD}{\pi}\right)^{\frac{1}{2}}$$

Figure 74 shows the XRR spectra of TiO_{2-x}–C NT and $SiTiO_{2-x}$–C NT. The critical angle for total reflection α_c for the TiO_{2-x}–C NT electrode (black curve) is observed at 0.27° as a high intensity peak. In the spectrum of the $SiTiO_{2-x}$–C NT electrode (red), two peaks are observed, particularly well visible in the inset of Figure 74, at 0.18° and 0.27°. Porous materials have a lower bulk density than their in compact form. Therefore, their SLD, which is proportional to the density, is lower and consequently also the corresponding critical angle (see equation 29). The low angle peak 0.18° in the case of $SiTiO_{2-x}$–C NT can thus be attributed to porous Si with a porosity of ~35% (see equation 31). Increasing the incident angle above the critical angle for total reflection, the reflections from the different interfaces interfere, giving rise to interference fringes called Kiessing fringes. The period between these fringes (δQ_z) depends on the film thickness (t). Therefore, applying equation 30, the film thickness (t) can be calculated.

Equation 30 $$t = \frac{2\pi}{\delta Q_z}$$

The nanotubular arrays of the electrodes represent layers with a very high roughness, which is known to drastically reduce the Fresnel reflectivity of a layer and smear out the electronic density profile. The reflectivity pattern of TiO_{2-x}–C NT shows very weak Kiessing fringes, with a

slightly varying periodicity, corresponding to a film thickness of 7 (±2) nm, which can be attributed to a thin rutile layer formed upon annealing between the Ti substrate and the bottom surface of the nanotubes [37]. This layer might have a varying thickness along the sample plane, which could cause the observed variation in periodicity of the Kiessing fringes. The reflectivity pattern of $SiTiO_{2-x}$–C NT shows distinct Kiessing fringes corresponding to a reflecting layer thickness of 14 (±1) nm. A similar layer thickness was calculated, from the thickening of the walls of the nanotubes after Si deposition for the $SiTiO_{2-x}$–C NT electrodes observed by SEM, for the deposited Si layer. The Parratt recursion method [66] could not be employed for fitting of these spectra since the Nevot-Croce approximation is invalid for such films having a roughness comparable to their thickness.

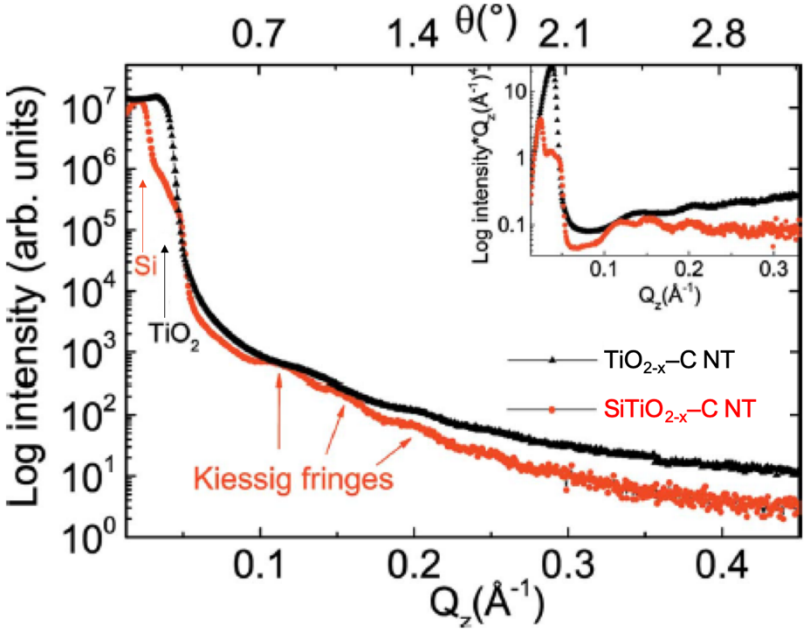

Figure 74 XRR spectra of TiO_{2-x}–C NT (black) and $SiTiO_{2-x}$–C NT (red). Vertical arrows indicate the positions of the critical angles of total external reflection of porous Si and porous TiO_2. Inset: normalized spectra with enhanced Kiessig fringes. [138]

GISAXS

GISAXS is performed to probe the surface morphology over the entire electrode surface and within the volume of the nanotubular arrays, delivering statistically averaged values for the inner tube radius and inter-tubular distance, as well as mean porosity values. Changes in morphology in the plane of the surface film and in direction perpendicular to the surface are followed by comparing the two dimensional spectra of the compact Ti film on the Si wafer before the nanotube formation, the TiO_{2-x}–C NT electrode, and the $SiTiO_{2-x}$–C NT electrode formed by coating the TiO_{2-x}–C NT electrode with Si.

Figure 75 displays the GISAXS patterns with corresponding vertical cuts for the compact Ti substrate, before nanotubes are formed, which however has a 2-3 nm thick surface oxide, and TiO_{2-x}–C NT. The TiO_{2-x}–C NT sample shows a higher scattering intensity. The incident angle for both measurements is fixed at 0.35°, which is above the critical angle for total reflection for compact Ti (0.296°) and compact anatase TiO_2 (0.275°) and consequently also higher than the critical angle of porous Ti or porous TiO_2 [140,149]. Therefore, beside the specular peak, the material specific Yoneda peaks of the different materials are also visible with positions corresponding to the respective critical angles of total reflection. The Yoneda peak of the compact Ti film at Q_z = 0.45 nm^{-1} corresponds to an SLD_{expt} value of $3.2x10^{-5}$ $Å^{-2}$ and thus to a critical angle of 0.28° (see equations 27 and 29). The same compact Ti peak is also visible in the TiO_{2-x}–C NT corresponding to a film of Ti, which was not consumed in the nanotube formation, between the Si substrate and the nanotubes. The Yoneda peak of TiO_2 in TiO_{2-x}–C NT is found at 0.39 nm^{-1} corresponding to an SLD_{expt} value of $1.6x10^{-5}$ $Å^{-2}$ and thus to a critical angle of 0.20°. The porosity P of the examined films can be calculated from the reduction in SLD compared to the theoretical values for the bulk materials using equation 31, wherein SLD_{expt} is the experimentally obtained SLD and SLD_{th} is the corresponding theoretical value for the bulk material [140,141]. With the measured values, the porosity of the compact Ti film on the Si wafer is 10% and the porosity of anatase TiO_2 in TiO_{2-x}–C NT is 49%.

Equation 31 $$P = 1 - \left(\frac{SLD_{expt}}{SLD_{th}}\right)$$

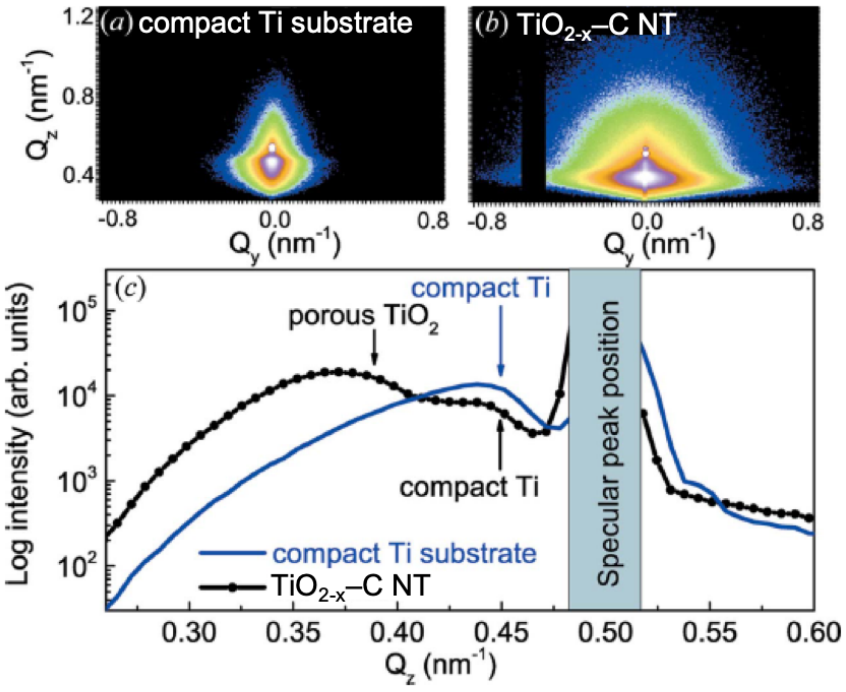

Figure 75 Two dimensional GISAXS pattern of (a) 1 µm thick compact Ti film with a 2-3 nm thick surface oxide on a Si wafer and (b) TiO_{2-x}–C NT. (c) Vertical line cuts along Q_z of both 2D spectra at $Q_y = 0$. The incident angle is 0.35°, which is above the critical angles of the materials, thus material specific Yoneda peaks are observed having a different position for each material. From [138]

In order to shift the sensitivity of the measurement from the substrate towards the nanotubular array and resolve the nanotubular structure, the incident angle was reduced to 0.26°. Moving the incident angle down from 0.35° to 0.26°, the Yoneda peak of TiO_{2-x}–C NT (porous TiO_2), which depends on the incident angle (see Equation 27 for Q_z with $\alpha_f = \alpha_c$) moves up from 0.20° toward the specular peak and reaches it at 0.26°. At this position, the scattering intensity for TiO_{2-x}–C NT (porous TiO_2) is maximal. This incident angle is below the critical angles of bulk Ti and bulk TiO_2, and above the critical angles of compact and porous Si. Figure 76 shows the 2D GISAXS spectra of TiO_{2-x}–C NT and $SiTiO_{2-x}$–C NT, and the horizontal cuts at the height of the specular peak $Q_z = 0.37$ nm^{-1} (0.26°) coinciding with the Yoneda peak of the TiO_{2-x}–C NT (porous TiO_2). In both spectra, side peaks are clearly visible (indicated with arrows) at the height of the specular peak (coinciding with the Yoneda peak of the TiO_{2-x}–C NT) indicating a well-defined lateral structure of the porous TiO_2. The two horizontal cuts are fitted with a model comprising the form and structure factors of two different cylinder species (I and II) as scattering objects distributed over a one dimensional paracrystal. The form factors set the cylindrical shape with the two radii, whereas the structure factors denote the periodical spacing between cylinders of the same kind. The model returns for TiO_{2-x}–C NT a cylinder radius (inner tube radius) of 50 (±7) nm and a spacing (intertubular distance) of 95 (±6) nm for the first type of

cylinders (I), and 7 (±3) nm and 42 (±6) nm radius and spacing, respectively, for the second type of cylinders (II). The peak corresponding to the first type of structure (I) is more prominent indicating a higher share of this structure on the surface. The fit of the horizontal cut of the $SiTiO_{2-x}$–C NT pattern, with the same underlying model, returns the same spacings between the first and second cylinder species as in TiO_{2-x}–C NT, and the same radius of the second type of cylinders. However, the radius of the first type of cylinders is reduced to 29 (±7) nm corresponding to the reduction in inner tube radius for $SiTiO_{2-x}$–C NT after the coating with Si.

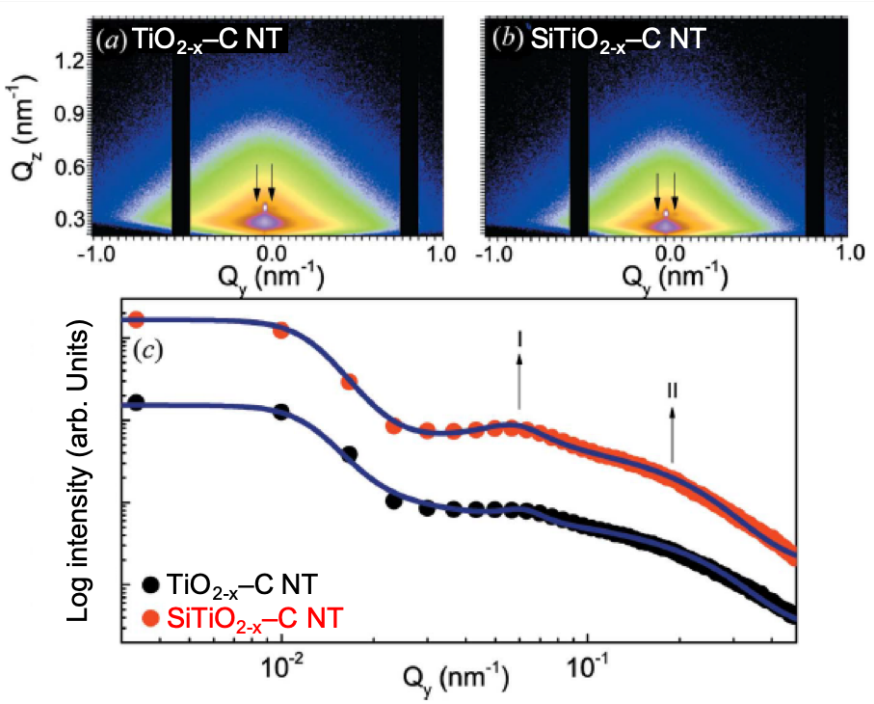

Figure 76 Two dimensional GISAXS pattern of (a) TiO_{2-x}–C NT and (b) $SiTiO_{2-x}$–C NT. The arrows point at the prominent side peaks corresponding to a well-defined lateral structure. (c) Horizontal line cuts along Q_y of both 2D spectra at the position of the specular peak $Q_z = 0.37\ nm^{-1}$ overlapping with the Yoneda peak of TiO_{2-x}–C NT and corresponding fits (blue line). One of the cuts is shifted upwards for clarity. The incident angle is 0.26°, which is below the critical angle of compact Ti and compact TiO_2 and above the critical angles of compact, and porous Si. From [138]

TOF-GISANS

In order to analyze the morphology of the nanotubular arrays with depth sensitivity, TOF-GISANS is performed on TiO_{2-x}–C NT and $SiTiO_{2-x}$–C NT at a fixed incidence angle of 0.3°. Figure 77 displays the two-dimensional GISANS patterns for different neutron wavelengths, increasing from bottom to top, extracted from the TOF-GISANS measurements on TiO_{2-x}–C NT and $SiTiO_{2-x}$–C NT. Low wavelengths probe high depths covering the whole layer thickness, whereas high wavelengths are only sensitive to the surface of the layer.

The 2D images show neutrons which are reflected and scattered in the half-plane above the probed surface as well as neutrons which are transmitted through the stack of titania nanotubes, titanium metal and Si wafer. The intense beam that is directly transmitted is blocked by a rectangular beam-stop to avoid oversaturation of the detector and the remaining signals from the transmitted neutrons are not used in the analysis. At lower wavelengths, the wavelength dependent Yoneda peak is visible along with the specular peak. In contrast to the Yoned peak, the position of the specular peak marking the position of the reflected beam, does not dependent on wavelength but only on the incident angle. As the wavelength increases, the Yoneda peak moves towards the specular peak, until the two peaks overlap. With increasing wavelength the contribution from the nanotubular layer increases and diffuse scattering at the height of the Yoneda peak becomes increasingly visible as a horizontal spread of the signal, indicating a well-defined lateral structure. The diffuse scattering signal becomes significant at neutron wavelengths of 0.45 nm for TiO_{2-x}–C NT and 0.55 nm for $SiTiO_{2-x}$–C NT.

This difference indicates that Si deposition introduces some structural inhomogeneities in the lateral structures of the film layer below the Si-coated upper portion. At low wavelengths, the relative intensity of the signal originating from the nanotubes is low. Furthermore, as can be seen in the SEM micrographs of Figure 72, the diameter of the nanotubes increases from top to bottom and their sidewalls have a significant surface roughness. Both effects reduce the degree of order in the structure. In other words, the parameters of the scattering objects, which are averaged over the probed layer thickness, have a larger spread with increasing probed depth. The neutrons are transmitted through the sample at all wavelengths, thus always probing the whole thickness of the sample.

Increasing the probed depth therefore means, increasing the relative contribution of the lower portion of the nanotubes with respect to their upper parts and decreasing the total contribution of the nanotubes with respect to the substrate, which reduces the intensity of the diffuse scattering. Therefore, at low wavelength, the diffuse scattering from the nanotubular arrays is not observed. The diffuse scattering along Q_y, at the Q_z height of the Yoneda peak, originates from the material causing the Yoneda peak, and carries information about the lateral structure of the material. Figure 78 shows horizontal cuts of the 2D patterns of Figure 77 along Q_y, at the Q_z height of the Yoneda peak for each wavelength for TiO_{2-x}–C NT and $SiTiO_{2-x}$–C NT. The results are fitted using the same model as the one used to fit the GISAXS data with an additional larger cylindrical species (III) added to fit the data at the low Q_y values accessible with GISANS, which are outside the range of GISAXS. The parameters of the structures delivered by the model for TiO_{2-x}–C NT and $SiTiO_{2-x}$–C NT are presented in Table 3. Species I represents the most prominent structure followed by species II and III. As expected the spacing between the cylindrical species does not change after Si deposition since the positions of their centers is set by the nanotubes and is independent of the wall thickness. In contrast, the radius of all three cylindrical species is reduced after Si deposition. This means that the cylinders used to simulate the scattering behavior of the nanotubes most probably correspond to the cylindrical void of the nanotubes and possibly to the narrow voids between the nanotubes but not to the cylindrical outer-surface of the nanotubes which is widening upon silicon deposition and not shrinking. The large scattering species III most likely correspond to large nanotube pores formed by merging of two or three nanotubes as observed by SEM (see Figure 72).

Table 3 Results from fitting the TiO_{2-x}–C NT and $SiTiO_{2-x}$–C NT spectra of Figure 78 using a model comprising three types of cylindrical species (I, II and III) with their corresponding radii and center to center spacing. Species I being the most prominent followed by II and III.

species	I		II		III	
	radius [nm]	spacing [nm]	radius [nm]	spacing [nm]	radius [nm]	spacing [nm]
TiO_{2-x}–C NT	45 (±5)	94 (±6)	8 (±2)	38 (±3)	60 (±10)	210 (±30)
$SiTiO_{2-x}$–C NT	23 (±3)	94 (±6)	6 (±2)	38 (±3)	55 (±10)	210 (±30)

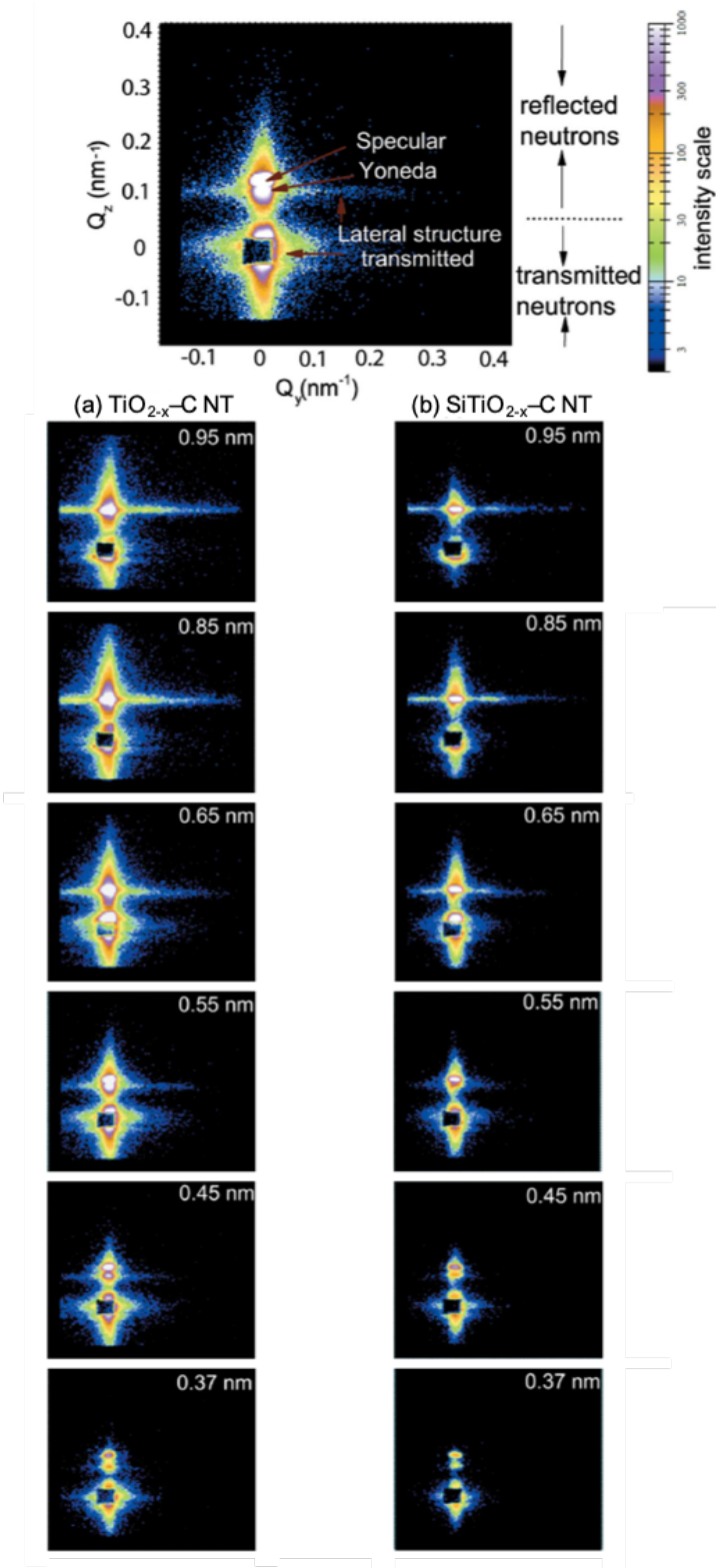

Figure 77 Top: representative two-dimensional GISANS pattern with arrows indicating the different features and a color scale indicating measured intensity. Bottom: selected two-dimensional GISANS patterns extracted from TOF-GISANS for different wavelengths indicated in each 2D image for (a) TiO_{2-x}–C NT and (b) $SiTiO_{2-x}$–C NT. From [138]

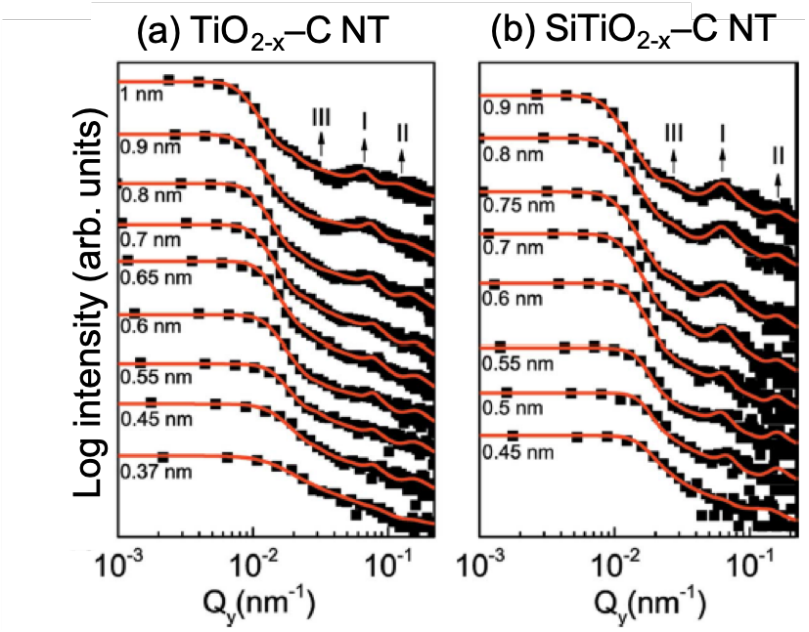

Figure 78 Horizontal cuts of the 2D patterns of Figure 77 along Q_y, at the Q_z height of the Yoneda peak for each wavelength for (a) TiO_{2-x}–C NT and (b) $SiTiO_{2-x}$–C NT. Red lines show fitted curves with peaks indicating the three types of structures used for modeling. The curves are shifted vertically for clarity. From [138]

As discussed above, the material specific Yoneda peak marks the critical angle for total reflection of the material, which is a function of the SLD and the wavelength (see Equation 29). TOF-GISANS provides the position of the Yoneda peak (the critical angle) for various wavelengths. By plotting the critical angle versus the corresponding wavelength, which have a linear dependence, the SLD of the material can be obtained from the slope of the linear fit. With the SLD and Equation 31, the porosity of the material can be calculated.

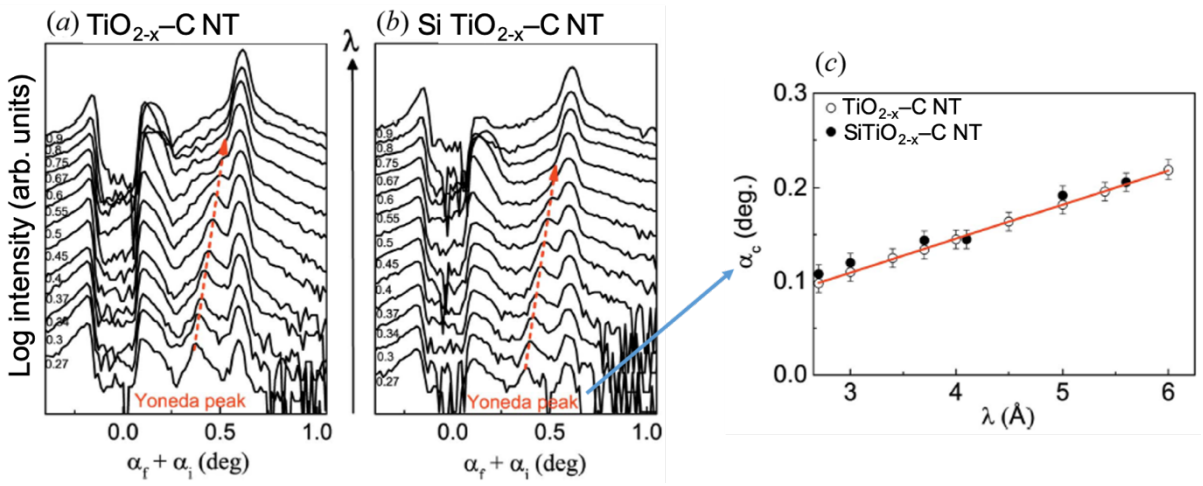

Figure 79 Vertical line cuts along Q_z at Q_y =0 of 2D GISANS patterns of (a) TiO_{2-x}–C NT and (b) $SiTiO_{2-x}$–C NT for different neutron wavelengths increasing from 0.27 nm (bottom) to 0.9 nm (top). The curves are shifted vertically for clarity and the position of the Yoneda peak is marked. The origin of the horizontal axis is set at the position of the transmitted beam and the Q_z values are transformed in exit angles according to equation 27. (c) Yoneda peak positions in terms of critical angle versus neutron wavelength extracted from vertical line cuts along Q_z at Q_y =0 of 2D GISANS patterns of TiO_{2-x}–C NT (hollow circles) and $SiTiO_{2-x}$–C NT (filled circles). [138]

Figure 79 shows vertical line cuts along Q_z at Q_y =0 of 2D GISANS patterns, as the ones displayed in Figure 77, of TiO_{2-x}–C NT and $SiTiO_{2-x}$–C NT for different neutron wavelengths. These cuts represent the changes in structure, in direction perpendicular to the film surface, averaged over different film depths. With increasing wavelength, the Yoneda peak is moving towards the specular peak, as described above, until the two peaks overlap at a wavelength around 0.67 nm. The positions of the Yoneda peak in terms of critical angle for the different wavelengths is plotted against wavelength for TiO_{2-x}–C NT and $SiTiO_{2-x}$–C NT. Both electrode materials exhibit, in the range of error, the same SLD_{expt} value of 1.26×10^{-6} Å^{-2}, calculated from the slope of the linear fit in Figure 79c. Using the theoretical value of SLD_{th} = 2.34×10^{-6} Å^{-2} for the neutron SLD of compact anatase TiO_2 and equation 31, the porosity of the TiO_{2-x}–C NT and $SiTiO_{2-x}$–C NT arrays is P = 46%. The Si coating in $SiTiO_{2-x}$–C NT is restricted to the top ~150 nm of the nanotube array, whereas the SLD calculated from the linear fit is averaged over the entire depth of the array. This explains why the porosity of the two materials, TiO_{2-x}–C NT and $SiTiO_{2-x}$–C NT, appears equal, in the range of error.

The nanotubular electrodes grown on Ti disks (Type 4, see chapter 4.1.4) TiO_{2-x}–C NT and $SiTiO_{2-x}$–C NT were tested in terms of their electrochemical performance as Li-ion anodes. Their morphological parameters examined by SEM and described above, were very similar to those of the electrodes examined via XRR, GISAXS and TOF-GISANS.

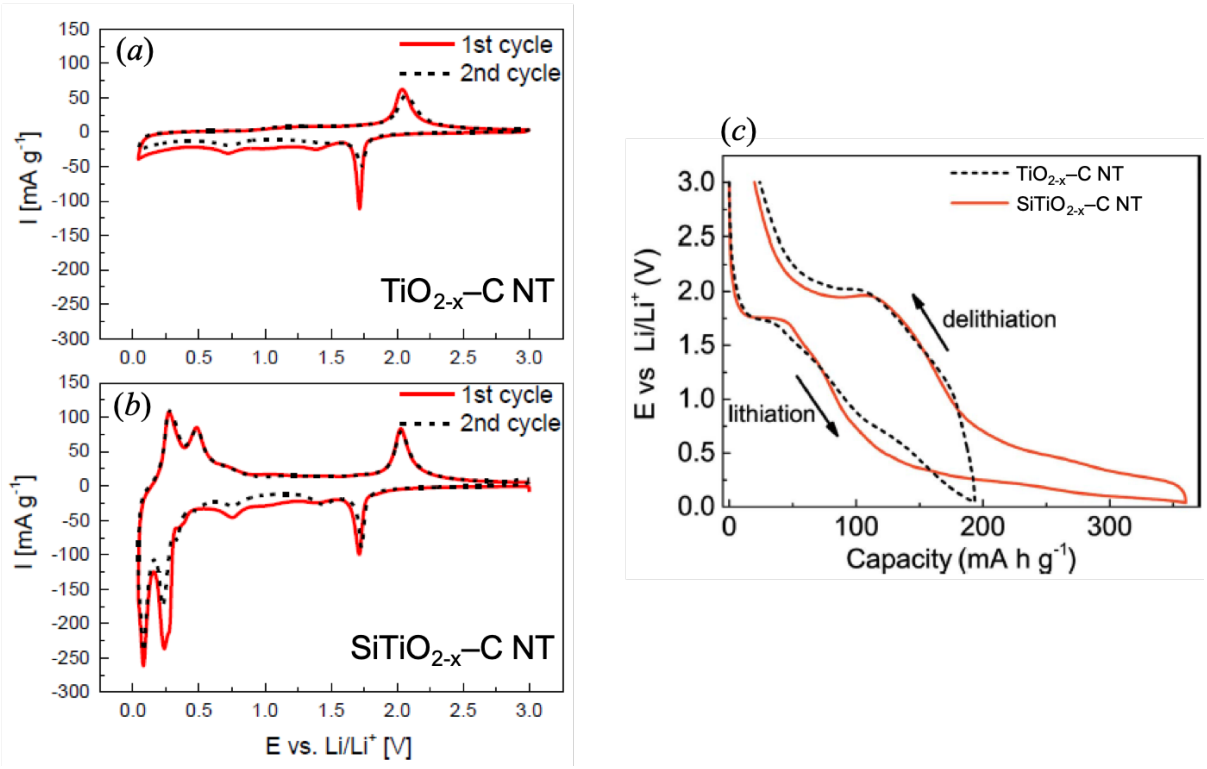

Figure 80 First (solid red line) and second (broken black line) cycle CV of (a) TiO_{2-x}–C NT and (b) $SiTiO_{2-x}$–C NT performed at 0.05 mV s^{-1}. (c) First cycle GCPL after two CV cycles of TiO_{2-x}–C NT (broken black line) and $SiTiO_{2-x}$–C NT (solid red line) at a constant current of 11.2 µA cm^{-2} (51 mA h g^{-1}). From [138]

Figure 80 shows the first two CV cycles and one galvanostatic cycle performed on TiO_{2-x}–C NT and $SiTiO_{2-x}$–C NT in the potential window 0.04-3 V. The two electrodes show the same behavior as the similar electrodes described in chapter 5.2 with the characteristic features for anatase TiO_2 and amorphous Si. The horizontal axis of Figure 80c displays the gravimetric specific capacity of the electrodes for lithium storage using the active mass of the electrodes calculated according to the method described in chapter 4.4 with the morphological parameters determined from SEM analysis. The TiO_{2-x}–C NT electrode has a specific gravimetric capacity of 194 mA h g^{-1} whereas $SiTiO_{2-x}$–C NT shows a capacity of 360 mA h g^{-1}, thus 166 mA h g^{-1} can be contributed to the Si coating.

Conclusions

SEM, XRD, XRR, GISAXS and TOF-GISANS were employed to determine the average morphological and structural parameters of titania nanotube arrays before and after coating the surface of the nanotubes with a thin layer of silicon. The local morphology of the nanotubes was observed directly in top view and cross-sections. With GISAXS the probed area is expanded to nearly the whole sample size (~2 cm) in beam direction and 0.1 mm across. TOF-GISANS covers the whole sample area while probing different scattering depths corresponding to the different wavelengths of the used neutrons. The most prominent intertubular distance (center to center) is found to be ~94 nm for both bare and silicon coated nanotubes, whereas the most prominent inner radius shrinks from 46 nm for bare nanotubes to 23 nm for silicon coated nanotubes. The porosity of the nanotubular arrays averaged over the entire film volume determined by TOF-GISANS is 46%. XRD revealed a preferential crystallographic orientation of the nanotubes such that their growth direction is along the anatase [001] direction. This orientation is shown in other studies on anatase nanotubes to be advantageous for lithiation/delithiation of the material. In the composite electrodes the contributions of silicon and anatase to the total lithium storage capacity are estimated to be 166 mA h g^{-1} and 194 mA h g^{-1}, respectively.

6 Summary and Conclusions

Self-organized TiO_2 nanotubular arrays (TiO_2 NT) have been grown electrochemically on Ti metal with different morphology parameters according to the requirements of the different studies, wherein nanotube lengths were in the order of 1 µm, tube diameters in the order of 80 nm and wall-thicknesses in the order of 10 nm. The arrays had a porosity in the order of 40%, a surface area of 30 $m^2\ g^{-1}$ and mass in the order of 140 µg for an electrode area of 50 mm^2.

Carbon modified anatase TiO_2 nanotubular arrays (TiO_{2-x} -C NT) have been synthesized *via* a carbothermal treatment of the TiO_2 NT in a gas flow reactor using acetylene as a carbon source. Anatase TiO_2 nanotubular arrays (TiO_{2-x} NT) have been produced using the same thermal treatment but without the addition of a carbon source.

Si coated TiO_{2-x} -C NT ($SiTiO_{2-x}$ -C NT) composite electrodes have been synthesized by the deposition of a thin (~10 nm) Si layer on the upper portion (upper ~140 nm) of the walls of the nanotubes of TiO_{2-x} -C NT.

In a first study, TiO_{2-x} NT and TiO_{2-x} -C NT electrodes were characterized using microscopic, (micro-)spectroscopic and diffractometric analysis tools (SEM, XPS, GID), and their Li insertion properties were examined electrochemically (CV, GCPL) in the potential window from 3 to 1.1 V vs. Li/Li^+.

In a second study TiO_{2-x} -C NT and $SiTiO_{2-x}$ -C NT electrodes were characterized and compared using SEM, XPS and EDX, wherein the electrochemical characterization (CV and GCPL) was carried out in an electrolyte with and without vinylene carbonate (VC) additive in the potential windows from 3 to 1.1 V vs. Li/Li^+ and from 0.04 to 3 V vs. Li/Li^+ .

In a third study, the neutron capture reaction of ^6Li, producing a triton and an α -particle ($^6Li(n,\alpha)^3H$), was used to measure and trace the Li areal concentration on the macroscopic two-dimensional surface of lithiated TiO_{2-x} -C NT and $SiTiO_{2-x}$ -C NT electrodes, producing two-dimensional Li areal concentration maps.

In a fourth study, grazing-incidence X-ray- and neutron-small-angle-scattering techniques (GISAXS and TOF-GISANS) were used to gain information on morphological parameters of the nanotubular arrays of TiO_{2-x} -C NT and $SiTiO_{2-x}$ -C NT electrodes with high statistical relevance over macroscopic electrode areas (15 mm x 0.1 mm for GISAXS and 20 mm x 20 mm for TOF-GISANS).

The four studies provided the following core insights:

1. Both TiO_{2-x} NT and TiO_{2-x} -C NT have the anatase TiO_2 structure wherein TiO_{2-x} -C NT electrodes have a superior lithium storage capacity of 320(±68) mA h g^{-1} compared to 180(±38) mA h g^{-1} for TiO_{2-x} NT at a cycling rate of 0.3C. At a cycling rate of 6C, TiO_{2-x} -C NT shows a capacity of 162(±35) mA h g^{-1} compared to 64(±14) mA h g^{-1} for the argon annealed nanotubes (TiO_{2-x} NT). TiO_{2-x} NT and TiO_{2-x}–C NT electrodes show 76% and 97% capacity retention (between the 2^{nd} and 110^{th} cycle), respectively. The superior lithium storage capacity and cycling stability of TiO_{2-x} -C NT is attributed to an enhanced bulk conductivity due to oxygen vacancies, enhanced surface electronic conductivity through a carbon layer formed on the surface and stabilization of the reduced titania bulk through the addition of carbon all together resulting in an improved overall (for Li^+ and e^-) conductivity.

2. $SiTiO_{2-x}$ -C NT composite electrodes have a superior lithium storage capacity of 556 mA h g^{-1}; compared to 273 mA h g^{-1} for TiO_{2-x} -C NT electrodes when lithiated down to 0.04 vs. Li/Li^+, wherein a VC additive in the electrolyte is essential for the cycling stability of the Si containing composite electrodes. 93% of the delithiation capacity of the $SiTiO_{2-x}$-C NT electrode in the VC containing electrolyte are retained after 30 cycles, whereas only 32% capacity are retained after 20 cycles in electrolyte without VC. This difference is attributed to the formation of a stable SEI in the presence of VC that prevents the disintegration of the active material. The high utilization of the two active materials Si and TiO_{2-x} -C in the composite electrodes are attributed mainly to the good conductivity of TiO_{2-x} -C and to the low thicknesses of the Si layer and the walls of the nanotubes.

3. The Li mapping method based on the $^{6}Li(n,\alpha)^{3}H$ reaction is a powerful tool for studying lithiated electrodes. A weakness of the method is that it cannot be used *in situ* due to the high concentration of Li in the electrolyte of a Li-ion cell. The Li concentrations in the electrodes were comparable (~10% difference) to the concentrations calculated from stored charge measured electrochemically for lithiation down to 1.1 V vs. Li/Li^{+}, but they were significantly lower (22-35% lower) for lithiation down to 0.04 V vs. Li/Li^{+}. This is attributed to the accumulation of charge on the surface of the electrodes at the low potential, which is washed away in the preparation steps for the subsequent triton analysis. The surface concentration maps of Li on the TiO_{2-x} -C NT and $SiTiO_{2-x}$ -C NT electrodes showed "hot spots" on the surfaces with a higher concentration (~1.6 times higher than the average) of Li, wherein some of them were found to originate from higher lengths of the nanotubes in these areas while others could not be associated with morphological differences or surface effects and were thus attributed to differing bulk properties of the active material.

4. The grazing-incidence small-angle-scattering techniques can only be used to characterize electrodes with a nanostructured active material when the surface-roughness of the carrier substrate is very low. Therefore, Ti coated Si wafer was used as a substrate for growing the nanotubular arrays instead of the polished Ti discs used in the other studies, and a slightly altered nanotube growth procedure. Surprisingly, the nanotubes were found to have a preferential crystallographic orientation such that their growth direction is along the anatase [001] direction, which was not observed for the arrays grown on Ti disk substrates. The GISAXS and TOF-GISANS experiments delivered the sizes and specific spacings of the most prominent scattering structures in the nanotubular electrodes with a high statistical relevance for macroscopic electrode areas. Mean values of macroscopic parameters like porosity, scattering length density and critical angle of total external reflection for X-rays and neutrons were determined averaging over macroscopic electrode areas and the full nanotubular layer depth.

   The most prominent intertubular distance (center to center) for the nanotubular arrays of the studied electrodes is found to be ~94 nm for both bare and silicon coated nanotubes, whereas the most prominent inner radius shrinks from 46 nm for bare nanotubes to 23 nm for silicon coated nanotubes. The porosity of the nanotubular arrays of both types of electrodes averaged over the entire film volume determined by TOF-GISANS is 46%. In the case of low mass per area electrodes, like in this study, the

porosity received from such scattering experiments can be used for a better estimation of the active mass of the electrodes, which is crucial for comparing the electrochemical performance of such electrodes with the state of the art and for estimating which lithiated phases are present in the material at different states of charge. The morphological parameters of the scattering structures can be used to spot changes in the active material after different manipulations, between its lithiated and delithiated state, or after prolonged cycling. Furthermore, these also allow a quick comparison between samples of the same kind and the determination of a standard deviation.

The focus of this work was set on the synthesis of an anode material for Li-ion batteries based on a well-organized nanostructured composite of two active materials and the extensive characterization of these materials applying electrochemical as well as physical and physical-chemical methods. Some of the utilized techniques are commonly applied in the field of battery research but rarely under constraints such as the ones imposed by the specific nanostructured electrodes prepared in this work. Other, less trivial analytic approaches were used on such battery-relevant materials for the first time giving valuable insights on their applicability under different conditions, and on the additional information that can be gained. The volume and active mass of the electrode materials synthesized in this work was very low compared to classical powder based battery electrodes. This made it necessary to design appropriate electrochemical cells, and to adapt all analysis techniques by carefully considering background effects and different sources of error.

The different properties of the samples were examined by overlapping techniques to further increase the certainty of the measured parameters. The large variety of applied analysis methods improved the understanding of the processes in the studied materials and also showed the limitations of the different techniques. This knowledge is essential for making a well-informed choice of analysis techniques in future studies on materials imposing similar challenges.

7 References

[1] F. T. Wagner, B. Lakshmanan, and M. F. Mathias, “Electrochemistry and the Future of the Automobile,” *J. Phys. Chem. Lett.*, vol. 1, no. 14, pp. 2204–2219, Jul. 2010, doi: 10.1021/jz100553m.

[2] P. Van den Bossche, F. Vergels, J. Van Mierlo, J. Matheys, and W. Van Autenboer, “SUBAT: An assessment of sustainable battery technology,” *J. Power Sources*, vol. 162, no. 2, pp. 913–919, Nov. 2006, doi: 10.1016/j.jpowsour.2005.07.039.

[3] J.-M. Tarascon and M. Armand, “Issues and challenges facing rechargeable lithium batteries,” *Nature*, vol. 414, no. 6861, pp. 359–367, Nov. 2001, [Online]. Available: http://dx.doi.org/10.1038/35104644.

[4] A. Auer and J. Kunze-Liebhäuser, “Recent progress in understanding ion storage in self-organized anodic TiO2 nanotubes,” *Small Methods*, vol. 3, no. 8, 2019, doi: 10.1002/smtd.201800385.

[5] S. Evers and L. F. Nazar, “New Approaches for High Energy Density Lithium - Sulfur Battery Cathodes,” *Acc. Chem. Res.*, vol. 46, no. 5, pp. 1135–1143, 2013.

[6] M. Cuisinier *et al.*, “Sulfur Speciation in Li–S Batteries Determined by Operando X-ray Absorption Spectroscopy,” *J. Phys. Chem. Lett.*, vol. 4, no. 19, pp. 3227–3232, Oct. 2013, doi: 10.1021/jz401763d.

[7] C. Barchasz, F. Molton, C. Duboc, J.-C. Leprêtre, S. Patoux, and F. Alloin, “Lithium/sulfur cell discharge mechanism: an original approach for intermediate species identification.,” *Anal. Chem.*, vol. 84, no. 9, pp. 3973–80, May 2012, doi: 10.1021/ac2032244.

[8] J. R. Dahn, “Phase diagram of LixC6,” *Phys. Rev. B*, vol. 44, no. 17, pp. 9170–9177, Nov. 1991, [Online]. Available: http://link.aps.org/doi/10.1103/PhysRevB.44.9170.

[9] M. N. Obrovac and L. Christensen, “Structural Changes in Silicon Anodes during Lithium Insertion/Extraction,” *Electrochem. Solid-State Lett.*, vol. 7, no. 5, pp. A93–A96, 2004, doi: 10.1149/1.1652421.

[10] S. D. Beattie, D. Larcher, M. Morcrette, B. Simon, and J.-M. Tarascon, “Si Electrodes for Li-Ion Batteries—A New Way to Look at an Old Problem,” *J. Electrochem. Soc.*, vol. 155, no. 2, pp. A158–A163, 2008, doi: 10.1149/1.2817828.

[11] J. W. Wang *et al.*, “Two-phase electrochemical lithiation in amorphous silicon.,” *Nano Lett.*, vol. 13, no. 2, pp. 709–715, Feb. 2013, doi: 10.1021/nl304379k.

[12] L. Chen, K. Wang, X. Xie, and J. Xie, “Effect of vinylene carbonate (VC) as electrolyte additive on electrochemical performance of Si film anode for lithium ion batteries,” *J. Power Sources*, vol. 174, no. 2, pp. 538–543, Dec. 2007, doi: 10.1016/j.jpowsour.2007.06.149.

[13] I. a. Profatilova, C. Stock, A. Schmitz, S. Passerini, and M. Winter, “Enhanced thermal stability of a lithiated nano-silicon electrode by fluoroethylene carbonate and vinylene carbonate,” *J. Power Sources*, vol. 222, pp. 140–149, Jan. 2013, doi: 10.1016/j.jpowsour.2012.08.066.

[14] L. Leveau, B. Laïk, J.-P. Pereira-Ramos, A. Gohier, P. Tran-Van, and C.-S. Cojocaru, “Cycling strategies for optimizing silicon nanowires performance as negative electrode for lithium battery,” *Electrochim. Acta*, vol. 157, pp. 218–224, 2015, doi: https://doi.org/10.1016/j.electacta.2015.01.037.

[15] S. Ohara, J. Suzuki, K. Sekine, and T. Takamura, “A thin film silicon anode for Li-ion batteries having a very large specific capacity and long cycle life,” *J. Power Sources*, vol. 136, no. 2, pp. 303–306, Oct. 2004, doi: 10.1016/j.jpowsour.2004.03.014.

[16] T. L. Kulova, a. M. Skundin, Y. V. Pleskov, E. I. Terukov, and O. I. Kon’kov, “Lithium insertion into amorphous silicon thin-film electrodes,” *J. Electroanal. Chem.*, vol. 600, no. 1, pp. 217–225, Feb. 2007, doi: 10.1016/j.jelechem.2006.07.002.

[17] S. K. Soni, B. W. Sheldon, X. Xiao, and A. Tokranov, “Thickness effects on the lithiation of amorphous silicon thin films,” *Scr. Mater.*, vol. 64, no. 4, pp. 307–310, Feb. 2011, doi: 10.1016/j.scriptamat.2010.10.003.

[18] M. Green, E. Fielder, B. Scrosati, M. Wachtler, and J. S. Moreno, “Structured Silicon Anodes for Lithium Battery Applications,” *Electrochem. Solid-State Lett.*, vol. 6, no. 5, pp. A75–A79, 2003, doi: 10.1149/1.1563094.

[19] W. J. H. Borghols, “Lithium insertion in nanostructured titanates,” 2010.

[20] A. Nyman, M. Behm, and G. Lindbergh, “Electrochemical characterisation and modelling of the mass transport phenomena in LiPF6–EC–EMC electrolyte,” *Electrochim. Acta*, vol. 53, no. 22, pp. 6356–6365, Sep. 2008, doi: 10.1016/j.electacta.2008.04.023.

[21] P. Yu, B. N. Popov, J. A. Ritter, and R. E. White, “Determination of the Lithium Ion Diffusion Coefficient in Graphite,” *J. Electrochem. Soc.*, vol. 146, no. 1, pp. 8–14, Jan. 1999, doi: 10.1149/1.1391556.

[22] M. Wagemaker, A. P. M. Kentgens, A. A. Van Well, and F. M. Mulder, “Two Phase Morphology Limits Lithium Diffusion in TiO 2 (Anatase): A 7 Li MAS NMR Study,” vol. 2, no. 16, pp. 11454–11461, 2001.

[23] Q. Xu and G. Wan, “Rechargeable Li/LiMn2O4 batteries with a polymeric solid electrolyte,” *J. Power Sources*, vol. 41, no. 3, pp. 315–320, Jan. 1993, doi: http://dx.doi.org/10.1016/0378-7753(93)80049-U.

[24] P. P. Prosini, M. Lisi, D. Zane, and M. Pasquali, “Determination of the chemical diffusion coefficient of lithium in LiFePO 4,” vol. 148, pp. 45–51, 2002.

[25] L. A. Tio, K. Shen, H. Chen, F. Klaver, F. M. Mulder, and M. Wagemaker, “Impact of Particle Size on the Non-Equilibrium Phase Transition of Lithium-Inserted Anatase TiO 2,” 2014, doi: 10.1021/cm4037346.

[26] S. K. Panda, Y. Yoon, H. S. Jung, W.-S. Yoon, and H. Shin, “Nanoscale size effect of titania (anatase) nanotubes with uniform wall thickness as high performance anode for lithium-ion secondary battery,” *J. Power Sources*, vol. 204, pp. 162–167, Apr. 2012, doi: 10.1016/j.jpowsour.2011.12.048.

[27] M. Wagemaker, G. J. Kearley, A. A. van Well, H. Mutka, and F. M. Mulder, “Multiple Li Positions inside Oxygen Octahedra in Lithiated TiO2 Anatase,” *J. Am. Chem. Soc.*, vol. 125, no. 3, pp. 840–848, Jan. 2003, doi: 10.1021/ja028165q.

[28] A. a. Belak, Y. Wang, and A. Van der Ven, “Kinetics of Anatase Electrodes: The Role of Ordering, Anisotropy, and Shape Memory Effects,” *Chem. Mater.*, vol. 24, no. 15, pp. 2894–2898, Aug. 2012, doi: 10.1021/cm300881t.

[29] S. K. Panda, S. Lee, W.-S. Yoon, and H. Shin, “Reversible phase transformation of titania (anatase) nanotubes upon electrochemical lithium-intercalation observed by ex situ transmission electron microscopy,” *J. Power Sources*, vol. 249, pp. 59–65, Mar. 2014, doi: 10.1016/j.jpowsour.2013.10.048.

[30] A. Auer, E. Portenkirchner, T. Götsch, C. Valero-Vidal, S. Penner, and J. Kunze-Liebhäuser, “Preferentially Oriented TiO2Nanotubes as Anode Material for Li-Ion Batteries: Insight into Li-Ion Storage and Lithiation Kinetics,” *ACS Appl. Mater. Interfaces*, vol. 9, no. 42, pp. 36828–36836, 2017, doi: 10.1021/acsami.7b11388.

[31] V. Likodimos, T. Stergiopoulos, P. Falaras, J. Kunze, and P. Schmuki, “Phase Composition, Size, Orientation, and Antenna Effects of Self-Assembled Anodized Titania Nanotube Arrays: A Polarized Micro-Raman Investigation,” *J. Phys. Chem. C*, vol. 112, no. 33, pp. 12687–12696, Aug. 2008, doi: 10.1021/jp8027462.

[32] Z. Yang, Z. Ma, D. Pan, D. Chen, F. Xu, and S. Chen, “Enhancing the performance of front-illuminated dye-sensitized solar cells with highly [001] oriented, single-crystal-like TiO2nanotube arrays,” *Ceram. Int.*, vol. 40, no. 1 PART A, pp. 173–180, 2014, doi: 10.1016/j.ceramint.2013.05.119.

[33] J. Shin, J. H. Joo, D. Samuelis, and J. Maier, “Oxygen-Deficient TiO2−δ Nanoparticles via Hydrogen Reduction for High Rate Capability Lithium Batteries,” *Chem. Mater.*, vol. 24, pp. 543–551, 2012.

[34] Z. Lu, C.-T. Yip, L. Wang, H. Huang, and L. Zhou, “Hydrogenated TiO 2 Nanotube Arrays as High-Rate Anodes for Lithium-Ion Microbatteries,” *Chempluschem*, vol. 77, no. 11, pp. 991–1000, Nov. 2012, doi: 10.1002/cplu.201200104.

[35] J. M. Macak *et al.*, “TiO2 nanotubes: Self-organized electrochemical formation, properties and applications,” *Curr. Opin. Solid State Mater. Sci.*, vol. 11, no. 1–2, pp. 3–18, Feb. 2007, doi: 10.1016/j.cossms.2007.08.004.

[36] T. Xia *et al.*, “Amorphous carbon-coated TiO2 nanocrystals for improved lithium-ion battery and photocatalytic performance,” *Nano Energy*, vol. 6, pp. 109–118, 2014, doi: 10.1016/j.nanoen.2014.03.012.

[37] D. Fang, Z. Luo, K. Huang, and D. C. Lagoudas, “Effect of heat treatment on morphology, crystalline structure and photocatalysis properties of TiO2 nanotubes on Ti substrate and freestanding membrane,” *Appl. Surf. Sci.*, vol. 257, no. 15, pp. 6451–6461, Feb. 2011, doi: 10.1016/j.apsusc.2011.02.037.

[38] A. Ghicov *et al.*, “TiO2 nanotubes in dye-sensitized solar cells: critical factors for the conversion efficiency.,” *Chem. Asian J.*, vol. 4, no. 4, pp. 520–5, Apr. 2009, doi: 10.1002/asia.200800441.

[39] I. Hanzu, V. Hornebecq, T. Djenizian, and P. Knauth, “In situ study of electrochromic properties of self-assembled TiO2 nanotubes,” *Comptes Rendus Chim.*, vol. 16, no. 1, pp. 96–102, Jan. 2013, doi: http://dx.doi.org/10.1016/j.crci.2012.11.005.

[40] P. Roy, S. Berger, and P. Schmuki, “TiO2 nanotubes: synthesis and applications.,” *Angew. Chem. Int. Ed. Engl.*, vol. 50, no. 13, pp. 2904–2939, Mar. 2011, doi: 10.1002/anie.201001374.

[41] N. Cabrera and N. F. Mott, “Theory of the oxidation of metals,” *Rep. Prog. Phys.*, vol. 163, 1949.

[42] Y. Xu and X. Yan, “Chapter 2 Physical Fundamentals of Chemical Vapour Deposition Gas Laws and Kinetic Theory,” *Chem. Vap. Depos. An Integr. Eng. Des. Adv. Mater.*, pp. 1–44, 2010, doi: 10.1007/978-1-84882-894-0_2.

[43] R. Curley, T. Mccormack, and M. Phipps, “Low-pressure CVD and Plasma- Enhanced CVD,” no. Cvd, pp. 1–5, 2012.

[44] M. J. Kushner, “A model for the discharge kinetics and plasma chemistry during plasma enhanced chemical vapor deposition of amorphous silicon,” *J. Appl. Phys.*, vol. 63, no. 8, pp. 2532–2551, Apr. 1988, doi: 10.1063/1.340989.

[45] A. J. Bard and L. R. Faulkner, “ELECTROCHEMICAL METHODS Fundamentals and Applications,” John Wiley & Sons, Inc., 2001.

[46] M. Doyle, T. F. Fuller, and J. Newman, “Modeling of Galvanostatic Charge and Discharge of the Lithium/Polymer/Insertion Cell,” *J. Electrochem. Soc.*, vol. 140, no. 6, pp. 1526–1533, 1993, doi: 10.1149/1.2221597.

[47] M. Doyle, T. F. Fuller, and J. Newman, “The importance of the lithium ion transference number in lithium/polymer cells,” *Electrochim. Acta*, vol. 39, no. 13, pp. 2073–2081, 1994, doi: 10.1016/0013-4686(94)85091-7.

[48] T. F. Fuller, M. Doyle, and J. Newman, “Relaxation Phenomena in Lithium-Ion-Insertion Cells,” *J. Electrochem. Soc.*, vol. 141, no. 4, pp. 982–990, 1994.

[49] D. G. Goodwin, H. Zhu, A. M. Colclasure, and R. J. Kee, “Modeling Electrochemical Oxidation of Hydrogen on Ni–YSZ Pattern Anodes,” *J. Electrochem. Soc.*, vol. 156, no. 9, pp. B1004–B1021, 2009, doi: 10.1149/1.3148331.

[50] A. M. Colclasure and R. J. Kee, “Thermodynamically consistent modeling of elementary electrochemistry in lithium-ion batteries,” *Electrochim. Acta*, vol. 55, no. 28, pp. 8960–8973, 2010, doi: 10.1016/j.electacta.2010.08.018.

[51] J. S. Newman, *Electrochemical systems*, 2nd ed. Englewood Cliffs (N.J.): Prentice-Hall, 1991.

[52] K. Smith and C. Y. Wang, “Solid-state diffusion limitations on pulse operation of a lithium ion cell for hybrid electric vehicles,” *J. Power Sources*, vol. 161, no. 1, pp. 628–639, 2006, doi: 10.1016/j.jpowsour.2006.03.050.

[53] N. Sato, *Electrochemistry at Metal and Semiconductor Electrodes*. Elsevier Science B.V., 1998.

[54] C. H. Hamann, A. Hamnett, and W. Vielstich, *Electrochemistry, 2nd, Completely Revised and Updated Edition*. Wiley-VCH Verlag GmbH & Co. KGaA, 2007.

[55] M. E. Orazem and B. Tribollet, *Electrochemical Impedance Spectroscopy*. John Wiley & Sons, Inc., 2008.

[56] K. Izutsu, *Electrochemistry in Nonaqueous Solutions*. Weinheim, Germany: Wiley-VCH Verlag GmbH & Co. KGaA, 2009.

[57] J. I. Goldstein *et al.*, *Scanning Electron Microscopy and X-ray Microanalysis*. Boston, MA: Springer US, 2003.

[58] W. Demtröder, *Experimentalphysik 3*. Berlin, Heidelberg: Springer Berlin Heidelberg, 2010.

[59] R. Loudon, “The Raman effect in crystals,” *Adv. Phys.*, vol. 13, no. 52, pp. 423–482, Oct. 1964, doi: 10.1080/00018736400101051.

[60] F. Siebert and P. Hildebrandt, “Theory of Infrared Absorption and Raman Spectroscopy ,” in *Vibrational Spectroscopy in Life Science*, Wiley-VCH Verlag GmbH & Co. KGaA, 2008, pp. 11–61.

[61] P. Vandenabeele, *Practical Raman Spectroscopy*. John Wiley & Sons, Ltd, 2013.

[62] J. C. V. Gilmore and I.S., *Surface Analysis – The Principal Techniques 2nd Edition*. 2009.

[63] R. White, *Chromatography/Fourier Transform Infrared Spectroscopy and its Applications*. 1989.

[64] D. Attwood, *Soft X-Rays and Extreme Ultraviolet Radiation: Principles and Applications*. 2007.

[65] J. Als-Nielsen and D. McMorrow, *Elements of Modern X-ray Physics*. Hoboken, NJ, USA: Wiley, 2011.

[66] L. G. Parratt, "Surface Studies of Solids by Total Reflection of X-Rays," *Phys. Rev.*, vol. 95, no. 2, pp. 359–369, Jul. 1954, doi: 10.1103/PhysRev.95.359.

[67] F. Abelès and J. P. Radium, "La théorie générale des couches minces Florin Abelès To cite this version : HAL Id : jpa-00234261 I ;," vol. 11, no. 7, pp. 307–309, 1950.

[68] L. Névot and P. Croce, "Caractérisation des surfaces par réflexion rasante de rayons X. Application à l'étude du polissage de quelques verres silicates," *Rev. Phys. Appliquée*, vol. 15, no. 3, pp. 761–779, 1980, doi: 10.1051/rphysap:01980001503076100.

[69] G. H. Vineyard, "Grazing-incidence diffraction and the distorted-wave approximation for the study of surfaces," *Phys. Rev. B*, vol. 26, no. 8, pp. 4146–4159, Oct. 1982, [Online]. Available: https://link.aps.org/doi/10.1103/PhysRevB.26.4146.

[70] Y. Yoneda, "Anomalous Surface Reflection of X Rays," *Phys. Rev.*, vol. 131, no. 5, pp. 2010–2013, Sep. 1963, [Online]. Available: https://link.aps.org/doi/10.1103/PhysRev.131.2010.

[71] A. Meyer (Institute of Physical Chemistry; University of Hamburg), "GISAXS." http://www.gisaxs.de.

[72] E. Walenta, "Small angle x-ray scattering. Von O. GLATTER und O. KRATKY. London: Academic Press Inc. Ltd. 1982. ISBN 0-12-286280-5. X, 515 Seiten.," *Acta Polym.*, vol. 36, no. 5, p. 296, 1985, doi: 10.1002/actp.1985.010360520.

[73] G. Renaud, R. Lazzari, and F. Leroy, "Probing surface and interface morphology with Grazing Incidence Small Angle X-Ray Scattering," *Surf. Sci. Rep.*, vol. 64, no. 8, pp. 255–380, 2009, doi: 10.1016/j.surfrep.2009.07.002.

[74] A. K. Singh, *Advanced X-ray Techniques in Research And Industries*. Ios Pr Inc, 2005.

[75] C. S. Fadley, “Basic concepts of X-ray photoelectron spectroscopy.” in Electron Spectroscopy: Theory, Techniques, and Applications, C. R. Brundle and A. D. Baker, Eds., vol. 2, London: Academic Press, ch. 1, pp. 1–156, 1978, [Online]. Available: http://fadley.physics.ucdavis.edu/BasicConceptsofXPS.pdf.

[76] A. B. Christie, “X-ray photoelectron spectroscopy.” in Methods of Surface Analysis, Techniques and Applications, J. M. Walls, Ed., Cambridge: Cambridge University Press, ch. 5, pp. 127–168, 1989, doi: 10.1002/bbpc.19890930931.

[77] S. Hüfner, “Photoelectron Spectroscopy, Principles and Applications.” 3rd ed. Belin Heidelberg: Springer-Verlag, 2003, doi: 10.1007/978-3-662-09280-4.

[78] “Research Neutron Source Heinz Maier-Leibnitz (FRM II) Technical University of Munich.”

[79] O. Wunnicke *et al.*, “Stabilization of Thin Polymeric Bilayer Films on Top of Semiconductor Surfaces,” *Langmuir*, vol. 19, no. 20, pp. 8511–8520, Sep. 2003, doi: 10.1021/la0344837.

[80] M. Stamm and D. W. Schubert, “Interfaces Between Incompatible Polymers,” *Annu. Rev. Mater. Sci.*, vol. 25, no. 1, pp. 325–356, Aug. 1995, doi: 10.1146/annurev.ms.25.080195.001545.

[81] R. Kampmann *et al.*, “Horizontal ToF-neutron reflectometer REFSANS at FRM-II Munich/Germany: First tests and status,” *Phys. B Condens. Matter*, vol. 385–386, pp. 1161–1163, 2006, doi: https://doi.org/10.1016/j.physb.2006.05.399.

[82] P. Müller-Buschbaum, E. Metwalli, J.-F. Moulin, V. Kudryashov, M. Haese-Seiller, and R. Kampmann, “Time of flight grazing incidence small angle neutron scattering,” *Eur. Phys. J. Spec. Top.*, vol. 167, no. 1, pp. 107–112, Feb. 2009, doi: 10.1140/epjst/e2009-00944-5.

[83] G. Kaune, M. Haese-Seiller, R. Kampmann, J.-F. Moulin, Q. Zhong, and P. Müller-Buschbaum, “TOF-GISANS investigation of polymer infiltration in mesoporous TiO2 films for photovoltaic applications,” *J. Polym. Sci. Part B Polym. Phys.*, vol. 48, no. 14, pp. 1628–1635, Mar. 2010, doi: 10.1002/polb.21964.

[84] D. R. Tilley *et al.*, “Energy levels of light nuclei A=5, 6, 7,” *Nucl. Phys. A*, vol. 708, no. 1, pp. 3–163, 2002, doi: https://doi.org/10.1016/S0375-9474(02)00597-3.

[85] B. Pritychenko and S. F. Mughabghab, “Neutron Thermal Cross Sections, Westcott Factors, Resonance Integrals, Maxwellian Averaged Cross Sections and Astrophysical Reaction Rates Calculated from the ENDF/B-VII.1, JEFF-3.1.2, JENDL-4.0, ROSFOND-2010, CENDL-3.1 and EAF-2010 Evaluated Data Librari,” *Nucl. Data Sheets*, vol. 113, no. 12, pp. 3120–3144, 2012, doi: https://doi.org/10.1016/j.nds.2012.11.007.

[86] A. L. Meier, “Determination of lithium isotopes at natural abundance levels by atomic absorption spectrometry,” *Anal. Chem.*, vol. 54, no. 13, pp. 2158–2161, Nov. 1982, doi: 10.1021/ac00250a007.

[87] L. Canella, P. Kudějová, R. Schulze, A. Türler, and J. Jolie, “Characterisation and optimisation of the new Prompt Gamma-ray Activation Analysis (PGAA) facility at FRM II,” *Nucl. Instruments Methods Phys. Res. Sect. A Accel. Spectrometers, Detect. Assoc. Equip.*, vol. 636, no. 1, pp. 108–113, 2011, doi: https://doi.org/10.1016/j.nima.2011.01.126.

[88] J. Lichtinger *et al.*, “Position sensitive measurement of lithium traces in brain tissue with neutrons,” *Med. Phys.*, vol. 40, no. 2, p. n/a-n/a, 2013, doi: 10.1118/1.4774053.

[89] M. Lindroos and Ö. Skeppstedt, “A position sensitive photon detector used as a charged particle detector,” *Nucl. Instruments Methods Phys. Res. Sect. A Accel. Spectrometers, Detect. Assoc. Equip.*, vol. 306, no. 1, pp. 225–228, 1991, doi: https://doi.org/10.1016/0168-9002(91)90325-K.

[90] Q. L. Wu *et al.*, “Aligned TiO2 Nanotube Arrays As Durable Lithium-Ion Battery Negative Electrodes,” *J. Phys. Chem. C*, vol. 116, no. 35, pp. 18669–18677, Sep. 2012, doi: 10.1021/jp3072266.

[91] K. Zhu, Q. Wang, J.-H. Kim, A. A. Pesaran, and A. J. Frank, “Pseudocapacitive Lithium-Ion Storage in Oriented Anatase TiO2 Nanotube Arrays,” *J. Phys. Chem. C*, vol. 116, no. 22, pp. 11895–11899, Jun. 2012, doi: 10.1021/jp301884x.

[92] G. Neri, J. Lichtinger, J. Brumbarov, C. Rüdiger, R. Gernhäuser, and J. Kunze-Liebhäuser, “Tracking areal lithium densities from neutron activation - Quantitative Li determination in self-organized TiO2 nanotube anode materials for Li-ion batteries,” *Phys. Chem. Chem. Phys.*, vol. 19, no. 12, pp. 8602–8611, 2017, doi: 10.1039/c7cp00180k.

[93] J. Brumbarov, J. P. Vivek, S. Leonardi, C. Valero-Vidal, E. Portenkirchner, and J. Kunze-Liebhäuser, “Oxygen deficient, carbon coated self-organized TiO 2 nanotubes as anode material for Li-ion intercalation,” *J. Mater. Chem. A*, vol. 3, no. 32, pp. 16469–16477, 2015, doi: 10.1039/C5TA03621F.

[94] T. Ohzuku, T. Kodama, and T. Hirai, “Electrochemistry of anatase titanium dioxide in lithium nonaqueous cells,” *J. Power Sources*, vol. 14, pp. 153–166, 1985.

[95] M. Mancini, P. Kubiak, J. Geserick, R. Marassi, N. Hüsing, and M. Wohlfahrt-Mehrens, “Mesoporous anatase TiO2 composite electrodes: Electrochemical characterization and high rate performances,” *J. Power Sources*, vol. 189, no. 1, pp. 585–589, Apr. 2009, doi: 10.1016/j.jpowsour.2008.10.050.

[96] R. Hahn *et al.*, “Semimetallic TiO2 nanotubes.,” *Angew. Chem. Int. Ed. Engl.*, vol. 48, no. 39, pp. 7236–7239, Jan. 2009, doi: 10.1002/anie.200902207.

[97] J. Xu, C. Jia, B. Cao, and W. F. Zhang, “Electrochemical properties of anatase TiO2 nanotubes as an anode material for lithium-ion batteries,” *Electrochim. Acta*, vol. 52, no. 28, pp. 8044–8047, 2007, doi: 10.1016/j.electacta.2007.06.077.

[98] Q. Wang, Z. Wen, and J. Li, “Solvent-Controlled Synthesis and Electrochemical Lithium Storage of One-Dimensional TiO2 Nanostructures,” *Inorg. Chem.*, vol. 45, no. 17, pp. 6944–6949, Aug. 2006, doi: 10.1021/ic060477x.

[99] G. F. Ortiz, I. Hanzu, T. Djenizian, P. Lavela, J. L. Tirado, and P. Knauth, “Alternative Li-Ion Battery Electrode Based on Self-Organized Titania Nanotubes,” *Chem. Mater.*, vol. 21, no. 1, pp. 63–67, Jan. 2009, doi: 10.1021/cm801670u.

[100] R. van de Krol, A. Goossens, and J. Schoonman, “Spatial Extent of Lithium Intercalation in Anatase TiO2,” *J. Phys. Chem. B*, vol. 103, no. 34, pp. 7151–7159, Aug. 1999, doi: 10.1021/jp9909964.

[101] J. Brumbarov and J. Kunze-Liebhäuser, “Silicon on conductive self-organized TiO2 nanotubes – A high capacity anode material for Li-ion batteries,” *J. Power Sources*, vol. 258, pp. 129–133, Jul. 2014, doi: 10.1016/j.jpowsour.2014.02.049.

[102] F. Yubero, A. Barranco, J. A. Mejias, J. P. Espinos, and A. R. Gonzalez-Elipe, “Spectroscopic characterisation and chemical reactivity of silicon monoxide layers deposited on Cu (100),” *Surf. Sci.*, vol. 458, pp. 229–238, 2000.

[103] F. G. Bell and L. Ley, “Photoemission study of SiOx (0<x<2) alloys,” *Phys. Rev. B*, vol. 37, no. 14, pp. 8383–8393, 1988.

[104] C. Rüdiger *et al.*, “Surface analytical study of carbothermally reduced titania films for electrocatalysis application,” *Electrochim. Acta*, vol. 71, pp. 1–9, Jun. 2012, doi: 10.1016/j.electacta.2012.02.044.

[105] V. Baranchugov, E. Markevich, E. Pollak, G. Salitra, and D. Aurbach, “Amorphous silicon thin films as a high capacity anodes for Li-ion batteries in ionic liquid electrolytes,” *Electrochem. commun.*, vol. 9, no. 4, pp. 796–800, Apr. 2007, doi: 10.1016/j.elecom.2006.11.014.

[106] L. B. Chen, J. Y. Xie, H. C. Yu, and T. H. Wang, “An amorphous Si thin film anode with high capacity and long cycling life for lithium ion batteries,” *J. Appl. Electrochem.*, vol. 39, no. 8, pp. 1157–1162, Jan. 2009, doi: 10.1007/s10800-008-9774-1.

[107] C. Pereira-Nabais *et al.*, “Interphase chemistry of Si electrodes used as anodes in Li-ion batteries,” *Appl. Surf. Sci.*, vol. 266, pp. 5–16, Feb. 2013, doi: 10.1016/j.apsusc.2012.10.165.

[108] H. Ota, Y. Sakata, A. Inoue, and S. Yamaguchi, “Analysis of Vinylene Carbonate Derived SEI Layers on Graphite Anode,” *J. Electrochem. Soc.*, vol. 151, no. 10, p. A1659, 2004, doi: 10.1149/1.1785795.

[109] I. Buchberger *et al.*, “Aging Analysis of Graphite/LiNi $_{1/3}$ Mn $_{1/3}$ Co $_{1/3}$ O $_{2}$ Cells Using XRD, PGAA, and AC Impedance,” *J. Electrochem. Soc.*, vol. 162, no. 14, pp. A2737–A2746, 2015, doi: 10.1149/2.0721514jes.

[110] M. Wagemaker, a P. M. Kentgens, and F. M. Mulder, “Equilibrium lithium transport between nanocrystalline phases in intercalated TiO(2) anatase.,” *Nature*, vol. 418, no. 6896, pp. 397–399, Jul. 2002, doi: 10.1038/nature00901.

[111] S. Brutti, V. Gentili, H. Menard, B. Scrosati, and P. G. Bruce, “TiO2-(B) Nanotubes as Anodes for Lithium Batteries: Origin and Mitigation of Irreversible Capacity,” *Adv. Energy Mater.*, vol. 2, no. 3, pp. 322–327, 2012, doi: 10.1002/aenm.201100492.

[112] S. K. Aghara, S. Venkatraman, A. Manthiram, and E. Alvarez II, “Investigation of hydrogen content in chemically delithiated lithium-ion battery cathodes using prompt gamma activation analysis,” *J. Radioanal. Nucl. Chem.*, vol. 265, no. 2, pp. 321–328, 2005, doi: 10.1007/s10967-005-0828-0.

[113] F. Wang *et al.*, “Chemical Distribution and Bonding of Lithium in Intercalated Graphite: Identification with Optimized Electron Energy Loss Spectroscopy,” *ACS Nano*, vol. 5, no. 2, pp. 1190–1197, Feb. 2011, doi: 10.1021/nn1028168.

[114] D. Santhanagopalan *et al.*, “Interface Limited Lithium Transport in Solid-State Batteries,” *J. Phys. Chem. Lett.*, vol. 5, no. 2, pp. 298–303, Jan. 2014, doi: 10.1021/jz402467x.

[115] D. Wang, L. Liu, X. Sun, and T.-K. Sham, “Observation of lithiation-induced structural variations in TiO2 nanotube arrays by X-ray absorption fine structure,” *J. Mater. Chem. A*, vol. 3, no. 1, pp. 412–419, 2015, doi: 10.1039/C4TA04873C.

[116] K. Lee, A. Mazare, and P. Schmuki, “One-Dimensional Titanium Dioxide Nanomaterials: Nanotubes,” *Chem. Rev.*, vol. 114, no. 19, pp. 9385–9454, Oct. 2014, doi: 10.1021/cr500061m.

[117] “Temperature-dependent structural transformations of hydrothermally synthesized cubic Li2TiO3 studied by in-situ neutron diffraction ,” *Zeitschrift für Kristallographie Crystalline Materials* , vol. 226. p. 53, 2011, doi: 10.1524/zkri.2011.1286.

[118] H. Xiong *et al.*, “Self-Improving Anode for Lithium-Ion Batteries Based on Amorphous to Cubic Phase Transition in TiO 2 Nanotubes,” pp. 3181–3187, 2012.

[119] W. J. H. Borghols *et al.*, “Lithium Storage in Amorphous TiO[sub 2] Nanoparticles,” *J. Electrochem. Soc.*, vol. 157, no. 5, p. A582, 2010, doi: 10.1149/1.3332806.

[120] M. Wan, W. Li, Y. Long, and Y. Tu, “Electrochemical determination of tryptophan based on Si-doped nano-TiO2 modified glassy carbon electrode,” *Anal. Methods*, vol. 4, no. 9, pp. 2860–2865, 2012, doi: 10.1039/C2AY25474C.

[121] S. Liu *et al.*, “Foamed single-crystalline anatase nanocrystals exhibiting enhanced photocatalytic activity,” *J. Mater. Chem. A*, vol. 3, no. 34, pp. 17837–17848, 2015, doi: 10.1039/C5TA04682C.

[122] G. Li, L. Li, J. Boerio-Goates, and B. F. Woodfield, “High Purity Anatase TiO2 Nanocrystals: Near Room-Temperature Synthesis, Grain Growth Kinetics, and Surface Hydration Chemistry,” *J. Am. Chem. Soc.*, vol. 127, no. 24, pp. 8659–8666, Jun. 2005, doi: 10.1021/ja050517g.

[123] T. Bezrodna, G. Puchkovska, V. Shimanovska, I. Chashechnikova, T. Khalyavka, and J. Baran, “Pyridine-TiO2 surface interaction as a probe for surface active centers analysis,” *Appl. Surf. Sci.*, vol. 214, no. 1, pp. 222–231, 2003, doi: https://doi.org/10.1016/S0169-4332(03)00346-5.

[124] E. Filippo *et al.*, “Efficient, Green Non-Aqueous Microwave-Assisted Synthesis of Anatase TiO_2 and Pt Loaded TiO_2 Nanorods with High Photocatalytic Performance,” *Nanomater. Nanotechnol.*, vol. 5, p. 31, 2015, doi: 10.5772/61147.

[125] X. Li, H. Liu, J. Wang, H. Cui, X. Zhang, and F. Han, “Preparation of YAG:Nd nano-sized powder by co-precipitation method,” *Mater. Sci. Eng. A*, vol. 379, no. 1, pp. 347–350, 2004, doi: https://doi.org/10.1016/j.msea.2004.03.014.

[126] J. T. Kloprogge, D. Wharton, L. Hickey, and R. L. Frost, “Infrared and Raman study of interlayer anions CO32−, NO3−, SO42− and ClO4− in Mg/Al-hydrotalcite,” *Am. Mineral.*, vol. 87, no. 5–6, pp. 623–629, May 2002, [Online]. Available: http://dx.doi.org/10.2138/am-2002-5-604.

[127] P. Yang, Q. Tang, and B. He, “Toward elevated light harvesting: efficient dye-sensitized solar cells with titanium dioxide/silica photoanodes,” *RSC Adv.*, vol. 5, no. 57, pp. 46260–46266, 2015, doi: 10.1039/C5RA06584D.

[128] Y. Li *et al.*, “Molecular assembly and luminescent properties of europium polymeric hybrid material based on Si–O–Ti hosts,” *Mater. Lett.*, vol. 152, pp. 170–172, 2015, doi: https://doi.org/10.1016/j.matlet.2015.03.127.

[129] C. Rudiger *et al.*, “Fabrication of Ti substrate grain dependent C/TiO2 composites through carbothermal treatment of anodic TiO2,” *Phys. Chem. Chem. Phys.*, vol. 18, no. 13, pp. 9220–9231, 2016, doi: 10.1039/C5CP07727C.

[130] S. Xiao *et al.*, “CNTs threaded (001) exposed TiO2 with high activity in photocatalytic NO oxidation,” *Nanoscale*, vol. 8, no. 5, pp. 2899–2907, 2016, doi: 10.1039/C5NR07589K.

[131] J. Tang and H. M. Meng, “TiO2-modified CNx nanowires as a Pt electrocatalyst support with high activity and durability for the oxygen reduction reaction,” *Phys. Chem. Chem. Phys.*, vol. 18, no. 3, pp. 1500–1506, 2016, doi: 10.1039/C5CP06115F.

[132] S. P. S. Porto, P. A. Fleury, and T. C. Damen, “Raman Spectra of TiO2, MgF2, ZnF2, FeF2, and MnF2,” *Phys. Rev.*, vol. 154, no. 2, pp. 522–526, Feb. 1967, [Online]. Available: https://link.aps.org/doi/10.1103/PhysRev.154.522.

[133] J. Zhang, M. Li, Z. Feng, J. Chen, and C. Li, “UV Raman Spectroscopic Study on TiO2. I. Phase Transformation at the Surface and in the Bulk,” *J. Phys. Chem. B*, vol. 110, no. 2, pp. 927–935, Jan. 2006, doi: 10.1021/jp0552473.

[134] M. Smirnov and R. Baddour-Hadjean, “Li intercalation in TiO2 anatase: Raman spectroscopy and lattice dynamic studies,” *J. Chem. Phys.*, vol. 121, no. 5, pp. 2348–2355, Jul. 2004, doi: 10.1063/1.1767993.

[135] A. C. Ferrari and J. Robertson, “Interpretation of Raman spectra of disordered and amorphous carbon,” *Phys. Rev. B*, vol. 61, no. 20, pp. 14095–14107, May 2000, [Online]. Available: https://link.aps.org/doi/10.1103/PhysRevB.61.14095.

[136] C. Li, “Identifying the isolated transition metal ions/oxides in molecular sieves and on oxide supports by UV resonance Raman spectroscopy,” *J. Catal.*, vol. 216, no. 1, pp. 203–212, 2003, doi: https://doi.org/10.1016/S0021-9517(02)00107-0.

[137] G. Busca, G. Ramis, J. M. G. Amores, V. S. Escribano, and P. Piaggio, “FT Raman and FTIR studies of titanias and metatitanate powders,” *J. Chem. Soc. Faraday Trans.*, vol. 90, no. 20, pp. 3181–3190, 1994, doi: 10.1039/FT9949003181.

[138] N. Paul *et al.*, “GISAXS and TOF-GISANS studies on surface and depth morphology of self-organized TiO 2 nanotube arrays: model anode material in Li-ion batteries,” *J. Appl. Crystallogr.*, vol. 48, no. 2, pp. 444–454, Apr. 2015, doi: 10.1107/S1600576715002204.

[139] J. Mane Mane *et al.*, “GISAXS study of carbon nanotubes grown by CVD,” *Phys. status solidi – Rapid Res. Lett.*, vol. 1, no. 3, pp. 122–124, 2007, doi: 10.1002/pssr.200701046.

[140] G. Kaune, M. Haese-Seiller, R. Kampmann, J.-F. Moulin, Q. Zhong, and P. Müller-Buschbaum, “TOF-GISANS investigation of polymer infiltration in mesoporous TiO2 films for photovoltaic applications,” *J. Polym. Sci. Part B Polym. Phys.*, vol. 48, no. 14, pp. 1628–1635, 2010, doi: 10.1002/polb.21964.

[141] M. Rawolle *et al.*, “Infiltration of Polymer Hole-Conductor into Mesoporous Titania Structures for Solid-State Dye-Sensitized Solar Cells,” *ACS Appl. Mater. Interfaces*, vol. 5, no. 3, pp. 719–729, Feb. 2013, doi: 10.1021/am302255c.

[142] H. Dosch, B. W. Batterman, and D. C. Wack, “Depth-Controlled Grazing-Incidence Diffraction of Synchrotron X Radiation,” *Phys. Rev. Lett.*, vol. 56, no. 11, pp. 1144–1147, Mar. 1986, [Online]. Available: https://link.aps.org/doi/10.1103/PhysRevLett.56.1144.

[143] P. Müller-Buschbaum, G. Kaune, M. Haese-Seiller, and J.-F. Moulin, “Morphology determination of defect-rich diblock copolymer films with time-of-flight grazing-incidence small-angle neutron scattering,” *J. Appl. Crystallogr.*, vol. 47, no. 4, pp. 1228–1237, 2014, doi: 10.1107/S1600576714010991.

[144] R. Lazzari, “IsGISAXS: a program for grazing-incidence small-angle X-ray scattering analysis of supported islands,” *J. Appl. Crystallogr.*, vol. 35, no. 4, pp. 406–421, Aug. 2002, doi: 10.1107/S0021889802006088.

[145] K. Sarkar, C. J. Schaffer, D. M. Gonzalez, A. Naumann, J. Perlich, and P. Muller-Buschbaum, “Tuning the pore size of ZnO nano-grids via time-dependent solvent annealing,” *J. Mater. Chem. A*, vol. 2, no. 19, pp. 6945–6951, 2014, doi: 10.1039/C4TA00489B.

[146] A. Paul, N. Paul, P. Müller-Buschbaum, A. Bauer, and P. Böni, “Superparamagnetic regular nanopillar-like structures studied by grazing-incidence X-ray scattering: Effect of vertical correlation,” *J. Appl. Crystallogr.*, vol. 47, no. 3, pp. 1065–1076, 2014, doi: 10.1107/S1600576714008188.

[147] P. Ziegler *et al.*, “Self-organization of Fe clusters on mesoporous TiO2 templates,” *J. Appl. Crystallogr.*, vol. 47, no. 6, pp. 1921–1930, Dec. 2014, doi: 10.1107/S1600576714021049.

[148] B. Prasai, B. Cai, M. Rice, J. Lewis, and D. Drabold, *Properties of amorphous and crystalline titanium dioxide from first principles*, vol. 47. 2012.

[149] M. Rawolle *et al.*, “Nanostructuring of Titania Thin Films by a Combination of Microfluidics and Block-Copolymer-Based Sol–Gel Templating,” *Small*, vol. 7, no. 7, pp. 884–891, 2011, doi: 10.1002/smll.201001734.

8 Abbreviations

2D - two dimensional

AFM - atomic force microscopy

ATR-FTIR - attenuated total reflection Fourier-transform infra-red spectroscopy

BA - Born approximation

BSE - back scattered electrons

CE - counter electrode

CV - cyclic voltammogram

CVD - chemical vapor deposition

DC - direct current

DMC - dimethyl carbonate

DWBA - distorted wave Born approximation

EC - ethylene carbonate

EC - electrochemistry

EDL - electric double layer

EDX - energy dispersive X-ray analysis

EMC - ethyl methyl carbonate

FDWBA - effective form factor in distorted wave Born approximation

FEC - fluoroethylene-carbonate

FWHM - full width at half maximum

GCPL - galvanostatic cycling with potential limitation

GID - grazing incidence diffraction

GISANS - grazing incidence small angle neutron scattering

GISAXS - grazing incidence small angle X-ray scattering

GIUSAXS - grazing incidence ultra-small angle X- ray scattering

HDPP - high density polypropylene

IHP - inner Helmholtz plane

IR - infra red light

LFP - LiFePO4

NMR - nuclear magnetic resonance spectroscopy

OCP - open circuit potential

OHP - outer Helmholtz plane

OX - oxidized species

PECVD - plasma enhanced chemical vapor deposition

PFA - perfluoralkoxy-polymer

PGAA - prompt gamma-ray activation analysis

PNPI - Petersburg nuclear physics institute

PSD - silicon position-sensing UV photon detector

PTFE - polytetrafluoroethylene

RE - reference electrode

RED - reduced species

RF - radio frequency

RT - room temperature

SAED - selected area electron diffraction

SAXS - small angle X- ray scattering

sccm - standard cubic centimeter

SCL - space charge layer

SE - secondary electrons

SEI - solid Elektrolyte interface

SEM - scanning electron microscopy

SLD - scattering length density

STM - scanning tunneling microscopy

TEM - transmission electron microscopy

TOF-GISANS - time-of-flight grazing incidence small angle neutron scattering

UV - ultra violet light

VC - vinylene-carbonate

WE - working electrode

XPS - X-ray photo-electron spectroscopy

XRD - X-ray diffraction

XRR - X-ray reflectivity / X-ray reflectometry

9 Acknowledgments

My deepest gratitude goes to my dear family, my parents Krassimir and Elka Brumbarov, my sister Tzvetina, my beloved wife Irina and my two precious little girls Maya and Nora, who always supported me with all they have, believed in me and gave me all their love. I thank my parents in law Milko and Jasmina for the support they gave me and for helping out with the girls in the “COVID-19 time” when I was writing the last parts of this thesis.

I thank Prof. Dr. Julia Kunze-Liebhäuser for having me as her PhD student and sharing her office with me, for her guidance, for the freedom and trust she has given me to follow own research ideas and for the good time I had in her newly formed group.

I would like to thank Prof. Dr. Peter Müller-Buschbaum and Prof. Dr. Nora Brambilla for being the referees of this thesis.

I thank Dr. Fabio Di Fonzo from Instituto Italiano di Tecnologia for giving me the chance to try out new (risky) silicon deposition techniques, for the great time I had in his lab and for showing me the culinary highlights of Milan.

I thank my fellow researchers Celine Rüdiger, Christoph Traunsteiner, Carlos Valero-Vidal, Konstantinos Antonopoulos, Rianne Schöffler, Tine Brülle and Cornelia Ostermayr for the great time I had in the research group, for all the laughs and discussions we had, for sharing their knowledge with me and helping me out whenever I needed help. Special thanks go to Silvia Leonardi who spent many hours teaching me how to do SEM and how to synthesize titania nanotubes. I thank Siegfried Schreier for the support in building new experimental setups and for the musical accompaniment of our lab parties. At the end I also want to thank Markus Haß for excepting the hand drawn cell-designs I was giving him and producing real high-quality objects out of them in the workshop.

10 List of Publications

1. **J. Brumbarov**, J. P. Vivek, S. Leonardi, C. Valero-Vidal, E. Portenkirchner, and J. Kunze-Liebhäuser, "Oxygen deficient, carbon coated self-organized TiO 2 nanotubes as anode material for Li-ion intercalation," *J. Mater. Chem. A*, vol. 3, no. 32, pp. 16469–16477, 2015, doi: 10.1039/C5TA03621F.

2. **J. Brumbarov** and J. Kunze-Liebhäuser, "Silicon on conductive self-organized TiO2 nanotubes – A high capacity anode material for Li-ion batteries," *J. Power Sources*, vol. 258, pp. 129–133, Jul. 2014, doi: 10.1016/j.jpowsour.2014.02.049.

3. E. Portenkirchner, G. Neri, J. Lichtinger, **J. Brumbarov**, C. Rüdiger, R. Gernhäuser, and J. Kunze-Liebhäuser, "Tracking areal lithium densities from neutron activation - Quantitative Li determination in self-organized TiO2 nanotube anode materials for Li-ion batteries," *Phys. Chem. Chem. Phys.*, vol. 19, no. 12, pp. 8602–8611, 2017, doi: 10.1039/c7cp00180k.

4. N. Paul, **J. Brumbarov**, A. Paul, Y. Chen, J.F. Moulin, P. Müller-Buschbaum, J. Kunze-Liebhäuser, R. Gilles, "GISAXS and TOF-GISANS studies on surface and depth morphology of self-organized TiO 2 nanotube arrays: model anode material in Li-ion batteries," *J. Appl. Crystallogr.*, vol. 48, no. 2, pp. 444–454, Apr. 2015, doi: 10.1107/S1600576715002204.

5. C. Rüdiger, **J. Brumbarov**, F.Wiesinger, S.Leonardi, O. Paschos, C.Valero-Vidal, J. Kunze-Liebhäuser , "Ethanol Oxidation on TiOx Cy -Supported Pt Nanoparticles," *ChemCatChem*, vol. 5, no. 11, pp. 3219–3223, Nov. 2013, doi: 10.1002/cctc.201300217.